# Investigating the Magnetic Properties of Tissue with MRI Phase at 7T

by

Benjamin Charles Tendler, MPhys

Thesis submitted to the University of Nottingham
for the degree of Doctor of Philosophy




Sir Peter Mansfield Imaging Centre
University of Nottingham
2017

**Abstract**

In this thesis, the potential of MRI phase to reveal the magnetic properties of tissue is thoroughly investigated. Extending beyond the well established field of quantitative susceptibility mapping (QSM), consideration is given to the influence of susceptibility anisotropy, chemical exchange, non-spherical susceptibility inclusions and multi-compartmental signal evolution from both a theoretical and experimental viewpoint.

The first experimental chapter discusses a collaborative project with Cardiff University Brain Research Imaging Centre (CUBRIC) and the Department of Neurobiology in Tel-Aviv University to investigate neuroplasticity changes in rats. In this chapter the contribution from the SPMIC is described, detailing an analysis pipeline to generate and optimise isotropic susceptibility and $R_2^*(\vec{r})$ maps from multi-echo gradient echo (GE) *in-vivo* rat datasets obtained on a 7T Bruker Biospec 70/30 MR system.

The second experimental chapter investigates the potential of frequency difference mapping (FDM), a recently developed phase processing technique which characterises multi-compartmental signal evolution to probe microstructure content. In this chapter, a novel FDM processing algorithm is introduced which does not require the use of sophisticated phase unwrapping and image filtering. To test the effectiveness of the FDM algorithm on experimental data, ten healthy volunteers underwent a single-slice, sagittal, multi-echo GE scan on a Philips Achieva 7T MR system. Results revealed consistent contrast over the corpus callosum relative to the surrounding tissue and a high sensitivity to small changes in microstructure content. Though fitting experimental magnitude and frequency difference evolution to a three-pool white matter model, the signal evolution over the corpus callosum is described in terms of physical properties of the nerve fibres.

The final experimental chapter investigates the magnetic properties of skeletal muscle. A skeletal muscle sample (in the form of a section of pork tenderloin) was placed within an agar phantom and scanned via a multi-orientation, dual-echo GE protocol on a Philips Achieva 7T MR system. Measured phase data were post-processed and novel least-squares minimisation algorithms were developed to investigate the isotropic susceptibility, anisotropic susceptibility, chemical exchange and cylindrical microstructure inclusion properties of the sample. Analysis revealed that the skeletal muscle sample was significantly more diamagnetic than agar, $\chi_I = (-121 \pm 22)$ppb, and a large chemical exchange contribution was also observed within the tissue, $E = (31 \pm 11)$ppb, relative to the surrounding agar. The experimental protocol was not sensitive enough to reveal quantitative information about the anisotropic susceptibility properties of the sample, yielding an an upper bound of 10 ppb. No evidence of cylindrical susceptibility inclusions was observed within the experimental field perturbation maps.

To my Grandfather, Lawrence ‘Lawrie’ Edison

**Acknowledgements**

Without the support of those around me, this thesis would have not been possible. My experience has been shaped by colleagues at the Sir Peter Mansfield Imaging Centre and I leave with nothing but long-lasting friendships, knowledge, and positive memories (minus a few extensive scanning sessions and some agar based mishaps...). I thank everybody who I have had the opportunity of sharing my time with in Nottingham; to be surrounded by so many friendly faces has made my journey all the more enjoyable.

To my supervisor, Professor Richard Bowtell, for his guidance throughout the PhD process. I feel very fortunate to have had a supervisor who not only provided me with the opportunity to develop as a researcher, but a friendly and encouraging mentor whose knowledge appears to have no limits. To Dr Samuel Wharton, whose support during the initial period of my PhD provided me with a head start into the world of QSM. And to Dr Matthew Cronin, my susceptibility partner in crime and friend, who has been there for me throughout.

To my parents, Gail and Marc, whose love, care and guidance throughout my life have made me the person I am today. Perhaps I would not be writing this now had you not told me off for my bad school report all those years ago! To my siblings, Daniel and Hannah (and Leo!), my sister-in-law Talia, my nana Helena, my auntie Karen, my uncle Simon and cousins Matthew, Natalie and Talia, who made every journey home more special. To my uncle Saul, auntie Katherine and cousins Isaac, Esther and Reuben, for opening your doors to me in Nottingham. Your hospitality and support during this period will not be forgotten.

Finally, to my girlfriend Carolina, for her love, kindness and encouragement throughout this adventure. Without you, this journey would not have been the same. I look forward to what the future holds for us. Eu amo-te!

# Contents


**1 Introduction** **1**

**2 Theory of Nuclear Magnetic Resonance (NMR)** **3**

2.1 What is NMR? . . . 3

2.2 Quantum Mechanical Origin of Spin . . . 4

2.2.1 Angular Momentum . . . 4

2.2.2 The Zeeman Effect . . . 4

2.2.3 Spin . . . 5

2.2.4 Nuclear Spin and the Hydrogen Nucleus . . . 6

2.2.5 The Nuclear-Zeeman Effect in Hydrogen . . . 7

2.2.6 Application to Experimental MRI . . . 8

2.3 Classical Model of Angular Momentum . . . 8

2.3.1 Why Use a Classical Description? . . . 8

2.3.2 Classical Model of Atomic Orbital Angular Momentum . . . 9

2.3.3 Classical Model of Atomic Spin Angular Momentum . . . 10

2.4 Macroscopic Description of NMR . . . 10

2.4.1 Magnetisation . . . 10

2.4.2 Relaxation-Free Bloch Equation . . . 11

2.4.3 $T_1$ and $T_2$ Relaxation . . . 12

2.4.4 $T_2^*$ Relaxation . . . 12

2.4.5 The Rotating Frame . . . 13

2.4.6 Application of RF Pulses . . . 13

**3 Theory of Magnetic Resonance Imaging (MRI)** **17**

3.1 Introduction . . . 17

3.2 Magnetic Field Gradients . . . 17

3.2.1 Definition and Use . . . 17

3.2.2 Spatial Encoding in 1D . . . 18

3.2.3 Sampling Over $k$-space . . . 21

3.3 Encoding in Multiple Dimensions . . . 22

3.3.1 Definitions of the Signal and $k$-space . . . 22

3.3.2 Phase Encoding . . . 23
3.4 Gradient Echo Sequence . . . 25
3.4.1 Definition . . . 25
3.4.2 1D Gradient Echo and the Echo-Time . . . 26
3.4.3 Multiple Dimensions and non-Cartesian Sampling . . . 26
3.4.4 Slice-Selection . . . 29
3.4.5 Multi Echo Acquisitions . . . 30
3.4.6 Image Resolution . . . 30
3.5 Impact of Relaxation . . . 31
3.5.1 Influence of Echo Time and Repetition Time on Signal Contrast in GE Sequences . . . 31
3.5.2 Flip Angle and the FLASH Sequence . . . 33
3.6 Magnitude and Phase Contrast . . . 35

**4 Theory of Isotropic Susceptibility 39**
4.1 What is Susceptibility? . . . 39
4.1.1 Definition and Units . . . 39
4.1.2 Relationship Between $\vec{B}$, $\vec{H}$ and $\vec{M}$ . . . 40
4.1.3 Diamagnetism, Paramagnetism and the Value of $\chi_I$ . . . 41
4.2 Magnetic Field Properties . . . 42
4.2.1 Magnetostatics and the Scalar Potential . . . 42
4.2.2 The Demagnetising Field . . . 45
4.2.3 The Sphere of Lorentz . . . 46
4.3 Utilising $k$-Space to Describe Field Perturbations Generated from Arbitrary Susceptibility Distributions . . . 49
4.3.1 Derivation . . . 49
4.3.2 Interpretation . . . 50
4.3.3 Comparison to Analytical Solutions . . . 51

**5 Phase Processing and Generation of Isotropic Quantitative Susceptibility Maps 58**
5.1 Why Does Phase Require Processing? . . . 58
5.2 Phase Unwrapping . . . 59
5.2.1 Phase Wraps: Identification and Cause . . . 59
5.2.2 Echo Time based Unwrapping . . . 60
5.2.3 Path based Unwrapping . . . 62
5.2.4 Laplacian-Based Unwrapping . . . 64
5.2.5 Nonlinear Voxelwise Temporal Fitting to Signal . . . 67
5.3 Background Field Removal . . . 67

5.3.1 Background Fields: Identification and Cause . . . . . 67
5.3.2 High Pass Filtering . . . . . 67
5.3.3 Laplacian Filtering . . . . . 68
5.3.4 Projection onto Dipole Fields . . . . . 73
5.3.5 Other Techniques . . . . . 73
5.4 Generating Isotropic Quantitative Susceptibility Maps . . . . . 74
5.4.1 Motivation and Challenges . . . . . 74
5.4.2 Ill-Posed Problems . . . . . 76
5.4.3 Direct Inversion Techniques . . . . . 78
5.4.4 Multiple Orientation Sampling . . . . . 81
5.4.5 Least Squares Minimisation with Regularisation . . . . . 83
5.5 Available Software . . . . . 89

**6 Establishing a Data Analysis Pipeline for *in-vivo* Quantitative Susceptibility Mapping in the Rodent Brain 96**
6.1 Introduction . . . . . 96
6.2 Susceptibility as a Myelin Biomarker . . . . . 97
6.3 Experimental Data Collection . . . . . 98
6.4 Generating $R_2^*$ Maps . . . . . 99
6.5 Generating Isotropic Quantitative Susceptibility Maps . . . . . 100
6.5.1 Phase Unwrapping . . . . . 100
6.5.2 Background Field Removal . . . . . 104
6.5.3 Generation of Isotropic Susceptibility Maps . . . . . 105
6.6 Discussion and Future work . . . . . 108

**7 Beyond Isotropic Susceptibility 119**
7.1 Anisotropic Susceptibility . . . . . 119
7.1.1 Motivation . . . . . 119
7.1.2 Theory . . . . . 121
7.1.3 Properties of the Susceptibility Tensor . . . . . 122
7.1.4 Susceptibility Tensor Imaging . . . . . 122
7.1.5 Approximation and Regularisation . . . . . 125
7.2 Chemical Exchange . . . . . 126
7.3 Non-Spherical Microstructural Susceptibility Inclusions . . . . . 127
7.3.1 Introduction . . . . . 127
7.3.2 Simulated Example of the Impact of Cylindrically Symmetric Tissue Architecture . . . . . 129
7.3.3 Evidence in White matter . . . . . 135
7.4 Compartmentalisation . . . . . 135

7.4.1 What is Compartmentalisation? . . . 135
7.4.2 $T_2$ Compartmentalisation of White Matter . . . 137
7.4.3 $T_2^*$ and $\Delta f$ Compartmentalisation in White Matter . . . 140
7.4.4 $T_1$ Compartmentalisation in White Matter . . . 142
7.4.5 Considerations of Compartmentalisation . . . 142

**8 Frequency Difference Mapping Applied to the Corpus Callosum at 7T 149**
8.1 Introduction . . . 149
8.2 Frequency Difference Mapping . . . 150
8.2.1 Introduction . . . 150
8.2.2 FDM Protocol . . . 151
8.2.3 Advantages of FDM . . . 154
8.3 Creating a Model of Myelinated Nerve Fibres . . . 155
8.3.1 Requirements . . . 155
8.3.2 Geometric Structure of Myelinated Nerve Fibre Model . . . 155
8.3.3 Modelling Susceptibility in Myelin . . . 157
8.3.4 Modelling Chemical Exchange in Myelin . . . 157
8.3.5 Application to the Three-Pool Model . . . 158
8.4 Method . . . 158
8.5 Applying FDM to Phantom and Brain Data . . . 160
8.6 Results . . . 162
8.7 Discussion . . . 173
8.8 Conclusion . . . 178

**9 Examination of the Magnetic Properties of Skeletal Muscle Tissue at 7T 183**
9.1 Introduction . . . 183
9.2 Motivation . . . 184
9.3 Method . . . 185
9.3.1 Experimental Prep and Data Collection . . . 185
9.3.2 Post-Processing of Experimental Data . . . 186
9.3.3 Least Squares Minimisation . . . 187
9.4 Isotropic Susceptibility Minimisation . . . 191
9.5 Isotropic Susceptibility and Chemical Exchange Minimisation . . . 195
9.6 Susceptibility Tensor and Chemical Exchange Minimisation . . . 199
9.7 Discussion . . . 205
9.8 Conclusion . . . 210

**10 Conclusion** **213**
10.1 Overview . . . . . 213
10.2 Future Work . . . . . 214
10.3 Final Remarks . . . . . 215

# Chapter 1

# Introduction

Access to higher field strengths and improved processing techniques has opened up new opportunities for exploiting the contrast provided by gradient echo (GE) phase datasets. Phase images are already widely used within a clinical setting via susceptibility weighted imaging (SWI), which utilises phase to improve visual contrast in an abundance of regions including blood vessels and brain lesions. However, understanding the sources of underlying contrast in phase images is still an area of ongoing research. The ambition of this thesis is to examine (though both theory and experiment) the sources of contrast within phase datasets, extending beyond the traditional model considering isotropic susceptibility as the source of all phase contrast and examining the impact of susceptibility anisotropy, chemical exchange, non-spherical susceptibility inclusions and multi-compartment signal evolution.

In *Chapter 2*, the theoretical considerations of nuclear magnetic resonance (NMR) are discussed, investigating both the quantum and classical model of NMR before continuing to the treatment of macroscopic systems. *Chapter 3* extends this discussion to considerations in magnetic resonance imaging (MRI) experiments, with a focus on the gradient echo (GE) sequence utilised throughout this thesis.

*Chapter 4* discusses the theoretical considerations of both isotropic susceptibility and quantitative susceptibility mapping (QSM), a well established research area focused on obtaining isotropic susceptibility maps from GE phase data. A thorough description of the post-processing pipeline utilised in QSM, including the limitations and advantages of different techniques are discussed in *Chapter 5*. *Chapter 6* provides the first experimental chapter within this thesis, where a full analysis pipeline to quantify the isotropic susceptibility properties of rat brains *in-vivo* is developed and discussed.

Further work in this thesis extends beyond a model of isotropic susceptibility, with *Chapter 7* examining the theoretical considerations of anisotropic susceptibility,

chemical exchange, non-spherical susceptibility inclusions and signal compartmentalisation. Beyond theoretical considerations, an extensive discussion is provided on experimental observations corresponding to these magnetic properties and how they can be quantified within phase datasets. *Chapter 8* details an experiment exploring multi-compartment signal evolution over the corpus callosum via implementation of a novel frequency difference mapping (FDM) algorithm. Combining experimental results with a model of white matter, results are quantified in terms of isotropic susceptibility, anisotropic susceptibility and chemical exchange, in addition to quantifying the relative fractions of axonal, myelin and extracellular space in white matter. *Chapter 9* describes an experiment investigating the magnetic properties of skeletal muscle, examining the properties of isotropic susceptibility, anisotropic susceptibility, chemical exchange and non-spherical susceptibility inclusions in an *ex-vivo* sample of pork tenderloin. *Chapter 10* presents the concluding remarks for this thesis, with a final discussion of the work presented and the impact of the experimental findings.

# Chapter 2

# Theory of Nuclear Magnetic Resonance (NMR)

## 2.1 What is NMR?

Nuclear Magnetic Resonance (NMR) is a branch of physics that exploits the interaction between atoms and externally applied magnetic fields to describe the magnetic properties of a system. These magnetic properties are of great interest to researchers as they provide an insight into the atomic structure of the system being examined, in addition to any chemical interactions taking place. NMR forms the foundation of magnetic resonance imaging (MRI), a sophisticated application of NMR which provides images of macroscopic systems which reflect the underlying magnetic properties.

The magnetic properties of systems observed in NMR experiments arise due to the quantum mechanical properties of atomic nuclei. However, under MRI conditions a classically approximated model can be considered sufficient in effectively explaining observations, in addition to creating a model of underlying physics which is simple to interpret. These approximations arise due to the low sensitivity of MRI, which is concerned with bulk effects rather than single nuclei. In addition, the majority of MRI experiments are based on signals from hydrogen nuclei, which are composed of a single proton and have relatively simple properties.

In this chapter, the quantum mechanical foundation of spin will be described and interpreted, in addition to the classical model commonly encountered in MRI. An interpretation of relaxation in bulk atomic systems will be introduced, in addition to an explanation of how the interaction of systems with applied radiofrequency (RF) pulses form the basis of NMR experiments. Three text-books [1–3] have been used to compile the majority of the theory within this chapter. Other sources not contained within these books are listed within the text.

## 2.2 Quantum Mechanical Origin of Spin

### 2.2.1 Angular Momentum

Angular momentum is an integral property of quantum systems and is essential in creating a model that is consistent with observations in NMR experiments. Orbital angular momentum, $\vec{L}$, is defined classically as:

$$\vec{L} = \vec{r} \times \vec{p} \tag{2.1}$$

where $\vec{r}$ is the radial position, $\vec{p}$ is the momentum and $\times$ represents the cross product between two vectors. From the Schrödinger equation, $\vec{L}$ can be redefined as a quantum mechanical operator via the correspondence principle:

$$\begin{aligned} \hat{L} &= \hat{R} \times \hat{P} \\ &= -i\hbar\vec{r} \times \nabla \end{aligned} \tag{2.2}$$

where $\hat{R} = \vec{r}$ and $\hat{P} = -i\hbar\nabla$. The operator $\hat{L}$ has distinctive commutation properties:

$$\begin{aligned} [\hat{L}_k, \hat{L}_l] &= i\hbar\varepsilon_{klm}\hat{L}_m \\ [\hat{L}^2, \hat{L}_k] &= 0 \end{aligned} \tag{2.3}$$

where $[,]$ denotes the commutation relationship, $\varepsilon_{klm}$ denotes the Levi-Civita symbol and $\hat{L}_{k,l,m}$ refers to the $\hat{x}$, $\hat{y}$ or $\hat{z}$ components of $\hat{L}$. Two notable properties of $\hat{L}$ can be obtained when operating on a wavefunction, $|\psi\rangle$:

$$\begin{aligned} \hat{L}^2 |\psi\rangle &= \hbar^2 l\,(l+1)\,|\psi\rangle \\ \hat{L}_z |\psi\rangle &= m_l\hbar\,|\psi\rangle \end{aligned} \tag{2.4}$$

where $l \in \mathbb{N}_0$ and $m_l = -l, -l+1, ..., -l+n, ..., l$, with $n \in \mathbb{N}_0$. Here $|\psi\rangle$ is an eigenfunction of both $\hat{L}^2$ and $\hat{L}_z$ as described in Equation 2.3. The eigenvalues $\hbar^2 l(l+1)$ and $m_l\hbar$ are the squared magnitude, $|\vec{L}|^2$, and the magnitude of the $\hat{z}$ component, $|\vec{L_z}|$, of the angular momentum respectively.

An important observation is that both $\hat{L}^2$ and $\hat{L}_z$ commute with the energy operator, $\hat{H}$, which is a function of $\hat{L}^2$. This implies that the value of $l$ has a direct impact on the observed energy eigenvalue as determined by $\hat{H}\,|\psi\rangle$. However, as $|\psi\rangle$ is a simultaneous eigenfunction of $\hat{L}_z$, $m_l$ values are energetically degenerate.

### 2.2.2 The Zeeman Effect

The magnetic moment, $\hat{\mu}_L$, has been experimentally defined in terms of $\hat{L}$ as:

$$\hat{\mu}_L = \gamma_L\hat{L} \tag{2.5}$$

where $\gamma_L$ is the orbital gyromagnetic ratio. When an external magnetic field, $B_0\hat{z}$, is applied the energy operator, $\hat{H}$, is perturbed via an additional energy term, $\hat{U}_L$:

$$\begin{aligned}\hat{U}_L &= -\hat{\mu}_L \cdot B_0\hat{z} \\ &= -\gamma B_0 \hat{L}_z.\end{aligned} \tag{2.6}$$

As this term contains $\hat{L_z}$, it can be determined that the inclusion of $\hat{U}_L$ via the application of an externally applied magnetic field removes the degeneracy on $m_l$. In an external magnetic field, an atom with orbital angular momentum $l$ will have $(2l+1)$ measurable energy states, with energy levels proportional to to $m_l$. This is known as the Zeeman effect.

### 2.2.3 Spin

Spin is a quantum mechanical property of atoms describing an 'intrinsic' form of angular momentum, which is distinctive from $\hat{L}$ and fundamental for explaining the observed phenomena in NMR experiments. The first experimental evidence for spin was observed in 1922 by Stern and Gerlach, who described the quantisation of angular momentum of silver atoms placed in an inhomogeneous magnetic field. For an atom in the ground state ($l = 0$, $m_l = 0$), in an applied magnetic field a single energy level is expected to exist as defined by Equation 2.6. However, experimental evidence indicated that the ground state atoms had two distinct energy levels, which implied two states of angular momentum. Since this could not be explained by the model of orbital angular momentum, the concept of spin, an 'intrinsic' angular momentum, was therefore developed.

To be considered a form of angular momentum, the spin operator, $\hat{S}$, must be consistent with the commutation properties in Equation 2.3. A solution to the following problem:

$$\begin{aligned}\hat{S}^2 \left|\Psi\right\rangle &= \alpha \left|\Psi\right\rangle \\ \hat{S}_z \left|\Psi\right\rangle &= \beta \left|\Psi\right\rangle\end{aligned} \tag{2.7}$$

must be found, consistent with Equation 2.3 to understand the origin of spin and determine eigenvalues $\alpha$ and $\beta$ for an eigenfunction $\Psi$. From the introduction of raising and lowering operators $\hat{S}_+ = \hat{S}_x + i\hat{S}_y$ and $\hat{S}_- = \hat{S}_x - i\hat{S}_y$, $\alpha$ and $\beta$ can be determined as:

$$\begin{aligned}\hat{S}^2 \left|\Psi\right\rangle &= \hbar^2 s\left(s+1\right)\left|\Psi\right\rangle \\ \hat{S}_z \left|\Psi\right\rangle &= m_s \hbar \left|\Psi\right\rangle\end{aligned} \tag{2.8}$$

where $s \in \frac{\mathbb{N}_{\geq 0}}{2}$ and $m_s = -s, -s+1, ..., -s+n, ..., s$, with $n \in \mathbb{N}_0$. The half-integer values of $s$ explain the inconsistency observed in Stern and Gerlach's experiment on ground state atoms. This is described for the hydrogen nucleus in Section 2.2.5.

Spin is commonly interpreted as a classical 'rotation' about an axis through the centre of an atom. This interpretation can be considered justified from the description of $\hat{S}$ as an intrinsic form of angular momentum based on the same commutation properties as $\hat{L}$. Furthermore, the application of $\hat{S}_\pm$ operators on $|\Psi\rangle$ modifies the eigenfunction $|\Psi\rangle \rightarrow \hat{S}_\pm |\Psi\rangle$, raising or lowering the eigenvalue $m_s$. $\hat{S}_\pm$ can be interpreted as transverse angular momentum operators. However spin is a purely quantum mechanical property and attempts to define spin classically will lead to rotation velocities greater than the speed of light, $c$.

### 2.2.4 Nuclear Spin and the Hydrogen Nucleus

Nuclear spin is described by the quantum operator $\hat{I}$, which has identical properties to the $\hat{S}$ operator. $\hat{I}^2$ and $\hat{I}_z$ are defined by the quantum numbers $I$ and $m_I$, which are analogous to $s$ and $m_s$:

$$\begin{aligned} \hat{I}^2 |\Psi\rangle &= \hbar^2 I (I+1) |\Psi\rangle \\ \hat{I}_z |\Psi\rangle &= m_I \hbar |\Psi\rangle . \end{aligned} \tag{2.9}$$

Nucleons (protons and neutrons) are spin-$\frac{1}{2}$ particles and the combination of neutrons and protons defines the total nuclear spin of an atom. The specific value of an atom's ground state nuclear spin can be challenging to obtain and requires modelling of the detailed nuclear structure. However, simple rules defining a nucleus as having either integer or half-integer spin exist and are dependent only upon the total number of protons and neutrons within the nucleus. These rules are outlined in Table 2.1.

The nucleus of interest in MRI is generally that of hydrogen, a spin-$\frac{1}{2}$ particle consisting of a single proton. The hydrogen nucleus is a single ground state nucleon, defined by the quantum numbers $l = 0$, $m_l = 0$, $I = \frac{1}{2}$ and $m_I = \pm\frac{1}{2}$.

| **Atomic Number (Z)** | **Mass number (A)** | **Spin** |
|---|---|---|
| Even | Even | 0 |
| Even | Odd | $\frac{2n-1}{2}$ |
| Odd | Odd | $\frac{2n-1}{2}$ |
| Odd | Even | $n$ |

Table 2.1: Definitions for nuclear particle spin, $I$, based on the atomic and mass number of a nucleus. Here $n \in \mathbb{N}_{\geq 0}$.

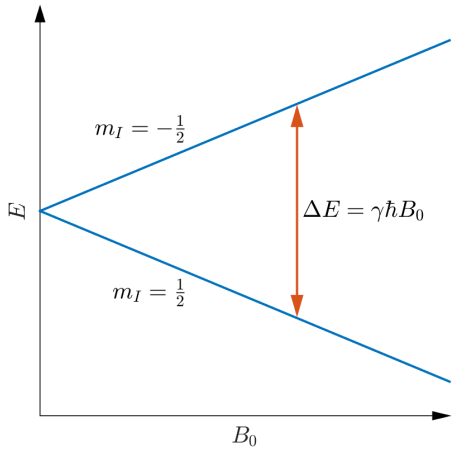



Figure 2.1: Impact of the nuclear Zeeman effect. A static magnetic field, $B_0$, shifts the energy levels of the $m_I = \pm\frac{1}{2}$ states.

### 2.2.5 The Nuclear-Zeeman Effect in Hydrogen

The nuclear magnetic moment, $\hat{\mu}_I$, has been experimentally defined in terms of $\hat{I}$ as:

$$\hat{\mu}_I = \gamma_I \hat{I} \tag{2.10}$$

where $\gamma_I$ is the nuclear-spin gyromagnetic ratio. Using a similar approach to that described in Section 2.2.2, a ground state hydrogen nucleus in an external magnetic field will have two energy levels, defined by the operator $\hat{U}_I$:

$$\begin{aligned} \hat{U}_I &= -\hat{\mu}_I \cdot B_0 \hat{z} \\ &= -\gamma B_0 \hat{I}_z \end{aligned} \tag{2.11}$$

and from Equation 2.9:

$$\begin{aligned} \hat{U}_I \left|+\tfrac{1}{2}\right\rangle &= -\frac{\gamma B_0 \hbar}{2} \left|+\tfrac{1}{2}\right\rangle \\ \hat{U}_I \left|-\tfrac{1}{2}\right\rangle &= +\frac{\gamma B_0 \hbar}{2} \left|-\tfrac{1}{2}\right\rangle \end{aligned} \tag{2.12}$$

where $\left|+\frac{1}{2}\right\rangle$ and $\left|-\frac{1}{2}\right\rangle$ denote the $m_I{=}\pm\frac{1}{2}$ states. In an external magnetic field, a nucleus with spin $I$ will have $(2I+1)$ measurable spin states, with energy levels proportional to $m_I$. This splitting of energy levels in a magnetic field is known as the nuclear Zeeman effect.

The nuclear Zeeman effect for a hydrogen nucleus is visualised in Figure 2.1. An increased $B_0$ leads to an increased difference in energy, $\Delta E$, between the two spin states. The difference in energy between the spin states is defined as:

$$\begin{aligned} \Delta E &= E_{m_I=-\frac{1}{2}} - E_{m_I=+\frac{1}{2}} \\ &= \gamma\hbar B_0 \end{aligned} \tag{2.13}$$

The Planck-Einstein relationship defines the relationship between $E$ and the angular frequency, $\omega$:

$$E = \hbar\omega \tag{2.14}$$

and combining Equations 2.13 and 2.14 gives:

$$\omega_0 = \gamma B_0. \tag{2.15}$$

This is known as the Larmor equation and relates the precession frequency of atoms with the applied magnetic field. $\omega_0$ is known as the Larmor frequency.

### 2.2.6 Application to Experimental MRI

Equations 2.13-2.15 provide the basis for experimental MRI. If a photon of energy $E = \hbar\omega_0$ interacts with a hydrogen nucleus in an applied magnetic field, it will lead to a transition of the nucleus from the $m_I = \frac{1}{2}$ state to the $m_I = -\frac{1}{2}$ state. If $E \neq \hbar\omega_0$, there will be no observed transition of spin states.
For a hydrogen nucleus, $\gamma_{^1\mathrm{H}} \approx 267.5 \times 10^6\,\mathrm{rad\,s^{-1}\,T^{-1}}$. The frequency, $f_0 = \frac{\omega_0}{2\pi}$, of an applied photon is in the MHz range at the field strengths used in MRI (at 7T, $f_0 \approx 298\,\mathrm{MHz}$). MHz frequencies are in the radiofrequency (RF) band, and in NMR and MRI photons applied to cause spin-state transitions are sent in ensembles known as RF pulses.

## 2.3 Classical Model of Angular Momentum

### 2.3.1 Why Use a Classical Description?

It is not possible for a classical model to explain all of the fundamental observations in NMR experiments. The most notable of these observations is the requirement for an incoming photon to have energy $E = \hbar\omega_0$ to cause spin-state transitions. Additionally, the concept of 'half-integer spin' has no basis in a classical description.
As discussed in the previous section, the hydrogen nucleus is a spin-$\frac{1}{2}$ particle. Spin-$\frac{1}{2}$ particles are more simple to describe as they are not sensitive to nuclear multipole effects, which would distort the spherical symmetry of the nucleus and induce a more complex interaction with an applied magnetic field. When examining macroscopic systems of spin-$\frac{1}{2}$ particles, certain approximations can be made to derive a classical model which produces results that are in good agreement with observation. In addition, the classical model provides an excellent visualisation of the interaction of particles with applied magnetic fields and RF pulses. For these reasons, a classical model is used to describe simple interactions in NMR and is

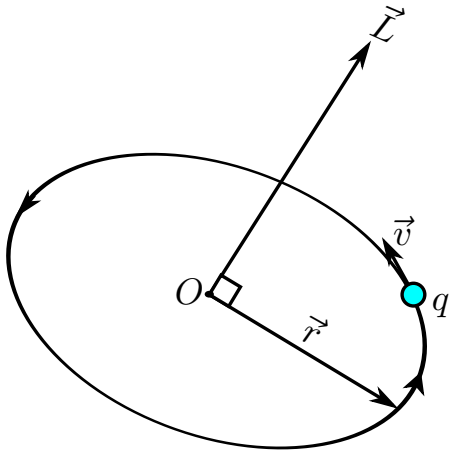



Figure 2.2: Visualisation of a particle of mass $m$, and charge $q$, orbiting a central point $O$, with angular momentum, $\vec{L}$.

often preferred in MRI, which is usually concerned with observing macroscopic systems of hydrogen nuclei.

### 2.3.2 Classical Model of Atomic Orbital Angular Momentum

A model can be visualised of a particle rapidly orbiting a central point in a classical orbit, with velocity $\vec{v}$, mass $m$, orbital radius $R$ and charge $q$. This is visualised in Figure 2.2. From the classical definition of orbital angular momentum in Equation 2.1:

$$\vec{L} = Rmv\hat{n} \tag{2.16}$$

where $\hat{n}$ is a unit vector perpendicular to the orbital plane. The closed atomic orbit implies that the magnetic moment of the system, $\vec{\mu}_L$, can be described in terms of a current loop. For a current loop, $\vec{\mu}_L$ is defined as the product of the current, $I$, with the enclosed loop area, $A$:

$$\vec{\mu}_L = IA\hat{n}. \tag{2.17}$$

Furthermore, the current can be defined in terms of the charge and the revolution frequency, $f$, of the atom around the central point:

$$I = qf. \tag{2.18}$$

Combining the above equations and considering the geometry of the model, a description of the magnetic moment in terms of orbital angular momentum can be derived:

$$\vec{\mu_L} = \frac{q}{2m}\vec{L}. \tag{2.19}$$

Comparing this with Equation 2.5, the orbital gyromagnetic ratio, $\gamma_L$, can be defined classically as:

$$\gamma_L = \frac{q}{2m}. \tag{2.20}$$

### 2.3.3 Classical Model of Atomic Spin Angular Momentum

Considering the similarities between the quantum mechanical operators $\hat{L}$ and $\hat{I}$ describing angular momentum, it would be reasonable to assume from Equation 2.19 that the spin magnetic moment of a nucleon, $\vec{\mu_I}$, could be classically defined as:

$$\vec{\mu_I} = \frac{q}{2m}\vec{I}, \tag{2.21}$$

However, experimental evidence indicates that this does not effectively describe the observed nuclear magnetic moment, which is further scaled by a dimensionless factor, $g$:

$$\vec{\mu_I} = g\frac{q}{2m}\vec{I}. \tag{2.22}$$

$g$ is known as the g-factor and cannot be derived classically, requiring considerations of quantum mechanics beyond the Schrödinger equation. Furthermore, the value of $g$ depends on the particle being considered ($g_{\text{proton}} \approx 5.59$ and $g_{\text{electron}} \approx -2$).

## 2.4 Macroscopic Description of NMR

### 2.4.1 Magnetisation

As briefly mentioned in Sections 2.1 and 2.3.1, NMR is concerned with the examination of bulk atomic effects. In this description, interactions between individual magnetic moments are considered small enough to be ignored and NMR phenomena are described in a macroscopic, semi-classical model. One such macroscopic property is the magnetisation, $\vec{M}$, defined as the volume density of magnetic moments within a system:

$$\vec{M} = \frac{1}{V}\sum_{k=1}^{N}\vec{\mu}_k \tag{2.23}$$

where $V$ is the volume of the system and $N$ is the total number of particles.
For a system of hydrogen nuclei in an external magnetic field, it cannot be automatically assumed that all nuclei will be in the energetically favourable spin-up, $+\frac{1}{2}$, state, due to the presence of environmental thermal energy. Ignoring interactions between individual magnetic moments, in the presence of an environment

with temperature $T$, the ratio of spin-up, $+\frac{1}{2}$, to spin-down, $-\frac{1}{2}$, nuclei can be described via Maxwell-Boltzmann statistics:

$$\frac{N_{+\frac{1}{2}}}{N_{-\frac{1}{2}}} = e^{\frac{\gamma\hbar B_0}{k_B T}} \tag{2.24}$$

where $N_{\pm\frac{1}{2}}$ is the number of spin up/spin down nuclei in the system, $k_B$ is the Boltzmann constant and $\gamma\hbar B_0$ is determined from Equation 2.13. The population difference can be approximated by noting that in MRI we only consider the high temperature limit ($\gamma\hbar B_0 << k_B T$) and can therefore expand the exponential in Equation 2.24 as a Maclaurin series. Approximating $N_{+\frac{1}{2}} \approx N_{-\frac{1}{2}} \approx \frac{N}{2}$:

$$\Delta N \approx N\frac{\gamma\hbar B_0}{2k_B T} \tag{2.25}$$

Combining this with Equation 2.23 and noting that $\vec{\mu}_{+\frac{1}{2}} = \frac{\gamma\hbar}{2}\hat{z}$:

$$|\vec{M}_0| \approx \frac{N\left(\gamma\hbar\right)^2 B_0}{4Vk_B T}. \tag{2.26}$$

### 2.4.2 Relaxation-Free Bloch Equation

The Bloch equation characterises the temporal evolution of magnetisation in macroscopic systems. Empirically derived in 1946 [4] in an identical form to what is found in current NMR textbooks, the Bloch equation has been successful in classically describing interactions of bulk atomic systems with applied magnetic fields. The original derivation considers a classical angular momentum, $\vec{L}$, analogous to the form in Section 2.3.2. From the classical definition of torque:

$$\vec{\tau} = \frac{d\vec{L}}{dt} \tag{2.27}$$

and considering the mathematical formalisms in Section 2.3 and Equation 2.23, the temporal evolution of magnetisation, $\vec{M}(t)$ can be defined as:

$$\frac{d\vec{M}(t)}{dt} = \gamma\vec{M}(t) \times \vec{B}. \tag{2.28}$$

This formula is known as the Bloch equation, defined for a macroscopic system which does not undergo relaxation and describes the precession of magnetisation in an applied magnetic field. Considering a static magnetic field in the $\hat{z}$-direction ($\vec{B} = |\vec{B}| \cdot \hat{z}$) and defining transverse magnetisation in a complex representation ($M_+ = M_x + iM_y$):

$$\begin{aligned} M_+(t) &= M_{+_0} e^{-i\omega t} \\ M_z(t) &= M_{z_0} \end{aligned} \tag{2.29}$$

where $M_{+_0,z_0}$ are the initial magnetisation of the transverse and parallel components to $\vec{B}$. These equations define the 'precession' of the magnetisation in an applied magnetic field at frequency $\omega = \gamma|\vec{B}|$.

### 2.4.3 $T_1$ and $T_2$ Relaxation

The previous section implies that in the presence of an applied static magnetic field in the $\hat{z}$ direction, $M_+(t)$ will continuously precess with magnitude $M_{+_0}$ and $M_z(t)$ will remain constant with magnitude $M_{z_0}$. However the energy density of the macroscopic system:

$$U_M = -\vec{M} \cdot \vec{B} \tag{2.30}$$

requires that to reach the most energetically favourable state, $|\vec{M}_z|$ must be maximised. In this situation, $|\vec{M}_+| = 0$ and $|\vec{M}_z| = |\vec{M}_0|$. If a system is perturbed from this thermal equilibrium, interactions of spins with the thermal environment will lead to the system returning to this energetically favourable equilibrium state in a process known as longitudinal (spin-lattice) relaxation, characterised by the longitudinal relaxation constant, $T_1$.

A second form of relaxation exists, known as transverse (spin-spin) relaxation, characterised by the transverse relaxation constant, $T_2$. This form of relaxation occurs due to interactions between the magnetic fields of neighbouring nuclei. Spin-spin relaxation conserves energy within the system, as energy is transferred between neighbouring spins. However, the relaxation leads to a loss of coherence and an effective 'cancelling' within the system, reducing the magnitude of transverse magnetisation.

Equation 2.28 can be modified to include the effects of relaxation:

$$\frac{d\vec{M}(t)}{dt} = \gamma\vec{M}(t) \times \vec{B} + \frac{1}{T_1}\left(M_0 - M_z(t)\right) - \frac{M_x(t) + M_y(t)}{T_2}. \tag{2.31}$$

The equivalent set of formulas for Equation 2.29 including relaxation are:

$$\begin{aligned} M_+(t) &= M_{+_0} e^{-\frac{t}{T_2}} e^{-i\omega t} \\ M_z(t) &= M_{z_0} e^{-\frac{t}{T_1}} + M_0\left(1 - e^{-\frac{t}{T_1}}\right) \end{aligned} \tag{2.32}$$

where it can be observed that as $t \to \infty$, $M_+ \to 0$ and $M_z \to M_0$.

### 2.4.4 $T_2^*$ Relaxation

Experimentally the transverse magnetisation is found to decay according to a perturbed rate, characterised by a $T_2^*$ relaxation time:

$$\frac{1}{T_2^*} = \frac{1}{T_2} + \frac{1}{T_2'}. \tag{2.33}$$

$T_2'$ is an additional relaxation constant induced by field inhomogeneities, defining the signal evolution:

$$M_+(t) = M_{+_0} e^{-\frac{t}{T_2^*}} e^{-i\omega t}. \tag{2.34}$$

$T_2'$ effects can be induced due to an experimentally applied inhomogeneous $B_0$ field, but can additionally be induced by structural inclusions that locally perturb the experienced field of the sample due to their induced magnetisation, including effects from magnetic susceptibility (theoretical considerations discussed in Chapters 4 and 7). $T_2'$ effects can provide further detailed information about the underlying structure of tissue, but are not always desirable and can be removed via the selected application of RF pulses.

### 2.4.5 The Rotating Frame

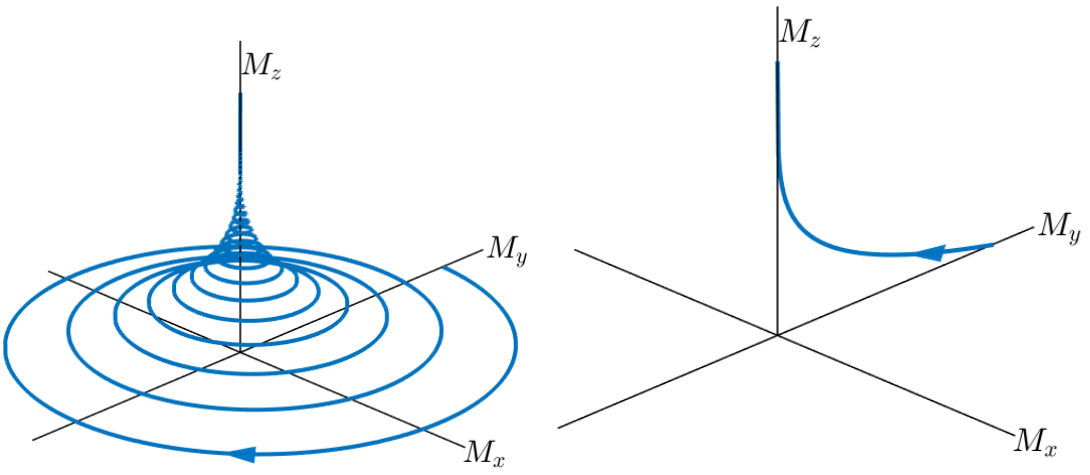
To simplify our description of precessing magnetisation, the rotating frame can be considered. As defined in Sections 2.4.2 and 2.4.3, a system perturbed from thermal equilibrium in a static magnetic field, $|\vec{B}| \cdot \hat{z}$, will precess at frequency $\omega$, around the axis of the applied magnetic field while returning to thermal equilibrium via relaxation processes. This is visualised in Figure 2.3a.
By considering the system in a rotating frame with an angular frequency equal to the Larmor frequency, precession at $\omega_0$ can be ignored. Defining $\omega' = \omega - \omega_0$ and applying the rotating frame to Equation 2.32:

$$\begin{aligned} M_+(t) &= M_{+_0} e^{-\frac{t}{T_2}} e^{-i\omega' t} \\ M_z(t) &= M_{z0} e^{-\frac{t}{T_1}} + M_0 \left(1 - e^{-\frac{t}{T_1}}\right). \end{aligned} \tag{2.35}$$

When $\omega = \omega_0$, the evolution of magnetisation can be described as an exponential decay, as visualised in Figure 2.3b.
The rotating frame provides a reference to examine signals that deviate from a specific Larmor frequency. For example, the Larmor frequency of hydrogen in a static magnetic field, $\vec{B_0}$, can be taken as a reference, defining $\omega_0 = \gamma_{^1\mathrm{H}} |\vec{B_0}|$ and therefore $\omega' = 0$. However the magnetic fields produced by the atomic environment surrounding the hydrogen atom lead to small deviations from the Larmor frequency ($\vec{B} \neq B_0\hat{z}$ and $\omega' \neq 0$), which can provide further information about the magnetic properties of the system.

### 2.4.6 Application of RF Pulses

RF pulses are used to perturb the magnetisation vector, $\vec{M}$, away from thermal equilibrium. RF pulses are generated as a time-varying magnetic field, $\vec{B}_1(t)$, with magnitude $|\vec{B}_1|$ ($|\vec{B}_1| \ll |\vec{B}_0|$), oscillating at frequency, $\omega_{rf}$ ($\omega_{rf} = \omega_0$ when the system is on resonance). From the Bloch equation, an applied RF pulse can be visualised as 'tipping' the macroscopic magnetisation vector into the transverse plane. RF pulses are transmitted experimentally inside an NMR system using




(a) Magnetisation returning to equilibrium

(b) Magnetisation returning to equilibrium in rotating frame

Figure 2.3: The return of magnetisation to equilibrium after being perturbed into the $xy$ plane, where $\vec{B} = |B_0|\hat{z}$ (from Equation 2.39, $\varphi = 90^o$). This is known as a 'free-induction decay' experiment. In the static frame (Figure 2.3a) the system oscillates around the equilibrium point at $\omega = \omega_0$ while exponentially returning to the equilibrium state ($|M_z| = |M_0|$). In the rotating frame ($\omega' = 0$), only the exponential decay is observed.

transmit coils. Two transmit coils can be combined to apply an RF pulse in quadrature:

$$\vec{B}_1(t) = |\vec{B}_1|(\hat{x}\cos\omega_0 t - \hat{y}\sin\omega_0 t). \tag{2.36}$$

The field experienced by the system in the $\hat{z}$-direction is perturbed from $|\vec{B_0}|\hat{z}$ due to the magnetic environment, defining the total magnetic field in the rotating frame as follows:

$$\vec{B}' = \left|\frac{\omega'}{\gamma}\right| \hat{z}' + |\vec{B}_1|\hat{x}' \tag{2.37}$$

where $x'$, $y'$ and $z'$ refer to the rotating frame coordinates. When $\vec{B} = |\vec{B}_0|\hat{z}$:

$$\vec{B}' = |\vec{B}_1|\hat{x}' \tag{2.38}$$

From Equation 2.31, it can be determined that the application of $\vec{B_1}$ rotates the magnetisation around the $\hat{x}'$ axis into the transverse plane at frequency $\omega_1 = \gamma|\vec{B_1}|$. The system will subsequently return to thermal equilibrium following the description in Equation 2.32. The angle of rotation about the $x'$ axis, $\varphi$, is determined as:

$$\varphi = \gamma|\vec{B_1}|t \tag{2.39}$$

where $t$ is the RF pulse duration. The simplest NMR experiment is known as a free-induction decay, when an RF pulse of $\varphi = 90^o$ is applied to the system (visualised in Figure 2.4). The subsequent signal decay is $T_2^*$ weighted (Section 2.4.4).

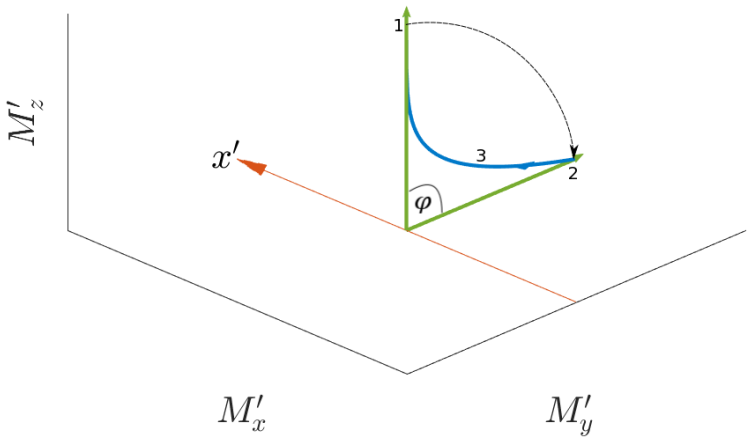



Figure 2.4: Application of $\vec{B}_1$ causes a rotation of the magnetisation along the $x'$ axis into the $x'y'$ plane (black line). The initial magnetisation (green line - 1) rotates into the $x'y'$ plane (2) and subsequently returns to equilibrium via a free-induction decay (3).

# Bibliography

[1] Alastair IM Rae. *Quantum mechanics $5^{th}$ edition*. CRC press, 2007.

[2] Malcolm H Levitt. *Spin dynamics: basics of nuclear magnetic resonance*. John Wiley & Sons, 2001.

[3] E Mark Haacke, Robert W Brown, Michael R Thompson, Ramesh Venkatesan, et al. *Magnetic resonance imaging: physical principles and sequence design*, volume 82. Wiley-Liss New York:, 1999.

[4] Felix Bloch. Nuclear induction. *Physical review*, 70(7-8):460, 1946.

# Chapter 3

# Theory of Magnetic Resonance Imaging (MRI)

## 3.1 Introduction

In this chapter the use of magnetic field gradients to sample single and multi-dimensional $k$-space in MRI is introduced. The fundamental concepts of frequency encoding, phase encoding, slice selection and multi-echo acquisitions are described, with a significant focus on the role of these techniques in gradient-echo sequences. The impact of echo time, repetition time and flip angle as a means to provide relaxation contrast in tissues is discussed, in addition to their utilisation in speeding up MRI acquisitions. Finally, the details of generating magnitude and phase images from a gradient-echo dataset are introduced. Within this chapter a significant portion of the theory has been obtained from [1]. Other sources not contained within this book are listed within the text.

## 3.2 Magnetic Field Gradients

### 3.2.1 Definition and Use

In MRI, linear magnetic field gradients are used to encode information about spatial position: rather than considering systems as point sources, magnetic field gradients allow a system to be spatially characterised. Magnetic field gradients can be applied along one, two, or three orthogonal directions, which provides an equivalent dimensionality of spatial encoding. Defining $\vec{B}_0$ along the $z$-dimension and considering three orthogonal gradients, $G_{x,y,z}$:

$$B_z\left(x,y,z\right) = \left(B_0 + G_x x + G_y y + G_z z\right) \tag{3.1}$$

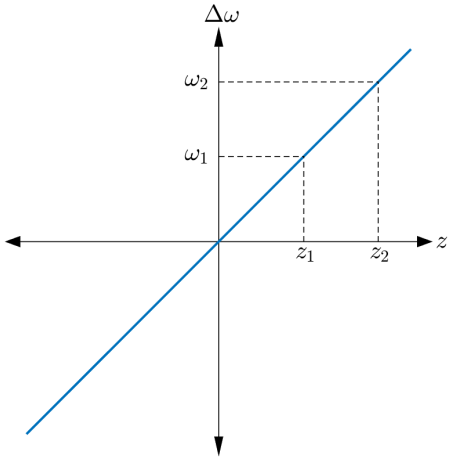



Figure 3.1: Impact of a 1D magnetic field gradient applied in the $z$-direction. Along the $z$-dimension, $\Delta\omega(z) = \gamma G_z z$. At the isocentre ($z = 0$), $\omega = \omega_0$.

where $G_{x,y,z} = \frac{\partial B_z}{\partial x,y,z}$. From the Larmor equation (Equation 2.15):

$$\begin{aligned} \omega(x, y, z) &= \gamma\left(B_0 + G_x x + G_y y + G_z z\right) \\ &= \omega_0 + \Delta\omega(x, y, z). \end{aligned} \tag{3.2}$$

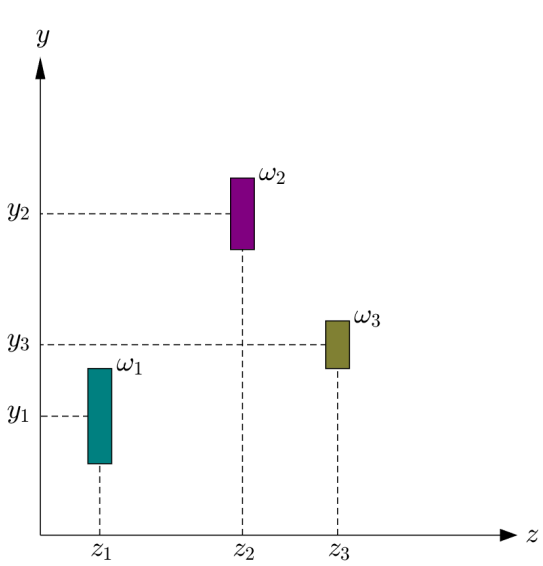
Here it can be determined that the application of magnetic field gradients linearly perturbs $\omega_0$ by an amount $\Delta\omega(x, y, z)$, which can be interpreted as transforming $\omega_0$ into a spatially varying precession frequency, $\omega(x, y, z)$.
In a typical MR system, $G = O(10)\mathrm{mT\,m^{-1}}$, producing field perturbations that are orders of magnitude smaller than $B_0$, with the 7T system at the Sir Peter Mansfield Imaging Centre operating with a gradient strength of $40\mathrm{mT\,m^{-1}}$. However, the field perturbations are significant enough to be detected and utilised in spatially encoding the NMR signal.

### 3.2.2 Spatial Encoding in 1D

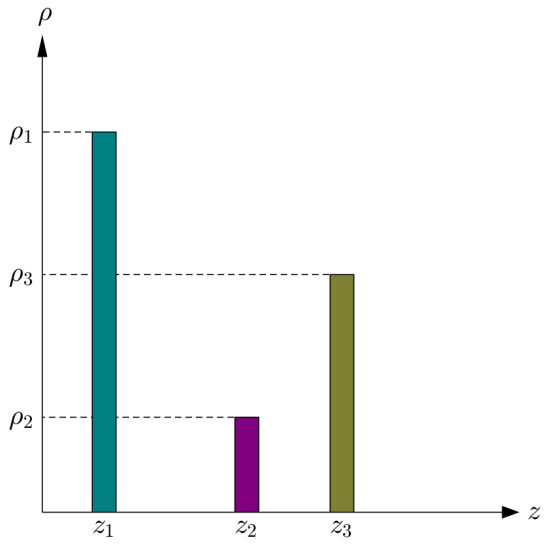
A magnetic field gradient applied along a single dimension will spatially vary $\omega$ along the same dimension. For example, if a $z$-gradient is applied:

$$\omega(z) = \omega_0 + \gamma G_z z. \tag{3.3}$$

This is visualised in Figure 3.1. The technique of spatially encoding $\omega_0$ with magnetic field gradients is known as frequency encoding and has wide applications in MRI. To understand how this can be utilised for spatial encoding, imagine a series of objects placed within a static magnetic field, with an applied 1D gradient along the $z$-dimension. An example system is visualised in Figure 3.2a. A simple NMR experiment is performed on the system, where an RF pulse of a sufficiently wide bandwidth is applied to perturb spins in all the objects simultaneously from




(a) Three objects in a magnetic field




(b) Signal amplitudes as a function of position

Figure 3.2: Three objects of arbitrary proton density, $\rho_1$, $\rho_2$, and $\rho_3$, are placed within a static magnetic field and a magnetic field gradient is applied along the $z$-direction. This is visualised in the $yz$-plane (Figure 3.2a). As these objects are in different positions along the $z$-dimension, they will each experience a difference precession frequency, $\omega_{1,2,3}$. The proton density (Figure 3.2b) for each object can be determined by measuring the signal intensity at each frequency. Note scales are for illustrative purposes only

thermal equilibrium. The received signal from the subsequent signal evolution will be proportional to the linear superposition of signals from each individual object:

$$S(t) \propto \sum_{k=1}^{n} \rho_k \left(T_1, T_2, T_2^*\right) e^{-i\omega_k t} \tag{3.4}$$

where $k$ refers to the $k^{\text{th}}$ object and $\rho(T_1, T_2, T_2^*)$ corresponds to the proton density weighted by the effects of relaxation. Frequency encoding provides a spatially varying $\omega$ proportional to position along the $z$-dimension (Equation 3.3). Without frequency encoding, Equation 3.4 would simplify to:

$$S(t) \propto e^{-i\omega_0 t} \sum_{k=1}^{n} \rho_k \left(T_1, T_2, T_2^*\right) \tag{3.5}$$

and there would be no variable which can give an indication of spatial position within the system.

Equation 3.4 can be generalised as a continuous function. To simplify further, relaxation effects will ignored and the rotating frame about $\omega_0$ will be considered (discussed in Section 2.4.5), defining $\Delta\omega = \gamma G_z z$:

$$S(t) \propto \int_{-\infty}^{\infty} \rho\left(\Delta\omega\right) e^{-i\Delta\omega t}\, d\Delta\omega \tag{3.6}$$

which can be redefined in terms of the spatial position variable, $z$:

$$S(t) \propto \int_{-\infty}^{\infty} \rho\,(z)\, e^{-i\gamma G_z z t}\, dz. \tag{3.7}$$

A spatial frequency variable, $k_z$, can be defined as $k_z = \gamma G_z t$, measured in units of $\mathrm{m}^{-1}$:

$$S(k_z) \propto \int_{-\infty}^{\infty} \rho(z) e^{-ik_z z}\, dz. \tag{3.8}$$

$\rho(z)$ can then be determined via the Fourier transform of $S(k_z)$:

$$\rho(z) \propto \int_{-\infty}^{\infty} S\,(k_z)\, e^{ik_z z}\, dk_z. \tag{3.9}$$

From the application of a magnetic field gradient, it is therefore possible to determine $\rho(z)$ as a function of spatial position to differentiate objects along the $z$-dimension (Figure 3.2b).

The detected frequency encoded signal consists of the cumulative sum of the signal from each individual spin within a system, as described in Equation 3.6. The subsequent signal evolution can be analysed to determine the frequency contributions of the system. To examine this further, consider a 1D system of constant spatial density $\rho$ and length $L_z$ within an MRI scanner whose magnetisation has been perturbed from thermal equilibrium, with an applied magnetic field gradient providing a maximum frequency perturbations $\Delta\omega = \pm\omega_{G_z}$ at the edges of the object. For simplicity it will be assumed that the object does not experience any relaxation effects and without the presence of a magnetic field gradient, all nuclei oscillate at the Larmor frequency, $\omega_0$. From Equation 3.6, the temporal signal evolution can be determined as evolving via:

$$S(t) \propto \rho\omega_{G_z} \operatorname{sinc} \omega_{G_z} t \tag{3.10}$$

and the signal is modulated by a sinc function. Therefore it can be realised that even without considering the effects of relaxation, subsequent dephasing induced by the magnetic field gradient will lead to a temporal loss of amplitude in the detected signal which can be used to determine the properties of the original system. This can be redefined in terms of $k$-space:

$$S(k_z) \propto \rho \frac{L_z}{2} \operatorname{sinc}\left(\frac{L_z k_z}{2}\right) \tag{3.11}$$

If the $k$-space evolution of the signal can be sufficiently sampled, it will provide the experimenter with enough information to reconstruct the spin density of the

original object. From Equation 3.9:

$$\int_{-\infty}^{\infty} \rho \frac{L_z}{2} \operatorname{sinc}\left(\frac{L_z k_z}{2}\right) e^{ik_z z}\, dk_z \propto \begin{cases} \rho & \text{if } -\frac{L_z}{2} \leq z \leq \frac{L_z}{2} \\ 0 & \text{otherwise} \end{cases}. \tag{3.12}$$

For an 1D object of constant spatial density $\rho$, the signal will evolve via a sinc function. As the objects spin density becomes a more complex function of spatial position, the signal evolution will also increase in complexity. A few simple examples are given in Table 3.1.

### 3.2.3 Sampling Over $k$-space

From the definition of $k_z$:

$$k_z = \gamma G_z t \tag{3.13}$$

it can be observed that to sample over different values of $k_z$, two methods can be considered. Firstly, a constant gradient, $G_z$, can be applied, with signals sampled at different values of $t$. Secondly, a repeated experimental protocol can be designed, involving varying $G_z$ and sampling the signal at an identical $t$ in each repetition. It is simple to realise that the first method, where $G_z$ remains constant is experimentally faster and simpler to perform.
Consider a spin density, $\rho(z)$, sampled from $k_z = 0$ to $k_{\max}$. The path in $k$-space is shown in Figure 3.3. The signal is sampled during the traversal through $k$-space. Though $k_z$ is defined over both positive and negative values, from the information

| **Spin density ($\boldsymbol{\rho}$)** | $\boldsymbol{S(k_z)}$ |
|---|---|
| $\rho(z) = \begin{cases} \rho & \text{for } -\frac{L_z}{2} \leq z \leq \frac{L_z}{2} \\ 0 & \text{otherwise} \end{cases}$ | $\propto \rho \frac{L_z}{2} \operatorname{sinc}\left(\frac{L_z k_z}{2}\right)$ |
| $\rho(z) = \begin{cases} \rho_1 & \text{if } -\frac{L_z}{2} \leq z \leq 0 \\ \rho_2 & \text{if } 0 < z \leq \frac{L_z}{2} \\ 0 & \text{otherwise} \end{cases}$ | $\propto \frac{L_z}{4} \operatorname{sinc}\left(\frac{L_z k_z}{4}\right) \cdot \left(\rho_1 e^{i\frac{L_z k_z}{4}} + \rho_2 e^{-i\frac{L_z k_z}{4}}\right)$ |
| $\rho(z) = \begin{cases} \rho \cdot \lvert z \rvert & \text{if } -\frac{L_z}{2} \leq z \leq \frac{L_z}{2} \\ 0 & \text{otherwise} \end{cases}$ | $\propto \rho \left(\frac{L_z^2}{4} \operatorname{sinc}\left(\frac{L_z k_z}{2}\right) + \frac{1}{k_z^2} \cos\frac{L_z k_z}{2} - \frac{2}{k_z^2}\right)$ |

Table 3.1: A few examples of the form of the $k$-space signal evolution, $S(k_z)$, for 1D objects of varying spin-density.

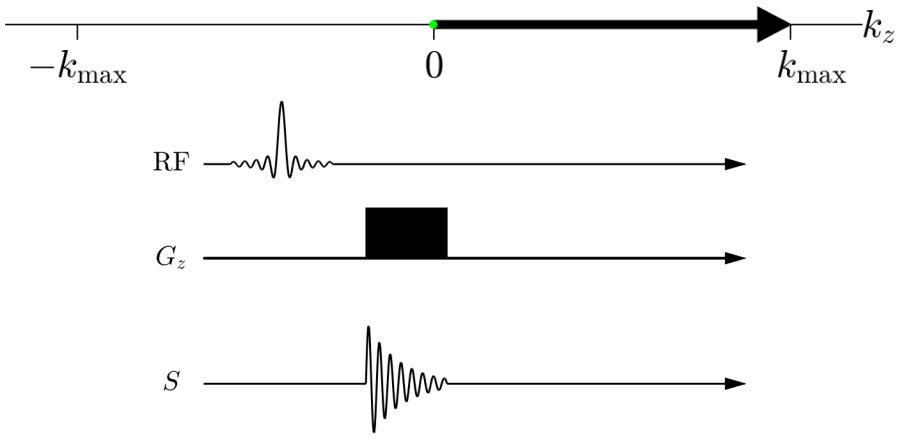



Figure 3.3: Path through $k$-space for an arbitrary 1D nuclear spin density sampled between $k_z = 0$ (green dot) to $k_{\max}$, with corresponding sequence diagram below. In sequence diagrams, gradients are represented by blocks above and below the $G_{x,y,z}$ lines to represent positive and negative gradients respectively, with signal sampling over the regions where $S$ is represented by an exponentially modified oscillating function. The RF pulse is represented by a sinc function and time defined horizontally within the diagram. Note that objects are not to scale and are for illustrative purposes only. This type of representation will be used in all sequence diagrams shown in this thesis.

provided so far it is not possible to sample both positive and negative values of $k$-space in a single acquisition, as $t \geq 0$. Section 3.4 discusses a method for sampling between $-k_{\max}$ and $k_{\max}$, known as a 'gradient-echo', which forms an integral part of this thesis.

## 3.3 Encoding in Multiple Dimensions

### 3.3.1 Definitions of the Signal and $k$-space

2D and 3D spatial-encoding is a simple extension of the 1D method, requiring magnetic field gradients that can be applied across two and three dimensions respectively. The 1D definition of $S(k_z)$ in Equation 3.8 is extended to multiple dimensions as follows:

$$\begin{aligned} S(\vec{k}) &\propto \int_{-\infty}^{\infty} \rho(x,y,z) e^{-i\left(k_x x + k_y y + k_z z\right)}\, dz\, dy\, dx \\ &\propto \int_{-\infty}^{\infty} \rho(\vec{r}) e^{-i\vec{k}\cdot\vec{r}}\, d^3r \end{aligned} \tag{3.14}$$

where $d^3r$ is a volume element, $\vec{k} = k_x\hat{i} + k_y\hat{j} + k_z\hat{k}$ and $\vec{r} = x\hat{i} + y\hat{j} + z\hat{k}$. $\rho(\vec{r})$ can then be determined via the Fourier transform of $S(\vec{k})$:

$$\rho(\vec{r}) \propto \int_{-\infty}^{\infty} S(\vec{k}) e^{i\vec{k}\cdot\vec{r}}\, d^3k \tag{3.15}$$

where $d^3k$ is a volume element in $k$-space.

If $k$-space can be sufficiently sampled over a multi-dimensional system, then it will be possible to reconstruct the full spin density, $\rho(\vec{r})$. As discussed in Section 3.2.3, magnetic field gradients can be utilised to traverse through $k$-space. For a multi-dimensional system, Equation 3.13 can be extended:

$$\begin{aligned} k_x &= \gamma G_x t \\ k_y &= \gamma G_y t \\ k_z &= \gamma G_z t \end{aligned} \tag{3.16}$$

and it can be realised that orthogonal magnetic field gradients can be used to sample $k$-space in multiple dimensions.

### 3.3.2 Phase Encoding

Section 3.2.2 revealed how frequency encoding can provide information about a 1D system by sampling a 1D line of $k$-space. To expand this concept to 2D and 3D systems, a second form of encoding, known as 'phase encoding' must be introduced.

Phase encoding utilises the same methodology as frequency encoding, with the magnetic field gradient applied perpendicular to the frequency encoding direction. However, rather than sampling the signal during phase encoding, the applied gradient is simply used to traverse in a direction perpendicular to the frequency encoding direction in $k$-space. Frequency encoding is then repeated along the same dimension as the original frequency encoding, leading to the collection of a new line of $k$-space. The direction along which frequency encoding is applied is known as the 'read' direction. An example $k$-space excursion is shown in Figure 3.4.

Phase encoding can therefore be defined as the method of taking steps along the $k$-space dimensions orthogonal to the frequency encoding dimension, without sampling the signal. Once the phase encoding gradient has been switched off, the magnetisation will precess at the same frequency prior to the application of the phase encoding gradient. However, the phase of the transverse magnetisation will have been modified due to the applied phase encoding gradient such that it varies along the phase encoded direction. This is the origin of the the name 'phase

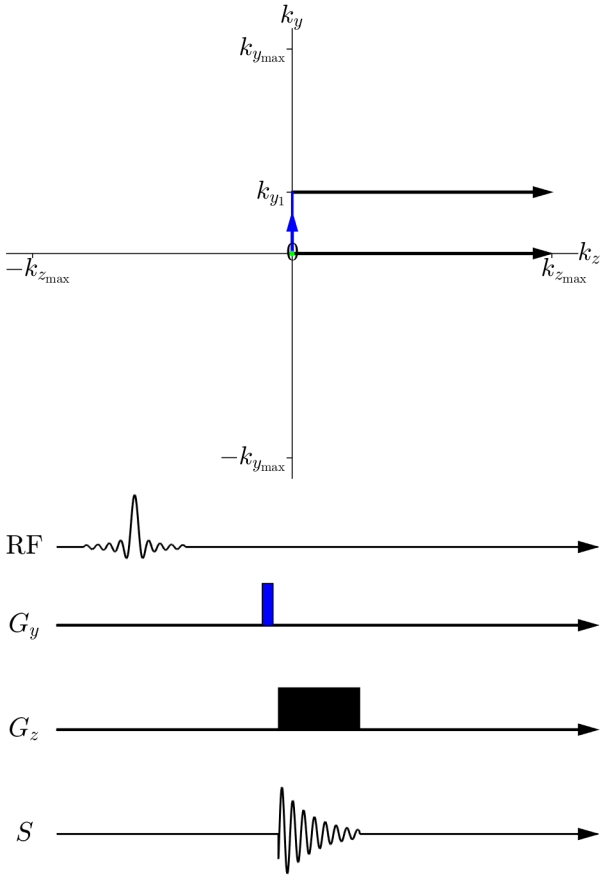



Figure 3.4: Path through $k$-space for sampling different $k$-space lines for an arbitrary 2D nuclear spin density, with corresponding sequence diagram. The lines in blue indicate the phase encoding direction, with the starting point at $[0, 0]$ marked in green. Rather than being restricted to the $k$-space line at $k_z = 0$, phase encoding allows the $k_y$ axis to be traversed. Here the signal is sampled along the $k_z$-dimension, defining $z$ as the read direction.

encoding' and begins to describe how perpendicular gradients traverse through $k$-space to allow multi-dimensional spatial encoding.

As an example, the 1D system of constant spatial density will be revisited. However, now the system will be expanded to 2D, with lengths $L_z$ and $L_y$ along the $z$- and $y$- dimensions respectively, with two orthogonal gradients $G_z$ and $G_y$. For this 2D system, the signal with simultaneously applied gradients can be described mathematically by:

$$S(\vec{k}) \propto \rho \int_{-\frac{L_y}{2}}^{\frac{L_y}{2}} \int_{-\frac{L_z}{2}}^{\frac{L_z}{2}} e^{-i\left(k_y y + k_z z\right)} \, dz \, dy \tag{3.17}$$

with a solution given via an expansion to Equation 3.11 to include the $y$-dimension:

$$S(\vec{k}) \propto \rho \frac{L_y}{2} \frac{L_z}{2} \operatorname{sinc} \frac{L_y k_y}{2} \operatorname{sinc} \frac{L_z k_y}{2}. \tag{3.18}$$

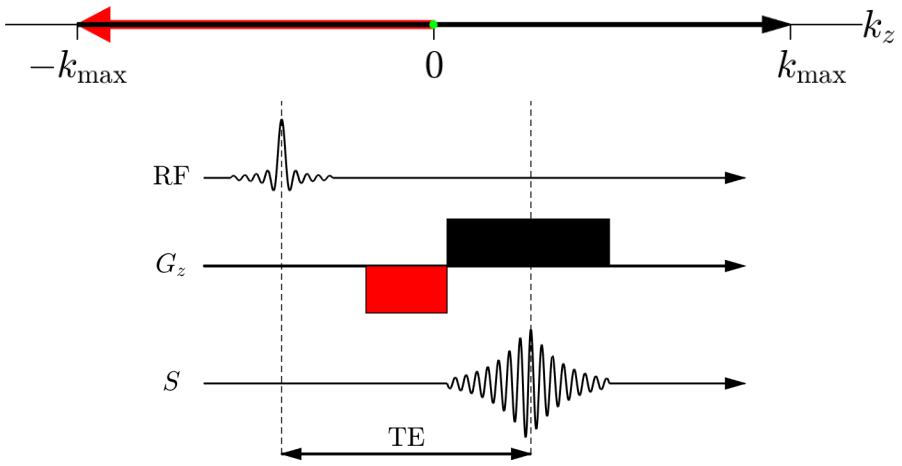



Figure 3.5: Path through $k$-space for an arbitrary 1D nuclear spin density sampled from $k_z = -k_{\max}$ to $k_{\max}$, with sequence diagram below. To achieve this, first a negative gradient, known as a 'dephasing' gradient, is applied to shift $k$ from 0 (green point) to $-k_{\max}$ (red line). During the application of the negative gradient, no signal is sampled. Then a positive gradient, known as the 'rephasing gradient' is applied to traverse the whole line of $k$-space (black line), with the signal being sampled during this process. The use of two gradient lobes to sample all of $k$-space is known as a 'gradient-echo'. The time between the middle of the RF pulse and the condition in Equation 3.22 being satisfied is defined as the echo time, TE.

## 3.4 Gradient Echo Sequence

### 3.4.1 Definition

The gradient echo (GE) sequence is one of the simplest sequences that can be applied in MRI. GE sequences utilise both positive and negative gradients to sample over positive and negative $k$-space coordinates and generate a $T_2^*$ weighted signal ($T_2^*$ relaxation properties are discussed in Section 2.4.4). The distinctive property of GE sequences is that they do not remove the effects of dephasing induced by local magnetic field perturbations. This could be seen as problematic; contributions from an inhomogeneous $B_0$ field will not be removed in GE experiments, leading to image artefacts. However, field perturbations generated from the magnetic properties of the system, including magnetic susceptibility (discussed in Chapter 4) and chemical exchange (discussed in Section 7.2) will contribute to image contrast and provide an experimenter with a further insight into the structure and composition of the system. Referring back to the title of this thesis, to examine the magnetic properties of tissue, GE sequences must be utilised. Within this thesis, GE sequences are therefore almost exclusively used, as they form the foundation of phase imaging.

### 3.4.2 1D Gradient Echo and the Echo-Time

For a 1D system along the $z$-dimension, the temporal phase evolution induced by a magnetic field gradient is defined as:

$$\begin{aligned} \phi_G(t, z) &= -\Delta\omega t \\ &= -\gamma G_z z \cdot t \end{aligned} \tag{3.19}$$

with phase defined as evolving negatively for a positive frequency offset. Equation 3.19 can be redefined in terms of $k$-space:

$$\begin{aligned} \phi_G(k_z, z) &= -\gamma G_z t \cdot z \\ &= -k_z z. \end{aligned} \tag{3.20}$$

For a single gradient application, $G_z = -G$, $k_z$ will be confined to negative values as $t$ can only take positive values. To sample over both +ve and -ve values of $k$-space, a second gradient, known as a 'rephasing gradient' is required. The rephasing gradient is applied with opposite polarity to the original gradient (subsequently known as the 'dephasing' gradient), $G_z = G$. $G_z$ is now a function of time, $G_z(t)$. To account for the time dependence of $G_z(t)$, $k_z$ is generalised as follows:

$$k_z = \int_0^t \gamma G_z(t)\, dt. \tag{3.21}$$

When $\phi_G = 0$, the transverse magnetisation is in-phase and therefore spatially invariant, defined by the following condition:

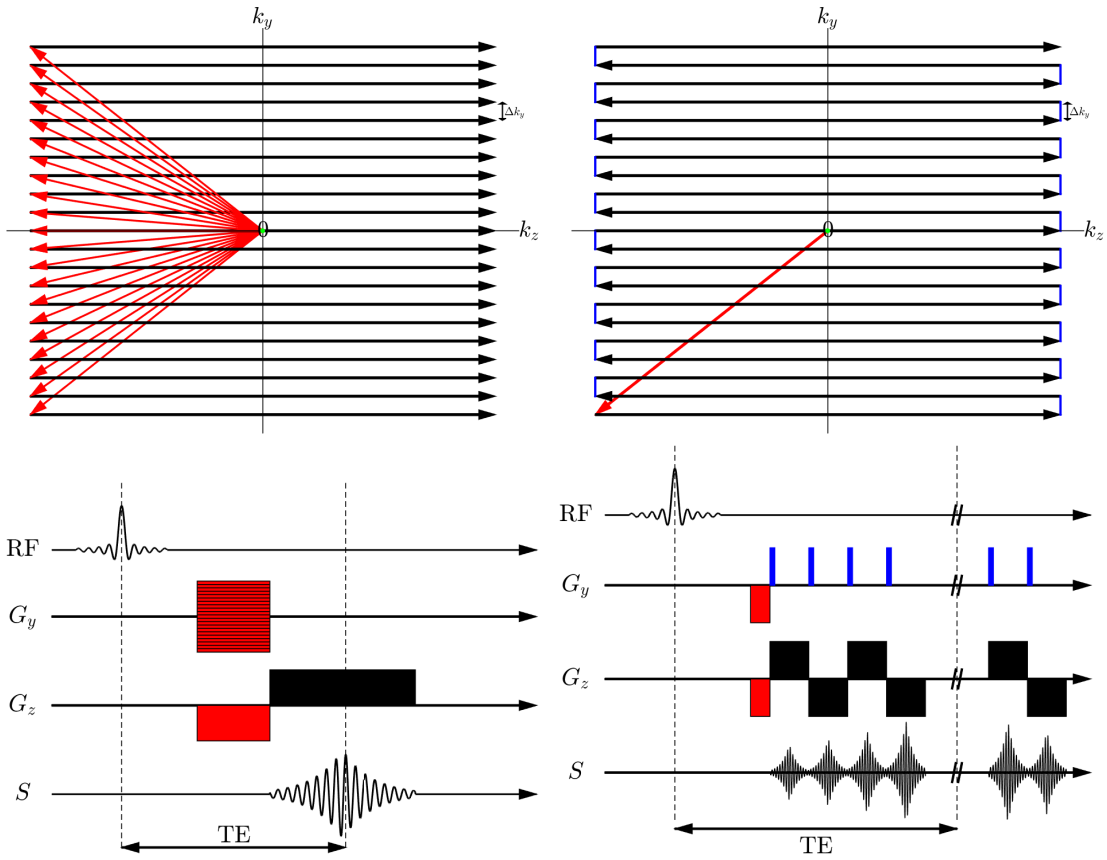
$$\int dt G(t) = 0. \tag{3.22}$$

The time at which this condition is achieved is known as the 'echo-time' (TE), where dephasing of transverse magnetisation induced by the magnetic field gradients has been removed. This is visualised for a 1D system in Figure 3.5.

### 3.4.3 Multiple Dimensions and non-Cartesian Sampling

The extension to multiple dimensions utilises both positive and negative gradients in conjunction with frequency and phase encoding to sample a multi-dimensional array of points in $k$-space. An example is shown in Figure 3.6 for 2D Cartesian $k$-space sampling.

In Figure 3.6a, a new RF pulse is applied per $k$-space line acquisition, with the assumption that the magnetisation has returned to thermal equilibrium between pulses, due to the impact of relaxation (discussed in detail for MRI acquisitions in Section 3.5; theory of relaxation provided in Section 2.4). Different relative strengths of the two orthogonal phase encoding gradients are used to acquire the




(a) 2DFT GE sequence with Cartesian sampling.

(b) 2D EPI GE sequence with Cartesian sampling.

Figure 3.6: Utilising two forms of GE acquisition to sample a full set of $k$-space lines for an arbitrary 2D nuclear spin density, with corresponding sequence diagrams. The starting points at $[0, 0]$ are marked in green. The lines in blue indicate the phase encoding direction, with the red arrows indicating the initial dephasing gradients, generated by simultaneous application of $z$ and $y$ gradients. From this position, lines of $k$-space can be sampled via the 2DFT GE acquisition in Figure 3.6a or the EPI GE acquisition in Figure 3.6b. In the 2DFT sequence diagram (Figure 3.6a), the black lines on the $G_y$ phase encoding gradient represent repeats of the sequence at different values of $G_y$. In the EPI sequence diagram (Figure 3.6b) the black slashes on all axes represent further repeats of the $G_y$ and $G_z$ gradients, with more signal sampling to obtain the full 2D $k$-space dataset. For the EPI scan, the TE is defined as the time from RF excitation to acquisition of the centre of $k$-space ($[k_z, k_y] = [0, 0]$).

full 2D $k$-space data. This is known as a 2D Fourier transform (2DFT) acquisition, with the time between RF pulses known as the repetition time, TR. However, waiting for magnetisation to return to thermal equilibrium is not actually required and it is possible to obtain a full 2D image from a single RF pulse, by utilising a trapezoidal, periodic read gradient to generate a train of gradient echoes and applying small phase encoding steps between echoes. This is known as an 'echo-planar' imaging (EPI) [2] sequence and is shown in Figure 3.6b. To extend to a 3D $k$-space acquisition, a second phase encoding gradient along the remaining

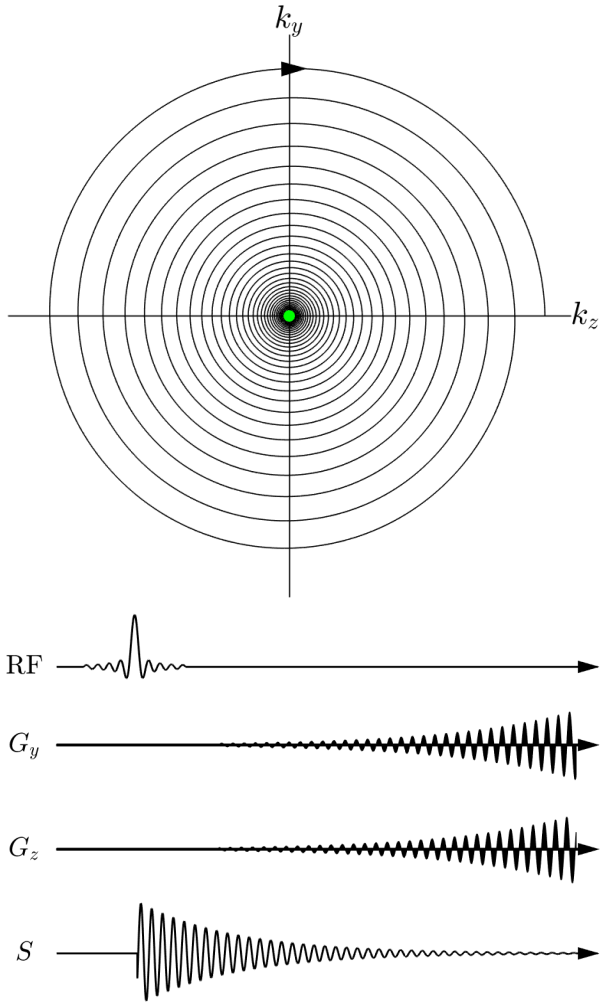



Figure 3.7: Spiral path sampling $k$-space for an arbitrary 2D nuclear spin density, known as 'spiral-EPI' [3], with sequence diagram below. The starting point at $[0, 0]$ is marked in green. Rather than being restricted to Cartesian sampling, simultaneous $z$- and $y$- gradients are applied of the form $G_z = f(t)\cos\beta t$ and $G_y = f(t)\sin\beta t$, where $f(t)$ is an increasing function of time and $\beta$ is a real constant. In the above figure, $f(t) = e^{\alpha t}$, where $\alpha$ is a real constant. These gradients applied simultaneously form the spiral path seen in the image.

dimension is required to sample all three dimensions of $k$-space.

An important observation is that gradients can be applied simultaneously to traverse lines of $k$-space that are not parallel to the gradient axes. In Figure 3.6 this is shown with the initial dephasing gradient traversing through $k$-space diagonally from the simultaneous application of $y$- and $z$- gradients. Simultaneous gradient application begins to reveal the versatility of $k$-space sampling. An example of non-Cartesian sampling is shown in Figure 3.7.

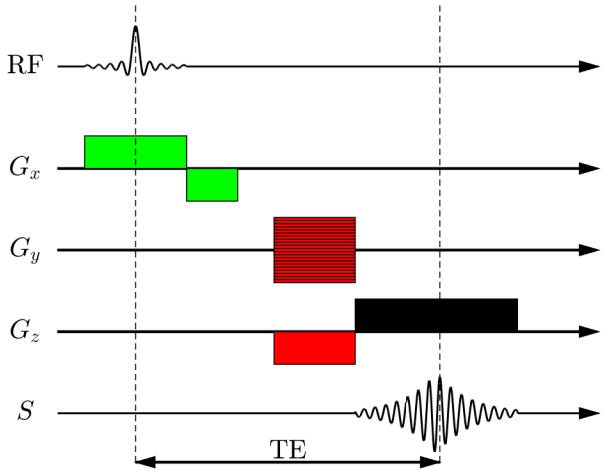



Figure 3.8: Sequence diagram for a slice-selective 2DFT sequence. The slice selection gradient is applied simultaneously with the RF pulse and shown in green. A rephasing pulse is applied after the slice selection gradient to ensure all spins in the slice start in phase. Details of the 2DFT sequence are outlined in Figure 3.6.

### 3.4.4 Slice-Selection

RF pulses combined with magnetic field gradients can be used to perturb the magnetisation of a user-defined 2D volume within a 3D system from thermal equilibrium. Once a 2D slice has been selected, further applications of magnetic gradients can be utilised to generate a 2D dataset as described in previous sections. To understand how slice-selection can be achieved, consider a gradient, $G$, applied along the $x$-dimension with an RF pulse of frequency $\omega_k$ and bandwidth $\Delta\omega_k$ simultaneously applied. The RF pulse will perturb the spin states of a 2D slice at position $x = \frac{\omega_k}{\gamma G}$ and of width $\Delta x = \frac{\Delta\omega_k}{\gamma G}$ from thermal equilibrium.
Manipulation of magnetic gradients provides an experimenter with the possibility of obtaining slices of user-defined thickness and orientation. By varying $\omega_k$ or the strength/direction of $G$, a different 2D slice can be selected. Rather than being confined to orthogonal slices along the $x$-, $y$- and $z$-dimensions, gradients can be linearly combined to select 2D slices of arbitrary orientations, defining the slice direction as:

$$\text{slice direction} = \frac{G_x\hat{x} + G_y\hat{y} + G_z\hat{z}}{\left(G_x^2 + G_y^2 + G_z^2\right)^{\frac{1}{2}}}. \tag{3.23}$$

Slice thickness can be adjusted by varying $\Delta\omega$ or $(G_x^2 + G_y^2 + G_z^2)^{\frac{1}{2}}$. A sequence diagram for a slice-selective 2DFT sequence is visualised in Figure 3.8.

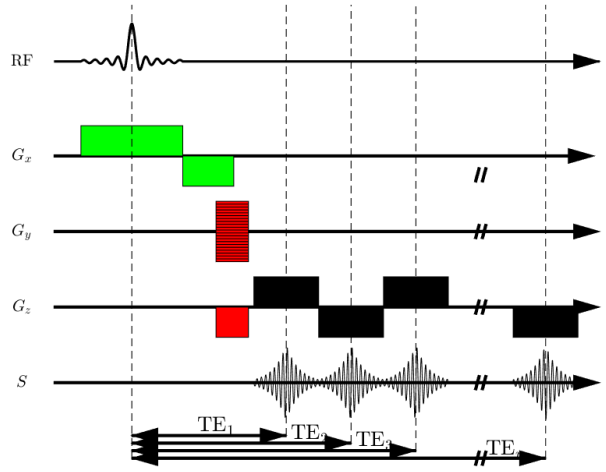



Figure 3.9: Sequence diagram for a multi-echo 2DFT sequence with $n$ echoes. Details of 2DFT sequence are outlined in Figure 3.6.

### 3.4.5 Multi Echo Acquisitions

Extension from a single TE acquisition to a multi-echo acquisition can be achieved via sampling the same line of $k$-space at different TE values. The TE is a user defined input, with values restricted by the properties of the gradient system limiting the speed of $k$-space acquisition within the system. The ability to vary TE is of particular use when examining the relaxation properties of a system (discussed in Section 3.5). A sequence diagram for a multi-echo 2DFT sequence is shown in Figure 3.9.

### 3.4.6 Image Resolution

A theoretical approach to MRI provides the opportunity to define continuous, infinitely sampled signals to perform analysis (examples in Table 3.1). However, experimentally this is not possible. The sampling rate and range of $k$-space sampled have a direct impact on both the field of view (FOV) and the resolution of the collected datasets.

An experiment can be considered on a system where data is sampled from $-k_{(x,y,z)_{\max}}$ to $k_{(x,y,z)_{\max}}$ with spacing of sampled points given by $\Delta k_{x,y,z} = \gamma G_{x,y,z} \Delta t$. The FOV and resolution are defined as:

$$\begin{aligned} \text{FOV} &= \frac{2\pi}{\Delta k_{x,y,z}} \\ \text{resolution} &= \frac{\pi}{k_{(x,y,z)_{\max}}} \end{aligned} \tag{3.24}$$

where it is observed that the FOV is related to the spacing of sampled points in $k$-space, $\Delta k_{x,y,z}$ and the resolution is related to the extent of sampled $k$-space,

$2k_{(x,y,z)_{\max}}$. This inverse relationship is consistent with the concept of $k$-space as the 'reciprocal-space' of an image.

## 3.5 Impact of Relaxation

Signal relaxation (defined in Sections 2.4.3 and 2.4.4) provides the experimenter with valuable information about the magnetic properties of the system. With this in mind, it is important to consider both the impact of relaxation on signal contrast, in addition to the restrictions that relaxation imposes on performing a successful MRI experiment. In this section, both of these will be considered, with a focus on the impact on GE sequences, as they are used almost exclusively throughout this thesis.

### 3.5.1 Influence of Echo Time and Repetition Time on Signal Contrast in GE Sequences

The relaxation properties of tissue dictate the observed contrast in GE images. It is well established that different magnetic environments, including those found within body tissues are characterised by different $T_1$, $T_2$ and $T_2^*$ relaxation constants. With an understanding of these relaxation constants, sequences can be developed to manipulate the signal intensity from tissues and the contrast between tissues. A comparison of $T_1$, $T_2$ and $T_2^*$ relaxation constants for grey and white matter at different field strengths is displayed in Table 3.2.
Previous work in this chapter has not given consideration to signal relaxation. From the discussion in previous sections, the time at which a signal is sampled

| **Field Strength (T)** | **Grey matter $T_1$ (ms)** | **White matter $T_1$ (ms)** |
|---|---|---|
| 1.5 | $1197 \pm 34$ | $646 \pm 32$ |
| 3 | $1607 \pm 112$ | $838 \pm 50$ |
| 7 | $1939 \pm 150$ | $1126 \pm 97$ |
| | **Grey matter $T_2$ (ms) (Frontal)** | **White matter $T_2$ (ms)** |
| 1.5 | $87 \pm 4$ | $80 \pm 3$ |
| 3 | $76 \pm 5$ | $71 \pm 5$ |
| 7 | $47 \pm 9$ | $47 \pm 1$ |
| | **Grey matter $T_2^*$ (ms)** | **White matter $T_2^*$ (ms)** |
| 1.5 | $84.0 \pm 0.8$ | $66.2 \pm 1.9$ |
| 3 | $66.0 \pm 1.4$ | $53.2 \pm 1.2$ |
| 7 | $33.2 \pm 1.3$ | $26.8 \pm 1.2$ |

Table 3.2: $T_1$ [4], $T_2$ [5] and $T_2^*$ [6] times for grey and white matter at 1.5, 3 and 7T.

(defined by the echo time, TE, discussed in Section 3.4.2) would have no impact on the observed tissue contrast, which would be proportional to the spin density, $\rho$, of the tissue. However the Bloch equations for a GE sequence:

$$\begin{aligned} M_z &= M_{z_0} e^{-\frac{\mathrm{TE}}{T_1}} + M_0 \left(1 - e^{-\frac{\mathrm{TE}}{T_1}}\right) \\ M_+ &= M_{+_0} e^{-\frac{\mathrm{TE}}{T_2^*}} e^{-i\Delta\omega \mathrm{TE}} \end{aligned} \tag{3.25}$$

reveal the impact of $T_1$ and $T_2^*$ relaxation on tissue contrast (parameters outlined and discussed in Sections 2.4.3 and 2.4.4). Here the time, $t$, has been replaced with the echo time, TE. Following a $90^o$ pulse, the signal detected will be $T_2^*$-weighted. A second parameter, known as the repetition time, TR, is additionally used to weight the signal. The TR is defined as the time between applied RF pulses used to tip the magnetisation into the transverse plane. So far within this thesis, no consideration has been given to the idea of applying further RF pulses before the magnetisation has returned to thermal equilibrium ($M_z = M_0$). However, re-excitation before magnetisation has returned to thermal equilibrium can provide the experimenter with $T_1$ signal weighting, in addition to a reduced acquisition time (discussed further in Section 3.5.2).
Following a $90^o$ pulse, signal will evolve as follows:

$$\begin{aligned} M_z(t) &= M_0 \left(1 - e^{-\frac{t}{T_1}}\right) \\ M_+(t) &= M_0 e^{-\frac{t}{T_2^*}} e^{-i\Delta\omega t} \end{aligned} \tag{3.26}$$

where all the magnetisation will initially be in the transverse plane ($M_{+_0} = M_0$, $M_{z_0} = 0$). However, following repeated applications of the $90^o$ RF pulse before the condition $M_z = M_0$ is obtained, the signal projected into the transverse plane is proportional to the longitudinal magnetisation that is recovered in the TR period ($M_z = M_0(1 - e^{-\frac{\mathrm{TR}}{T_1}})$):

$$M_+(t) = M_0(1 - e^{-\frac{\mathrm{TR}}{T_1}}) e^{-\frac{t}{T_2^*}} e^{-i\Delta\omega t} \tag{3.27}$$

where $t$ is the time since the last RF pulse. Replacing $t$ with TE:

$$M_+(\mathrm{TE}) = M_0(1 - e^{-\frac{\mathrm{TR}}{T_1}}) e^{-\frac{\mathrm{TE}}{T_2^*}} e^{-i\Delta\omega \mathrm{TE}} \tag{3.28}$$

the dependence of relaxation contrast on TR and TE can be observed. A quick examination of Equation 3.28 indicates that for a system undergoing repeated RF pulse excitations, a short TR and short TE will provide greater $T_1$ weighting, whereas a long TR and long TE will provide greater $T_2^*$ weighting. A long TR and short TE will provide weighting to the proton density, $\rho$, as $\rho \propto M_0$.
Beyond $T_1$, $T_2^*$ and $\rho$ weighting of a system, knowledge of the $T_1$ and $T_2^*$ times of

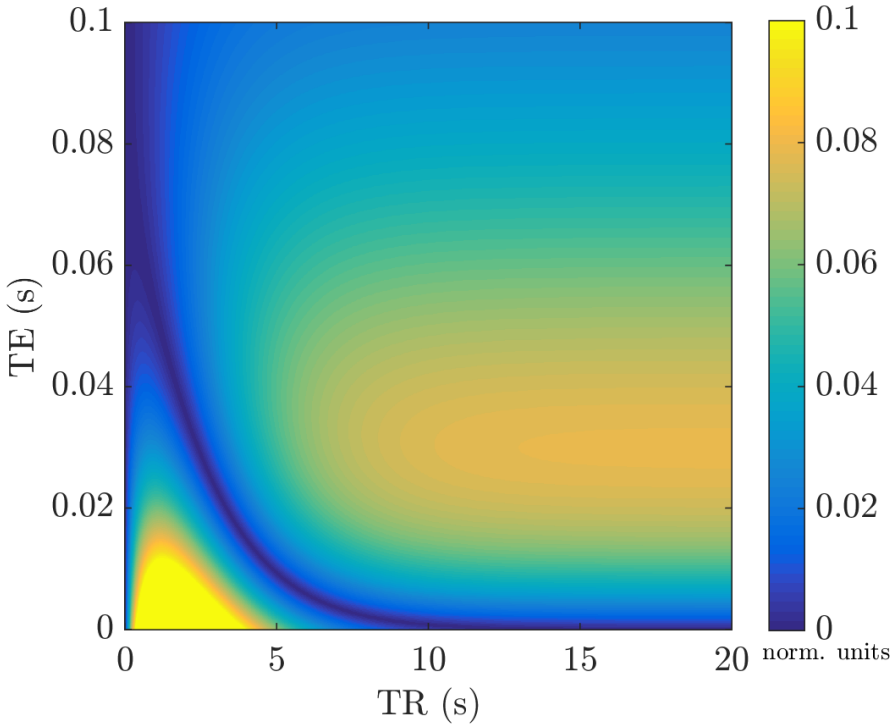



Figure 3.10: Using the values of $T_1$ and $T_2^*$ for grey and white matter at 7 T (defined in Table 3.2), $|C|$ was determined for different values of TE and TR, with $M_{0_A} = M_{0_B} = 1$.

different tissues provides the experimenter with the opportunity to manipulate the TR and TE to maximise contrast between tissue types. The magnitude contrast, $|\mathrm{C}(t)|$, between two samples, A and B, is defined as $|M_{+_A}(t) - M_{+_B}(t)|$:

$$|\mathrm{C}(t)| = \left| M_{0_A}(1 - e^{-\frac{\mathrm{TR}}{T_{1_A}}})e^{-\frac{\mathrm{TE}}{T^*_{2_A}}} - M_{0_B}(1 - e^{-\frac{\mathrm{TR}}{T_{1_B}}})e^{-\frac{\mathrm{TE}}{T^*_{2_B}}} \right| \tag{3.29}$$

where $|\ldots|$ defines the absolute difference. From this, optimal parameters can be selected to discriminate between tissue types. This is visualised for grey and white matter in Figure 3.10.

### 3.5.2 Flip Angle and the FLASH Sequence

In Section 2.4.6, the influence of the RF pulse on spin ensembles was discussed. The 'flip angle', defined as the angle of rotation, $\alpha$, in Equation 2.39 was introduced as the angle through which the macroscopic magnetisation vector is rotated by the RF pulse. Previous work within this chapter has considered RF pulses with a $90^o$ flip angle, after application of which the magnetisation is rotated into the transverse plane and signal is maximised. However, the flip angle is an additional, user defined variable, which can be manipulated via adjusting the RF pulse strength and duration.

A typical rule of thumb in MRI is that for magnetisation to have returned to thermal equilibrium ($M_z = M_0$) after RF pulse excitation, a waiting time of $\sim 5T_1$ is

required. This can be provided experimentally without problem, with no hardware constraints preventing data collection. However, the significant length of time between RF pulses would make imaging incredibly time consuming in a number of cases and reduce the practicality of *in-vivo* scanning, where scan times need to be kept to a minimum. In the previous section, it was noted how a short TR can provide $T_1$ weighting to an image. The flip angle allows the user to further manipulate contrast and optimise the signal when TR $< 5T_1$.

For a $90^o$ flip angle, the steady state magnetisation recovers between repeated RF acquisitions as follows:

$$M_z = M_0(1 - e^{-\frac{\mathrm{TR}}{T_1}}) \tag{3.30}$$

with the solution for transverse magnetisation defined in Equation 3.28. However, when $\alpha < 90°$:

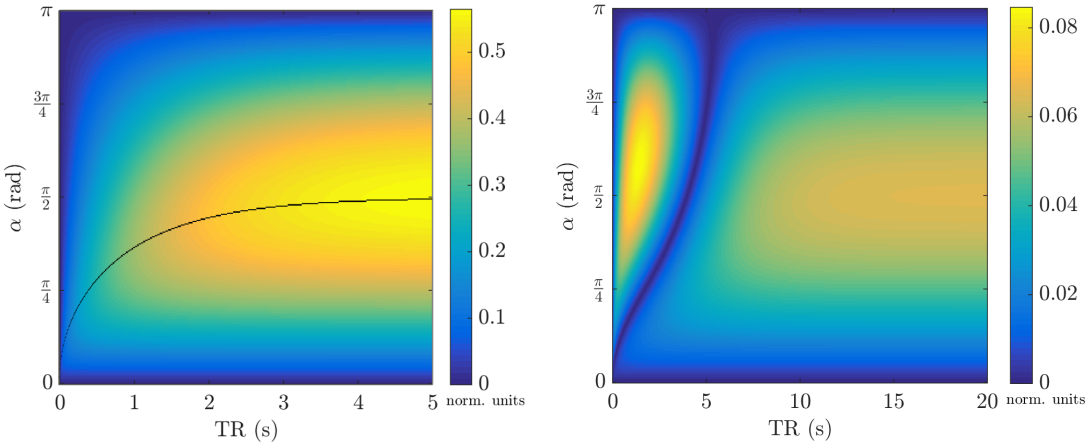
$$M_z = M_{z_{\mathrm{init}}} e^{-\frac{\mathrm{TR}}{T_1}} \cos\alpha + M_0(1 - e^{-\frac{\mathrm{TR}}{T_1}}) \tag{3.31}$$

where $M_{z_{\mathrm{init}}}$ and $M_z$ are the longitudinal magnetisation before and after the RF pulse respectively. Here it can be observed that when $\alpha = 90^o$, the condition in Equation 3.30 is returned. In the steady state, $M_{z_{\mathrm{init}}} = M_z$ and the magnetisation will evolve as follows:

$$\begin{aligned} M_z &= \frac{M_0\left(1 - e^{-\frac{\mathrm{TR}}{T_1}}\right)}{1 - e^{-\frac{\mathrm{TR}}{T_1}}\cos\alpha} \\ M_+(t) &= M_0 \sin\alpha \frac{\left(1 - e^{-\frac{\mathrm{TR}}{T_1}}\right)}{1 - e^{-\frac{\mathrm{TR}}{T_1}}\cos\alpha} e^{-\frac{\mathrm{TE}}{T_2^*}} e^{-i\Delta\omega \mathrm{TE}} \end{aligned} \tag{3.32}$$

where it can be determined that when $\alpha = \arccos e^{-\frac{\mathrm{TR}}{T_1}}$, $M_+(t)$ has a maximum. This is known as the 'Ernst angle' and is visualised in Figure 3.11a. Similar to the discussion in Section 3.5.1, $\alpha$ can be used to manipulate contrast between different tissue types. This is visualised in Figure 3.11b.

Sequences that utilise this method are most commonly known as 'fast low angle shot' (FLASH) sequences [7], though are also commonly known as SPGR (spoiled gradient echo) and T1FFE ($T_1$ fast field echo) sequences, depending on the scanner provider (FLASH - Siemens, SPGR - General Electric, T1FFE - Philips). When TR $\gg T_2$, transverse magnetisation vanishes between RF pulses. This is known as a steady state incoherent (SSI) signal. However, if TR $= O(T_2)$, transverse magnetisation can reach a steady state, known as a steady state coherent (SSC) signal. To prevent the transverse magnetisation from contributing to the signal, spoiling mechanisms must be applied. The SSI signal is considered 'naturally' spoiled, whereas spoiling mechanisms, applied through the application of phase incremented RF pulses and gradient modification are utilised to dephase the transverse magnetisation in SSC sequences [8].




(a) $|M_+|$ with labelled Ernst angle (b) |C|

Figure 3.11: Using the values of $T_1$ and $T_2^*$ for grey and white matter at 7 T (defined in Table 3.2), the magnitude of transverse magnetisation, $|M_+|$ for white matter (Figure 3.11a) and contrast magnitude, |C| between grey and white matter (Figure 3.11b) were determined for different values of TR and $\alpha$. Here TE = 15 ms for both datasets and the black line in Figure 3.11a indicates the Ernst angle for each TR.

## 3.6 Magnitude and Phase Contrast

For a GE sequence, the detected signal is defined in the rotating frame as follows:

$$S(t) = S_0 e^{-\frac{t}{T_2^*}} e^{-i\Delta\omega t} \tag{3.33}$$

where $S_0$ is the signal amplitude. Within this thesis, $S(t)$ will be regularly used in place of the transverse magnetisation, $M_+(t)$. To prevent confusion, magnetisation has and will continue to be defined as the magnetization of the system, useful for theoretical discussion, whereas $S(t)$ is the detected signal from the MRI acquisition, defining $S(t) \propto M_+(t)$.

Equation 3.33 appears considerably simpler than some of the equations produced from the discussion in Section 3.5. If $S(t) \propto M_+(t)$, it could be considered that for a GE sequence with flip angle $\alpha$ and repetition time TR, from Equation 3.32, the signal should evolve via:

$$S(t) = S_0 \sin\alpha \frac{\left(1 - e^{-\frac{\mathrm{TR}}{T_1}}\right)}{1 - e^{-\frac{\mathrm{TR}}{T_1}} \cos\alpha} e^{-\frac{t}{T_2^*}} e^{-i\Delta\omega t}. \tag{3.34}$$

However, it is simple to note that $\sin\alpha \frac{(1-e^{-\frac{\mathrm{TR}}{T_1}})}{1-e^{-\frac{\mathrm{TR}}{T_1}}\cos\alpha}$ is a constant, which can be absorbed into the $S_0$ term, reducing the formula to Equation 3.33. Though an longer TR can give rise to an higher signal-to-noise (SNR) as it allows the spins to recover their longitudinal relaxation, it also increases the length of time to acquire a single line of $k$-space. A trade off between the TR and experimental

repetition time must be determined, with SNR $\propto \sqrt{\mathrm{N_{acq}}}$ where $\mathrm{N_{acq}}$ is the number of acquisitions per line of $k$-space.

Phase is represented by the symbol $\phi$ and is intrinsically related to the frequency perturbations, $\phi(t) = -\Delta\omega t$. Magnitude and phase contrast are defined as follows

$$\begin{aligned} \mathrm{Mag}(t) &= |S(t)| = |S_0| e^{-\frac{t}{T_2^*}} \\ \mathrm{Phase}(t) &= \arctan\left(\frac{\mathrm{im}\, S(t)}{\mathrm{re}\, S(t)}\right) = \phi_w(t) \end{aligned} \tag{3.35}$$

where $\mathrm{re}\, S(t)$ and $\mathrm{im}\, S(t)$ define the real and imaginary components of the signal respectively, $\phi_w(t)$ defines the wrapped phase and arctan defines the 4-quadrant arctangent function. Here it can be observed that the magnitude data is a $T_2^*$-weighted signal. The output of $\phi_{\mathrm{w}}(t)$, rather than $\phi(t)$ is due to the periodical nature of the arctan function being bound between $\pm\pi$. To examine phase contrast further, it is necessary to convert $\phi_{\mathrm{w}}(t)$ to the 'true' phase, $\phi(t)$, also known as the unwrapped phase. This critical step will be discussed in detail in the next chapter with regards to processing phase contrast. However at this stage it is not necessary and for the remainder of this chapter, it will be assumed that $\phi_w(t) = \phi(t)$.

The sign convention of $\phi(t)$ varies within literature, with numerous papers associating a positive phase evolution, $\phi > 0$ with a negative frequency perturbation $-\Delta\omega$ (previously discussed in Section 3.4.2). This convention varies between literature as different scanner brands define signal evolution by with their own sign convention. Within this thesis, experimental results will be presented with the sign convention utilised by the scanner in the experimental chapter. Theoretical considerations will utilise the negative sign convention as discussed above.

Finally, within literature, $\phi$, $\Delta\omega$, linear frequency perturbations, $\Delta f$ and magnetic field perturbations, $\Delta B$, are regularly used and interchanged, even within the context of a single journal paper. It is important to remember that the relationships between these four variables are simply multiplications/divisions by scalar constants. A simple insight into this relationship would be to consider the Larmor equation (Equation 2.15) multiplied by time, $t$:

$$\phi(t) = \gamma \Delta B t. \tag{3.36}$$

These relationships are summarised in Table 3.3. Within this thesis, interchange between these four variables will occur, to describe phenomena in a clear and accessible manner and to directly compare to pre-existing literature.

| **Variable** | $\boldsymbol{\phi(t)}$ | $\boldsymbol{\Delta B}$ | $\boldsymbol{\Delta\omega}$ | $\boldsymbol{\Delta f}$ |
|---|---|---|---|---|
| $\boldsymbol{\phi(t)}$ | - | $\phi(t) = -\gamma\Delta B t$ | $\phi(t) = -\Delta\omega t$ | $\phi(t) = -2\pi\Delta f t$ |
| $\boldsymbol{\Delta B}$ | $\Delta B = -\frac{\phi(t)}{\gamma t}$ | - | $\Delta B = \frac{\Delta\omega}{\gamma}$ | $\Delta B = \frac{2\pi\Delta f}{\gamma}$ |
| $\boldsymbol{\Delta\omega}$ | $\Delta\omega = -\frac{\phi(t)}{t}$ | $\Delta\omega = \gamma\Delta B$ | - | $\Delta\omega = 2\pi\Delta f$ |
| $\boldsymbol{\Delta f}$ | $\Delta f = -\frac{\phi(t)}{2\pi t}$ | $\Delta f = \frac{\gamma\Delta B}{2\pi}$ | $\Delta f = \frac{\Delta\omega}{2\pi}$ | - |

Table 3.3: Look up table for the relationships between $\phi(t)$, $\Delta B$, $\Delta\omega$ and $\Delta f$, assuming a negative sign convention. For a positive sign convention, replace the $-$ sign with $+$. $\gamma = 267.513 \times 10^6\,\mathrm{rad\,s^{-1}\,T^{-1}}$ for proton MRI.

# Bibliography


[1] E Mark Haacke, Robert W Brown, Michael R Thompson, Ramesh Venkatesan, et al. *Magnetic resonance imaging: physical principles and sequence design*, volume 82. Wiley-Liss New York:, 1999.

[2] P Mansfield, Andrew A Maudsley, and T Bains. Fast scan proton density imaging by NMR. *Journal of Physics E: Scientific Instruments*, 9(4):271, 1976.

[3] CB Ahn, JH Kim, and ZH Cho. High-speed spiral-scan echo planar NMR imaging-I. *IEEE transactions on medical imaging*, 5(1):2–7, 1986.

[4] PJ Wright, OE Mougin, JJ Totman, AM Peters, MJ Brookes, R Coxon, PE Morris, M Clemence, ST Francis, RW Bowtell, et al. Water proton $T_1$ measurements in brain tissue at 7, 3, and 1.5 T using IR-EPI, IR-TSE, and MPRAGE: results and optimization. *Magnetic Resonance Materials in Physics, Biology and Medicine*, 21(1-2):121–130, 2008.

[5] Eleanor F Cox and Penny A Gowland. Simultaneous quantification of $T_2$ and $T_2^{'}$ using a combined gradient echo-spin echo sequence at ultrahigh field. *Magnetic resonance in medicine*, 64(5):1440–1445, 2010.

[6] Andrew M Peters, Matthew J Brookes, Frank G Hoogenraad, Penny A Gowland, Susan T Francis, Peter G Morris, and Richard Bowtell. $T_2^*$ measurements in human brain at 1.5, 3 and 7 T. *Magnetic resonance imaging*, 25(6):748–753, 2007.

[7] Axel Haase, Jens Frahm, Dieter Matthaei, W Hanicke, and K-D Merboldt. FLASH imaging. Rapid NMR imaging using low flip-angle pulses. *Journal of Magnetic Resonance (1969)*, 67(2):258–266, 1986.

[8] Michael Markl and Jochen Leupold. Gradient echo imaging. *Journal of Magnetic Resonance Imaging*, 35(6):1274–1289, 2012.

# Chapter 4

# Theory of Isotropic Susceptibility

## 4.1 What is Susceptibility?

### 4.1.1 Definition and Units

Magnetic susceptibility in its simplest definition describes how 'susceptible' a material is to an applied magnetic field, $\vec{H}$ (units $\mathrm{A\,m^{-1}}$), and what form of interaction takes place when the material is exposed to a magnetic field. Mathematically, isotropic susceptibility is typically characterised by a scalar constant, $\chi_I$, which relates the magnetisation, $\vec{M}$, of a system to $\vec{H}$ as follows:

$$\vec{M} = \chi_I \vec{H}. \tag{4.1}$$

Isotropic magnetic susceptibility can be more rigorously defined in a matrix formalism, as a 3x3 symmetric tensor $\underline{\underline{\chi_I}}$ [1], formed by multiplying the scalar constant $\chi_I$ by the identity matrix $\underline{\underline{I}}$:

$$\underline{\underline{\chi_I}} = \chi_I \underline{\underline{I}} = \begin{bmatrix} \chi_I & 0 & 0 \\ 0 & \chi_I & 0 \\ 0 & 0 & \chi_I \end{bmatrix}. \tag{4.2}$$

For the discussion of isotropic susceptibility alone, it is only necessary to consider $\underline{\underline{\chi_I}}$ as a scalar constant, $\chi_I$, which is how it will be referred to for the remainder of this chapter. In Section 7.1, an extension to anisotropic susceptibility is discussed. Equation 4.1 is based on the assumptions that:

1. When $\vec{H} = \vec{0}$, $\vec{M} = \vec{0}$.
2. $\vec{M}$ varies linearly with field strength.

Both these assumptions can be considered valid under the experimental conditions in which MRI is performed [2]. Ferromagnets ($M_0 \neq 0$) are typically incompatible

with MRI experiments, due to both considerations of safety and image distortion. Non-linear components of magnetisation can exist in non-ferromagnetic materials, but any deviations from the linear relationship in Equation 4.1 are small at the field strengths used in MRI and can be ignored.

$\chi_I$ is typically defined as a dimensionless constant in units of parts per million (ppm), known as the volume magnetic susceptibility. The convention of ppm is convenient in experimental MRI as tissues in the body have susceptibilities on the order of $10^{-6}$. For example, human tissue has a typical susceptibility of $-11 \times 10^{-6}$ to $-7 \times 10^{-6}$ [2], which is equivalent to $-11\,\text{ppm}$ to $-7\,\text{ppm}$. A few common definitions of susceptibility used in the literature are outlined in Table 4.1, though these are rarely encountered within MRI susceptibility literature. Within this thesis, susceptibility is defined in terms of the volume susceptibility with units of ppm or ppb (parts per billion).

### 4.1.2 Relationship Between $\vec{B}$, $\vec{H}$ and $\vec{M}$

In a vacuum, the total field, $\vec{B}$ (units T), is equivalent to the static total field, $\vec{B}_0$, and is locally proportional to the applied static field strength, $\vec{H}_0$, as follows:

$$\vec{B}_0 = \mu_0 \vec{H}_0 \tag{4.3}$$

where $\mu_0$ is the magnetic permeability of free space ($4\pi\,10^{-7}\,\text{N}\,\text{A}^{-2}$). However, when an object is placed within the vacuum, $\vec{B}$ is perturbed due to the presence of the object's magnetisation, $\vec{M}$, as follows:

$$\vec{B} = \mu_0 \left( \vec{H} + \vec{M} \right) \tag{4.4}$$

where $\vec{H} \neq \vec{H}_0$. The perturbation of $\vec{H}$ from $\vec{H}_0$ is critical in understanding the influence of $\vec{M}$ on the applied field strength and is discussed further in Section 4.2.2. Combining Equations 4.1 and 4.4, $\vec{B}$ can be equivalently defined in terms of $\chi_I$:

$$\vec{B} = \mu_0 \left(1 + \chi_I\right) \vec{H} \tag{4.5}$$

| **Susceptibility** | **Formula** | **Units (SI)** |
|---|---|---|
| Volume Susceptibility $\chi$ | $\chi = \frac{\lvert\vec{M}\rvert}{\lvert\vec{H}\rvert}$ | Dimensionless |
| Mass Susceptibility $\chi_m$ | $\chi_m = \frac{\chi}{\rho}$ | $\text{m}^3\,\text{kg}^{-1}$ |
| Molar Susceptibility $\chi_M$ | $\chi_M = \frac{\chi \cdot \text{MW}}{\rho}$ | $\text{m}^3\,\text{mol}^{-1}$ |

Table 4.1: Commonly used definitions of susceptibility. Here $\rho$ is the mass density and MW is the molecular weight in units of $\text{kg}\,\text{mol}^{-1}$ Within this thesis, susceptibility is defined in terms of the volume susceptibility. Definitions obtained from [2].

$(1 + \chi_I)$ is commonly characterised in literature as the relative magnetic permeability, $\mu_r$, defining:

$$\begin{aligned} \vec{B} &= \mu_0 \mu_r \vec{H} \\ &= \mu \vec{H} \end{aligned} \tag{4.6}$$

where $\mu = \mu_0 \mu_r$. Within this thesis, the use of $\mu_r$ and $\mu$ will be avoided to ensure all definitions are in terms of $\chi_I$.

### 4.1.3 Diamagnetism, Paramagnetism and the Value of $\chi_I$

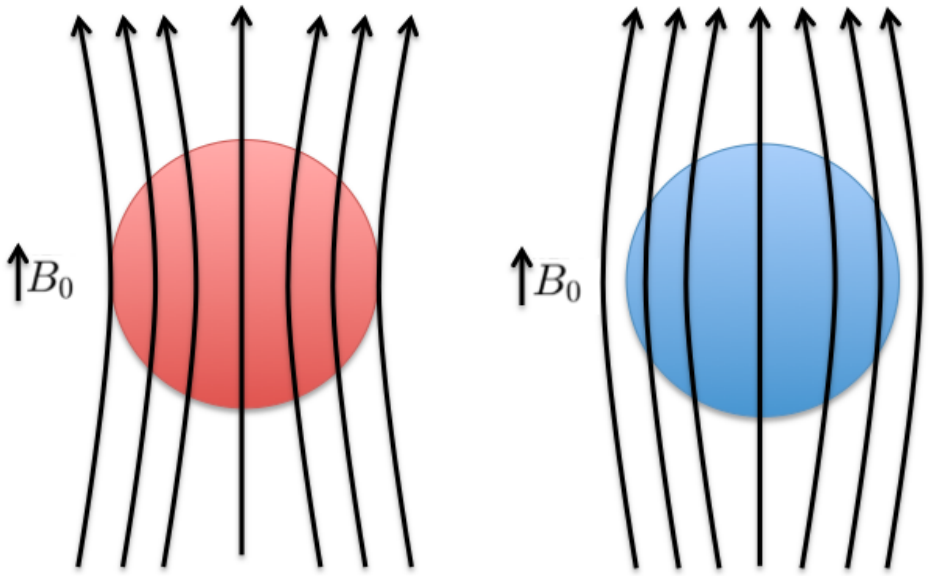
There are numerous atomic mechanisms that modify the value of susceptibility, which combine to form a single value of $\chi_I$ in an atomic system [2]. In MRI, it is generally sufficient to classify materials as one of two types: diamagnetic or paramagnetic [3, 4]. Diamagnetism arises from the interaction of orbital electrons with the externally applied magnetic field, generating an induced magnetic moment opposing $\vec{H}$, reducing $\vec{B}$. Paramagnetism arises in atoms with non-zero electron spin, where the unpaired electrons' magnetic moments align with the applied $\vec{H}$ field to increase $\vec{B}$. All atomic systems have diamagnetic properties, whereas only those with unpaired electrons have paramagnetic properties. The magnitude of the diamagnetism is typically much smaller than paramagnetism, due to the strength of the electron's magnetic moment.

Equation 4.5 reveals that a positive $\chi_I$ increases $\vec{B}$, whereas a negative $\chi_I$ decreases $\vec{B}$ (visualised in Figure 4.1). Though the mechanisms that contribute to diamagnetism and paramagnetism are different, the sign of $\chi_I$ reveals whether an atomic system has diamagnetic or paramagnetic properties, purely through the contribution to the $\vec{B}$ field. MRI experiments are insensitive to the different atomic mechanisms that generate $\chi_I$. Therefore materials with a negative $\chi_I$ are considered purely diamagnetic, whereas those with a positive $\chi_I$ are considered purely paramagnetic. For example, hydrogen, a spin-$\frac{1}{2}$ atom is paramagnetic in isolation (however, when hydrogen combines with oxygen to form water, the molecule is diamagnetic).

The magnitude of $\chi_I$ can reveal further information about the magnetic properties of an atomic system. This must be considered carefully as different atomic systems with vastly different atomic mechanisms can lead to very similar values of $\chi_I$ [2]. However, with an underlying insight into the composition of a system, the

| **Constituent** | Water | Cortical bone | Blood (deoxygenated) | Ferritin |
|---|---|---|---|---|
| $\boldsymbol{\chi_I}$ **(ppm)** | $-9.05$ | -8.86 | -7.90 | 520 |

Table 4.2: $\chi_I$ values for common tissue constituents, obtained from [2].




(a) $\chi > 0$ (b) $\chi < 0$

Figure 4.1: Comparison of the impact of a paramagnetic object (red - Figure 4.1a) and a diamagnetic object (blue - Figure 4.1b) an on externally applied magnetic field. The paramagnetic object causes an increase in the $\vec{B}$ field (indicated by an increased density of lines) whereas the diamagnetic object induces the opposite effect.

sign and magnitude of $\chi_I$ can be used to obtain information about the underlying structure. From the perspective of MRI, with knowledge of the $\chi_I$ values of different tissue constituents, if it is possible to obtain a map of $\chi_I$ over the tissue, it will be possible to infer the composition. An example of some commonly obtained $\chi_I$ values for tissue constituents are detailed in Table 4.2.

## 4.2 Magnetic Field Properties

### 4.2.1 Magnetostatics and the Scalar Potential

MRI is largely concerned with the magnetostatic regime, where fields are considered time-independent. Though this may not be valid when considering the presence of magnetic gradients and field fluctuations, these perturbations are small relative to the static field and can be ignored when considering GE acquisitions. With these approximations and ignoring eddy current contributions (which can also be considered small), the free current density, $\vec{J}_f$ can be set equal to zero [5], so that Maxwell's equations can be written as:

$$\begin{aligned} \nabla \cdot \vec{B}(\vec{r}) &= 0 \\ \nabla \times \vec{H}(\vec{r}) &= 0 \end{aligned} \tag{4.7}$$

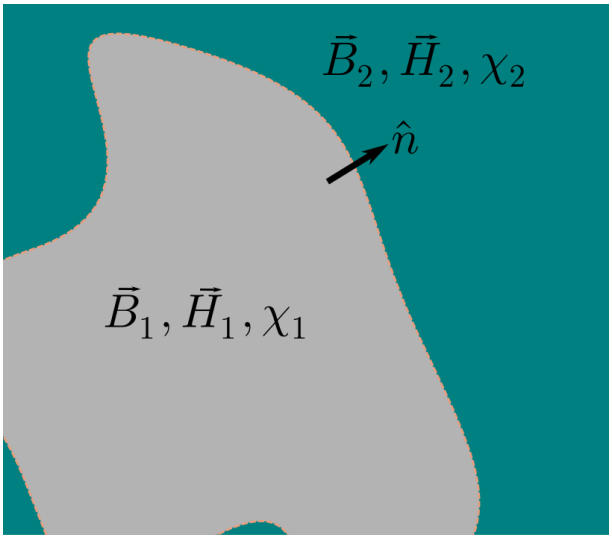



Figure 4.2: Two arbitrary regions of susceptibility $\chi_1$ and $\chi_2$. The conditions in Equation 4.8 indicate that $\vec{H}(\vec{r})$ is continuous along the surface between the two objects and $\vec{B}(\vec{r})$ is continuous perpendicular to the surface.

where $\vec{r}$ is a spatial position coordinate. This implies that $\vec{B}$ is a purely rotational field and that $\vec{H}$ is a conservative (irrotational) field. Considering a heterogeneous object, made up of regions of different magnetic susceptibility as shown in Figure 4.2, from Equation 4.7, it can be determined that:

$$\begin{aligned} (\vec{B}_2 - \vec{B}_1) \cdot \hat{n} &= 0 \\ (\vec{H}_2 - \vec{H}_1) \times \hat{n} &= 0 \end{aligned} \tag{4.8}$$

where $\hat{n}$ is a unit vector perpendicular to a the boundary between regions of different susceptibility. This is most simply derived from the integral form of Equation 4.7:

$$\begin{aligned} \oint \vec{B}(\vec{r}) \cdot \hat{n}\, dS &= 0 \\ \oint \vec{H}(\vec{r}) \cdot d\vec{l} &= 0 \end{aligned} \tag{4.9}$$

where $\hat{n}\, dS$ is an area element perpendicular to the object's surface and $d\vec{l}$ is a line element. $\vec{B}$ and $\vec{H}$ can therefore be defined in terms of vector and scalar potentials:

$$\begin{aligned} \vec{B}(\vec{r}) &= \nabla \times \vec{A}(\vec{r}) \\ \vec{H}(\vec{r}) &= -\nabla \Phi(\vec{r}) \end{aligned} \tag{4.10}$$

where $\vec{A}(\vec{r})$ and $\Phi(\vec{r})$ are the magnetic vector and scalar potentials, respectively. Considering an object of magnetisation $\vec{M}(\vec{r})$ in an external field, a relationship can be derived between $\Phi(\vec{r})$ and $\vec{M}(\vec{r})$ by combining Equation 4.4 with Equations 4.7 and 4.10:

$$\nabla^2 \Phi(\vec{r}) = \nabla \cdot \vec{M}(\vec{r}) \tag{4.11}$$

If no sources of magnetisation are contained within a region, or a region has a constant, unbounded magnetisation, $\nabla \cdot \vec{M}(\vec{r}) = 0$ and Equation 4.11 reduces to:

$$\nabla^2 \Phi(\vec{r}) = 0. \tag{4.12}$$

Equations 4.11 and 4.12 are very well understood mathematically, as forms of Poisson's and Laplace's equations respectively. Defining $\nabla \cdot \vec{M}(\vec{r}) = -\rho_m(\vec{r})$, Equation 4.11 can be written as:

$$\nabla^2 \Phi(\vec{r}) = -\rho_m(\vec{r}) \tag{4.13}$$

or when rewritten in terms of $\vec{H}(\vec{r})$:

$$\nabla \cdot \vec{H}(\vec{r}) = -\rho_m(\vec{r}). \tag{4.14}$$

This equation has a striking similarity to Gauss' law ($\nabla \cdot \vec{E}(\vec{r}) = -\frac{\rho(\vec{r})}{\varepsilon_0}$, where $\rho(\vec{r})$ is the electric charge density and $\varepsilon_0$ is the permittivity of free space). $\rho_m(\vec{r})$ can be interpreted as a form of 'magnetic charge density'. Defining $q_m$ as a unit of 'magnetic charge', for a system consisting of a single unit of $q_m$ at point $\vec{r}'$:

$$\nabla^2 \Phi(\vec{r}) = -q_m \delta(\vec{r} - \vec{r}') \tag{4.15}$$

where $\delta(\vec{r} - \vec{r}')$ is the Dirac delta function [6]. The solution to this function utilises the well known form of Green's function for the 3D Laplacian operator [4]:

$$\nabla^2 \left( \frac{1}{|\vec{r} - \vec{r}'|} \right) = -4\pi \delta(\vec{r} - \vec{r}') \tag{4.16}$$

defining:

$$\Phi(\vec{r}) = \frac{q_m}{4\pi} \frac{1}{|\vec{r} - \vec{r}'|}. \tag{4.17}$$

For a system consisting of a continuous source of magnetic charge:

$$\rho_m(\vec{r}) = \int \rho_m(\vec{r}') \delta(\vec{r} - \vec{r}') \, dV' \tag{4.18}$$

where $dV'$ is a volume element and combining this with Equation 4.16 yields:

$$\rho_m(\vec{r}) = -\frac{1}{4\pi} \int \rho_m(\vec{r}') \nabla^2 \left( \frac{1}{|\vec{r} - \vec{r}'|} \right) dV'. \tag{4.19}$$

As the operator $\nabla^2$ is not a function of $d\vec{r}'$, it is independent of the integral and can be moved outside. Comparing this with Equation 4.13:

$$\begin{aligned} \Phi(\vec{r}) =& \frac{1}{4\pi} \int \frac{\rho_m(\vec{r}')}{|\vec{r} - \vec{r}'|} \, dV' \\ =& -\frac{1}{4\pi} \int \frac{\nabla' \cdot \vec{M}(\vec{r}')}{|\vec{r} - \vec{r}'|} \, dV' \end{aligned} \tag{4.20}$$

which can be further extended to for a multi-compartment object with numerous bound surfaces. Considering a source of magnetisation $\vec{M}$ bounded by surface $S$ (beyond the surface, $\vec{M}(\vec{r}) = 0$), $\Phi(\vec{r})$ can be generalised to include these boundary conditions:

$$\Phi(\vec{r}) = -\frac{1}{4\pi}\int_V \frac{\nabla' \cdot \vec{M}(\vec{r})}{|\vec{r} - \vec{r}'|}\, dV' + \frac{1}{4\pi}\oint_S \frac{\hat{n}' \cdot \vec{M}(\vec{r})}{|\vec{r} - \vec{r}'|}\, dS'. \tag{4.21}$$

With knowledge of the underlying magnetisation of a system, this equation can be used to determine the scalar potential. The magnetic field strength due to $\Phi(\vec{r})$ is known as the demagnetising field, $\vec{H}_d(\vec{r})$, which opposes $\vec{H}_0$. Measurement of $\vec{H}_d(\vec{r})$ can be utilised to determine the underlying magnetic susceptibility of a system.

### 4.2.2 The Demagnetising Field

In Section 4.1.2, it was briefly mentioned that in the presence of an object with magnetisation, $\vec{M}(\vec{r})$, the magnetic field strength would be perturbed from $\vec{H}_0$ to a previously undefined value, $\vec{H}(\vec{r})$. Equation 4.21 explains the origin of this perturbation. The demagnetising field, $\vec{H}_d(\vec{r})$, obtained from the solution of Equation 4.21 perturbs the $\vec{H}_0$ field as follows [2, 5, 7]:

$$\vec{H}(\vec{r}) = \vec{H}_0 + \vec{H}_d(\vec{r}). \tag{4.22}$$

As can be inferred from Equation 4.21, the properties of $\vec{H}_d(\vec{r})$ are complex. $\vec{H}_d(\vec{r})$ is a non-local field, dependent on the location, shape and distribution of $\vec{M}(\vec{r})$. For a system with multiple sources of magnetisation, the demagnetisation field experienced by one magnetisation source will consist of the sum of the self induced $\vec{H}_d(\vec{r})$ field, $\vec{H}_{d_{\text{self}}}(\vec{r})$, and the experienced $\vec{H}_d(\vec{r})$ field from other magnetisation sources, $\vec{H}_{d_{\text{oth}}}(\vec{r})$ [7]:

$$\vec{H}_d(\vec{r}) = \vec{H}_{d_{\text{self}}}(\vec{r}) + \vec{H}_{d_{\text{oth}}}(\vec{r}). \tag{4.23}$$

The complex relationship between $\vec{H}_d(\vec{r})$ and an arbitrary $\vec{M}(\vec{r})$ distribution is challenging to determine and in many cases, computationally impractical via the solution of Equation 4.21. However, for a few simple structures an analytical solution is available. For example, the internal demagnetisation field, $\vec{H}_{d_{\text{int}}}(\vec{r})$, inside an ellipsoidal structure can be reduced to a simple formalism [2]:

$$\vec{H}_{d_{\text{int}}}(\vec{r}) = -\alpha\vec{M} \tag{4.24}$$

where $\alpha$ is a scalar constant known as the demagnetisation factor. $\alpha$ depends on both the shape of the ellipsoid and the projection of the ellipsoidal axis of symmetry along the direction of $\vec{H}_0$, with the constraint that the combined sum

of $\alpha$ over the three principal axes of the ellipsoid, $\sum_{i=1}^{3} \alpha_i = 1$. $\alpha$ values over the three principle axes of a few ellipsoidal shapes are defined in Table 4.3. By combining Equations 4.1, 4.5, 4.22 and 4.24, the total internal field, $\vec{B}_{\text{int}}$, for an ellipsoid can be generalised as:

$$\vec{B}_{\text{int}} = \frac{1+\chi}{1+\alpha\chi}\vec{B}_0 \tag{4.25}$$

Assuming that $\chi_I \ll 1$ (a valid assumption in MRI - see Section 4.1.1), simple expressions for the field perturbations, $\Delta\vec{B}_{\text{int}}$, induced by ellipsoids can be determined. $\Delta\vec{B}_{\text{int}}$ values over the three principal axes of a few ellipsoidal shapes are defined in Table 4.3.

Analytical solutions for the external field, $\vec{B}_{\text{ext}}(\vec{r})$, have also been determined for ellipsoids. Solutions for the sphere and infinite cylinder are given in Table 4.4.

### 4.2.3 The Sphere of Lorentz

The sphere of Lorentz (SOL) [8] is an often-used but challenging-to-interpret construct. Its use is necessary to describe field perturbations accounting correctly for the non-continuous distribution of matter at the atomic scale and the interactions with surrounding atoms (Figure 4.3). In an 'idealised' situation, media would be

| **Shape** | Sphere | Infinite cylinder | Circular Disk |
|---|---|---|---|
| $\begin{bmatrix}\boldsymbol{\alpha_1}\\ \boldsymbol{\alpha_2}\\ \boldsymbol{\alpha_3}\end{bmatrix}, \begin{bmatrix}\boldsymbol{\Delta B_{\text{int}_1}}\\ \boldsymbol{\Delta B_{\text{int}_2}}\\ \boldsymbol{\Delta B_{\text{int}_3}}\end{bmatrix}$ | $\begin{bmatrix}\frac{1}{3}\\ \frac{1}{3}\\ \frac{1}{3}\end{bmatrix}, \begin{bmatrix}\frac{2\chi_I}{3}B_0\\ \frac{2\chi_I}{3}B_0\\ \frac{2\chi_I}{3}B_0\end{bmatrix}$ | $\begin{bmatrix}\frac{1}{2}\\ \frac{1}{2}\\ 0\end{bmatrix}, \begin{bmatrix}\frac{\chi_I}{2}B_0\\ \frac{\chi_I}{2}B_0\\ \chi_I B_0\end{bmatrix}$ | $\begin{bmatrix}0\\ 0\\ 1\end{bmatrix}, \begin{bmatrix}\chi_I B_0\\ \chi_I B_0\\ 0\end{bmatrix}$ |

Table 4.3: $\alpha$ values and induced internal field perturbations, $\Delta B_{\text{int}}$, along the three principle axes of ellipsoidal shapes with susceptibility $\chi_I$ [2]. Here, each row denotes $\alpha$ and $\Delta B_{\text{int}}$ for a single principal axis, assuming it is defined parallel to $\vec{B}_0$. The total internal field, $\vec{B}_{\text{int}} = \vec{B}_0 + \Delta\vec{B}_{\text{int}}$. The axis of symmetry for the cylinder and disk are defined to be along the third principal axis.

| **Shape** | **Field perturbations** |
|---|---|
| Sphere | $\Delta B_{\text{ext}}(\varrho, \Theta) = \frac{\chi_I a^3 B_0}{3\varrho^3}\left(3\cos^2\Theta - 1\right)$ |
| Cylinder | $\Delta B_{\text{ext}}(\rho, \phi, \theta) = \frac{\chi_I a^2 B_0}{2\rho^2}\cos 2\phi \sin^2\theta$ |

Table 4.4: Induced external field perturbations for the sphere and cylinder with susceptibility $\chi_I$ [3]. The total external field is $\vec{B}_{\text{ext}}(\vec{r}) = \vec{B}_0 + \Delta\vec{B}_{\text{ext}}(\vec{r})$. Here $a$ defines the radius of the sphere/cylinder, $\varrho$ and $\rho$ describe the radial coordinate of the sphere and cylinder respectively, $\Theta$ and $\phi$ defines the angle between the $\vec{B}_0$ field and $\vec{\varrho}$ and $\vec{\rho}$ for the sphere and cylinder respectively and $\theta$ defines the angle between the $\vec{B}_0$ field and the principle axis of the cylinder perpendicular to $\vec{\rho}$.

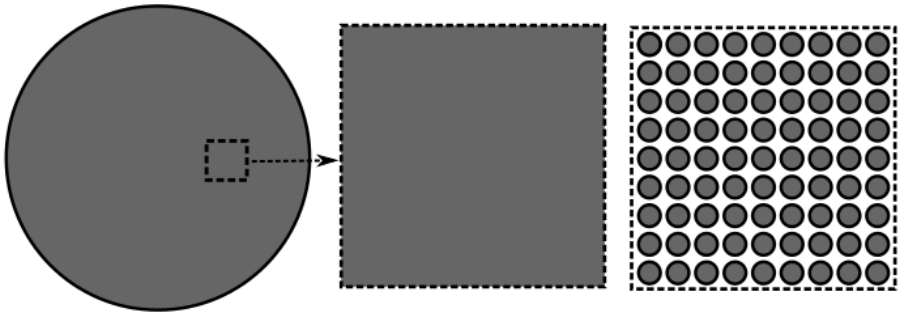


Figure 4.3: Why the sphere of Lorentz is required. Looking at the atomic scale of a structure (left), one could approximate the object to be continuous (middle), which would require no sphere of Lorentz approximation. However, in reality there will be screening effects due to the discrete nature of atomic structure (right). Image for visualisation purposes only.

continuous at the atomic scale, which is how magnetisation in previous discussions has been considered. However, due to the discretisation of atomic structures, there is an additional local screening effect which must be accounted for in field calculations. The SOL provides a simple and elegant solution, defining a spherical cavity around a spin significantly larger than the atomic spacing (Figure 4.4) [9]. Externally/internally to the SOL, the magnetisation is considered continuous/discrete respectively [10]. Using this approximation, the field experienced by a spin, $\vec{B}_{\text{spin}}$, will be equal to the sum of the macroscopic, internal, continuous field, $\vec{B}_{\text{int}}$ (described in the previous section) and the microscopic, internal, discrete field inside the SOL, $\vec{B}_{\text{SOL}_{\text{int}}}$, minus the contribution from the continuous SOL cavity, $\vec{B}_{\text{SOL}}$:

$$\vec{B}_{\text{spin}} = \vec{B}_{\text{int}} + \vec{B}_{\text{SOL}_{\text{int}}} - \vec{B}_{\text{SOL}}. \tag{4.26}$$

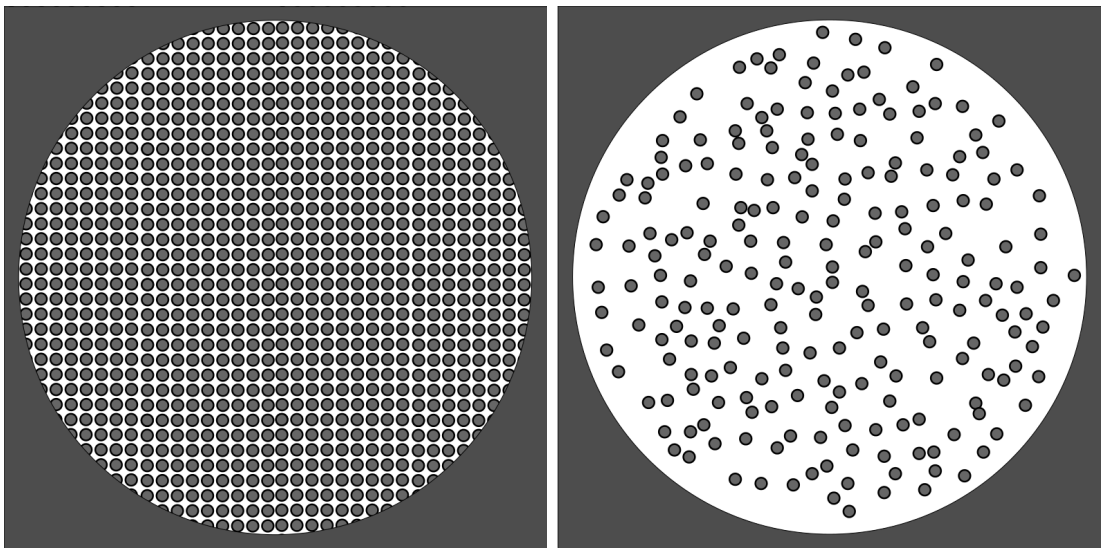
In an isotropic or rapidly diffusing medium, the average field experienced by a spin inside the SOL, $\vec{B}_{\text{SOL}_{\text{int}}}$, will average to zero, due to the cancellation of contributions from surrounding atoms. From the definition of a sphere's field contribution in Table 4.3:

$$\vec{B}_{\text{spin}} = \vec{B}_{\text{int}} - \frac{2\chi}{3}\vec{B}_0. \tag{4.27}$$

$\vec{B}_{\text{spin}}$ values for a few ellipsoidal shapes are given in Table 4.5. These can be considered as the values in Table 4.3, 'corrected' for the SOL. External to the region of magnetisation, the SOL is not required [3] and no correction is needed for the results in Table 4.4. This can be generalised for any distribution via Equation 4.5:

$$\begin{aligned} \vec{B}_{\text{spin}}(\vec{r}) &= \mu_0 \left(1 + \chi_I(\vec{r})\right) \vec{H}(\vec{r}) - \frac{2\chi_I(\vec{r})}{3}\vec{B}_0 \\ &= \vec{B}_0 \left(1 + \frac{1}{3}\chi_I(\vec{r})\right) + \vec{B}_d(\vec{r}) \end{aligned} \tag{4.28}$$

where $\vec{B}_d(\vec{r})$ is the demagnetising $\vec{B}(\vec{r})$ field and second order terms have been ignored.



(a) Isotropic atomic spacing (b) Randomised atomic spacing

Figure 4.4: The sphere of Lorentz is defined by a large spherical cavity, significantly larger than the average atomic spacing. It is valid for isotropic atomic spacing (Figure 4.4a) and randomised atomic spacing (Figure 4.4b) [11], where diffusion effects average the field perturbations sampled by a spin. Images for visualisation purposes only.

The implications of this for a spherical object are surprising. The SOL correction implies that for a sphere of susceptibility $\chi_I$, no net magnetic field perturbations will be generated inside the sphere. As a theoretical construct this is interesting. If a perfect sphere of susceptibility $\chi_I$ was placed in an MRI scanner, with no signal sampled outside the sphere, no field perturbations would be observed. The sphere of Lorentz is additionally valid when considering spherically symmetric susceptibility perturbers. An extension considering non-spherical susceptibility perturbers, in addition to the introduction of the generalised Lorentzian approximation (GLA) [12] is discussed in Section 7.3.

| **Shape** | Sphere | Infinite cylinder | Circular Disk |
|---|---|---|---|
| $\begin{bmatrix} \boldsymbol{\Delta B}_{\mathbf{spin_1}} \\ \boldsymbol{\Delta B}_{\mathbf{spin_2}} \\ \boldsymbol{\Delta B}_{\mathbf{spin_3}} \end{bmatrix}$ | $\begin{bmatrix} 0 \\ 0 \\ 0 \end{bmatrix}$ | $\begin{bmatrix} -\frac{\chi_I}{6} B_0 \\ -\frac{\chi_I}{6} B_0 \\ \frac{\chi_I}{3} B_0 \end{bmatrix}$ | $\begin{bmatrix} \frac{\chi_I}{3} B_0 \\ \frac{\chi_I}{3} B_0 \\ -\frac{2\chi_I}{3} B_0 \end{bmatrix}$ |

Table 4.5: $\Delta B_{\text{spin}}$ along the three principal axes of ellipsoidal shapes with susceptibility $\chi_I$, accounting for the effect of the SOL. Here, each row denotes $\Delta B_{\text{spin}}$ for a single principle axis, assuming it is defined parallel to $\vec{B}_0$ The total internal field perturbations, $\vec{B}_{\text{spin}} = \vec{B}_0 + \Delta\vec{B}_{\text{spin}}$. The axis of symmetry for the cylinder and disk are along the third principal axis.

## 4.3 Utilising $k$-Space to Describe Field Perturbations Generated from Arbitrary Susceptibility Distributions

### 4.3.1 Derivation

Due to the challenges in solving Equation 4.21, a more practical method of determining the magnetic field perturbations for an arbitrary susceptibility distribution is required. Though ellipsoidal shapes can be described analytically, the heterogeneous susceptibility distributions found in biological tissue cannot be accurately or simply reduced to the sum of numerous ellipsoidal susceptibility sources. One solution has been to utilise the properties of Fourier transforms to solve the previously described Poisson equation for scalar potentials (Equation 4.13) [5, 13]. Fourier transform operations are computationally advantageous when solving partial differential equations as they can be simply and quickly performed using the well established fast-Fourier transform algorithm [14]. By realising the appropriateness of taking first order approximations when solving for $\Phi(\vec{r})$, a simple relationship between $\vec{B}(\vec{r})$ and $\chi_I(\vec{r})$ can be determined.
Using the results in Section 4.2.1, Equation 4.5 can be written in the form of Equation 4.13:

$$\nabla^2\Phi(\vec{r}) = -\frac{\nabla\chi_I(\vec{r})\cdot\nabla\Phi(\vec{r})}{1+\chi_I(\vec{r})} \tag{4.29}$$

defining $\rho_m(\vec{r}) = -\frac{\nabla\chi_I(\vec{r})\cdot\nabla\Phi(\vec{r})}{1+\chi_I(\vec{r})}$. Again it can be observed that if no sources of $\chi_I$ are contained within a system, or a system has a constant, unbounded $\chi_I$, Equation 4.29 reduces to Laplace's equation. Defining $\Phi_{\text{total}}(\vec{r}) = -\vec{H_0}\cdot\vec{z}+\Phi(\vec{r})$, where $\vec{H}_d(\vec{r}) = -\nabla\Phi(\vec{r})$ (Equation 4.10), ignoring small second order terms:

$$\nabla^2\Phi(\vec{r}) = \vec{H}_0\cdot\frac{\partial\chi_I(\vec{r})}{\partial z}. \tag{4.30}$$

It is possible to describe first and second order differentials in terms of Fourier transforms [6]. The following rules apply for an arbitrary scalar function, $f(\vec{r})$:

$$\begin{aligned}
\nabla f(\vec{r}) &= \nabla\int_{-\infty}^{\infty} f(\vec{k})e^{i\vec{k}\cdot\vec{r}}\,d^3k \\
&= \mathcal{F}^{-1}\left[i\vec{k}\mathcal{F}\left[f(\vec{r})\right]\right] \\
\nabla^2 f(\vec{r}) &= \nabla^2\int_{-\infty}^{\infty} f(\vec{k})e^{i\vec{k}\cdot\vec{r}}\,d^3k \\
&= -\mathcal{F}^{-1}\left[k^2\mathcal{F}\left[f(\vec{r})\right]\right]
\end{aligned} \tag{4.31}$$

where $\mathcal{F}$ and $\mathcal{F}^{-1}$ denote the Fourier and inverse Fourier transform operator respectively. Applying these rules to Equation 4.30:

$$\Phi(\vec{r}) = -iH_0\mathcal{F}^{-1}\left[\frac{k_z}{k^2}\mathcal{F}\left[\chi_I(\vec{r})\right]\right] \tag{4.32}$$

where for further clarity the magnetic properties of the system have been defined as functions of the spatial position vector, $\vec{r}$. In MRI, the projection of $H_d(\vec{r})$ along the $\hat{B}_0$-dimension is experimentally measured. Defining this as the $z$-dimension and $\vec{H}_d(\vec{r}) = -\nabla\Phi(\vec{r})$:

$$H_{d_z}(\vec{r}) = -H_0\mathcal{F}^{-1}\left[\frac{k_z^2}{k^2}\mathcal{F}\left[\chi_I(\vec{r})\right]\right]. \tag{4.33}$$

Therefore from Equations 4.5 and 4.22, the total $\vec{B}$ field along the $z$-dimension can de determined:

$$\begin{aligned} B_z(\vec{r}) &= \left(1-\chi_I(\vec{r})\right)B_0\left(1-\mathcal{F}^{-1}\left[\frac{k_z^2}{k^2}\mathcal{F}\left[\chi_I(\vec{r})\right]\right]\right) \\ &\approx B_0 + \underbrace{B_0\cdot\mathcal{F}^{-1}\left[\left(1-\frac{k_z^2}{k^2}\right)\mathcal{F}\left[\chi_I(\vec{r})\right]\right]}_{\Delta B_z(\vec{r})} \end{aligned} \tag{4.34}$$

where small second order terms have been removed. All that is left is to include the effect of the SOL (Section 4.2.3). Utilising Equation 4.27:

$$B_{\text{spin}_z}(\vec{r}) = B_0 + \underbrace{B_0\cdot\mathcal{F}^{-1}\left[\left(\frac{1}{3}-\frac{k_z^2}{k^2}\right)\mathcal{F}\left[\chi_I(\vec{r})\right]\right]}_{\Delta B_{\text{spin}_z}(\vec{r})} \tag{4.35}$$

where it can be seen that a susceptibility distribution, $\chi_I(\vec{r})$, perturbs the total field experienced by a spin along the $z$-dimension by $\Delta B_{\text{spin}_z}(\vec{r})$.

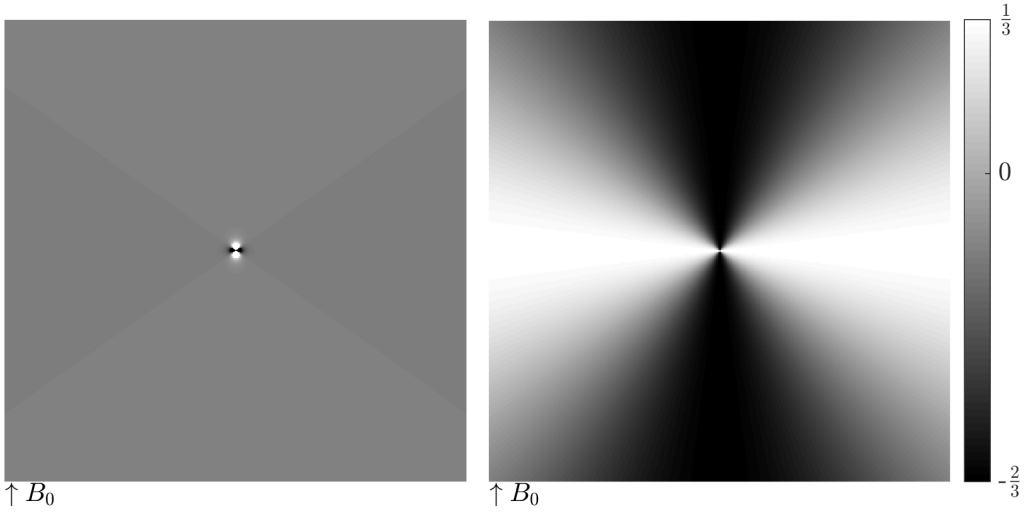
### 4.3.2 Interpretation

The convolution theorem states that for two scalar functions, $f(\vec{r})$ and $g(\vec{r})$ [6]:

$$\begin{aligned} f(\vec{r})\otimes g(\vec{r}) &= \mathcal{F}^{-1}\left[\mathcal{F}\left[f(\vec{r})\right]\cdot\mathcal{F}\left[g(\vec{r})\right]\right] \\ &= \mathcal{F}^{-1}\left[f(\vec{k})\cdot g(\vec{k})\right] \end{aligned} \tag{4.36}$$

where $\otimes$ is the convolution operator. Comparing this to Equation 4.35, $\Delta B_{\text{spin}_z}(\vec{r})$ can be defined as the $B_0$ scaled $r$-space convolution of a function, $d(\vec{r})$, with the susceptibility map, $\chi_I(\vec{r})$, where:

$$d(\vec{r}) = \mathcal{F}^{-1}\left[\frac{1}{3}-\frac{k_z^2}{k^2}\right] \tag{4.37}$$




(a) $d(\vec{r})$ (b) $d(\vec{k})$

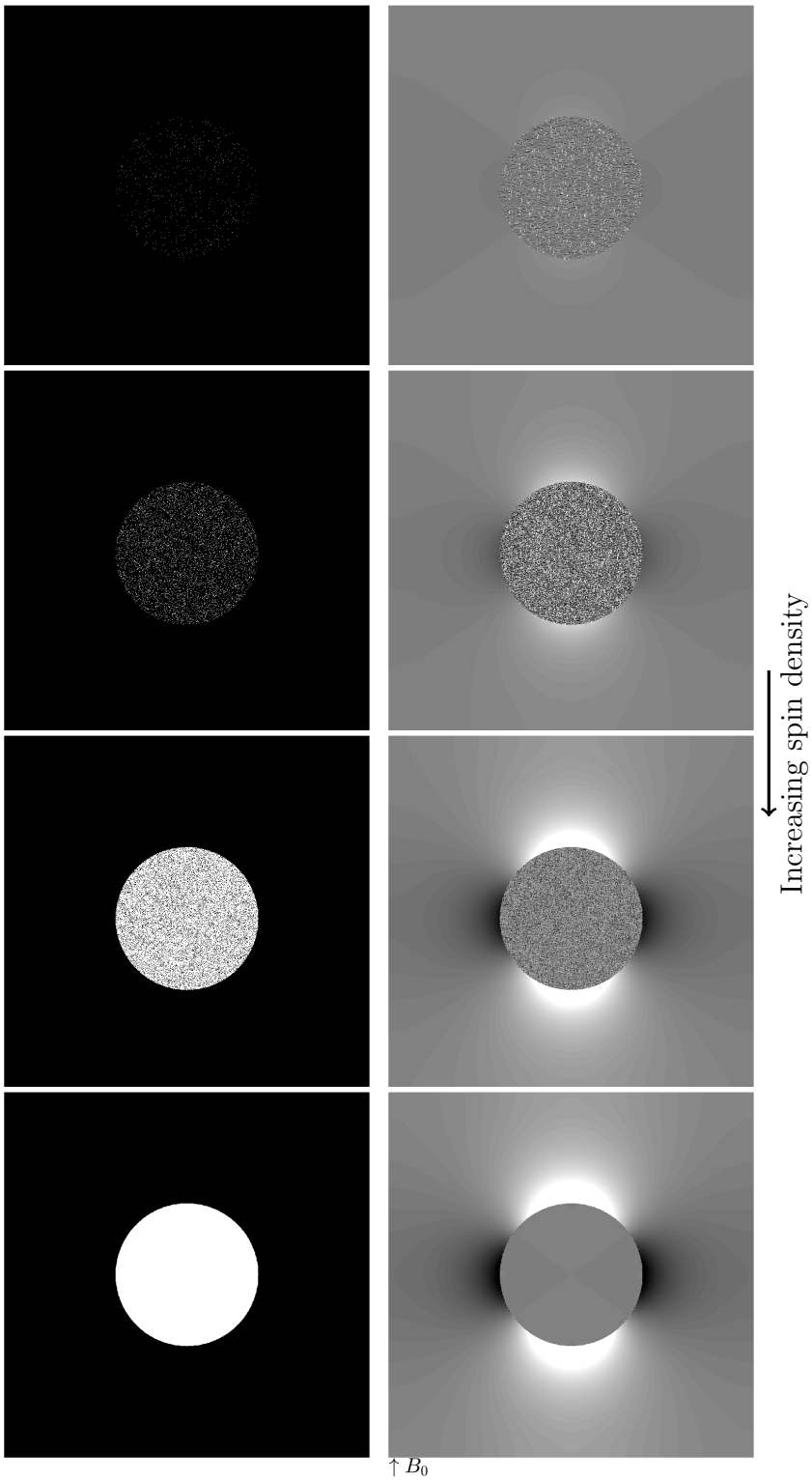
Figure 4.5: The dipole field visualised in $r$-space (Figure 4.5a) and $k$-space (Figure 4.5b).

defining $d(\vec{k}) = \frac{1}{3} - \frac{k_z^2}{k^2}$. $d(\vec{r})$ is known as the dipole field, the field induced by a point source of unit susceptibility perturbed by a unit $\vec{B}_0$ field along the $z$-dimension. $d(\vec{r})$ and $d(\vec{k})$ are visualised in Figure 4.5. Therefore $\Delta B_{\text{spin}_z}(\vec{r})$ can be interpreted as the sum of all field perturbations induced by a $\chi_I(\vec{r})$ map composed of infinitesimally small point sources. In the context of MRI, each voxel is considered a point source. Figure 4.6 provides an example of how the sum of the dipole fields generated from individual point sources leads to the field perturbations generated from a macroscopic object.

### 4.3.3 Comparison to Analytical Solutions

To test the robustness of this technique, a comparison can be made between $\Delta B_{\text{spin}_z}(\vec{r})$ for ellipsoids derived utilising the $k$-space method described above and the analytical solutions defined in Tables 4.4 and 4.5. The analytical form of $\Delta B_{\text{spin}_z}(\vec{r})$ for a sphere, parallel infinite cylinder and perpendicular infinite cylinder scaled by $\chi_I B_0$ were simulated and compared to the $k$-space simulations of identical structures. These are shown in Figure 4.7. Visual comparisons of the two datasets and examination of the line profiles show excellent agreement, with a few notable inconsistencies:

1. At the ellipsoid boundaries, the $k$-space simulations of the sphere and perpendicular infinite cylinder show considerable over/undershooting, most easily seen in the line profiles. This is due to the discrete nature of the fast Fourier transform algorithms being implemented and is known as 'Gibbs ringing' [3]. The representation of a sharp, step-function transition in $r$-




(a) $\chi_I(\vec{r})$ (b) $\Delta B_{\text{recon}}(\vec{r})$

Figure 4.6: Generating a macroscopic susceptibility distribution via summing dipole fields generated from point sources. Datasets simulated on a $1024\times1024\times1024\,\text{voxel}^3$ matrix, written in-house using MATLAB (Release 2013a, The MathWorks Inc., Natick, MA, United States) via the $k$-space protocol as discussed in Section 4.3.

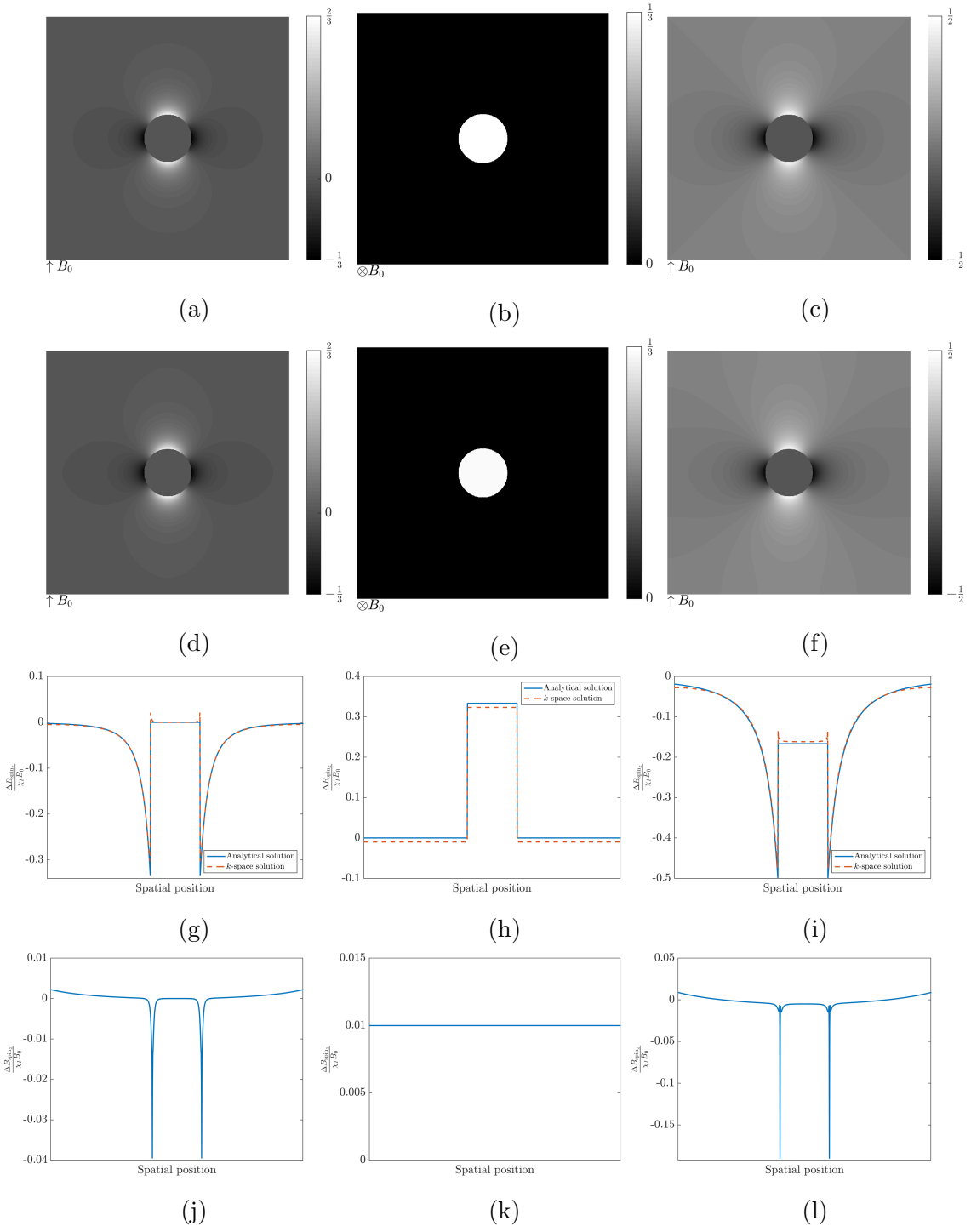


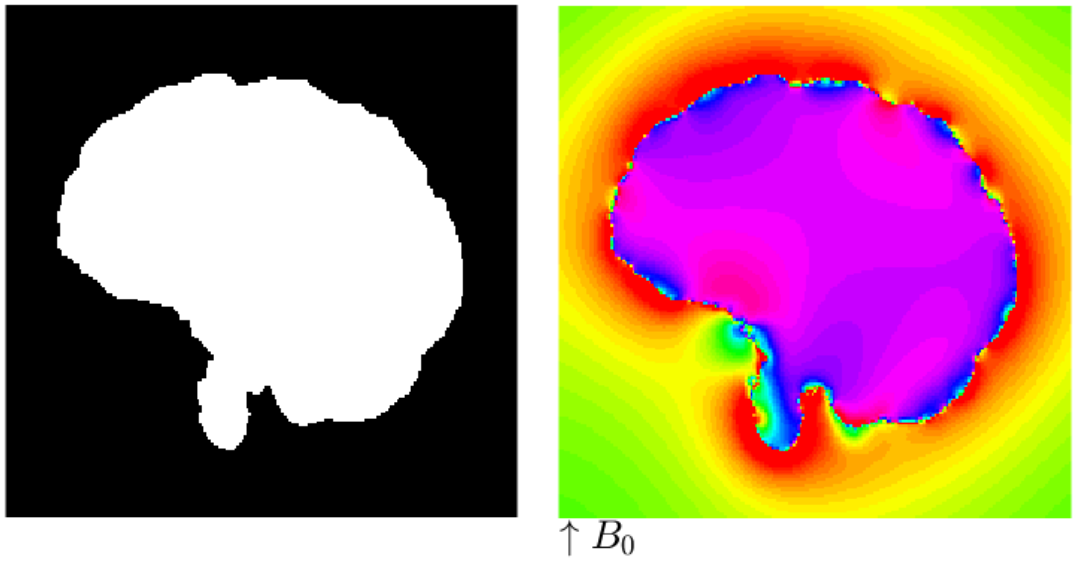

Figure 4.7: Figures 4.7a-4.7c display the analytical solutions of $\Delta B_{\text{spin}_z}(\vec{r})$ for the sphere, infinite cylinder parallel to $\vec{B}_0$ and infinite cylinder perpendicular to $\vec{B}_0$, calculated using the results in Tables 4.4 and 4.5. Figures 4.7d-4.7f display the identical simulations calculated using the $k$-space method. Figures 4.7g-4.7i compare the line profile horizontally traversing through the centre of the object, with Figures 4.7j-4.7l showing the difference (analytical simulation minus $k$-space simulation). Data simulated on a $1024\times1024\times1024$ voxel$^3$ matrix, written in-house using MATLAB (Release 2013a, The MathWorks Inc., Natick, MA, United States).

space requires a large range of frequency components to be represented sharply without artefact. As can be realised from the discussion of $r$- and $k$-space image resolution in Section 3.4.6, the maximum $k$-space frequency is inversely proportional to the $r$-space resolution. However, ringing artefacts in many cases are small relative to the overall field perturbations and can be ignored.

2. At the edge of the dataset matrix, the $k$-space simulations of the sphere and perpendicular infinite cylinder start to show an increased divergence from the analytical solution, due to the periodic boundary conditions imposed by the fast-Fourier transform algorithm [15]. This effect can be reduced via increasing the FOV in $r$-space and this also implies that smaller objects simulated using the $k$-space method will generate field perturbations closer to the analytical solution.

3. There is a DC offset generated between the analytical and $k$-space solution, most evident in the line profile of the parallel infinite cylinder. This is due to the form of the $k$-space dipole field, $d(\vec{k})$, as defined in Equation 4.37. The centre of $k$-space, corresponding to $k = 0$ is undefined [13] and set to zero, implying that there is no DC offset within the $k$-space simulation and $\sum_{\text{all voxels}} \Delta B_{\text{spin}_z}(\vec{r}) = 0$. However, this does not need to be the case analytically. This further implies that when using the $k$-space technique, all field perturbations are *relative* to the average field perturbation within the image.

For more complex structures beyond ellipsoids, it is not possible to simply derive an exact analytical form of $\Delta B_{\text{spin}_z}(\vec{r})$ due to the form of $\vec{H}_d(\vec{r})$ which cannot be simply determined. However, this is where the advantage of the $k$-space method is seen. Despite the imperfections in solutions generated by the $k$-space method as discussed above, it can be utilised to rapidly generate expected field perturbations for any arbitrary susceptibility distribution. An example is given in Figure 4.8. Describing these field perturbations as a solution to Equation 4.21 would be far more challenging.




(a) Brain mask (b) $\Delta B_{\mathrm{spin}_z}(\vec{r})$

Figure 4.8: Field perturbations generated from a 2D binary image of a brain mask. Despite the complicated boundary conditions in the image, by using the $k$-space method $\Delta B_{\mathrm{spin}_z}(\vec{r})$ can be generated in fractions of a second. Shown on a multi-colour map to emphasise the complexity of the field perturbations.

# Bibliography


[1] Samuel Wharton and Richard Bowtell. Effects of white matter microstructure on phase and susceptibility maps. *Magnetic resonance in medicine*, 73(3):1258–1269, 2015.

[2] John Schenck. The role of magnetic susceptibility in magnetic resonance imaging: MRI magnetic compatibility of the first and second kinds. *Med. Phys.*, 23(6):815–850, 1996.

[3] E Mark Haacke, Robert W Brown, Michael R Thompson, Ramesh Venkatesan, et al. *Magnetic resonance imaging: physical principles and sequence design*, volume 82. Wiley-Liss New York:, 1999.

[4] John David Jackson. *Classical electrodynamics*. Wiley, 1999.

[5] Rares Salomir, Baudouin Denis de Senneville, and Chrit TW Moonen. A fast calculation method for magnetic field inhomogeneity due to an arbitrary distribution of bulk susceptibility. *Concepts in Magnetic Resonance Part B: Magnetic Resonance Engineering*, 19(1):26–34, 2003.

[6] Ken F Riley, Mike P Hobson, and Stephen J Bence. Mathematical Methods for Physics and Engineering - Third Edition. *Cambridge University Press*, page 1362, 2006.

[7] Lin Li. Magnetic susceptibility quantification for arbitrarily shaped objects in inhomogeneous fields. *Magnetic resonance in medicine*, 46(5):907–916, 2001.

[8] CJ Durrant, MP Hertzberg, and PW Kuchel. Magnetic susceptibility: further insights into macroscopic and microscopic fields and the sphere of Lorentz. *Concepts in Magnetic Resonance Part A*, 18(1):72–95, 2003.

[9] Dmitriy A Yablonskiy, Xiang He, Jie Luo, and Alexander L Sukstanskii. Lorentz sphere versus generalized Lorentzian approach: What would lorentz say about it? *Magnetic resonance in medicine*, 72(1):4–7, 2014.

[10] Ferdinand Schweser, Andreas Deistung, and Jürgen R Reichenbach. Foundations of MRI phase imaging and processing for Quantitative Susceptibility Mapping (QSM). *Zeitschrift für Medizinische Physik*, 26(1):6–34, 2016.

[11] J Luo, X He, and DA Yablonskiy. Magnetic susceptibility induced white matter MR signal frequency shifts—experimental comparison between Lorentzian sphere and generalized Lorentzian approaches. *Magnetic resonance in medicine*, 71(3):1251–1263, 2014.

[12] Xiang He and Dmitriy A Yablonskiy. Biophysical mechanisms of phase contrast in gradient echo MRI. *Proceedings of the National Academy of Sciences*, 106(32):13558–13563, 2009.

[13] JP Marques and R Bowtell. Application of a Fourier-based method for rapid calculation of field inhomogeneity due to spatial variation of magnetic susceptibility. *Concepts in Magnetic Resonance Part B: Magnetic Resonance Engineering*, 25(1):65–78, 2005.

[14] James W Cooley and John W Tukey. An algorithm for the machine calculation of complex Fourier series. *Mathematics of computation*, 19(90):297–301, 1965.

[15] Dennis C Ghiglia and Mark D Pritt. *Two-dimensional phase unwrapping: theory, algorithms, and software*, volume 4. Wiley New York, 1998.

# Chapter 5

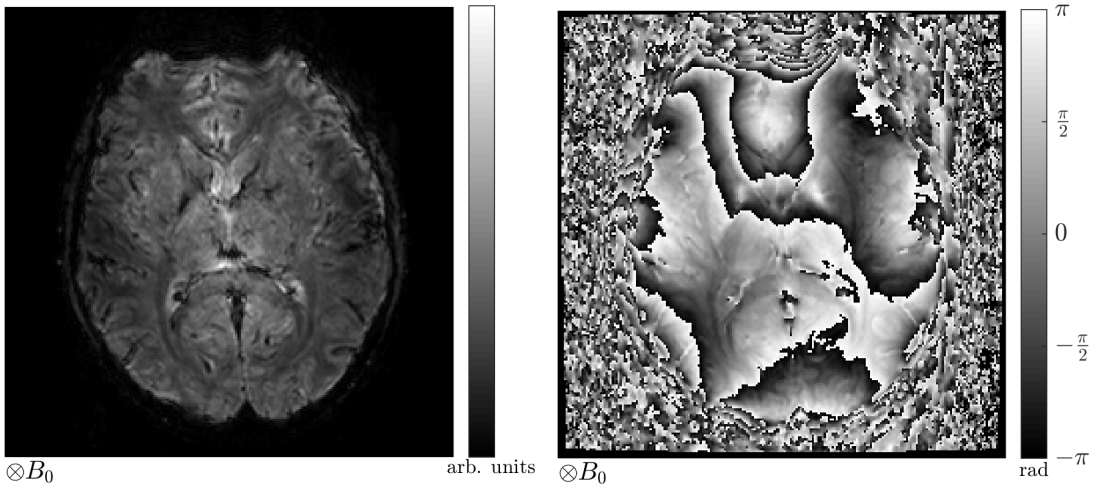
# Phase Processing and Generation of Isotropic Quantitative Susceptibility Maps

## 5.1 Why Does Phase Require Processing?

From the theory outlined in the previous two chapters, it could be hypothesised that the phase data obtained from a simple GE sequence provides the scanner operator with a direct representation of the field perturbations generated by local tissue. However, unprocessed phase, $\phi_{\mathrm{w}}(\vec{r})$, is overwhelmed with 'artefacts', causing significant challenges for an experimenter wanting to obtain useful anatomical information. Examples of unprocessed magnitude and phase images from an *in-vivo* volunteer scan are displayed in Figure 5.1.

With an in-depth understanding of the sources of contrast and 'artefacts' within phase data, $\phi_{\mathrm{w}}(\vec{r})$ can be processed to reveal anatomical information beyond what can be seen within magnitude images (Figure 5.2). The following sections outline the steps required in processing phase images: unwrapping and background field removal. Beyond this, methods are introduced for generating isotropic quantitative susceptibility maps from processed phase data.

In this chapter, wrapped and unwrapped phase will be denoted as $\phi_{\mathrm{w}}(\vec{r})$ and $\phi(\vec{r})$ respectively and quantified in units of radians. To simplify notation, measured field perturbations, which in the previous chapter were denoted as $\Delta B_{\mathrm{spin}_z}(\vec{r})$, will be written as $\Delta B(\vec{r})$. Experimental $\Delta B(\vec{r})$ maps will be displayed in Hz, as is commonly found in the phase processing literature. Theoretical concepts concerning phase evolution will be described in terms of the frequency offset, $\Delta f(\vec{r})$. Conversions between $\phi(\vec{r})$, $\Delta B(\vec{r})$, $\Delta f(\vec{r})$ and $\Delta\omega(\vec{r})$ can be performed using the information detailed in Table 3.3.




(a) Magnitude

(b) $\phi_{\mathrm{w}}(\vec{r})$

Figure 5.1: Comparison of unprocessed magnitude and phase images acquired from a volunteer *in-vivo*. Magnitude data collected directly from the scanner (Figure 5.1a) displays local tissue contrast, whereas phase data (Figure 5.1b) is overwhelmed with 'artefacts'. Image displayed is the $10^{\mathrm{th}}$ echo of a dataset collected on a Philips Achieva 7T scanner (FLASH scan, 10 echoes, $\mathrm{TE}_1$=1.27 ms, $\Delta$TE=3 ms, $\mathrm{TE}_{10}$=28.27 ms, resolution=0.89×0.89×1.2mm$^3$, FOV =200×200×120mm$^3$, 100 slices consisting of 224×224 voxels, TR=76.1 ms, flip angle=15°and acquisition time=657 s).

## 5.2 Phase Unwrapping

### 5.2.1 Phase Wraps: Identification and Cause

One of the most striking types of phase variation within $\phi_{\mathrm{w}}(\vec{r})$ maps (Figure 5.1b) are the sharp transition lines, that propagate throughout the entire FOV. These sharp transition lines appear unrelated to the local tissue structure, increase in number rapidly near to macroscopic boundaries and additionally increase in number with higher echo times. Known as 'wraps', these transitions are generated due to the definition of $\phi_{\mathrm{w}}(\vec{r})$:

$$\phi_{\mathrm{w}}(\vec{r}) = \arctan\left(\frac{\mathrm{im}\, S(\vec{r})}{\mathrm{re}\, S(\vec{r})}\right) \tag{5.1}$$

where arctan describes the 4-quadrant arctangent function, $S(\vec{r})$ is the detected signal and $\mathrm{re}\, S(\vec{r})$ and $\mathrm{im}\, S(\vec{r})$ define the real and imaginary components of the signal respectively. The origin of this equation is explained in Section 3.6. The periodic nature of the arctan function used in Equation 5.1 ensures that unprocessed phase data is bounded between $\pm\pi$. However, there is no requirement for the experimental phase evolution to be bounded between $\pm\pi$ and these limits are regularly exceeded in MRI experiments, leading to wraps when phase evolves beyond $\pi$ or $-\pi$. These effects become more prominent with higher field strengths

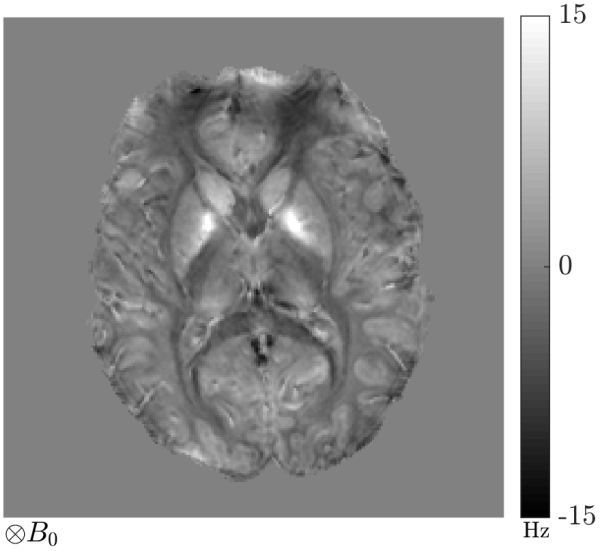



Figure 5.2: Processed phase image from Figure 5.1b (divided by first echo to remove initial phase offsets), revealing field perturbations, $\Delta B(\vec{r})$, from $\chi_I(\vec{r})$ sources within the brain. Note the increased anatomical contrast compared to the magnitude data in Figure 5.1a. Here phase data was filtered using a Laplacian unwrapper (Section 5.2.4) with fast-Fourier transform boundary conditions. Background fields removed via a Laplacian-based vSHARP filtering algorithm (Section 5.3.3), with $|\vec{r}_{max}| = 10\,\text{mm}$. vSHARP regularisation performed as a high-pass filter [1] (cut off frequency $= 0.015\,\text{mm}^{-1}$). Experimental parameters outlined in Figure 5.1.

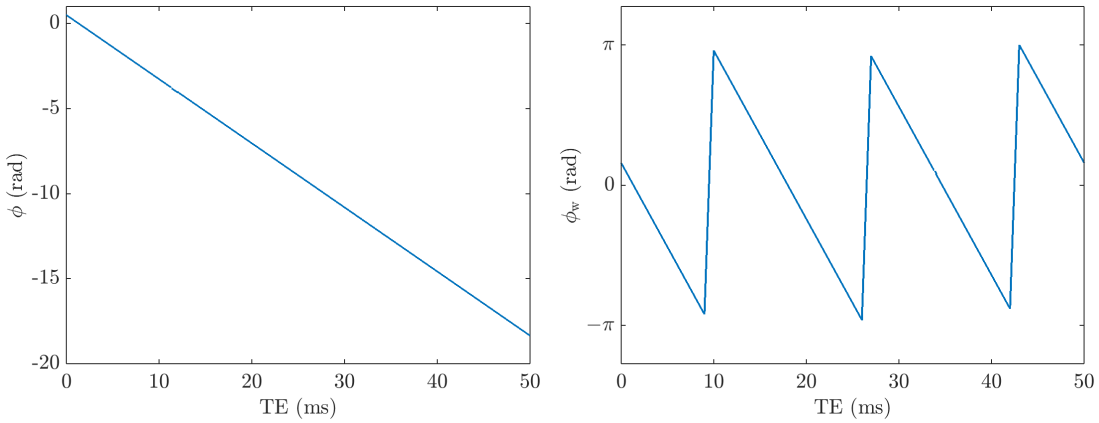
and in addition, as phase is a function of echo time, $\phi_w(\vec{r}, t)$, higher echo times will lead to more observed wraps. A simulated example of the effect of phase wrapping on a single voxel is demonstrated in Figure 5.3.

A simple solution to prevent wraps would be to collect experimental data at ultra-short echo times, to prevent the phase from evolving beyond the bound values of $\pm\pi$ within the image. However this method would often be impractical or impossible considering the requirements of the experimental acquisition and would also prevent numerous experimental hypotheses from being examined where echo times are required to be beyond the ultra-short limit. It would additionally restrict the scanner operator's control of the acquired contrast within the image as discussed in Section 3.5. Numerous methods for unwrapping phase data have been developed to circumvent the requirement for using ultra-short echo times.

### 5.2.2 Echo Time based Unwrapping

Figure 5.3b reveals that wraps generated by the imposed arctan function are characterised by phase jumps of magnitude $2\pi$. From this, a simple relationship between the wrapped phase, $\phi_{\text{w}}(\vec{r}, t)$, and the unwrapped phase, $\phi(\vec{r}, t)$, can be defined [2]:

$$\phi(\vec{r}, t) = \phi_{\text{w}}(\vec{r}, t) \pm 2\pi n(\vec{r}, t) \tag{5.2}$$




(a) Phase evolution

(b) Wrapped phase evolution

Figure 5.3: Simulated comparison of the phase evolution within a voxel. The natural evolution of phase within the voxel (Figure 5.3a) is experimentally observed as being bounded between $\pm\pi$ (Figure 5.3b) due to the arctan condition in Equation 5.1, leading to sharp transitions known as 'wraps'. Here $\Delta f = 60\,\text{Hz}$ and $\phi_0 = 0.5\,\text{rad}$ as defined in Equation 5.3.

where $n(\vec{r}, t) \in \mathbb{N}_0$. Therefore $\phi_\text{w}(\vec{r}, t)$ can be unwrapped by examining the temporal phase evolution of individual voxels within multi-echo GE data and adding/subtracting $2\pi$ whenever a phase shift equivalent to $2\pi$ occurs. Here voxels will be unwrapped individually, but due to the computational simplicity of this task it can be easily implemented and computed rapidly over an entire 3D volume. Unwrapped images can then be fitted to:

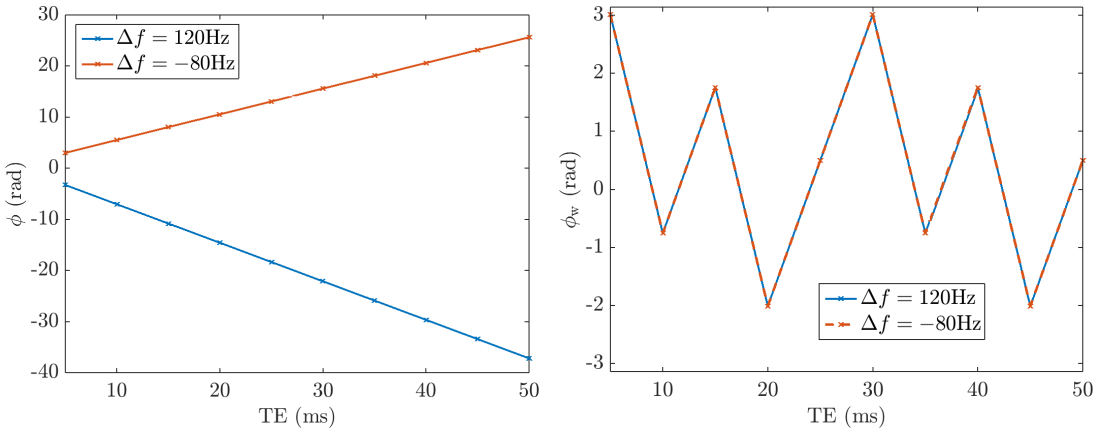
$$\phi(\vec{r}, t) = \phi_0(\vec{r}) - 2\pi\Delta f(\vec{r})t \tag{5.3}$$

where $\phi_0(\vec{r})$ defines echo-time independent contributions from experimentally induced phase offsets and the negative frequency convention has been utilised. As this is a linear problem it can be computed rapidly over an entire dataset.
This method can be used successfully to unwrap phase data. However there are two caveats that can prevent this method producing robust and reliable results:

1. If wraps occur in the image collected at the minimum echo time, these cannot be removed with echo time based unwrapping. This is because the voxelwise unwrapping process is referenced to the phase at the first echo. This commonly occurs in experimental data collection and can be caused by $\phi_0(\vec{r})$, in addition to a large field offset which causes significant phase accumulation even at the minimum echo time.

2. If phase is evolving at a rate greater than the Nyquist frequency:

$$f_{ny} = \frac{1}{2\Delta\text{TE}} \tag{5.4}$$




(a) $\phi(t)$ (b) $\phi_{\mathrm{w}}(t)$

Figure 5.4: Simulated comparison of the phase evolution for two voxels evolving at different frequencies, with samples collected every 5 ms ($\phi_0 = 0.5$ rad for both lines). The evolution of $\phi$ (Figure 5.4a) is significantly different between the two voxels. However, $\phi_{\mathrm{w}}$ (Figure 5.4b) is identical for both voxels. This is because the voxel evolving with $\Delta f = 120$ Hz evolves beyond the Nyquist frequency limit and therefore $\phi_{\mathrm{w}}\,(\Delta f = 120\,\mathrm{Hz})$ has a degenerate form evolving below the Nyquist frequency limit, which here is equal to $\phi_{\mathrm{w}}\,(\Delta f = -80\,\mathrm{Hz})$.

it will not be possible to resolve the 'correct' $\phi$, as it then is not possible to distinguish between rapidly and slowly evolving phase. This is due to the condition:

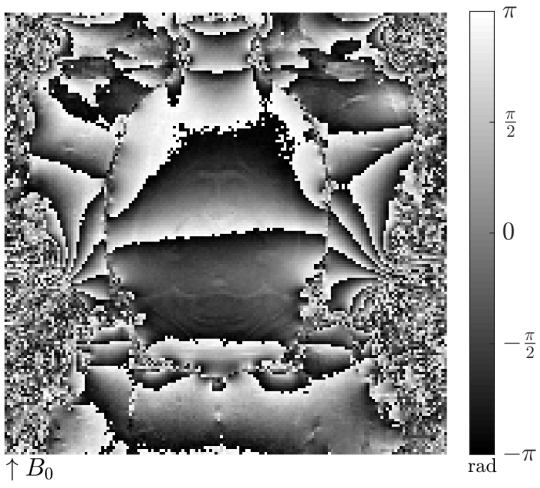
$$\phi_{\mathrm{w}}\left(2\pi\Delta f(\vec{r})\cdot\Delta\mathrm{TE}\right) = \phi_{\mathrm{w}}\left(2\pi\Delta f(\vec{r})\cdot\Delta\mathrm{TE}\pm 2\pi\right) \tag{5.5}$$

An example of this effect is shown in Figure 5.4.

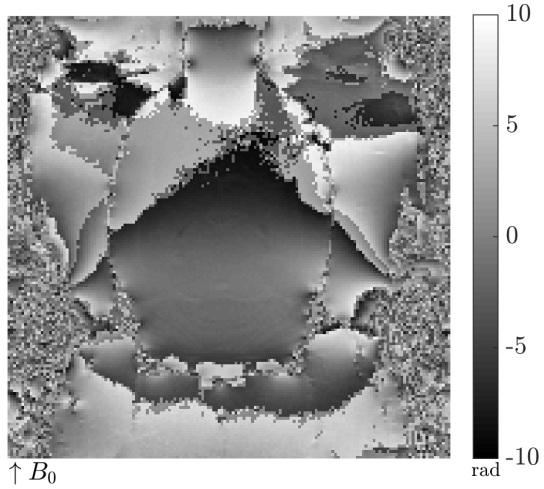
Under certain circumstances (low initial echo time and slow phase evolution) the echo-time-based unwrapping method can be successfully implemented. However, this method as a stand-alone will not be suitable in most experimental cases, as shown in Figure 5.5. Furthermore, this method can only be applied to multi-echo data, preventing its implementation when only a single echo is collected.

### 5.2.3 Path based Unwrapping

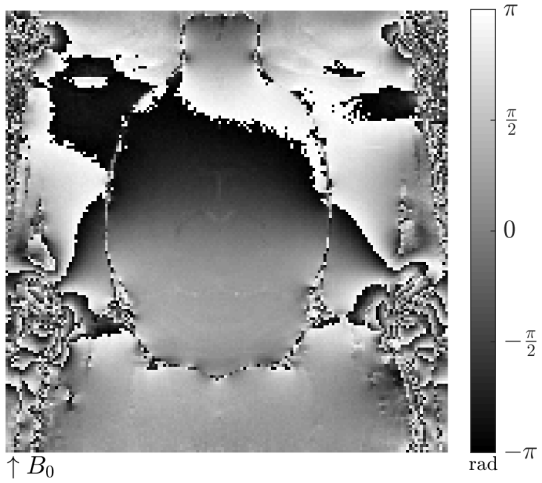
From an examination of Figure 5.5a, it can be hypothesised that single-echo phase datasets can be unwrapped individually based on the assumption that phase should vary smoothly throughout the image. Within a single echo image, Equation 5.2 remains valid and the unwrapping problem becomes more concerned with examining the spatial phase gradient, $\nabla\phi_{\mathrm{w}}(\vec{r})$ and adding/subtracting values of $2\pi n(\vec{r})$ to ensure $\nabla\phi_{\mathrm{w}}(\vec{r})$ is spatially smooth. Unfortunately, unlike echo-time-based unwrapping, path-based unwrapping is typically performed over a 2D (or 3D) region, producing a significant increase in complexity [3].




(a) $\phi_{\mathrm{w}}(\vec{r})$ - Third echo




(b) $\phi(\vec{r})$ - Third echo



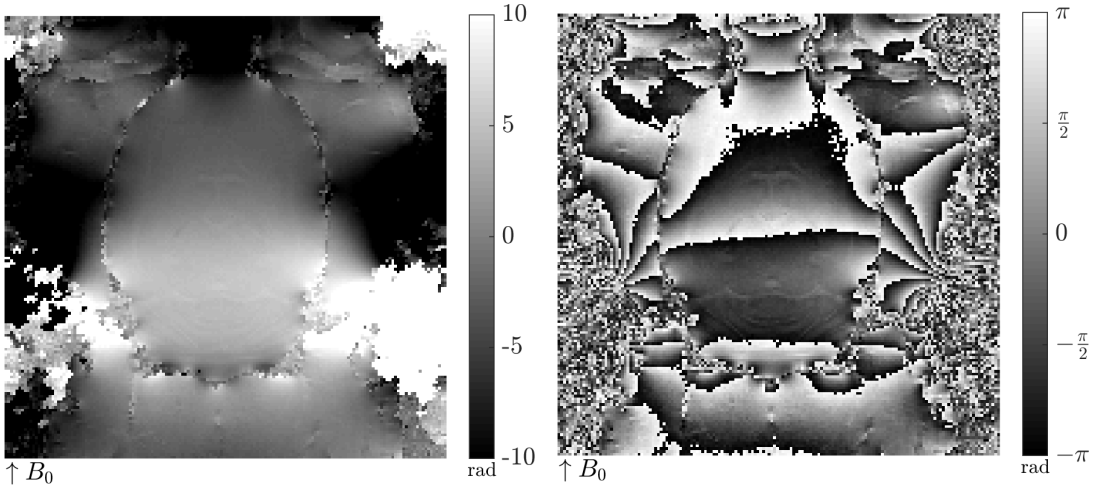

(c) $\phi_{\mathrm{w}}(\vec{r})$ - First echo

Figure 5.5: Example of echo-time-based unwrapping applied to multi-echo GE *in-vivo* rodent data. The wrapped data for the third and first echo are shown in Figures 5.5a and 5.5c. The unwrapped data (Figure 5.5b) shows successful unwrapping in certain regions, but the approach fails to unwrap the entire image due to rapidly evolving phase and wrapping within the first echo map (Figure 5.5c). Experimental parameters described in Section 6.3.

Examination of the numerous methods for path-based unwrapping is beyond the scope of this thesis. However it is important to note that the quality of the unwrapped image is dependent on the unwrapping algorithm implemented, in addition to the degree of wrapping. Analogous to the Nyquist condition (Equations 5.4 and 5.5), path based phase unwrapping is limited by a maximum allowed value of $|\nabla\phi_{\mathrm{w}}(\vec{r})|$, with the condition [4]:

$$\left|\nabla\phi_{\mathrm{w}}(\vec{r})\cdot\hat{x},\hat{y},\hat{z}\right| < \frac{\pi}{\Delta x},\frac{\pi}{\Delta y},\frac{\pi}{\Delta z} \tag{5.6}$$

where $\hat{x},\hat{y},\hat{z}$ are orthogonal unit vectors and $\Delta x,\Delta y,\Delta z$ indicate the voxel dimensions along $\hat{x},\hat{y},\hat{z}$. An example of the application of path-based unwrapping




(a) $\phi(\vec{r})$ (b) $\phi_{\text{rew}}(\vec{r})$

Figure 5.6: Example of applying path based unwrapping to the experimental data in Figure 5.5a [5]. Figure 5.6a shows successful unwrapping of experimental data over tissue containing regions. In addition, after rewrapping the unwrapped image (Figure 5.6b), $\phi_{\text{rew}}(\vec{r})$ is identical to $\phi_{\text{w}}(\vec{r})$ (Figure 5.5a), revealing the congruency of the path-based method.

is is shown in Figure 5.6.

### 5.2.4 Laplacian-Based Unwrapping

Laplacian-based unwrapping is commonly encountered in phase processing literature. It can rapidly unwrap phase images, be performed on a single echo dataset and is robust, with algorithms readily applied to a variety of experimental data without any requirement for parameter variation. The Laplacian approach is based on the following relation [6]:

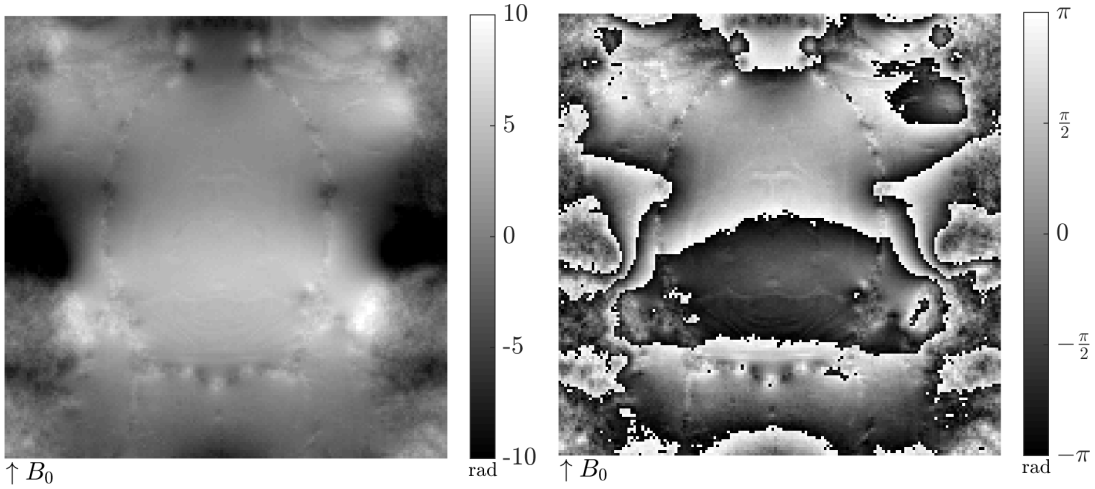
$$\begin{aligned} e^{i\phi_{\text{w}}(\vec{r})} &= e^{i\phi_{\text{w}}(\vec{r})\pm 2\pi n(\vec{r})} \\ &= e^{i\phi(\vec{r})}. \end{aligned} \tag{5.7}$$

Using this condition it is possible to derive a relationship between the Laplacians $\nabla^2\phi(\vec{r})$ and $\nabla^2\phi_{\text{w}}(\vec{r})$ [6]:

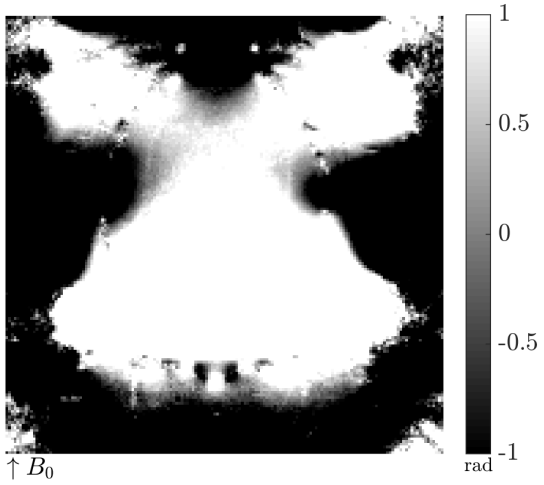
$$\nabla^2\phi(\vec{r}) = \cos\phi_{\text{w}}(\vec{r})\nabla^2\sin\phi_{\text{w}}(\vec{r}) - \sin\phi_{\text{w}}(\vec{r})\nabla^2\cos\phi_{\text{w}}(\vec{r}). \tag{5.8}$$

$\phi(\vec{r})$ can then be determined from $\nabla^2\phi(\vec{r})$ in terms of $\phi_{\text{w}}(\vec{r})$ by utilising the Fourier transform relationships for first and second order differentials (Equation 4.31). An experimental example of the implementation of Laplacian-based path unwrapping is shown in Figure 5.7a. However, when performing Laplacian unwrapping certain considerations must be taken into account:

1. Laplacian unwrapping performs an additional component of filtering of the data, due to the Laplacian of external field perturbations, $\nabla^2\Delta B_{\text{ext}}(\vec{r})$, being




(a) $\phi(\vec{r})$ (b) $\phi_{\text{rew}}(\vec{r})$




(c) $\phi(\vec{r})$ thresholded between $\pm 1$ rad

Figure 5.7: Example of unwrapping of Figure 5.5a using the Laplacian-based fast-Fourier transform approach. Figure 5.7a indicates that the image is successfully unwrapped. However, Figure 5.7c reveals that the unwrapped image has imposed periodic boundary conditions at the edges of the ROI. The combination of imposed boundary conditions and intrinsic filtering of the Laplacian-based method leads to the rewrapped phase (Figure 5.7b), $\phi_{\text{rew}}(\vec{r})$, failing to maintain the congruency condition when compared to Figure 5.5a.

equivalent to zero (discussed further in Section 5.3.3). In some circumstances this could be considered beneficial and its effect becomes negligible after applying background field removal (discussed in Section 5.3). However, it implies that the $\phi(\vec{r})$ is not congruent to $\phi_{\text{w}}(\vec{r})$ (Figure 5.7b).

2. Solving Equation 5.8 to obtain $\phi(\vec{r})$ requires the definition of boundary conditions [3, 6]. Unfortunately, MRI VOIs extend beyond signal containing regions, hence it is not possible to obtain adequate boundary information at the VOI boundary. Defining phase outside a user-defined ROI (defined here as signal containing regions) equal to zero is not an adequate solution,

as field perturbations exist within these regions, defining $\Delta B_{\mathrm{ROI_{ext}}}(\vec{r}) \neq 0$. The use of fast Fourier transforms to obtain $\phi(\vec{r})$ from $\nabla^2\phi(\vec{r})$ imposes the condition that the phase is periodic at the boundaries [3, 6], as the edge of the dataset and computational memory constraints prevent a solution via symmetrisation [7] being applied to 3D data sets. Periodic boundary conditions cannot be considered a natural property of MRI images, particularly when considering large, inhomogeneous field perturbations over the VOI. An example of this is shown in Figure 5.7c.

Previous literature [6] has described the application of the Laplacian protocol to determine the integer value of $n(\vec{r})$ from Equation 5.2:

$$n(\vec{r}) = \frac{1}{2\pi}\nabla^{-2}\left[\nabla^2\phi(\vec{r}) - \nabla^2\phi_{\mathrm{w}}(\vec{r})\right] \tag{5.9}$$

using fast cosine transforms to impose the Neumann boundary condition, $\nabla n_{\mathrm{edge}}(\vec{r}) = 0$, which can be considered a 'realistic' [6] boundary condition for $n(\vec{r})$. However, to date this protocol has not been applied in the MRI literature and further consideration indicates that this is likely due to the impact of the Laplacian operator on external field perturbations as discussed above. This prevents the solution to $\nabla^2\phi(\vec{r})$ and $\nabla^2\phi_{\mathrm{w}}(\vec{r})$ representing $\phi(\vec{r})$ in its entirety, preventing $n(\vec{r})$ from being accurately determined. Boundary condition problems in Laplacian unwrapping are typically avoided by padding the dataset with zeros, preventing a significant impact of the boundary conditions on the ROI.

3. As the boundary values of $\phi(\vec{r})$ are not known prior to the solution of Equation 5.8, resolving the Laplacian equation to obtain $\phi(\vec{r})$ removes any global phase offsets [4]. This implies that unlike the 'true' unwrapped phase, $\sum_{\text{all voxels}} \phi(\vec{r}) = 0$.

4. As the Laplacian approach is based on a single echo, it is still restricted by the condition in Equation 5.6, thus preventing areas of rapid phase evolution from being correctly unwrapped.

Despite these conditions, the Laplacian approach is very effective in unwrapping phase images. The effectiveness of Laplacian unwrapping and its simplicity in application explains its widespread adoption by the phase processing community and the observed convergence of this technique as the go-to method for phase unwrapping. Furthermore, the opportunity for combining phase unwrapping and background field removal simultaneously using Laplacian approaches is of great interest. This is discussed in Section 5.3.3.

### 5.2.5 Nonlinear Voxelwise Temporal Fitting to Signal

A further method to unwrap phase data is to fit the complex temporal signal evolution of each voxel to a function describing the expected temporal signal evolution using a non-linear least-squares minimisation [8]. This method is applied experimentally in Chapter 6. The underlying theory and protocol for this method is discussed in detail in Section 6.5.1.

## 5.3 Background Field Removal

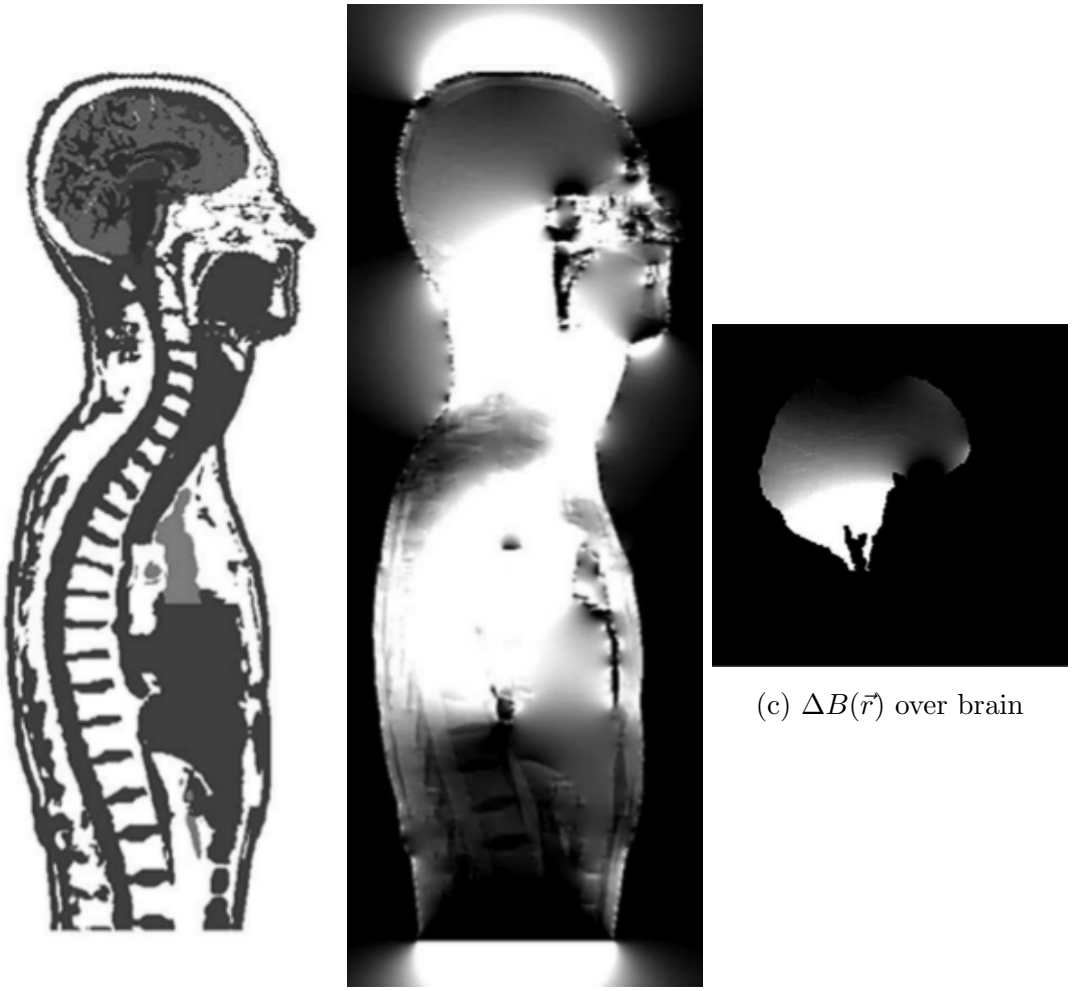
### 5.3.1 Background Fields: Identification and Cause

Examination of successfully unwrapped phase images (Figures 5.6a and 5.7a) reveals smooth phase variation over regions containing tissue content. However, in the presence of these variations, little is seen in terms of anatomical tissue contrast. The subtle anatomical information within the phase map is dominated by the contribution of external field perturbations (as discussed in Section 4.2) from both external $\chi_I$ sources and significant differences in $\chi_I$ between air-tissue interfaces. These additional sources of field perturbations are typically one to two orders of magnitude larger that the field perturbations induced by local tissue effects [9, 10]. Further contributors to background fields include small eddy current contributions and phase offsets [11].

It is incorrect to refer to these additional field perturbations as artefacts as they result from all the tissue contained within the MRI scanner. When imaging an ROI within the scanner, the bore of the scanner contains both the ROI and surrounding regions, leading to the observed field perturbations. This is visualised in Figure 5.8.

### 5.3.2 High Pass Filtering

External field variations appear slowly-varying over the ROI, implying that a simple high-pass filter could be sufficient to remove these contributions. Initial work examining phase processing, including the established field of susceptibility weighted imaging (SWI) [12] utilised high-pass filters to remove external field variations. Unfortunately high-pass filters are insensitive to the differences in low frequency contributions from internal and external $\chi_I$ sources, implying that low frequency field perturbations from tissue within the ROI will additionally be removed. To overcome this issue, more sophisticated methods have been developed to distinguish between internal and external field perturbations.

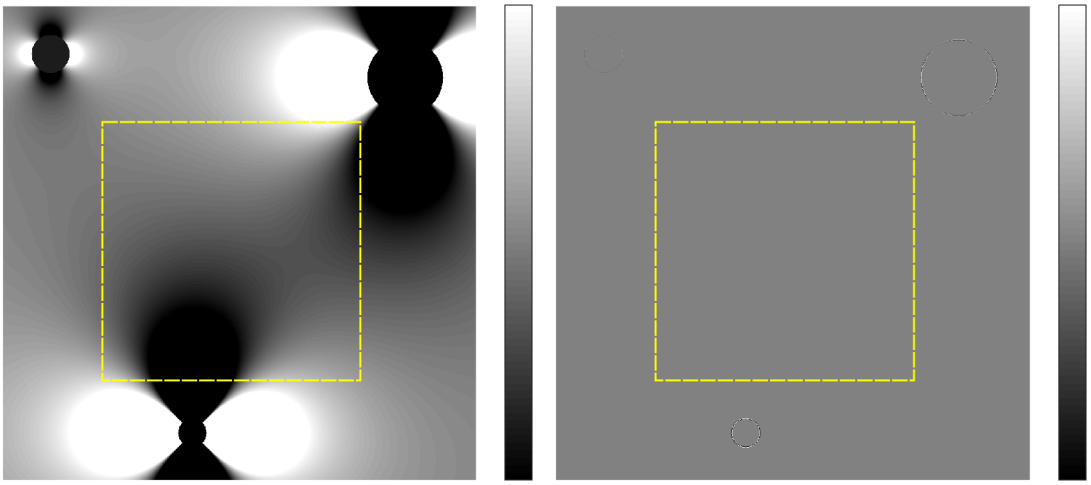


(a) $\chi_I(\vec{r})$ simulation (b) $\Delta B(\vec{r})$ simulation (c) $\Delta B(\vec{r})$ over brain

Figure 5.8: Simulation demonstrating the effect of external field perturbations on *in-vivo* brain imaging. When a subject is placed into an MRI scanner, it is not just the brain that enters the scanner, but the majority of the subjects body and surrounding air. When considering the field perturbations, all $\chi_I$ sources contained in the scanner bore need to be accounted for (Figure 5.8a). The field perturbations from external susceptibility sources (Figure 5.8b), dominate the phase, in particular the contribution from air-tissue boundaries. Therefore $\Delta B(\vec{r})$ over the ROI will contain contributions from external field perturbations (Figure 5.8c). Images modified from [1].

### 5.3.3 Laplacian Filtering

As discussed in Section 4.2.1, when an external $\vec{B}_0$ field is applied, the presence (or lack thereof) of sources of magnetisation within a ROI has a distinct effect on the magnetic fields within the ROI. In ROIs which do not contain a source of magnetisation, $\vec{M}(\vec{r}) = 0$, or which only contain homogeneous magnetisation, $\nabla \cdot \vec{M}(\vec{r}) = 0$, the field perturbations are harmonic [13] and Laplace's equation (Equation 4.12) describes the form of $\Delta B(\vec{r})$. This is visualised in Figure 5.9.
An interesting property of harmonic functions is described by the spherical mean



(a) $\Delta B(\vec{r})$ (b) $\nabla^2 \Delta B(\vec{r})$

Figure 5.9: Illustration of the Laplacian properties of external field sources. Figure 5.9a shows the field perturbations produced by three cylinders of arbitrary susceptibility. Imagine that the MRI FOV is defined by the yellow box and therefore the cylinders are sources of unwanted external field perturbations. As there are no sources of magnetisation within the FOV and the system is linear, if we took the Laplacian of $\Delta B(\vec{r})$ (Figure 5.9b), it would be zero everywhere inside the FOV. Data simulated on a $1024 \times 1024 \times 1024$ voxel$^3$ matrix using the analytical form of field perturbations (Tables 4.4 and 4.5), written in-house using MATLAB (Release 2013a, The MathWorks Inc., Natick, MA, United States).

value theorem [14]:

$$u(\vec{R}) = \frac{1}{\Gamma} \int_{\Omega} u\left(\vec{R} + \vec{r}\right) d\Omega \tag{5.10}$$

where $u(\vec{r})$ is a harmonic function ($\nabla^2 u(\vec{r}) = 0$), $\Omega$ defines a spherical volume or shell with radius $s$, $\Gamma$ is equal to the volume or surface area of $\Omega$ and $\vec{R}$ is the point at the centre of $\Omega$ (the centre of the sphere). This equation implies that for a harmonic function, the value at the centre of a spherically defined region, $u(\vec{R})$ is equal to the average value on a spherical surface/volume surrounding $u(\vec{R})$. If this property could be exploited to remove field perturbations generated by external $\chi_I$ sources, it would be of great significance, as unlike high-pass filtering it can theoretically discriminate [15] between low frequency field perturbations arising from internal and external sources of $\chi_I$.

The first widely adopted implementation of this method was described by Schweser et al. [16], known as Sophisticated Harmonic Artefact Reduction for Phase data (SHARP). SHARP filtering exploits the spherical mean value theorem by subtracting the convolution of $\Delta B(\vec{r})$ with a spherical shell/volume surrounding the point of interest (henceforth known as the spherical kernel), $\Omega$, from $\Delta B(\vec{r})$ as follows:

$$\Delta B'(\vec{r}) = \Delta B(\vec{r}) - \Omega \otimes \Delta B(\vec{r}) \tag{5.11}$$

over a user-defined ROI. As the system is linear, internal, $\Delta B_{\text{int}}(\vec{r})$, and external, $\Delta B_{\text{ext}}(\vec{r})$ field perturbations generated from internal, $\chi_{I_{\text{int}}}(\vec{r})$ and external, $\chi_{I_{\text{ext}}}(\vec{r})$ sources within a ROI can be defined separately:

$$\Delta B_{\text{ROI}}(\vec{r}) = \Delta B_{\text{int}}(\vec{r}) + \Delta B_{\text{ext}}(\vec{r}). \tag{5.12}$$

As $\Delta B_{\text{ext}}(\vec{r})$ obeys Laplace's equation within the ROI ($\nabla^2 \Delta B_{\text{ext}}(\vec{r}) = 0$), it is preserved in the convolution due to Equation 5.10. However, $\Delta B_{\text{int}}(\vec{r})$ does not obey Laplace's equation (besides zero field contributions [15]):

$$\nabla^2 \Delta B_{\text{int}}(\vec{r}) = \begin{cases} 0 & \text{if } \Delta B_{\text{int}}(\vec{r}) = 0 \\ \mathbb{R}_{\neq 0} & \text{otherwise} \end{cases}. \tag{5.13}$$

Therefore:

$$\begin{aligned} \Delta B'_{\text{ROI}}(\vec{r}) &= \Delta B_{\text{int}}(\vec{r}) + \Delta B_{\text{ext}}(\vec{r}) - \Omega \otimes \Delta B_{\text{int}}(\vec{r}) - \Omega \otimes \Delta B_{\text{ext}}(\vec{r}) \\ &= \Delta B_{\text{int}}(\vec{r}) - \Omega \otimes \Delta B_{\text{int}}(\vec{r}) \end{aligned}. \tag{5.14}$$

Rearranging, $\Delta B_{\text{int}}(\vec{r})$ can be defined as follows:

$$\Delta B_{\text{int}}(\vec{r}) = (\delta - \Omega) \otimes^{-1} \Delta B'_{\text{ROI}}(\vec{r}) \tag{5.15}$$

where $\delta$ is a unit function (taking a value of one at the centre of $\Omega$, zero otherwise). There are important considerations to take into account when utilising this method experimentally:

1. In a typical MRI experiment, field perturbations are not sampled over the entire dataset, requiring a well defined mask identifying signal generating regions.

2. The deconvolution step (Equation 5.15) requires regularisation [1] due to the 'ill-posedness' of the inversion.

3. The magnitude of the radius of $\Omega$, $s$ has a direct impact on both the SNR and the defined boundary of the image.

4. Boundary conditions will be violated at the edge of the ROI, inducing artefacts and requiring regularisation.

When obtaining a field perturbation map of the brain *in-vivo* using a standard GE sequence, field perturbations are not sampled over regions external to tissue (e.g in the sinuses and air surrounding the head) and in many regions external to the brain (e.g the skull and face), signal levels will be low. These regions will consequently

appear with very low SNR in images and to prevent errors being induced in processing, an ROI is defined over high SNR regions, setting $\Delta B_{\mathrm{ROI_{ext}}}(\vec{r}) = 0$, where $\mathrm{ROI_{ext}}$ defines the region external to the ROI. The condition $\Delta B_{\mathrm{ROI_{ext}}}(\vec{r}) = 0$, is incorrect due to the presence of both $\chi_I$ sources external and internal to the ROI. However, when determining $\nabla^2 \Delta B_{\mathrm{ROI}}(\vec{r})$, the ROI mask imposes the boundary condition, $\nabla^2 \Delta B_{\mathrm{ROI_{edge}}}(\vec{r}) = 0$, where $\mathrm{ROI_{edge}}$ defines the boundary of the ROI. This boundary condition is valid for field perturbations generated by $\chi_I$ sources within the ROI, $\Delta B_{\mathrm{int}}(\vec{r})$, and can be utilised to determine a unique solution for $\Delta B_{\mathrm{int}}(\vec{r})$ [15]. Unfortunately, it can be very difficult to define a precise mask due to the poor definition of tissue boundaries as a result of signal dephasing and partial volume effects, implying either an extremely conservative ROI is required or voxels containing low SNR will appear within the user defined ROI, leading to errors in the form of $\Delta B_{\mathrm{int}}(\vec{r})$.

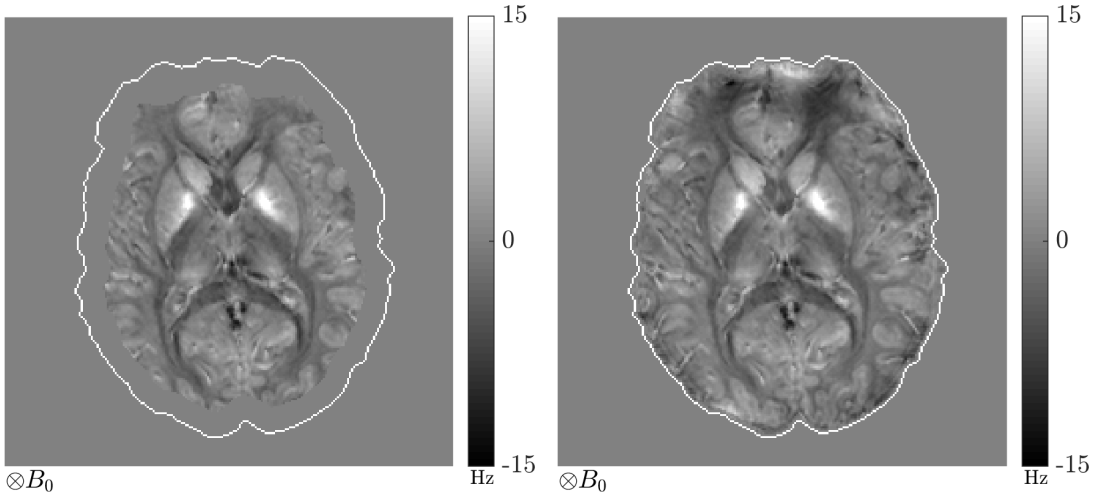
The deconvolution step requires division by $k^2$. As $k \to 0$, the problem becomes increasingly ill-posed (ill-posed problems are discussed further in Section 5.4.1) and noise components near the vicinity of $k = 0$ will be amplified.

When performing the convolution with $\Omega$ to remove harmonic field perturbations over the user defined ROI, an increased extent of the spherical surface/volume is preferable, as averaging over a larger radius $s$ reduces the error ($\propto \frac{1}{N^{\frac{1}{2}}}$ [14], where $N$ is the number of voxels being averaged). However, if a high SNR ROI has been defined, $\Omega$ cannot sample field perturbations beyond $\mathrm{ROI_{edge}}$ as the presence of noise will generate artefacts and violate the spherical mean value condition for external fields. To stop this from happening, $s$ is reduced as $\mathrm{ROI_{edge}}$ is reached [1, 17, 18], preventing any voxels within $\Omega$ containing $\Delta B_{\mathrm{ROI_{ext}}}(\vec{r})$. This is defined as follows:

$$s = \begin{cases} s_{\max} & \text{if } s_{\mathrm{b}} \geq s_{\max} \\ s_b & \text{otherwise} \end{cases} \tag{5.16}$$

where $s_{\max}$ is the maximum SHARP radius and $s_{\mathrm{b}}$ is the distance between the voxel of interest and $\mathrm{ROI_{edge}}$. This will increase the error near the ROI boundary due to a decreased number of voxels are being averaged when determining $\nabla^2 \Delta B_{\mathrm{int}}(\vec{r})$. However, it limits the loss of information to just a single voxel at the boundary. Additionally, higher values of $s_{\mathrm{b}}$ can be applied to experimental data, taking advantage of the increased SNR. This method is known as 'variable SHARP', or vSHARP [1, 17, 18]. An example of its use is shown in Figure 5.10.

The step change in $\chi_I$ at $\mathrm{ROI_{edge}}$ violates the condition $\nabla^2 \Delta B_{\mathrm{ROI_{edge}}}(\vec{r}) = 0$, inducing low-frequency inhomogeneities within $\Delta B_{\mathrm{int}}(\vec{r})$ in the deconvolution step due to the harmonic properties of the induced field perturbations over $\mathrm{ROI_{int}}$ [19]. A larger $s$ reduces the impact of this violation [19], however this requires regu-




(a) SHARP filtered (b) vSHARP filtered

Figure 5.10: Comparison of *in-vivo* brain data filtered with SHARP and vSHARP, with $s = 10\,\text{mm}$ and cut off frequency $= 0.015\,\text{mm}^{-1}$, where the boundary is indicated by the white line. With SHARP the volume of brain tissue lying within 10 mm of to the boundary is lost as $\Omega$ cannot be defined beyond the boundary. However with vSHARP, though there is a greater error near the boundary, by varying the kernel radius only a single voxel is lost. Experimental parameters outlined in Figure 5.1. Unwrapping protocol outlined in Figure 5.2.

larisation to effectively 'high-pass' filter the data and remove the low-frequency inhomogeneities.

To reduce the 'ill-posedness' of the deconvolution, the most common method of regularisation in SHARP literature is the use of truncated single value decomposition [1, 16] (theoretical considerations of truncated single value decomposition are discussed further in Section 5.4.3). Furthermore, the use of truncated single value decomposition imposes a high-pass filter operation, due to the requirement of thresholding low frequency components. Larger $s$ imposes a greater frequency variation per voxel in $k$-space and increases this filtering. A thorough analysis of this in the context of SHARP, with a particular focus on ensuring the regularisation is consistent between datasets is outlined in [1].

If $\Delta B(\vec{r})$ was defined outside the ROI, the harmonic signal could be determined and removed from the entire image in one step, extending Laplacian unwrapping (Section 5.2.4) to include background field removal. One method that utilises this approach is HARmonic PhasE REmovaL using the LAplacian operator (HARPERELLA) [9, 20], which estimates the Laplacian outside the ROI by solving the following minimisation problem (minimisation problems discussed in Section 5.4.5):

$$\min_{\nabla^2\phi_{\text{ROI}_{\text{ext}}}(\vec{r})} \left\| \Omega \otimes \nabla^2\phi_{\text{ROI}_{\text{ext}}}(\vec{r}) + \Omega \otimes \nabla^2\phi_{\text{ROI}_{\text{int+bou}}}(\vec{r}) - \Omega \otimes \nabla^2\phi_{\text{ROI}_{\text{int}}}(\vec{r}) \right\|_2^2 \quad (5.17)$$

where $\text{ROI}_{\text{int}}$, $\text{ROI}_{\text{bou}}$ and $\text{ROI}_{\text{ext}}$ refer to the region inside the ROI (distance $s$

from the boundary or beyond), region inside the ROI (less than distance $s$ from the boundary) and the region external to the ROI respectively. The Laplacian is calculated from Equation 5.8. Once $\nabla^2\phi(\vec{r})$ is determined over the entire dataset, $\phi(\vec{r})$ can be directly calculated.

### 5.3.4 Projection onto Dipole Fields

Another commonly used method of background field removal is known as projection onto dipole fields (PDF), which utilises the Hilbert projection theorem, considering the orthogonality of dipole fields generated internally and externally to an ROI to remove background field perturbations from within an ROI [21]. This is achieved by simulating the susceptibility distribution external to the ROI [21], $\chi_{I_{\text{ext}}}(\vec{r})$, and solving the following minimisation problem (minimisation problems discussed in Section 5.4.5):

$$\min_{\chi_{I_{\text{ext}}}(\vec{r})} \left\| M_{\text{ROI}}(\vec{r}) \cdot B_0 \cdot \mathcal{F}^{-1}\left[ d(\vec{k}) \cdot \mathcal{F}\left[\chi_{I_{\text{ext}}}(\vec{r})\right]\right] - M_{\text{ROI}}(\vec{r}) \cdot \Delta B(\vec{r}) \right\|_2^2, \quad (5.18)$$

where $M_{\text{ROI}}(\vec{r})$ is a mask of the ROI (further details of the origin of this equation are discussed within Sections 4.3 and 5.4). From this it is then possible to remove the background fields from the determined $\chi_{I_{\text{ext}}}$ distribution, defining:

$$\Delta B_{\text{int}}(\vec{r}) = \Delta B(\vec{r}) - B_0 \cdot \mathcal{F}^{-1}\left[ d(\vec{k}) \cdot \mathcal{F}\left[\chi_{I_{\text{ext}}}(\vec{r})\right]\right] \quad (5.19)$$

within the ROI. Similarly to the Laplacian techniques discussed previously, this technique suffers from increased error near ROI boundaries, due to violation of the orthogonality principle of dipole fields internal and external to the ROI [21]. In addition, the technique can only remove field perturbations described appropriately by the simulated external dipole fields [15]. However, PDF background field removal provides a fast, robust technique to resolve the internal field perturbations within an ROI, producing results with few internal artefacts [15] and superior results to high-pass filtering.

### 5.3.5 Other Techniques

A complete list of background field removal techniques cannot be fully described within this thesis. Readers with a further interest in background field removal methods and the advantages/disadvantages of different techniques are referred to a recent review paper by Schweser et al. [15]. Within this thesis, the background field removal described in experimental Chapters 6 and 9 is performed via vSHARP, with high-pass filter regularisation [1]. In Chapter 8, a novel phase processing technique to reveal microstructure contrast without the requirement of phase unwrapping and background field removal is discussed.

## 5.4 Generating Isotropic Quantitative Susceptibility Maps

### 5.4.1 Motivation and Challenges

In the previous chapter, a theoretical discussion of the role of $\chi_I$ in generating field perturbations was discussed, with an initial emphasis on how $\chi_I$ can reveal information about the underlying tissue structure. Previously in this chapter, methodology for generating field perturbation maps displaying local tissue contrast has been described. These field perturbation maps can show fantastic structural information as indicated in Figure 5.2. However, these maps still show non-local field effects, with contrast from individual structures dependent on both the shapes of structures and their orientations to the $\vec{B}_0$ field. An example of this is shown in Figure 5.11. Due to the non-local effects present in field perturbation maps and the complex relationship between $\chi_I(\vec{r})$ and $\Delta B(\vec{r})$, it is not possible to directly obtain quantitative information about tissue structure from processed phase images. Therefore it is necessary to transform the image into one showing the underlying $\chi_I(\vec{r})$ distribution.

In Section 4.3, a method of rapidly simulating $\Delta B(\vec{r})$ from $\chi_I(\vec{r})$ distributions using Fourier transforms was described. From examination of the theory, obtaining $\chi_I(\vec{r})$ from $\Delta B(\vec{r})$ should be a trivial problem. From Equation 4.35, it can be denoted:

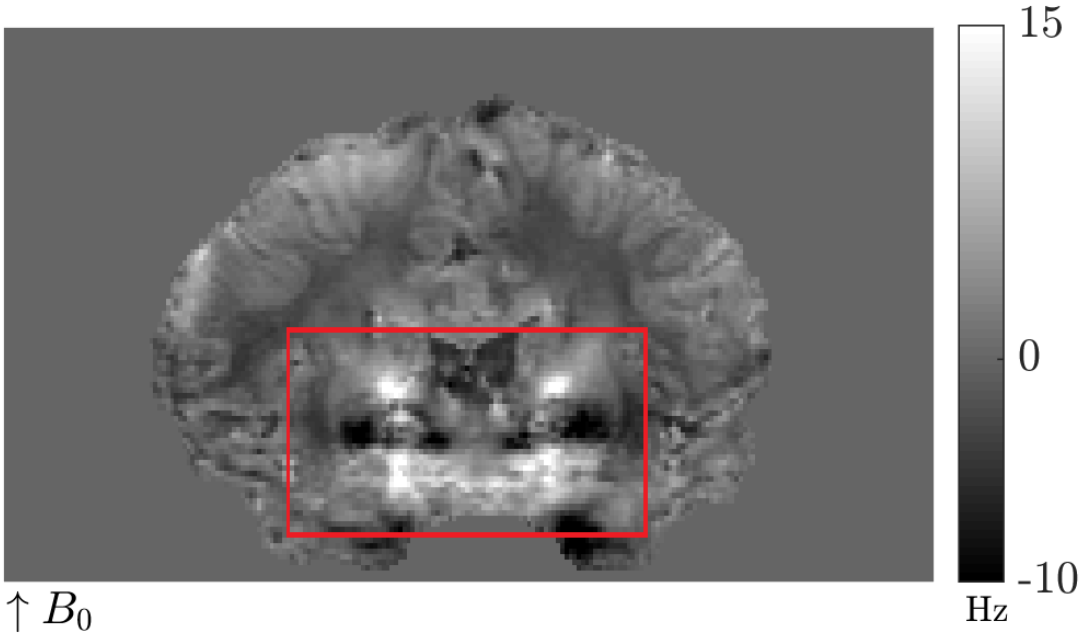
$$\frac{\Delta B(\vec{r})}{B_0} = \mathcal{F}^{-1}\left[d(\vec{k}) \cdot \mathcal{F}\left[\chi_I(\vec{r})\right]\right]. \tag{5.20}$$

Rearranging this yields:

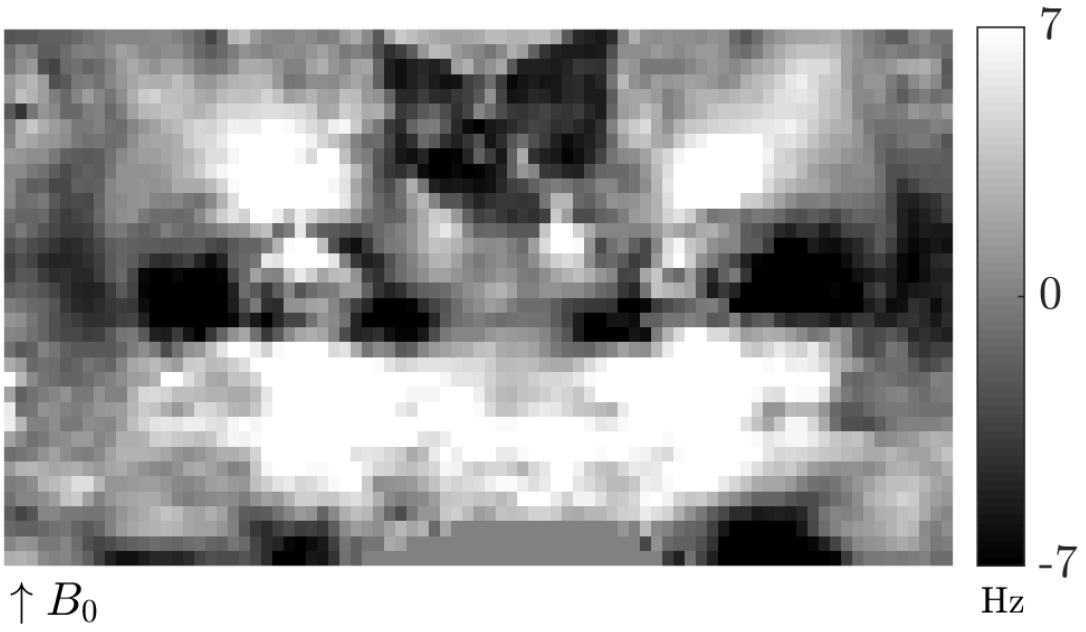
$$\chi_I(\vec{r}) = \mathcal{F}^{-1}\left[\frac{\mathcal{F}\left[\Delta B(\vec{r})\right]}{B_0 \cdot d(\vec{k})}\right]. \tag{5.21}$$

The form of $d(\vec{k})$ is known (Figure 4.5b) and $\Delta B(\vec{r})$ has been determined experimentally. Therefore by performing a Fourier transform operation on the experimental field perturbations, dividing by $B_0 \cdot d(\vec{k})$ and then taking the inverse Fourier transform, the underlying $\chi_I(\vec{r})$ distribution should be revealed. Figure 5.12a shows the results of applying this method to the field map depicted in Figure 5.2.

Examination of 5.12a reveals a problem. It is evident that this is not a local $\chi_I(\vec{r})$ map of the local field perturbations in Figure 5.2. The first assumption would be to consider that a mistake was made in the processing. However, reconstructing $\Delta B(\vec{r})$ from the $\chi_I(\vec{r})$ distribution in Figure 5.12a generates the $\Delta B(\vec{r})$ map in Figure 5.12b. This has a near identical form to Figure 5.2 (small errors generated due to the discrete nature of the fast Fourier transform algorithm). This implies

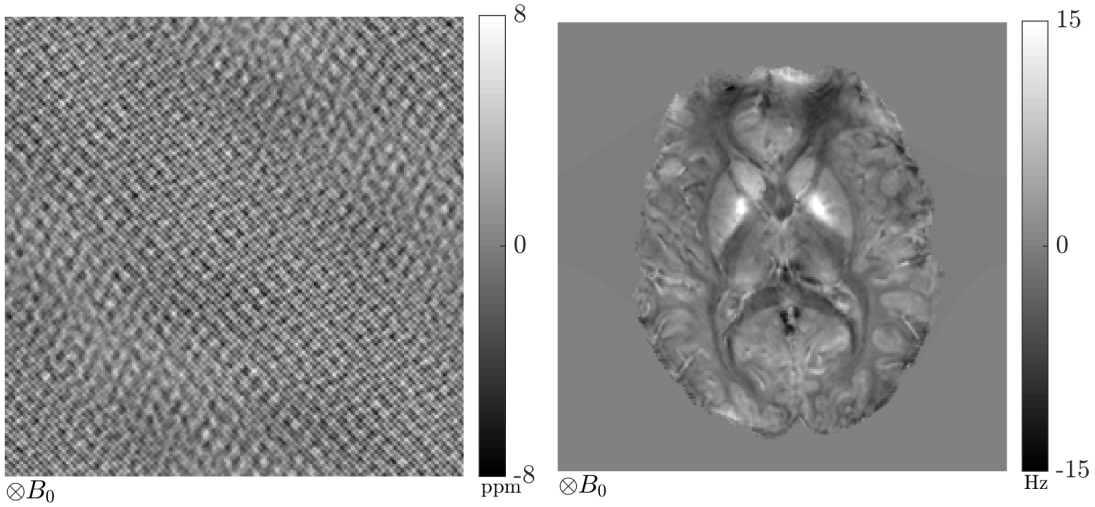



(a) $\Delta B(\vec{r})$




(b) $\Delta B(\vec{r})$ zoom

Figure 5.11: Coronal $\Delta B(\vec{r})$ map, generated from the *in-vivo* phase data presented in Figure 5.2 (Figure 5.11a), with the region within the red box highlighted in Figure 5.11b. The regions near the bottom of Figure 5.11a (globus pallidus and surrounding areas) show significant structural contrast. However when looking at these areas closely (Figure 5.11b), a large non-local dipole effect emerges from the regions, showing bright lobes vertically and dark lobes horizontally. These non-local field perturbations prevent field perturbation maps from revealing quantitative contrast. Experimental parameters outlined in Figure 5.1. Filtering protocol outlined in Figure 5.2.




(a) $\chi_I(\vec{r})$ (b) Reconstructed $\Delta B(\vec{r})$

Figure 5.12: $\chi_I(\vec{r})$ map generated via Equation 5.21 (Figure 5.12a) from the *in-vivo* phase data presented in Figure 5.2. Reconstructing $\Delta B(\vec{r})$ from Figure 5.12a generates Figure 5.12b.

that the $\chi_I(\vec{r})$ map in Figure 5.12a is a valid solution to Equation 5.21. So why does the $\chi_I(\vec{r})$ map look so poor? Is it representative of the underlying $\chi_I(\vec{r})$ distribution of a human brain?
Examining the form of $d(\vec{k})$:

$$d(\vec{k}) = \frac{1}{3} - \frac{k_z^2}{k^2} \tag{5.22}$$

it can be seen that when $\frac{k_z^2}{k^2} = \frac{1}{3}$, $d(\vec{k}) = 0$. This is visualised in Figure 5.13b, where 'cones' containing zero and near-zero values are observed in $d(\vec{k})$. Division by zero is not possible. In Figure 5.12a, $d(\vec{k})$ was discretized in such a way to avoid any voxels having a value exactly equal to zero. However, division by near-zero values can lead to huge amplification of noise present in $\Delta B(\vec{r})$, leading to errors in $\chi_I(\vec{r})$. This is known as an 'ill-posed' problem.

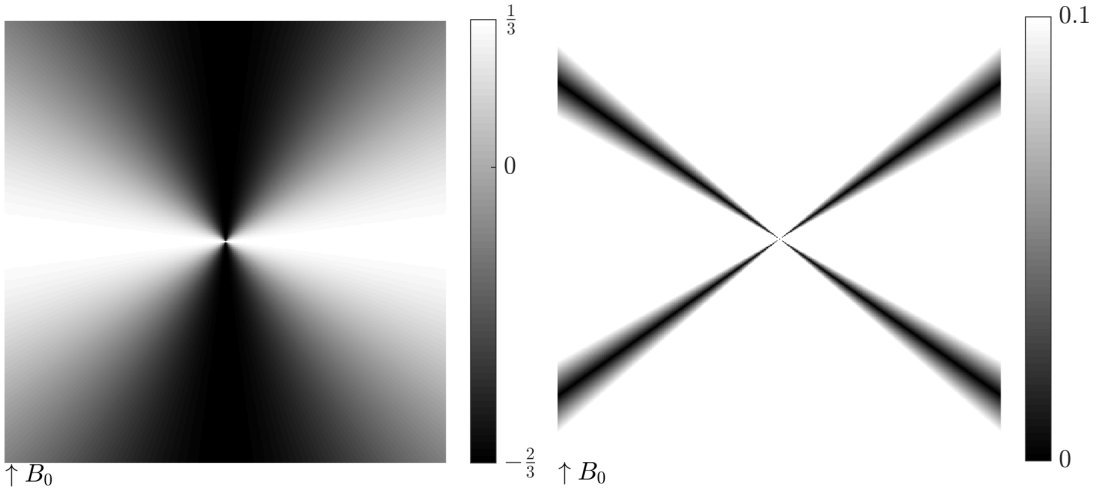
### 5.4.2 Ill-Posed Problems

The presence of zeros in $d(\vec{k})$ leads to an infinite number of possible $\chi_I(\vec{r})$ distributions that can generate the observed experimental field perturbations. This can be understood intuitively by considering the following problem:

$$3 \cdot x = 9. \tag{5.23}$$

The value of $x$ can be simply determined as equal to 3. Now consider the following problem

$$0 \cdot x = 0. \tag{5.24}$$




(a) $d(\vec{k})$ (b) $|d(\vec{k})|$ thresholded

Figure 5.13: The dipole field in $k$-space, $d(\vec{k})$ (Figure 5.13a), and the modulus of the dipole field in $k$-space, $|d(\vec{k})|$ (Figure 5.13b) thresholded between 0 and 0.1 to emphasise the 'cones' of near-zero values.

Any value of $x$ is a solution to the above equation. If a single, 'correct' value of $x$ exists, it cannot be determined using this information alone:

$$\begin{aligned} x &= \frac{0}{0} \\ &=? \end{aligned} \tag{5.25}$$

Equations 5.23 and 5.24 are known as forward problems, which can be generalised as:

$$\underline{\underline{A}}x = y \tag{5.26}$$

where $\underline{\underline{A}}$ is an operator matrix, $x$ is the input vector and and $y$ is the solution vector. The conversion $\chi_I(\vec{r}) \rightarrow \Delta B(\vec{r})$ is also a forward problem. Equation 5.25 is known as an inverse problem of the form:

$$x = \underline{\underline{A}}^{-1}y \tag{5.27}$$

where $\underline{\underline{A}}^{-1}$ is the inverse of $\underline{\underline{A}}$ and the conversion $\Delta B(\vec{r}) \rightarrow \chi_I(\vec{r})$ is an inverse problem. For an inverse problem to be 'well-posed' (as opposed to ill-posed), the matrix $\underline{\underline{A}}$ must be invertible. This requires the $\underline{\underline{A}}$ matrix to have no eigenvalues equal to zero.

In addition to being invertible the $\underline{\underline{A}}$ matrix must also be well-conditioned. Conditioning of the matrix is defined by its condition number $C$:

$$C = \frac{|\Lambda_{\max}|}{|\Lambda_{\min}|} \tag{5.28}$$

where $\Lambda_{\max/\min}$ are the maximum/minimum singular-values of $\underline{\underline{A}}^*\underline{\underline{A}}$, where $\underline{\underline{A}}^*$ is the conjugate-transpose of $\underline{\underline{A}}$. $C$ reflects the variation of function output relative

to the variation of function input. If the condition number is high, when solving the inverse problem small changes in the input matrix will lead to large changes in the output matrix. This is problematic when noise is considered, since when $C$ is high, small levels of noise in the input matrix will significantly alter the value of the output. By rewriting the $k$-space forward problem in a matrix-vector formalism for an N×N×N $\Delta B(\vec{r})$ matrix:

$$\begin{bmatrix} \Delta B(\vec{k})_{1,1,1} \\ \Delta B(\vec{k})_{1,1,2} \\ \Delta B(\vec{k})_{1,1,3} \\ \vdots \\ \Delta B(\vec{k})_{\mathrm{N,N,N}} \end{bmatrix} = \begin{bmatrix} d(\vec{k})_{1,1,1} & 0 & 0 & \cdots & 0 \\ 0 & d(\vec{k})_{1,1,2} & 0 & \cdots & 0 \\ 0 & 0 & d(\vec{k})_{1,1,3} & \cdots & 0 \\ \vdots & \vdots & \vdots & \ddots & \vdots \\ 0 & 0 & 0 & \cdots & d(\vec{k})_{\mathrm{N,N,N}} \end{bmatrix} \cdot \begin{bmatrix} \chi_I(\vec{k})_{1,1,1} \\ \chi_I(\vec{k})_{1,1,2} \\ \chi_I(\vec{k})_{1,1,3} \\ \vdots \\ \chi_I(\vec{k})_{\mathrm{N,N,N}} \end{bmatrix} \tag{5.29}$$

the $\underline{\underline{A}}$ matrix in the $k$-space forward problem is equivalent to a diagonal matrix of $d(\vec{k})$. Therefore each value of $|d(\vec{k})|$ represents a singular value of $\underline{\underline{A}}^*\underline{\underline{A}}$ and $C$ is infinite, as $d(\vec{k})$ contains zeros. Even if $d(\vec{k})$ could be made invertible by avoiding all values equal to zero via discretisation, the significant number of near-zero values generates a large $C$, ensuring that the inverse problem remains ill-posed and any small amount of noise existing in $\Delta B(\vec{r})$ will be hugely amplified in $\chi_I(\vec{r})$, as observed in Figure 5.12a. A significant amount of research has been directed towards finding successful ways to overcome the ill-posed nature of converting $\Delta B(\vec{r}) \rightarrow \chi_I(\vec{r})$. This has developed into the research field of Quantitative Susceptibility Mapping (QSM).

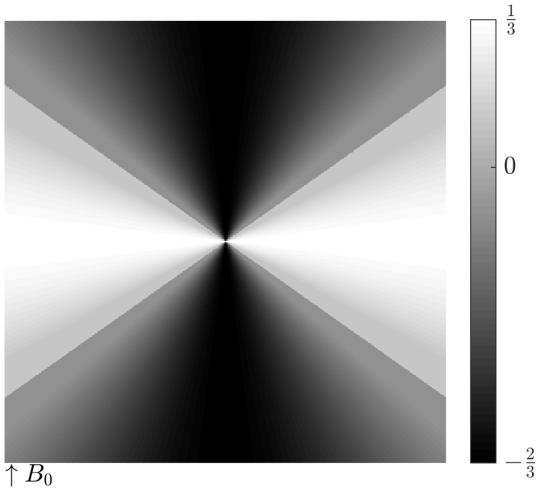
### 5.4.3 Direct Inversion Techniques

Direct inversion techniques utilise a form of truncated single value decomposition, which prevents the influence of zero or near-zero singular values from contributing significantly to inverse problems by setting all singular values below a certain threshold equal to the threshold, thus reducing the value of $C$:

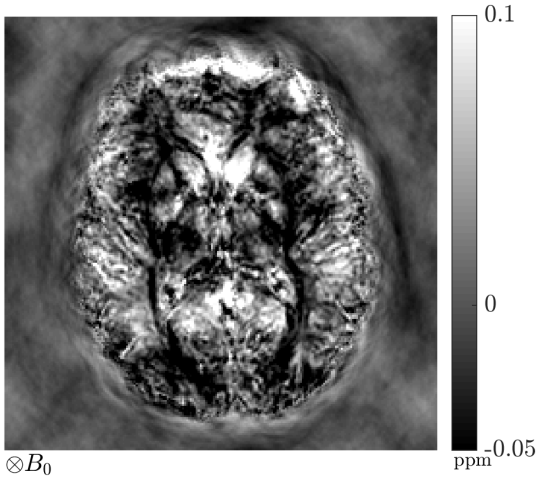
$$\Lambda_i = \begin{cases} \Lambda_i & \text{if } \Lambda_i \geq \Lambda_{\mathrm{thr}} \\ \Lambda_{\mathrm{thr}} & \text{otherwise} \end{cases} \tag{5.30}$$

where $\Lambda_{\mathrm{thr}}$ is a user defined threshold value. The first and most widely used method of truncated single value decomposition in QSM is known as the 'Thresholded $k$-space Division' (TKD) [22–24], where:

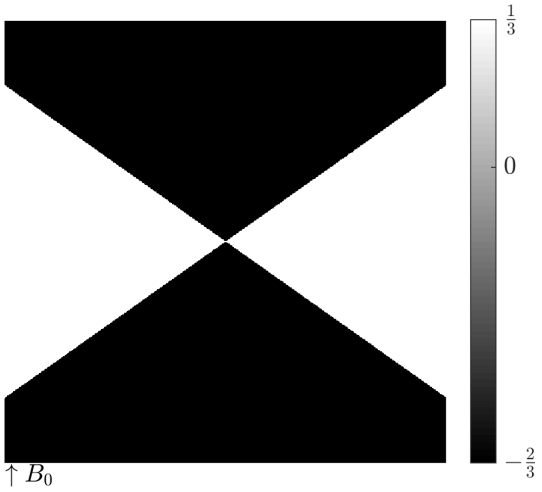
$$d(\vec{k}) = \begin{cases} \alpha_- & \text{if } d(\vec{k}) > \alpha_- \text{ and } d(\vec{k}) < 0 \\ \alpha_+ & \text{if } d(\vec{k}) \geq 0 \text{ and } d(\vec{k}) < \alpha_+ \\ d(\vec{k}) & \text{otherwise} \end{cases} \tag{5.31}$$



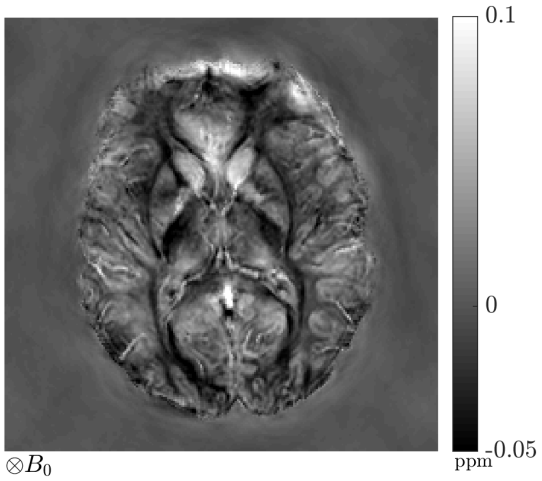

(a) Truncated $d(\vec{k})$ ($\alpha_{\pm} = \pm 0.1$)




(b) Reconstructed $\chi_I(\vec{r})$ ($\alpha_{\pm} = \pm 0.1$)




(c) Truncated $d(\vec{k})$ ($\alpha_{+/-} = +\frac{1}{3}/-\frac{2}{3}$)

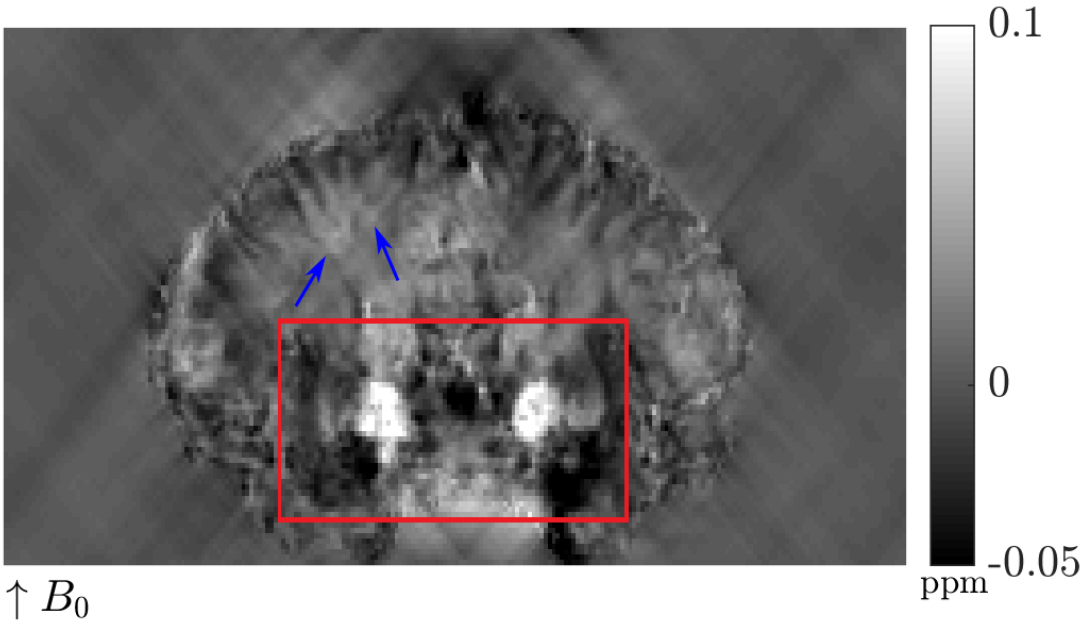



(d) Reconstructed $\chi_I(\vec{r})$ ($\alpha_{+/-} = +\frac{1}{3}/-\frac{2}{3}$)

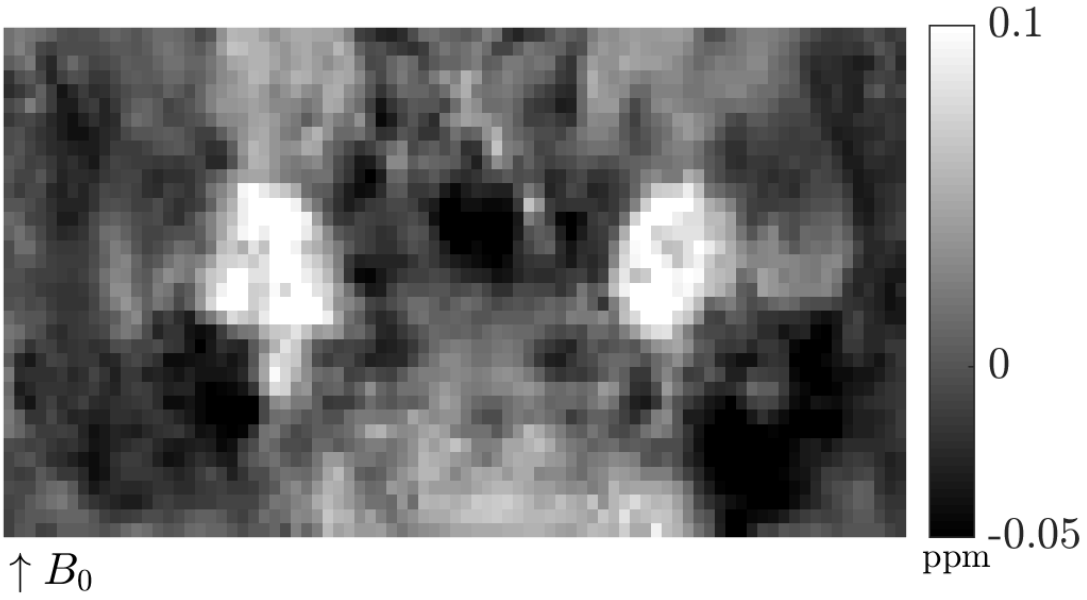
Figure 5.14: Modification of $d(\vec{k})$ (Figures 5.14a and 5.14c) via the TKD method as described in Equation 5.31. Figures 5.14b and 5.14d show the reconstructed $\chi_I(\vec{r})$ for the data in Figure 5.2 using both truncated forms of $d(\vec{k})$.

and $\alpha_{\pm}$ are user defined constants. An example of a TKD-modified $d(\vec{k})$ is shown in Figure 5.14a. The $\chi_I(\vec{r})$ map reconstructed from the field map shown in Figure 5.2 using this form of $d(\vec{k})$ is displayed in Figure 5.14b. It shows a remarkable improvement over the original direct inversion shown in Figure 5.12a, but still contains considerable noise artefacts. Following reference [24] and using the optimised $\alpha_+ = \frac{1}{3}$ and $\alpha_- = -\frac{2}{3}$ (Figure 5.14c), produces the $\chi_I(\vec{r})$ map shown in Figure 5.14d.

The TKD method can produce $\chi_I(\vec{r})$ maps quickly and effectively. However, streaking artefacts are observed within the $\vec{r}$-space images most evident in the coronal and sagittal image planes (example in Figure 5.15a). The TKD method will intrinsically induce streaking artefacts due to modification of the dipole field,




(a) $\chi_I(\vec{r})$




(b) $\chi_I(\vec{r})$ zoom

Figure 5.15: Coronal $\chi_I(\vec{r})$ map, generated from the $\Delta B(\vec{r})$ map in Figure 5.11a using TKD, with $\alpha_{+/-} = \frac{1}{3}/-\frac{2}{3}$ (Figure 5.15a), with the region within the red box highlighted in Figure 5.15b. Corresponding axial image shown in Figure 5.14d. In this orientation, the streaking artefacts from the truncated dipole field are more apparent (blue arrows). Comparing the zoomed $\chi_I(\vec{r})$ (Figure 5.15b) to the corresponding field perturbation map (Figure 5.11b), the non-local dipole field pattern has been removed, providing the experimenter with local $\chi_I(\vec{r})$ information. Experimental parameters outlined in Figure 5.1. Filtering protocol outlined in Figure 5.2.

even if the original data is noise- and artefact-free. However, as the modification is so simple to implement and only modifies the form of $d(\vec{k})$, at a minimum it is

an excellent comparison algorithm when performing a QSM study utilising a more complex algorithm.
Further details, including how to correct for the effective underestimation of $\chi_I(\vec{r})$ when performing TKD are discussed in [24]. Another excellent direct inversion algorithm for producing a (near) streak-free estimate of susceptibility is the fastQSM algorithm [25], which combines the principle of TKD with additional filtering and averaging.
The advantage of using $\chi_I(\vec{r})$ to quantify tissue properties can now be observed by comparing Figures 5.11b and 5.15b. In the $\chi_I(\vec{r})$ map, the non-local dipole field pattern has been removed, providing the experimenter with $\chi_I(\vec{r})$ information that can be considered more 'quantitative' as $\chi_I(\vec{r})$ values correspond to local properties of the individual voxels.

### 5.4.4 Multiple Orientation Sampling

By scanning an object at multiple orientations to the $\vec{B}_0$ field, sufficient sampling can be obtained of field perturbations over the zero and near-zero values of $d(\vec{k})$ to constrain the form of $\chi_I(\vec{r})$ and generate a well-posed problem with a unique solution. For different orientations to $\vec{B}_0$, $d(\vec{k})$ can be generalised as follows [26]:

$$d(\vec{k}) = \frac{1}{3} - \frac{k_{zp}^2}{k^2} \tag{5.32}$$

where $k_{zp}$ is the projection of the object's $\vec{k}$ coordinate onto $\vec{B}_0$. Assuming $\vec{B}_0$ is initially directed along the $z$-direction [23]:

$$d(k, \vec{\theta}, \phi) = \frac{1}{3} - \frac{\left(k_x \sin\phi - k_y \sin\theta \cos\phi + k_z \cos\theta \cos\phi\right)^2}{k^2} \tag{5.33}$$

where $\theta$ and $\phi$ are rotations around the $x$- and $y$-axes respectively. The $\underline{\underline{A}}$ matrix in Equation 5.29 can then be redefined as follows:

$$\underline{\underline{A}} = \begin{bmatrix} d(\vec{k},\theta_1,\phi_1)_{1,1,1} & 0 & 0 & 0 & 0 & \cdots & 0 \\ d(\vec{k},\theta_2,\phi_2)_{1,1,1} & 0 & 0 & 0 & 0 & \cdots & 0 \\ \vdots & \vdots & \vdots & \vdots & \vdots & \cdots & \vdots \\ d(\vec{k},\theta_S,\phi_S)_{1,1,1} & 0 & 0 & 0 & 0 & \cdots & 0 \\ 0 & d(\vec{k},\theta_1,\phi_1)_{1,1,2} & 0 & 0 & 0 & \cdots & 0 \\ 0 & d(\vec{k},\theta_2,\phi_2)_{1,1,2} & 0 & 0 & 0 & \cdots & 0 \\ \vdots & \vdots & \vdots & \vdots & \vdots & \cdots & \vdots \\ 0 & d(\vec{k},\theta_S,\phi_S)_{1,1,2} & 0 & 0 & 0 & \cdots & 0 \\ \vdots & \vdots & \vdots & \vdots & \vdots & \ddots & \vdots \\ 0 & 0 & 0 & 0 & 0 & \cdots & d(\vec{k},\theta_1,\phi_1)_{\mathrm{N,N,N}} \\ 0 & 0 & 0 & 0 & 0 & \cdots & d(\vec{k},\theta_2,\phi_2)_{\mathrm{N,N,N}} \\ \vdots & \vdots & \vdots & \vdots & \vdots & \cdots & \vdots \\ 0 & 0 & 0 & 0 & 0 & \cdots & d(\vec{k},\theta_S,\phi_S)_{\mathrm{N,N,N}} \end{bmatrix} \tag{5.34}$$

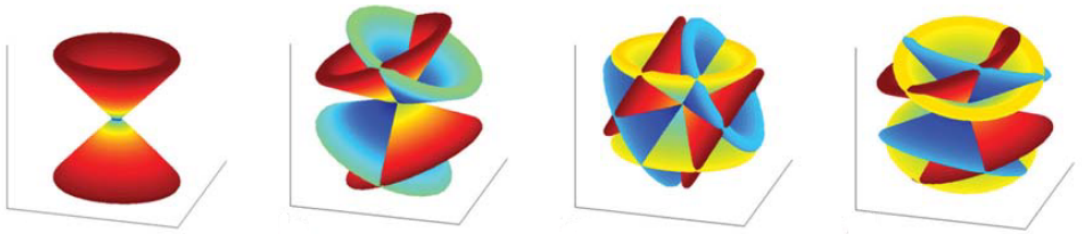
where $S$ is the number of sampled orientations. For a series of multiple-orientation scans [26]:

$$C = \frac{\max \sqrt{\sum_{s=1}^{S} d(\vec{k},\theta_s,\phi_s)^2}}{\min \sqrt{\sum_{s=1}^{S} d(\vec{k},\theta_s,\phi_s)^2}} \tag{5.35}$$

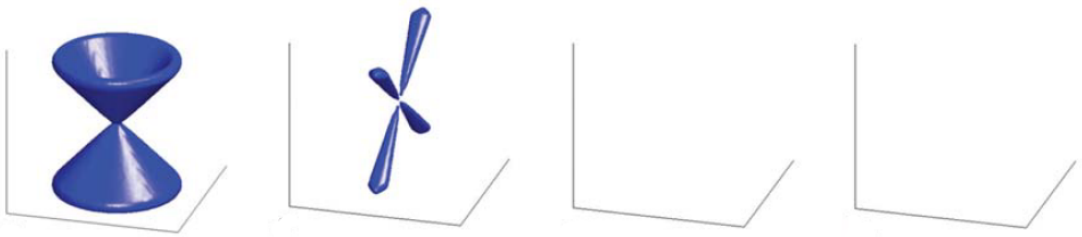
It has been determined that a minimum of three optimal orientations to $\vec{B}_0$ are required to generate a well-conditioned system [23, 26]. As the number of orientations increases, a more robust solution can be obtained. The method is known as Calculation of Susceptibility Through Multiple Orientation Sampling (COSMOS). A more intuitive way to understand this technique is shown in Figure 5.16.
There are however limitations to this technique:

1. The static $\vec{B}_0$ field cannot be rotated. This requires rotation of the object/subject within the bore to obtain scans with different orientations to $\vec{B}_0$. For *in-vivo* studies, this severely limits what is possible, due to both the rotation potential of the region of interest and the flexibility of the subject. However, for *ex-vivo* phantom studies, acquisitions at numerous angles to $\vec{B}_0$ can be simply performed, providing the phantom is not rotationally limited due to its size.

2. Acquiring scans at different orientations to $\vec{B}_0$ increases the amount of time required in the scanner by a factor equal to the number of orientations. This



(a) Near zero cones of $d(\vec{k})$



(b) Residual

Figure 5.16: 3D diagrams of the near-zero 'cone' of $d(\vec{k})$ (Figure 5.16a), with an increasing number of sampling orientations. As the number of orientations increases, the undersampled regions of the near-zero cone vanish. Image modified from [23].

increases the necessity for rapid acquisitions, which requires the development of optimised sequences, acceptance in reduction in scan quality, or both.

3. Any anisotropic susceptibility effects could reduce the accuracy of the obtained $\chi_I(\vec{r})$ map, as isotropy is assumed [27]. This is discussed further in Chapter 7.

Due to these limitations, COSMOS is most effective in phantom experiments without time restrictions. However, *in-vivo* experiments have also been performed [23, 28, 29] and COSMOS continues to be used as a 'gold standard' reference when developing single-orientation QSM methods.

### 5.4.5 Least Squares Minimisation with Regularisation

Current work in developing novel processing methods in single orientation QSM is focused on implementing iterative least squares minimisation algorithms to obtain $\chi_I(\vec{r})$. Least squares minimisations aim to solve the inverse problem $x = \underline{\underline{A}}^{-1}y$ by determining the form of $x$ that minimises:

$$\min_x \left\| \underline{\underline{A}}x - y \right\|_2^2 \tag{5.36}$$

where $\|...\|_2^2$ is the $l_2$ norm, defined as:

$$\|\underline{\underline{A}}x - y\|_2^2 = [\underline{\underline{A}}x - y]^*[\underline{\underline{A}}x - y] \tag{5.37}$$

If $\underline{\underline{A}}x = y$, $\|\underline{\underline{A}}x - y\|_2^2 = 0$ and the equation is minimised. By differentiating with respect to $x$, it can be determined that Equation 5.37 will be minimised when:

$$x = [\underline{\underline{A}}^* \underline{\underline{A}}]^{-1} \underline{\underline{A}}^* y \tag{5.38}$$

where $[\underline{\underline{A}}^* \underline{\underline{A}}]^{-1} \underline{\underline{A}}^*$ is known as the 'psuedoinverse'. In QSM the $l_2$ norm is is formed as:

$$\min_{\chi_I(\vec{r})} \left\| \underbrace{B_0 \cdot \mathcal{F}^{-1}\left[d(\vec{k}) \cdot \mathcal{F}\left[\chi_I(\vec{r})\right]\right]}_{\text{Equation 5.20}} - \Delta B(\vec{r}) \right\|_2^2 \tag{5.39}$$

defining the $\underline{\underline{A}}$ matrix as:

$$\underline{\underline{A}} = \underline{\underline{\mathrm{B_0} \mathcal{F}^{-1} \mathrm{D_k} \mathcal{F}}} \tag{5.40}$$

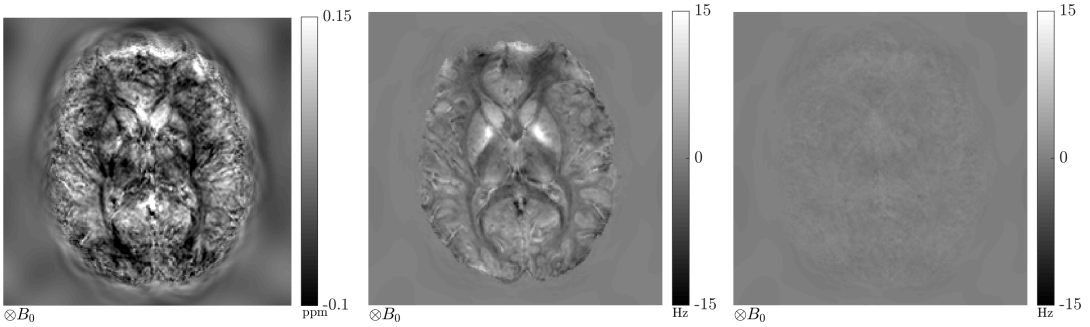
where $\underline{\underline{\mathrm{B_0}}}$ is the identity matrix scaled by $B_0$, $\underline{\underline{\mathcal{F}}}/\underline{\underline{\mathcal{F}}}^{-1}$ are the Fourier/inverse Fourier transform matrices respectively and $\underline{\underline{\mathrm{D_k}}}$ is a diagonal matrix with components of $d(k)$ along the diagonal (displayed in Equation 5.29). As $\underline{\underline{A}}$ is square, Equation 5.38 reduces to the direct inverse:

$$\chi_\mathrm{I} = [\underline{\underline{\mathrm{B_0} \mathcal{F}^{-1} \mathrm{D_k} \mathcal{F}}}]^{-1} \Delta \mathrm{B} \tag{5.41}$$

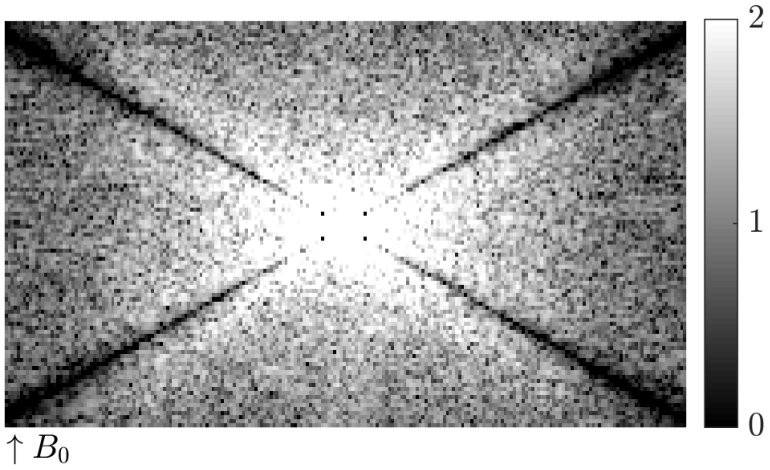
where $\chi_\mathrm{I}$ and $\Delta$B represent vectors of $\chi_I(\vec{r})$ and $\Delta B(\vec{r})$ respectively.
This minimisation is equivalent to the direct method introduced in Section 5.4.3. $\underline{\underline{A}}$ is still a non-invertible, ill-conditioned matrix. However, by using an iterative algorithm rather than a direct inversion to determine $\chi_I(\vec{r})$, $\underline{\underline{A}}^{-1}$ is never explicitly calculated. The process works as follows:

1. From a initial estimate of $\chi_I(\vec{r})$, calculate the matrix product $\underline{\underline{A}}\chi_\mathrm{I}$.
2. Subtract $\Delta$B from $\underline{\underline{A}}\chi_\mathrm{I}$ and determine the value of $\|\underline{\underline{A}}\chi_\mathrm{I} - \Delta\mathrm{B}\|_2^2$.
3. From the residual of $\|\underline{\underline{A}}\chi_\mathrm{I} - \Delta\mathrm{B}\|_2^2$, determine an improved estimate of $\chi_I(\vec{r})$ and repeat.

Conjugate gradient algorithms [30] are commonly utilised in QSM literature to obtain improved estimates of $\chi_I(\vec{r})$ to minimise the residual $\|\underline{\underline{A}}\chi_\mathrm{I} - \Delta\mathrm{B}\|_2^2$, typically via the computationally favourable LSQR algorithm [31]. As $\underline{\underline{A}}^{-1}$ is never explicitly formed, $\chi_I(\vec{r})$ can theoretically be obtained from the unmodified, non-invertable form of $d(\vec{k})$.
An example of the application of the minimisation algorithm is shown in Figure 5.17. For a low number of iterations/low tolerance threshold, the $\chi_I(\vec{r})$ map (Figure 5.17a) is more representative of the underlying anatomical structure compared to the direct inversion (Figure 5.12a), while maintaining an excellent fit to the experimental field perturbations (Figures 5.17b and 5.17c). However, the form of the




(a) $\chi_I(\vec{r})$ (b) $\Delta B_{\text{recon}}(\vec{r})$ (c) $\Delta B_{\text{recon}}(\vec{r}) - \Delta B(\vec{r})$




(d) $\chi_I(\vec{k})$

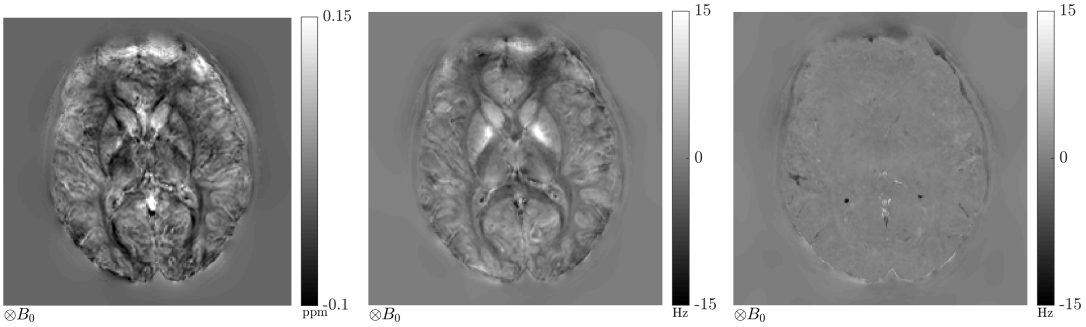
Figure 5.17: Application of the minimisation algorithm in Equation 5.39 to the $\Delta B(\vec{r})$ map in Figure 5.2. Minimisation performed using the LSQR algorithm in MATLAB (Release 2013a, The MathWorks Inc., Natick, MA, United States) restricted to 15 iterations and an initial estimate of $\chi_I(\vec{r}) = 0$. Figure 5.17a shows the generated $\chi_I(\vec{r})$ distribution, Figure 5.17b shows the reconstructed $\Delta B(\vec{r})$ map from $\chi_I(\vec{r})$, Figure 5.17c shows the residual from the original experimental data (relres = 0.20) and Figure 5.17d shows the corresponding $\chi_I(\vec{k})$ map of Figure 5.17a ($\log_{10}$ scale).

minimisation in Equation 5.39 is unregularised and still suffers from ill-posedness, as discussed earlier. Examination of Figure 5.17a reveals a difficult to interpret, noisy $\chi_I(\vec{r})$ distribution, which includes sources of $\chi_I(\vec{r})$ beyond the brain boundary. Examination of the corresponding $\chi_I(\vec{k})$ map (Figure 5.17d) reveals noisy, poorly defined $k$-space around the vicinity of $d(\vec{k}) = 0$. With an increased number of iterations and a reduced relative residual:

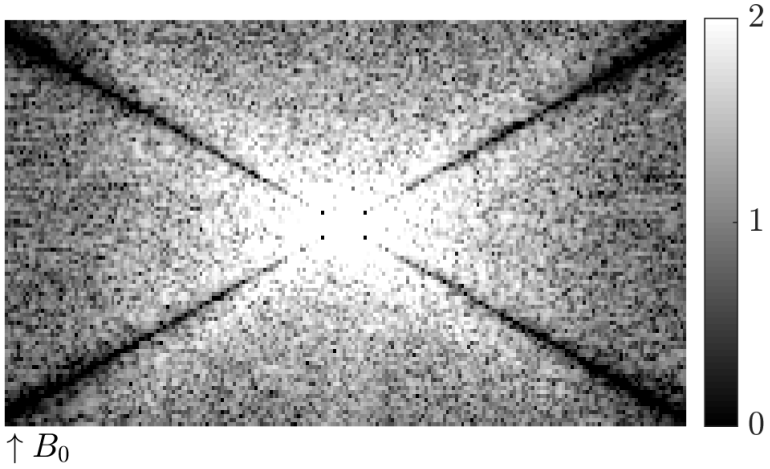
$$\text{relres} = \sqrt{\frac{\|A\chi_{\text{I}} - \Delta\text{B}\|_2^2}{\|\Delta\text{B}\|_2^2}} \tag{5.42}$$

the $\chi_I(\vec{r})$ map further deteriorates due to the noise sensitivity of the ill-posed problem.

Repeating this minimisation with an additional weighing matrix, the $\chi_I(\vec{r})$ map can be improved by applying greater weighting to regions with a high SNR, re-




(a) $\chi_I(\vec{r})$ (b) $\Delta B_{\text{recon}}(\vec{r})$ (c) $\Delta B_{\text{recon}}(\vec{r}) - \Delta B(\vec{r})$




(d) $\chi_I(\vec{k})$

Figure 5.18: Application of the minimisation algorithm in Equation 5.43 to the $\Delta B(\vec{r})$ map in Figure 5.2. Minimisation performed using the LSQR algorithm in MATLAB (Release 2013a, The MathWorks Inc., Natick, MA, United States) with 15 iterations and an initial estimate of $\chi_I(\vec{r}) = 0$. Figure 5.18a shows the generated $\chi_I(\vec{r})$ distribution, Figure 5.18b shows the reconstructed $\Delta B(\vec{r})$ distribution from $\chi_I(\vec{r})$, Figure 5.18c shows the residual from the original experimental data (relres = 0.20) and Figure 5.18d shows the $\chi_I(\vec{k})$ map of Figure 5.18a ($\log_{10}$ scale).

ducing the experimental noise contribution to the ill-posed problem. In this case, the following minimisation is performed [32] :

$$\min_{\chi_I(\vec{r})} \left\| \text{Mag}(\vec{r}) \cdot \left( B_0 \cdot \mathcal{F}^{-1} \left[ d(\vec{k}) \cdot \mathcal{F} \left[ \chi_I(\vec{r}) \right] \right] - \Delta B(\vec{r}) \right) \right\|_2^2 \tag{5.43}$$

where $\text{Mag}(\vec{r})$ is the corresponding magnitude data for the experimentally measured field perturbations. This is a good choice of weighting matrix as $\text{Mag}(\vec{r}) \propto$ SNR [33]. Results produced by Equation 5.43 are shown in Figure 5.18.
By weighting the fit to regions with higher SNR, a more robust $\chi_I(\vec{r})$ map is generated (Figure 5.18a), with less sensitivity to noise contained in the original $\Delta B(\vec{r})$ map. The reconstructed field perturbations (Figure 5.18b) maintain an excellent fit to the experimental data, (Figure 5.18c) while reducing the contribution of low

SNR components when compared to the unweighted form (Figure 5.17).
Though there is less contribution from low SNR components, the problem is still inherently ill-posed. Weighting the minimisation does not act to reduce the ill-posedness and $\chi_I(\vec{k})$ still reveals poorly defined $k$-space around the vicinity of $d(\vec{k}) = 0$ (Figure 5.18d), though the contribution is far less amplified compared to the unweighted version (Figure 5.17d). To reduce the fundamental ill-posedness of the problem, a regularisation term can be introduced in the minimisation of the form:

$$\min_x \left\{ \left\| \underline{\underline{A}} x - y \right\|_2^2 + \beta \left\| \underline{\underline{L}} x \right\|_2^2 \right\} \tag{5.44}$$

where $\underline{\underline{L}}$ is an operator matrix that is applied to $x$ and $\beta$ is a regularisation weighting coefficient. This is commonly referred to as Tikhonov regularisation [32] and can be interpreted as providing the minimisation algorithm with known properties of the solution to restrict the available results.
To understand the significance of regularisation an example will be presented. In the $\chi_I(\vec{r})$ maps shown in Figures 5.17a and 5.18a, it can be observed that $\chi_I$ sources exist beyond the brain boundary. From the previous discussion in Section 5.3.3, $\chi_I$ sources generating the $\Delta B(\vec{r})$ map in Figure 5.2 should be confined within a well defined ROI, here defined as lying within the brain boundary. If $\chi_I$ sources are restricted within the brain boundary, the determined $\chi_I(\vec{r})$ map may be more representative of the 'true' $\chi_I$ distribution. The following minimisation is performed:

$$\min_{\chi_I(\vec{r})} \left\{ \left\| \mathrm{Mag}(\vec{r}) \cdot \left( B_0 \cdot \mathcal{F}^{-1} \left[ d(\vec{k}) \cdot \mathcal{F} \left[ \chi_I(\vec{r}) \right] \right] - \Delta B(\vec{r}) \right) \right\|_2^2 + \beta^2 \left\| \mathrm{M_{inv}}(\vec{r}) \cdot \chi_I(\vec{r}) \right\|_2^2 \right\} \tag{5.45}$$

equivalent to Equation 5.43 with an additional regularisation term:

$$\beta^2 \left\| \mathrm{M_{inv}}(\vec{r}) \cdot \chi_I(\vec{r}) \right\|_2^2 \tag{5.46}$$

where $\mathrm{M_{inv}}(\vec{r})$ is the inverse of the brain mask:

$$\mathrm{M_{inv}}(\vec{r}) = \begin{cases} 1 & \text{outside brain} \\ 0 & \text{otherwise} \end{cases} \tag{5.47}$$

displayed in Figure 5.19. Examining Equation 5.45, it is determined that if $\beta > 0$, any source of $\chi_I$ generated in the region where $\mathrm{M_{inv}}(\vec{r}) = 1$ (henceforth known as $\chi_I(\mathrm{M_{inv}})$) will increase the value of the regularisation term. Therefore to minimise $\min_{\chi_I(\vec{r})}\{\ldots\}$, the optimal $\chi_I(\vec{r})$ map will balance the requirement of an appropriate form of $\chi_I(\vec{r})$ to simulate $\Delta B(\vec{r})$ with a form that minimises $\|\chi_I(\mathrm{M_{inv}})\|_2^2$. As $\beta \to \infty$, any $\chi_I$ source in the region where $\mathrm{M_{inv}} \neq 0$ will generate an infinitely

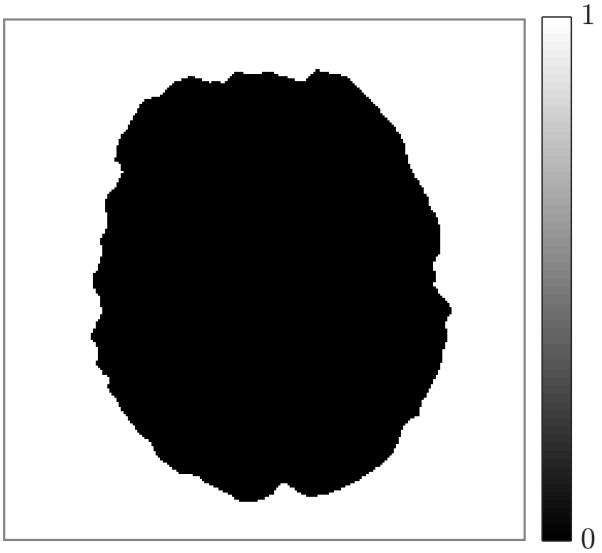
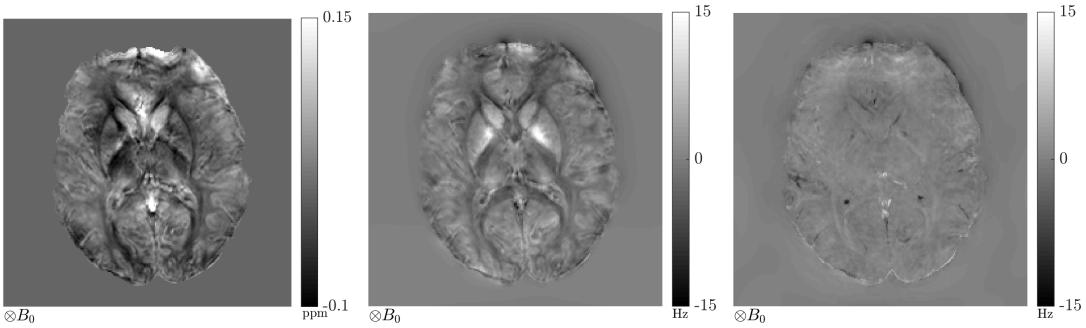
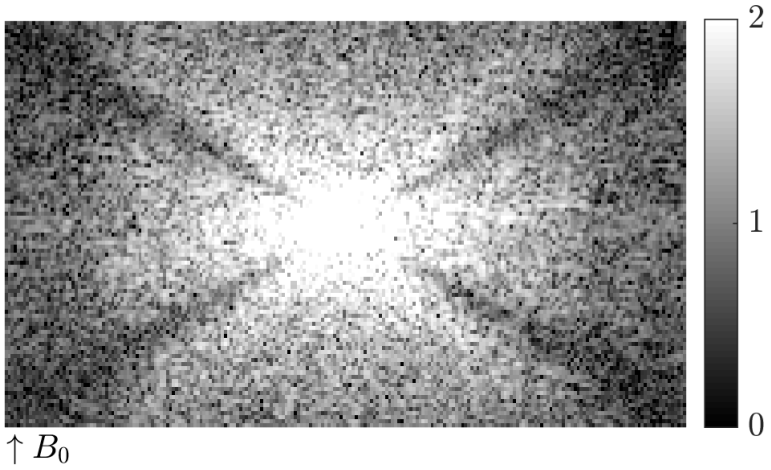



Figure 5.19: $M_{inv}(\vec{r})$.

high residual, preventing sources existing outside the brain.
An example of this is shown in Figure 5.20. Figure 5.20*a* shows a $\chi_I(\vec{r})$ distribution that is much more representative of the underlying brain structure. The reconstructed field perturbations (Figure 5.20b) have an increased residual compared to the unregularised solution (Figure 5.20c), but maintain good visual agreement. $\chi_I(\vec{k})$ reveals a more uniform $k$-space distribution around the vicinity of $d(\vec{k}) = 0$ (Figure 5.20d), indicating an improved implementation of the minimisation.
It is important to note that the regularisation above is not equivalent to obtaining an unregularised $\chi_I(\vec{r})$ map and subsequently multiplying the solution by a brain mask. Regularisation enforces a solution more representative of the underlying $\chi_I$ distribution by incorporating the properties *within* the minimisation. However, care must be taken when implementing these minimisation techniques and what properties are used for regularisation. In QSM, implementation of the mask [32] (described above) and gradient [29, 34] regularisation (described in the following experimental chapter in Section 6.5.3) are commonly utilised to generate $\chi_I(\vec{r})$ maps that are physically representative of the underlying $\chi_I$ distribution. However, minimisation algorithms are not sensitive to the difference between 'correct' and 'incorrect' regularisation priors. An example is shown in Figure 5.21, where regularisation was formed using the $M_{inv}$ mask shown in Figure 5.19 combined with an additional chequerboard pattern over the brain. Though the chequerboard pattern has no relationship to the underlying $\chi_I$ distribution, it will still be incorporated into the minimisation. Care must be taken to ensure priors are experimentally meaningful. Within this thesis, $\chi_I(\vec{r})$ maps (generated in experimental Chapters 6 and 9) utilise novel least-square minimisation algorithms to




(a) $\chi_I(\vec{r})$ (b) $\Delta B_{\text{recon}}(\vec{r})$ (c) $\Delta B_{\text{recon}}(\vec{r}) - \Delta B(\vec{r})$



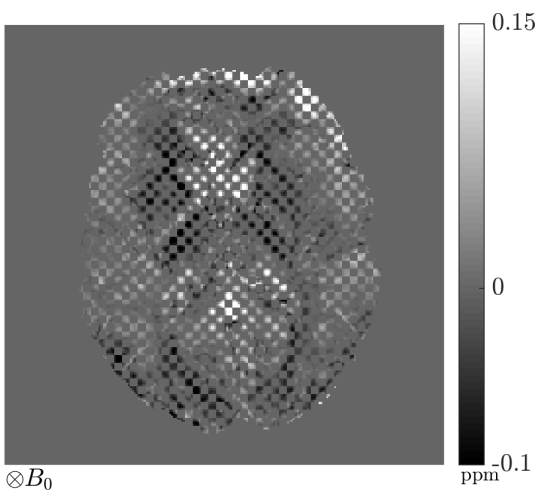

(d) $\chi_I(\vec{k})$

Figure 5.20: Application of the minimisation algorithm in Equation 5.45 to the $\Delta B(\vec{r})$ map in Figure 5.2, with $\beta = 10^8$. Minimisation performed using the LSQR algorithm in MATLAB (Release 2013a, The MathWorks Inc., Natick, MA, United States) with 15 iterations and an initial estimate of $\chi_I(\vec{r}) = 0$. Figure 5.20a shows the generated $\chi_I(\vec{r})$ distribution, Figure 5.20b shows the reconstructed $\Delta B(\vec{r})$ map from $\chi_I(\vec{r})$, Figure 5.20c shows the residual from the original experimental data (relres=0.43) and Figure 5.20d shows the $\chi_I(\vec{k})$ map of Figure 5.20a ($\log_{10}$ scale).

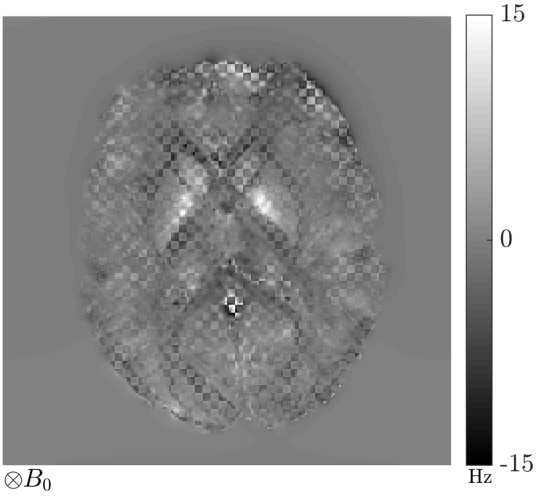
determine the underlying $\chi_I$ distributions. Details of the minimisations performed are described within the individual chapters.

## 5.5 Available Software

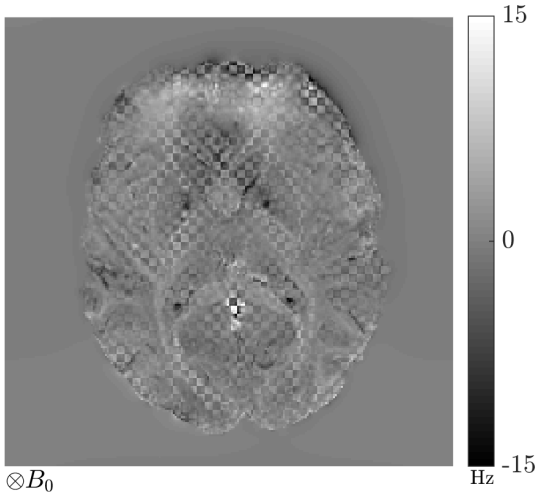
Due to the rapidly evolving field of QSM and the numerous advantages/disadvantages of different processing techniques, at present there is no consensus for the 'correct' method to generate quantitative susceptibility maps. However, some institutions have progressed in designing software packages to generate susceptibility maps from unprocessed phase data via a graphical user interface, enabling susceptibility maps to be generated without the requirement of significant knowledge of the underlying processing. The most notable of these are the MEDI toolbox [28] (Cornell



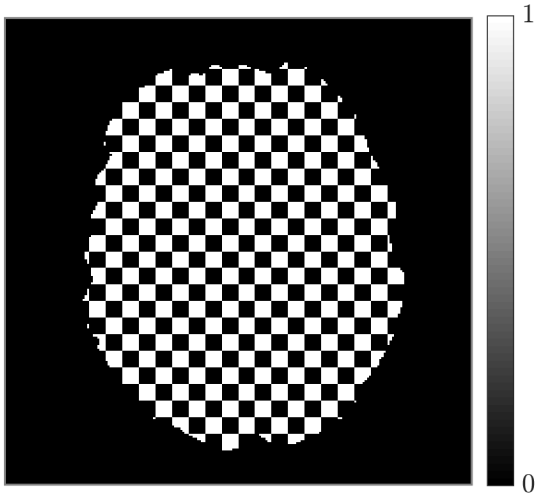

(a) $\chi_I(\vec{r})$




(b) $\Delta B_{\text{recon}}(\vec{r})$




(c) $\Delta B_{\text{recon}}(\vec{r}) - \Delta B(\vec{r})$




(d) $M_{\text{chequer}}$

Figure 5.21: Application of the minimisation algorithm in Equation 5.45 to the $\Delta B(\vec{r})$ map in Figure 5.2, where a chequerboard pattern has been incorporated into the regularisation mask, $M_{\text{inv}}$. Minimisation performed using the LSQR algorithm in MATLAB (Release 2013a, The MathWorks Inc., Natick, MA, United States) restricted to 15 iterations and an initial estimate of $\chi_I(\vec{r}) = 0$. Figure 5.21a shows the generated $\chi_I(\vec{r})$ distribution, Figure 5.21b shows the reconstructed $\Delta B(\vec{r})$ map from $\chi_I(\vec{r})$, Figure 5.21c shows the residual from the original experimental data, with relres = 0.64 and Figure 5.21d displays the chequerboard mask used in the minimisation.

MRI research lab) and STI suite [9] (Duke University School of Medicine), which provide a full QSM processing pipeline and the PRELUDE function [35] in the FSL toolbox [36] (FMRIB Oxford), which performs path-based phase unwrapping. At present all these packages are available freely online. However, though these software packages can provide a simple path to generate susceptibility maps, it is important to have a familiarity with the processing techniques utilised, to examine the outputs thoroughly and be familiar with the limitations of the methods

implemented. Furthermore, it is essential to check the unprocessed phase data obtained from the scanner before processing to ensure it is of the correct format, scaled between $\pm\pi$ and that if multiple channel receive coils are utilised, that the data has been combined correctly [37].

# Bibliography


[1] Pinar Senay Özbay, Andreas Deistung, Xiang Feng, Daniel Nanz, Jürgen Rainer Reichenbach, and Ferdinand Schweser. A comprehensive numerical analysis of background phase correction with V-SHARP. *NMR in Biomedicine*, 2016.

[2] Vyacheslav V Volkov and Yimei Zhu. Deterministic phase unwrapping in the presence of noise. *Optics letters*, 28(22):2156–2158, 2003.

[3] Dennis C Ghiglia and Mark D Pritt. *Two-dimensional phase unwrapping: theory, algorithms, and software*, volume 4. Wiley New York, 1998.

[4] S Moon-Ho Song, Sandy Napel, Norbert J Pelc, and Gary H Glover. Phase unwrapping of MR phase images using Poisson equation. *IEEE Transactions on Image Processing*, 4(5):667–676, 1995.

[5] Hussein S. Abdul-Rahman, Munther A. Gdeisat, David R. Burton, Michael J. Lalor, Francis Lilley, and Christopher J. Moore. Fast and robust three-dimensional best path phase unwrapping algorithm. *Appl. Opt.*, 46(26):6623–6635, Sep 2007.

[6] Marvin A Schofield and Yimei Zhu. Fast phase unwrapping algorithm for interferometric applications. *Optics letters*, 28(14):1194–1196, 2003.

[7] VV Volkov, Y Zhu, and M De Graef. A new symmetrized solution for phase retrieval using the transport of intensity equation. *Micron*, 33(5):411–416, 2002.

[8] Tian Liu, Cynthia Wisnieff, Min Lou, Weiwei Chen, Pascal Spincemaille, and Yi Wang. Nonlinear formulation of the magnetic field to source relationship for robust quantitative susceptibility mapping. *Magnetic resonance in medicine*, 69(2):467–476, 2013.

[9] Wei Li, Alexandru V Avram, Bing Wu, Xue Xiao, and Chunlei Liu. Integrated Laplacian-based phase unwrapping and background phase removal for

quantitative susceptibility mapping. *NMR in Biomedicine*, 27(2):219–227, 2014.

[10] Dong Zhou, Tian Liu, Pascal Spincemaille, and Yi Wang. Background field removal by solving the Laplacian boundary value problem. *NMR in Biomedicine*, 27(3):312–319, 2014.

[11] Hongfu Sun and Alan H Wilman. Background field removal using spherical mean value filtering and Tikhonov regularization. *Magnetic resonance in medicine*, 71(3):1151–1157, 2014.

[12] E Mark Haacke, Yingbiao Xu, Yu-Chung N Cheng, and Jürgen R Reichenbach. Susceptibility weighted imaging (SWI). *Magnetic resonance in medicine*, 52(3):612–618, 2004.

[13] John David Jackson. *Classical electrodynamics*. Wiley, 1999.

[14] Lin Li and John S Leigh. High-precision mapping of the magnetic field utilizing the harmonic function mean value property. *Journal of magnetic resonance*, 148(2):442–448, 2001.

[15] Ferdinand Schweser, Simon Daniel Robinson, Ludovic Rochefort, Wei Li, and Kristian Bredies. An illustrated comparison of processing methods for phase MRI and QSM: removal of background field contributions from sources outside the region of interest. *NMR in Biomedicine*, 2016.

[16] Ferdinand Schweser, Andreas Deistung, Berengar Wendel Lehr, and Jürgen Rainer Reichenbach. Quantitative imaging of intrinsic magnetic tissue properties using MRI signal phase: an approach to *in-vivo* brain iron metabolism? *Neuroimage*, 54(4):2789–2807, 2011.

[17] Wei Li, Bing Wu, and Chunlei Liu. Quantitative susceptibility mapping of human brain reflects spatial variation in tissue composition. *Neuroimage*, 55(4):1645–1656, 2011.

[18] Bing Wu, Wei Li, Arnaud Guidon, and Chunlei Liu. Whole brain susceptibility mapping using compressed sensing. *Magnetic resonance in medicine*, 67(1):137–147, 2012.

[19] Ferdinand Schweser, Andreas Deistung, and Jürgen R Reichenbach. Foundations of MRI phase imaging and processing for Quantitative Susceptibility Mapping (QSM). *Zeitschrift für Medizinische Physik*, 26(1):6–34, 2016.

[20] W Li, B Wu, and C Liu. iHARPERELLA: an improved method for integrated 3D phase unwrapping and background phase removal. In *Proc Int Soc Magn Reson Med*, volume 23, page 3313, 2015.

[21] Tian Liu, Ildar Khalidov, Ludovic de Rochefort, Pascal Spincemaille, Jing Liu, A John Tsiouris, and Yi Wang. A novel background field removal method for MRI using projection onto dipole fields. *NMR in Biomedicine*, 24(9):1129–1136, 2011.

[22] Karin Shmueli, Jacco A de Zwart, Peter van Gelderen, Tie-Qiang Li, Stephen J Dodd, and Jeff H Duyn. Magnetic susceptibility mapping of brain tissue *in-vivo* using MRI phase data. *Magnetic resonance in medicine*, 62(6):1510–1522, 2009.

[23] Sam Wharton, Andreas Schäfer, and Richard Bowtell. Susceptibility mapping in the human brain using threshold-based $k$-space division. *Magnetic resonance in medicine*, 63(5):1292–1304, 2010.

[24] Ferdinand Schweser, Andreas Deistung, Karsten Sommer, and Jürgen Rainer Reichenbach. Toward online reconstruction of quantitative susceptibility maps: superfast dipole inversion. *Magnetic resonance in medicine*, 69(6):1581–1593, 2013.

[25] Wei Li, Nian Wang, Fang Yu, Hui Han, Wei Cao, Rebecca Romero, Bundhit Tantiwongkosi, Timothy Q Duong, and Chunlei Liu. A method for estimating and removing streaking artifacts in quantitative susceptibility mapping. *Neuroimage*, 108:111–122, 2015.

[26] Tian Liu, Pascal Spincemaille, Ludovic de Rochefort, Bryan Kressler, and Yi Wang. Calculation of susceptibility through multiple orientation sampling (COSMOS): a method for conditioning the inverse problem from measured magnetic field map to susceptibility source image in MRI. *Magnetic Resonance in Medicine*, 61(1):196–204, 2009.

[27] Chunlei Liu. Susceptibility tensor imaging. *Magnetic resonance in medicine*, 63(6):1471–1477, 2010.

[28] Yi Wang and Tian Liu. Quantitative susceptibility mapping (QSM): decoding MRI data for a tissue magnetic biomarker. *Magnetic resonance in medicine*, 73(1):82–101, 2015.

[29] Ferdinand Schweser, Karsten Sommer, Andreas Deistung, and Jürgen Rainer Reichenbach. Quantitative susceptibility mapping for investigating subtle

susceptibility variations in the human brain. *Neuroimage*, 62(3):2083–2100, 2012.

[30] J. Nocedal and S. J. Wright. *Numerical Optimization*. Springer, 2nd edition, 2006.

[31] Christopher C Paige and Michael A Saunders. LSQR: An algorithm for sparse linear equations and sparse least squares. *ACM transactions on Mathematical Software*, 8(1):43–71, 1982.

[32] Ludovic de Rochefort, Tian Liu, Bryan Kressler, Jing Liu, Pascal Spincemaille, Vincent Lebon, Jianlin Wu, and Yi Wang. Quantitative susceptibility map reconstruction from MR phase data using bayesian regularization: validation and application to brain imaging. *Magnetic Resonance in Medicine*, 63(1):194–206, 2010.

[33] E Mark Haacke, Robert W Brown, Michael R Thompson, Ramesh Venkatesan, et al. *Magnetic resonance imaging: physical principles and sequence design*, volume 82. Wiley-Liss New York:, 1999.

[34] Tian Liu, Jing Liu, Ludovic de Rochefort, Pascal Spincemaille, Ildar Khalidov, James Robert Ledoux, and Yi Wang. Morphology enabled dipole inversion (MEDI) from a single-angle acquisition: comparison with COSMOS in human brain imaging. *Magnetic resonance in medicine*, 66(3):777–783, 2011.

[35] Mark Jenkinson. Fast, automated, N-dimensional phase-unwrapping algorithm. *Magnetic resonance in medicine*, 49(1):193–197, 2003.

[36] Mark Jenkinson, Christian F Beckmann, Timothy EJ Behrens, Mark W Woolrich, and Stephen M Smith. FSL. *Neuroimage*, 62(2):782–790, 2012.

[37] Simon Daniel Robinson, Kristian Bredies, Diana Khabipova, Barbara Dymerska, José P Marques, and Ferdinand Schweser. An illustrated comparison of processing methods for MR phase imaging and QSM: combining array coil signals and phase unwrapping. *NMR in Biomedicine*, 30(4), 2017.

# Chapter 6

# Establishing a Data Analysis Pipeline for *in-vivo* Quantitative Susceptibility Mapping in the Rodent Brain

## 6.1 Introduction

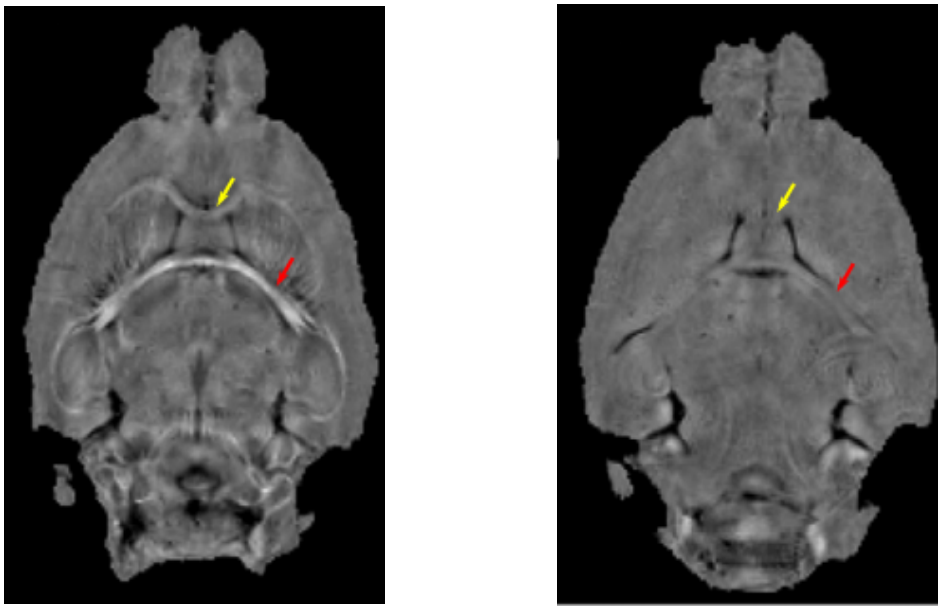
The project described in this chapter is part of a continuing collaboration between the Sir Peter Mansfield Imaging Centre (SPMIC), Cardiff University Brain Research Imaging Centre (CUBRIC - communication with Professor Derek Jones) and the Department of Neurobiology in Tel-Aviv University (communication with Dr Debbie Anaby), with the aim to examine neuroplasticity within rats. Neuroplasticity represents a change in the structural morphology of brain tissue induced by environmental reinforcement (e.g learning of a new skill [1]), physical adaptation due to tissue damage (e.g stroke [2]) or sensory loss [3], in addition to changes induced by the natural ageing process [4]. Recent studies involving diffusion tensor imaging (DTI) [5] have provided evidence that learning and memory tasks induce changes in white matter over short time periods in both humans [6] and rats [6, 7]. In both these studies, neuroplasticity was induced in rats by repeated training on the Morris water maze task [8], where rats are trained to swim towards a hidden platform in a pool of water.

In the collaborative project presented in this chapter, a similar training protocol was utilised. Over a period of five consecutive days, rats performed the Morris water maze task. Each day, the rats underwent two training sessions, each consisting of four attempts to find the hidden platform. On each of the four attempts, rats started the task at a different corner of the pool. If the platform was not found

after one minute, rats were guided to the platform.
Neuroplastic changes were examined via a multi-modal imaging approach, including DTI as per the previous studies [6, 7]. However, the distinction of this project compared to previous work is the additional utilisation of new techniques to examine the properties of white matter, including QSM (described in detail in Chapter 5), Composite Hindered and Restricted Model of Diffusion (CHARMED) imaging [9] and Magnetisation Transfer (MT) [10]. Rats were scanned before and immediately after the water maze training protocol was performed, with three rats scanned two-weeks after the water maze training protocol.
At the time of writing, the contribution from the SPMIC has been to design an analysis pipeline to obtain $\chi_I(\vec{r})$ and $R_2^*(\vec{r})$ maps from multi-echo GE *in-vivo* rat datasets obtained from the QSM scanning protocol. In this chapter the contribution from the SPMIC is described, detailing the analysis pipeline used to generate and optimise the $\chi_I(\vec{r})$ and $R_2^*(\vec{r})$ maps. In this chapter, field perturbations are described using the notation $\Delta f$ in units of Hz, defined as evolving *negatively* for a positive phase evolution as per the Bruker scanner's convention ($\phi = -2\pi\Delta f t$). Conversions can be performed using the information in Table 3.3.

## 6.2 Susceptibility as a Myelin Biomarker

Evidence suggests that myelin formation/reorganisation contributes to neuroplastic changes in learning [11] and QSM's sensitivity to myelin gives it great potential to examine neuroplasticity with high spatial resolution *in-vivo*. Myelin content is an important contributing factor to grey and white matter contrast in $\chi_I(\vec{r})$ maps, where contrast is hypothesised to be due to highly ordered, radially oriented lipid bilayers within the myelin sheath [12].
In a study involving dysmyelinating 'shiverer' mice [13] (characterised by a significantly reduced myelin content in white matter), little to no contrast was observed in $\chi_I(\vec{r})$ maps between grey and white matter compared to healthy controls (Figure 6.1). A second study involving shiverer mice [12] also showed a significant loss of susceptibility anisotropy (discussed in Section 7.1) compared to healthy controls, further supporting the hypothesis that white matter contrast in $\chi_I(\vec{r})$ maps is generated by lipid bilayers in the myelin sheath.
This evidence highlights the potential of QSM as a technique to investigate changes in myelination. White matter contrast in $\chi_I(\vec{r})$ maps appears sensitive to myelin content only [12, 13]. Rather than being a stand-alone technique, combining a QSM protocol with additional techniques sensitive to other white matter properties could provide complementary information to classify the underlying mecha-



(a) Control mouse

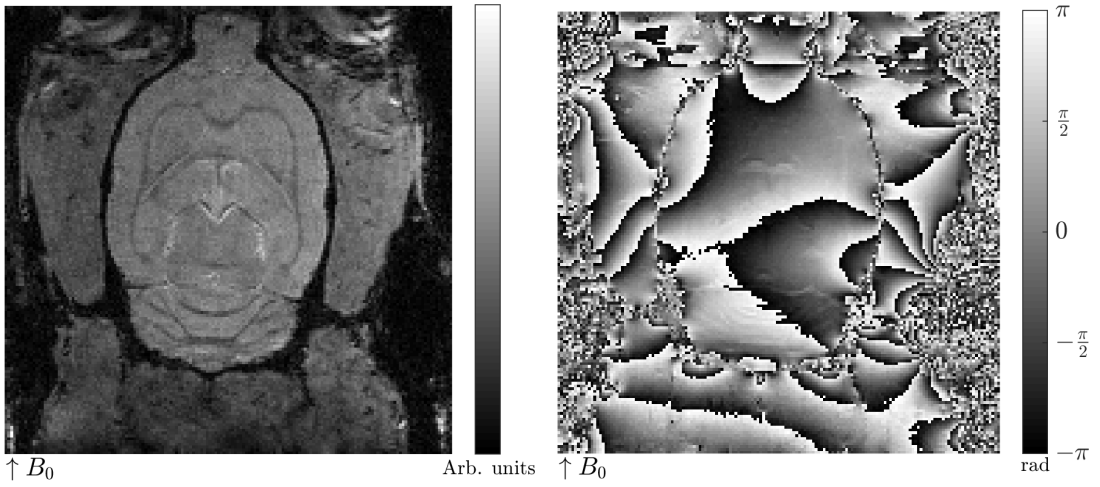
(b) Shiverer mouse

Figure 6.1: Quantitative susceptibility maps of an *ex-vivo* healthy, control mouse (Figure 6.1a) vs. an *ex-vivo* shiverer mouse (Figure 6.1b), with resolution of 0.086 mm$^3$. Note the loss of white matter/grey matter contrast over the corpus callosum (yellow arrow) and hippocampal commissure (red arrow). Image adapted from [13].

nisms of neuroplasticity. This could be theoretically achieved by using the multi-modal scanning protocol developed in this project.

## 6.3 Experimental Data Collection

Magnitude and phase data from the rat brain were collected *in-vivo* using a a multi-echo, GE sequence on a Bruker Biospec 70/30, 7T pre-clinical scanner (MGE sequence) at Tel-Aviv University. Each scan consisted of 8 echoes ($TE_1$=3.4 ms, $\Delta$TE=5.56 ms, $TE_8$=42.32 ms). Due to the multi-modal acquisition performed on each rat, sequences were optimised while minimising the acquisition time. A 3D volume, encompassing the entire brain was collected for each rat (resolution=0.185×0.185×0.370 mm$^3$, FOV =29.60×29.60× 11.84 mm$^3$, 32 slices consisting of 160×160 voxels), with TR=100 ms and flip angle=10°. Each dataset was collected in 510 s. At the time of writing, 13, 11 and 2 rats scanned before, after and two-weeks after performing the water maze task respectively have been analysed with this protocol. An example of unprocessed magnitude and phase data from a single rat is shown in Figure 6.2. The rats were additionally scanned via a three-shell CHARMED protocol (25 minutes for the acquisition) and a quantitative magnetisation transfer protocol including a $T_1$ mapping protocol (45 minutes




(a) $\mathrm{Mag}(\vec{r})$ (b) $\phi_{\mathrm{w}}(\vec{r})$

Figure 6.2: Unprocessed magnitude and phase data for the third-echo of a single *in-vivo* rat dataset. Experimental parameters outlined in Section 6.3.

for the acquisition), leading to a scan time of approximately 1.5 hours per rat. Rats were 3 months old when scanned.

## 6.4 Generating $R_2^*$ Maps

$R_2^*(\vec{r})$ maps were generated from the magnitude data by linearising the magnitude component of Equation 3.35:

$$\ln\left[\mathrm{Mag}(\vec{r})\right] = \ln\left|S_0(\vec{r})\right| - R_2^*(\vec{r}) \cdot \mathrm{TE} \tag{6.1}$$

where ln is the natural logarithm and $R_{2}* = \frac{1}{T_2^*}$. This can be rewritten in a voxelwise matrix formalism:

$$\underbrace{\begin{bmatrix} \ln \mathrm{mag}\,(\mathrm{TE}_1) \\ \ln \mathrm{mag}\,(\mathrm{TE}_2) \\ \vdots \\ \ln \mathrm{mag}\,(\mathrm{TE}_n) \end{bmatrix}}_{y} = \underbrace{\begin{bmatrix} 1 & \mathrm{TE}_1 \\ 1 & \mathrm{TE}_2 \\ \vdots & \vdots \\ 1 & \mathrm{TE}_n \end{bmatrix}}_{\underline{\underline{A}}} \cdot \underbrace{\begin{bmatrix} \ln|S_0| \\ -R_2^* \end{bmatrix}}_{x} \tag{6.2}$$

This formalism is identical to the forward problems discussed in Section 5.4.2 and $\ln|S_0(\vec{r})|$ and $R_2^*(\vec{r})$ are simply determined via multiplying both sides of Equation 6.2 by the inverse of the $\underline{\underline{A}}$ matrix for each voxel. As $\underline{\underline{A}}$ is noise-free and rectangular, it can be directly inverted using Equation 5.38 and as $\underline{\underline{A}}$ is small and identical for all voxels, this can be performed simultaneously on a full 3D dataset. Additional weighting of the linearised inversion as discussed in the previous chapter could have been implemented, including magnitude weighting to weight the fit to the

SNR of the experimental data. Though this would increase the time of analysis as $\underline{\underline{A}}$ would not be identical for every voxel (requiring analysis on a voxelwise basis), it can lead to improved fitting, particularly over regions of rapid $T_2^*$ decay.
The $R_2^*(\vec{r})$ protocol was entirely written in-house using MATLAB (Release 2013a, The MathWorks Inc., Natick, MA, United States). The matrix inversion was implemented via the MATLAB 'pinv' function. $R_2^*(\vec{r})$ maps for a single dataset recorded of a *in-vivo* rat brain (masked at the brain boundary) are shown in Figure 6.3.

## 6.5 Generating Isotropic Quantitative Susceptibility Maps

### 6.5.1 Phase Unwrapping

Experimental data was unwrapped using an echo-time based unwrapping technique. However, unlike the description in Section 5.2.2, $\Delta f(\vec{r})$ and $\phi_0(\vec{r})$ were calculated via a voxelwise fit to the the complex signal, $S(\vec{r})$.
In Section 5.2.2, it was discussed why it is not possible to perform a temporal unwrap to raw phase data via adding/subtracting values of $2\pi$, unless the data follow a certain 'ideal' form, free from phase wraps in the first echo and with phase evolution occurring at a rate below the Nyquist limit. However, a voxelwise iterative fit combined with an initial estimate $\Delta f(\vec{r})$ and $\phi_0(\vec{r})$ could provide a robust technique to unwrap data [14]. A protocol was implemented as follows:

1. A frequency estimate, $\Delta f_{\text{est}}(\vec{r})$, was obtained by obtaining the argument of the voxelwise complex division of the first two echoes:

$$\Delta f_{\text{est}}(\vec{r}) = \arg\left[\frac{e^{i\phi_{\text{w}}(\text{TE}_2,\vec{r})}}{e^{i\phi_{\text{w}}(\text{TE}_1,\vec{r})}}\right] \tag{6.3}$$

   followed by spatial unwrapping using a path-based unwrapping algorithm [15]. The unwrapped estimate was then scaled by $\frac{1}{2\pi\Delta\text{TE}}$ to convert it into $\Delta f_{\text{est}}(\vec{r})$.

2. The first echo, $\phi_{\text{w}}(\text{TE}_1,\vec{r})$, was spatially unwrapped using a path-based unwrapping algorithm [15]. A phase offset estimate, $\phi_{0_{\text{est}}}(\vec{r})$, was obtained by subtracting $2\pi\cdot\Delta f_{\text{est}}(\vec{r})\cdot\text{TE}_1$ from the spatially unwrapped first echo.

3. $S(\text{TE})$ was generated from experimental data:

$$S\left(\text{TE},\vec{r}\right) = \text{Mag}\left(\text{TE},\vec{r}\right)\cdot e^{i\phi_w(\text{TE},\vec{r})} \tag{6.4}$$

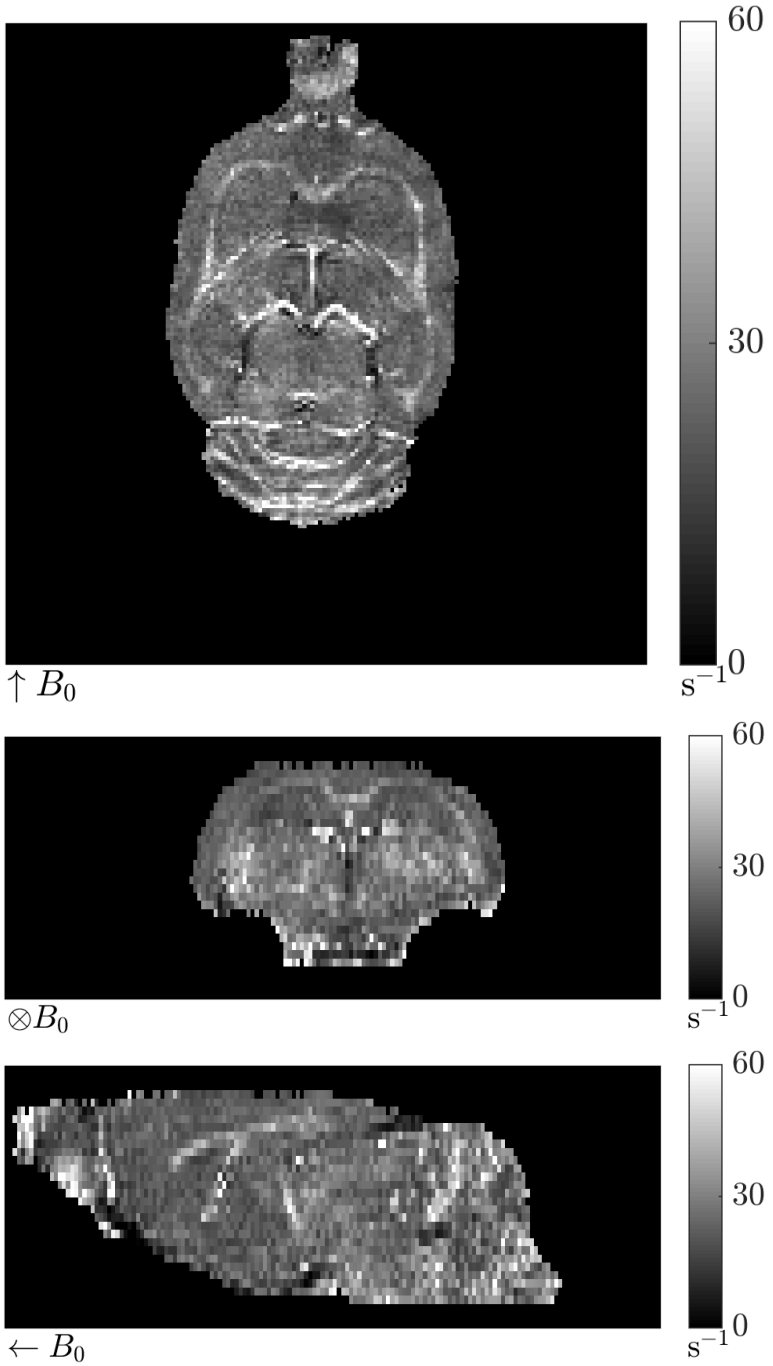
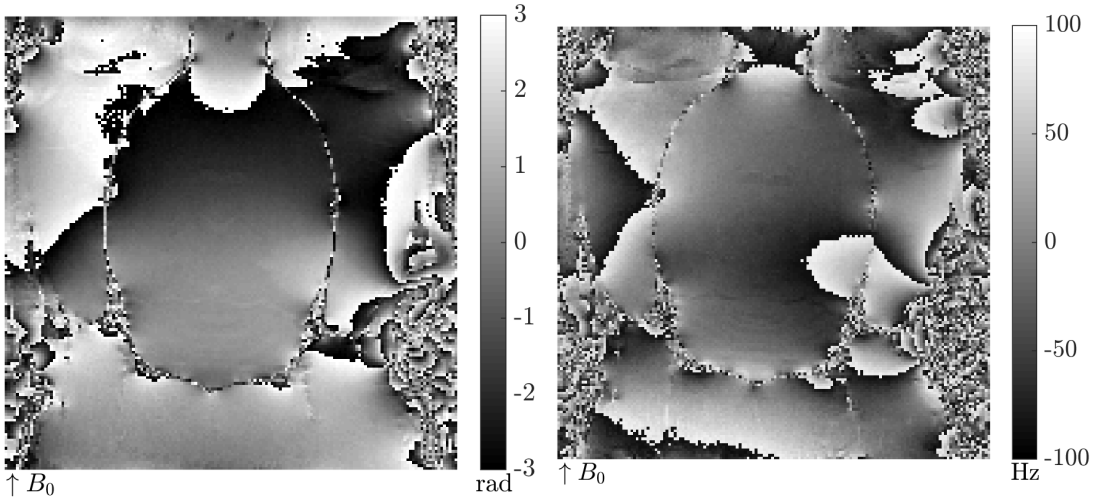



Figure 6.3: $R_2^*(\vec{r})$ maps for a single *in-vivo* rat brain in three planes. Protocol outlined in Section 6.4. Experimental parameters outlined in Section 6.3. Mask defined using protocol in Section 6.5.2.

where $\mathrm{Mag}(\mathrm{TE}, \vec{r})$ and $\phi_\mathrm{w}(\mathrm{TE}, \vec{r})$ are the measured signal magnitude and wrapped phase, respectively.

4. The measured complex signal was fitted to a simulated complex signal $S_\mathrm{sim}(\mathrm{TE}, \vec{r}) = \mathrm{mag}(\mathrm{TE}, \vec{r}) \cdot e^{i\left(\phi_0(\vec{r}) - 2\pi \cdot \Delta f(\vec{r}) \cdot \mathrm{TE}\right)}$ to determine $\phi_0(\vec{r})$ and $\Delta f(\vec{r})$ for the experimental data [14]. This was achieved using a voxelwise non-linear least-




(a) $\phi_{0_{\text{est}}}(\vec{r})$ (b) $\Delta f_{\text{est}}(\vec{r})$

Figure 6.4: Phase offset and frequency estimates for a single *in-vivo* data set obtained by applying an echo-time based unwrapping algorithm. Due to temporal phase evolution beyond the Nyquist limit, it is not possible to remove wraps, so as to estimate the phase offset and frequency. Experimental parameters outlined in Section 6.3.

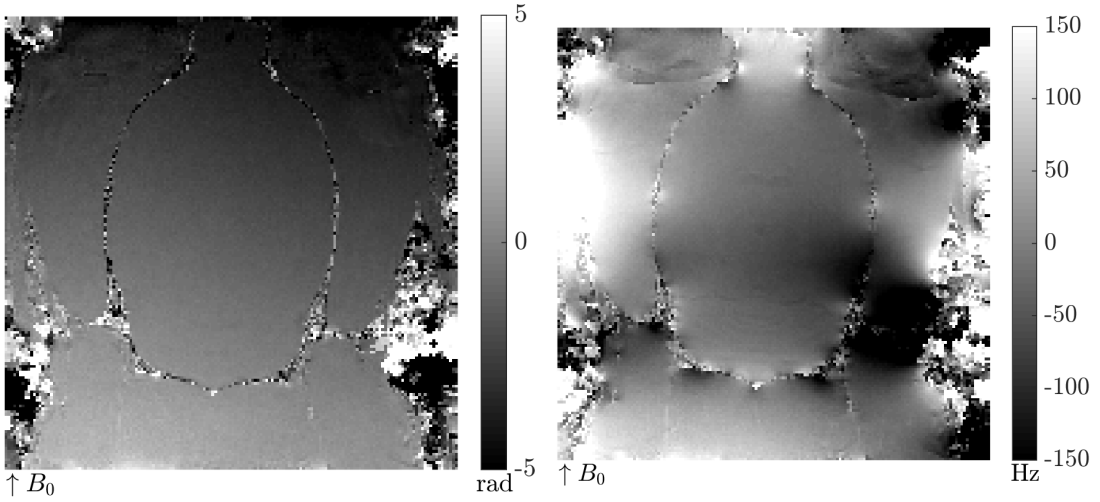
squares fitting algorithm, minimising the following problem:

$$\min_{\phi_0(\vec{r}),\Delta f(\vec{r})} \left\| \text{Mag}\left(\text{TE},\vec{r}\right) \cdot \left( S\left(\text{TE},\vec{r}\right) - S_{\text{sim}}\left(\text{TE},\vec{r}\right)\right)\right\|_2^2 \tag{6.5}$$

with $\phi_{0_{\text{est}}}(\vec{r})$ and $\Delta f_{\text{est}}(\vec{r})$ input as the initial estimates for $\phi_0(\vec{r})$ and $\Delta f(\vec{r})$ (details of the least squares minimisation are discussed in Section 5.4.5).

The unwrapping protocol was entirely written in-house using MATLAB (Release 2013a, The MathWorks Inc., Natick, MA, United States), apart from the path-based unwrapping algorithm [15] (code provided by original authors, adapted for use by the Medical Physics Group - FSU Jena). The non-linear least-squares fitting algorithm was implemented via the MATLAB 'lsqnonlin' function ('trust-region-reflective' algorithm, 10,000 iterations maximum, function tolerance = $10^{-4}$, step tolerance = $10^{-10}$) . Application of this protocol takes approximately five hours per 160×160×32 voxel dataset (32GB ram, 3.7GHz processor), when fitting to each voxel (tissue and background), individually.

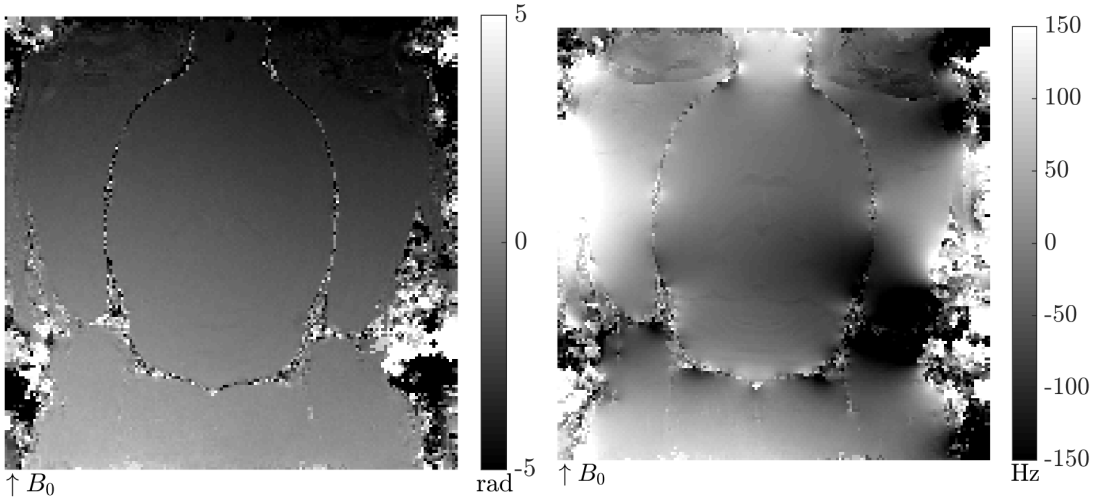
It is necessary to assess whether the estimates, $\phi_{0_{\text{est}}}(\vec{r})$ and $\Delta f_{\text{est}}(\vec{r})$, were sufficiently accurate to be used in the unwrapping protocol. Initial attempts to simply use an echo-time based unwrapping protocol as described in Section 5.2.2 to obtain $\phi_{0_{\text{est}}}(\vec{r})$ and $\Delta f_{\text{est}}(\vec{r})$ proved unreliable, failing to remove phase wraps as in many regions in the experimental data, phase evolved at a rate that was greater than the Nyquist limit (Figure 6.4). From the discussion in Section 5.2.3, path-based unwrapping can be challenging over 2D and 3D volumes, but is theoretically




(a) $\phi_{0_{\text{est}}}(\vec{r})$ (b) $\Delta f_{\text{est}}(\vec{r})$

Figure 6.5: Phase offset and frequency estimates for a single *in-vivo* data set, obtained by applying a path-based unwrapping algorithm [15]. Successful unwrapping over tissue-containing regions is observed. Experimental parameters outlined in Section 6.3.

achievable if Equation 5.6 is obeyed. The first two echoes in the data set used in the estimation protocol will have the lowest number of wraps. Equation 5.6 is more likely to be obeyed at these lower echo times and due to the low number of wraps, unwrapping will be simpler to perform. From examination of the obtained $\phi_{0_{\text{est}}}(\vec{r})$ and $\Delta f_{\text{est}}(\vec{r})$ maps, this method was successful in obtaining wrap-free estimates (example shown in Figure 6.5). Furthermore, as the voxelwise non-linear least squares minimisation in Equation 6.5 contains only two separable parameters, there is little computational challenge to obtain a robust calculation of $\phi_0(\vec{r})$ and $f(\vec{r})$. Therefore the estimate does not need to be precise, but sufficient to differentiate between Nyquist multiples of $\phi(\text{TE}, \vec{r})$ (example shown in Figure 5.4). Fitting to $S(\text{TE}, \vec{r})$ rather than $\phi_w(\text{TE}, \vec{r})$ significantly reduced the fitting error induced when using a least-squares fitting algorithm [14]. $S(\text{TE}, \vec{r})$ is not sensitive to wrapping as previously described in Equation 5.7. The least-squares fitting algorithm seeks to minimise the residual between $S(\text{TE}, \vec{r})$ and $S_{\text{sim}}(\text{TE}, \vec{r})$ (or $\phi_w(\text{TE}, \vec{r})$ and $\phi_{w_{\text{sim}}}(\text{TE}, \vec{r})$ for phase data), which is particularly problematic for $\phi_w(\text{TE}, \vec{r})$ when fitting to values near to $\pm\pi$, as small deviations of $\phi_0(\vec{r})$ and $\Delta f(\vec{r})$ can lead to large residual variations if wraps are generated. Furthermore, the noise distribution of $S(\text{TE}, \vec{r})$ follows a Gaussian distribution, while phase data has a more complicated noise behaviour [16] which creates further challenges in experimental fitting. By multiplying $S(\text{TE}, \vec{r})$ by the magnitude data, the residual is further weighted by the experimental SNR [17] and this provides the fit with a greater weighting of signal components with high SNR values. This is discussed in more detail in Section 5.4.5.




(a) $\phi_0(\vec{r})$ (b) $\Delta f(\vec{r})$

Figure 6.6: Phase offset and frequency perturbations calculated for a single *in-vivo* data set, obtained by applying Equation 6.5 to $S(\mathrm{TE}, \vec{r})$. Successful unwrapping over tissue-containing regions is observed, in addition to a significant increase in SNR compared to the initial estimate (Figure 6.5). Experimental parameters outlined in Section 6.3.

$\phi_0(\vec{r})$ and $\Delta f(\vec{r})$ calculated using this technique for a single data set are displayed in Figure 6.6. Results are consistent with the original estimate in Figure 6.5. However, a significant increase in SNR is observed compared to the initial estimates, as fitting was performed over eight echoes simultaneously. Examining the background-field-removed $\phi_0(\vec{r})$ and $\phi_{0_{\mathrm{est}}}(\vec{r})$ maps (details of background field removal protocol identical to those presented in the following section), with the assumption that $\phi_0(\vec{r})$ and $\phi_{0_{\mathrm{est}}}(\vec{r})$ maps should be homogeneous over tissue containing regions, the average decrease in the standard deviation of the fitted data was 25%, corresponding to a 33% increase in the SNR.

### 6.5.2 Background Field Removal

Background fields were removed using a Laplacian-based vSHARP filtering algorithm (described in Section 5.3.3), with $|\vec{r}_{\mathrm{max}}| = 6.5\,\mathrm{mm}$ and regularisation performed as a high-pass filter [18] (cut off frequency $= 0.003\,\mathrm{mm}^{-1}$). The ITK-SNAP Segment 3D tool [19] was used to generate brain masks, $\mathrm{M}(\vec{r})$ (example in Figure 6.7a).

After generating $\mathrm{M}(\vec{r})$, before performing vSHARP filtering, voxels containing unreliable phase, $\mathrm{M}_{\mathrm{un}}(\vec{r})$, were classified and removed. Firstly, the spatial variation of $\phi_0(\vec{r})$ was examined. In areas of reliable phase [20], $\phi_0(\vec{r})$ is expected to vary smoothly and voxels were considered unreliable if:

$$\left|\frac{\partial \phi_0}{\partial x}\right| + \left|\frac{\partial \phi_0}{\partial y}\right| + \left|\frac{\partial \phi_0}{\partial z}\right| \geq 4 \tag{6.6}$$



(a) $\mathrm{M}(\vec{r})$ (b) $\mathrm{M_{un}}(\vec{r})$ from $\phi_0(\vec{r})$ (c) $\mathrm{M_{un}}(\vec{r})$ from $R_2^*(\vec{r})$

Figure 6.7: Original mask (Figure 6.7a) generated using the ITK-SNAP Segment 3D tool [19] and voxels identified as having unreliable phase (Figures 6.7b and 6.7c). Experimental $\phi_0(\vec{r})$ and $\Delta f(\vec{r})$ maps for this data set shown in Figure 6.6. White voxels indicate the mask.

where the cut-off value was determined empirically (example in Figure 6.7b). Additionally, phase was empirically determined as unreliable in voxels where $R_2^* \geq 70\,\mathrm{s}^{-1}$ (example in Figure 6.7c).
The vSHARP protocol was written in-house using MATLAB (Release 2013a, The MathWorks Inc., Natick, MA, United States). Results of the vSHARP filtered data for a single rat brain are displayed in Figure 6.8.

### 6.5.3 Generation of Isotropic Susceptibility Maps

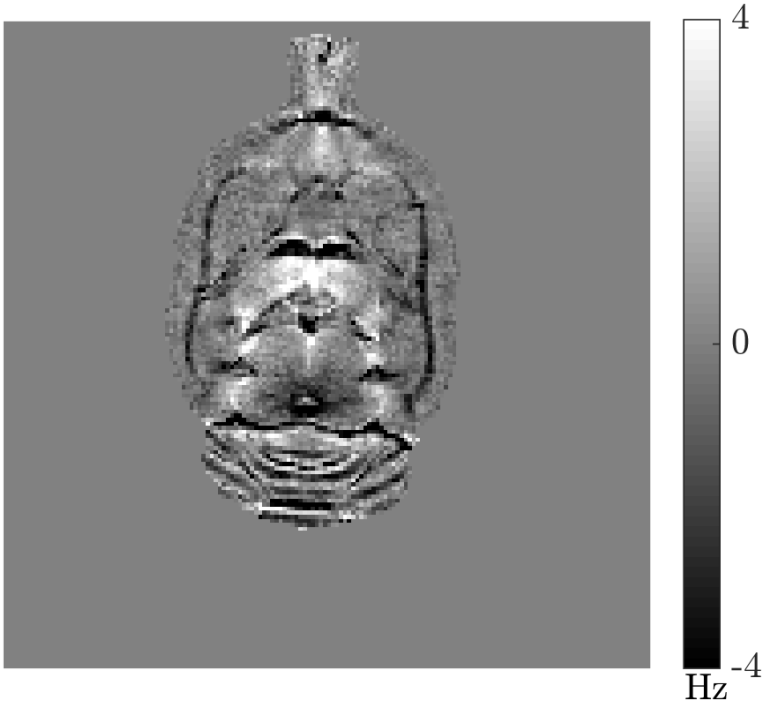
Frequency maps, $\Delta f_{\mathrm{filt}}(\vec{r})$, were first converted into ppm:

$$\Delta f_{\mathrm{ppm}}(\vec{r}) = \frac{\Delta f_{\mathrm{filt}}(\vec{r})}{B_0 \gamma_{^1\mathrm{H}} \cdot 10^6}. \tag{6.7}$$

Quantitative susceptibility maps were then obtained by using a magnitude-weighted least-squares minimisation, with regularisation provided by the mask and susceptibility gradient:

$$\min_{\chi_I(\vec{r})} \left( \left\| \mathrm{Mag}(\vec{r}) \left( f_0 \cdot \mathcal{F}^{-1} \left[ \mathcal{F} \left[ \chi_I(\vec{r}) \right] \cdot d(\vec{k}) \right] - \Delta f_{\mathrm{ppm}}(\vec{r}) \right) \right\|_2^2 + \beta_1^2 \left\| W_1(\vec{r}) \chi_I(\vec{r}) \right\|_2^2 + \sum_{l=1}^{3} \beta_2^2 \left\| W_{2l}(\vec{r}) \frac{\partial \chi_I(\vec{r})}{\partial l} \right\|_2^2 \right) \tag{6.8}$$

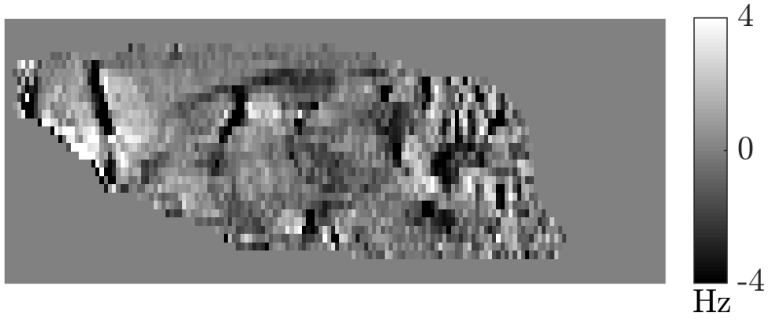
where $f_0 = \frac{\gamma B_0}{2\pi}$ is the resonance offset frequency, $\mathcal{F}/\mathcal{F}^{-1}$ are the Fourier/inverse Fourier transforms respectively, $\chi_I(\vec{r})$ is the isotropic susceptibility map (to be determined), $d(\vec{k})$ is the dipole field kernel, $W_1(\vec{r})$ is a mask of tissue outside the brain, $W_{2l}(\vec{r})$ represents the gradient regularisation masks ($l = 1, 2, 3$ corresponds




(a) $\Delta f_{\text{filt}}(\vec{r})$



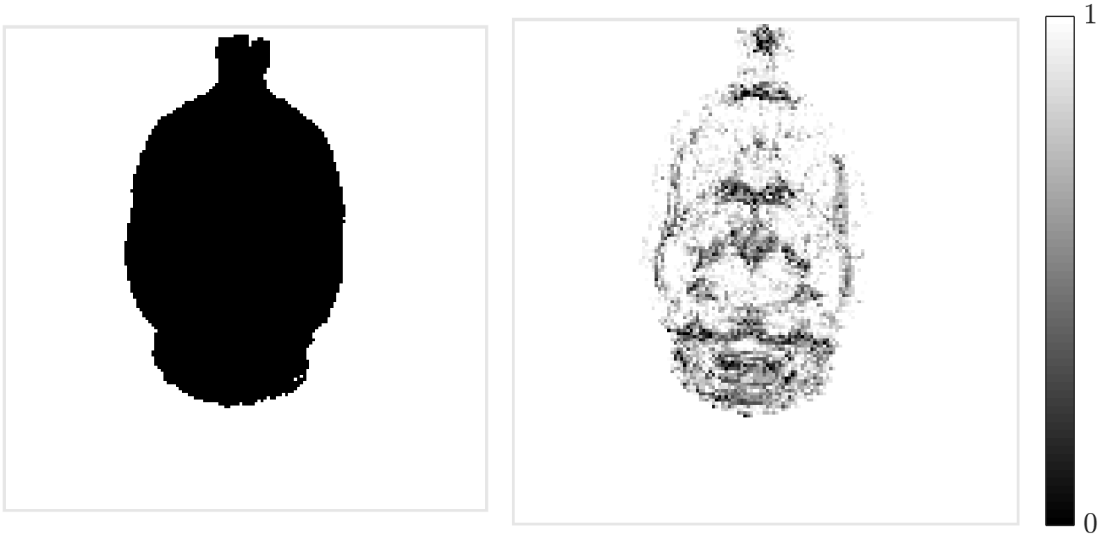

(b) $\Delta f_{\text{filt}}(\vec{r})$




(c) $\Delta f_{\text{filt}}(\vec{r})$

Figure 6.8: Filtered phase data for a single rat brain shown in three orthogonal planes. Protocol outlined in Section 6.5.2. Experimental $\phi_0(\vec{r})$ and $\Delta f(\vec{r})$ maps for this data set shown in Figure 6.6.

to directions $\hat{x}, \hat{y}$ and $\hat{z}$ respectively) and $\beta_{1,2}$ are regularisation weighting coefficients.




(a) $W_1(\vec{r})$

(b) $\sum_{l=1}^{3} \frac{W_{2l}(\vec{r})}{3}$

Figure 6.9: Weighting masks for susceptibility regularisation in Equation 6.8 for a single *in-vivo* rat brain. For visualisation purposes, $W_{2l}(\vec{r})$ is averaged over the $\hat{x}$, $\hat{y}$ and $\hat{z}$ directions. Scale identical for both images.

The first term in Equation 6.8 forms the standard minimisation required to generate susceptibility maps as discussed in Section 5.4.5. Magnitude and mask regularisation are also discussed in Section 5.4.5. $W_1(\vec{r})$ is displayed in Figure 6.9a, with $\beta_1$ set equal to $10^5$ to minimise the magnitude of the susceptibility sources external to the mask. The final term in Equation 6.8 is a gradient regularisation, designed to enforce constant susceptibility in regions where the mask $W_{2l}(\vec{r})$ is non-zero. In previous work [21] the gradient regularisation masks, $W_{2l}(\vec{r})$, were generated from the spatial gradients of the magnitude data. However, magnitude data does not display the same signal contrast as susceptibility maps and therefore will not have an identical gradient profile. This implies that magnitude data may not be the most suitable reference with which to weight the susceptibility gradient.

To provide a more suitable reference for regularisation, $W_{2l}(\vec{r})$ was generated from an estimated $\chi_I(\vec{r})$ map, achieved by performing the fastQSM protocol [22] on $\Delta f_{\text{ppm}}(\vec{r})$. fastQSM provides a smoothed estimate of a susceptibility map, $\chi_{\text{fastQSM}}(\vec{r})$, via direct-inversion and spatial filtering (details of direct inversion QSM discussed in Section 5.4.3). The gradient of $\chi_{\text{fastQSM}}(\vec{r})$, $\frac{\partial \chi_{\text{fastQSM}}(\vec{r})}{\partial l}$, should have a similar gradient profile to the underlying tissue susceptibility distribution and so forms a good choice of reference. $\frac{\partial \chi_{\text{fastQSM}}(\vec{r})}{\partial l}$ was calculated and subsequently low-pass filtered to reduce noise within the image. $W_{2l}$ was determined as

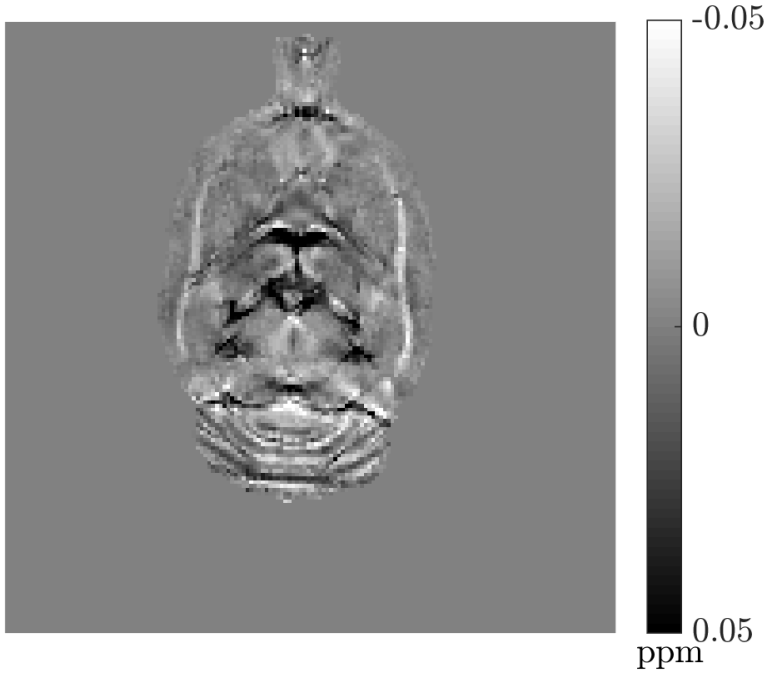
follows [22]:

$$W_{2l} = \begin{cases} 1 & \text{if } \left|\frac{\partial \chi_{\text{fastQSM}}(\vec{r})}{\partial l}\right| \leq G_{\min} \\ \left|\frac{G_{\max} - \frac{\partial \chi_{\text{fastQSM}}(\vec{r})}{\partial l}}{G_{\max} - G_{\min}}\right| & \text{if } G_{\min} < \left|\frac{\partial \chi_{\text{fastQSM}}(\vec{r})}{\partial l}\right| \leq G_{\max} \\ 0 & \text{otherwise} \end{cases} \tag{6.9}$$

where $G_{\min}$ and $G_{\max}$ were empirically determined as 0.010 and 0.034 respectively and $\beta_2$ was empirically determined as equal to 900 to give best results between gradient regularisation and minimisation, ensuring results were weighted towards the gradient but not over-smoothed. $W_{2l}$ is displayed in Figure 6.9b.
The minimisation algorithm was written in-house using MATLAB (Release 2013a, The MathWorks Inc., Natick, MA, United States) and implemented via the LSQR function (10 iterations maximum, tolerance = $10^{-6}$). $\chi_I(\vec{r})$ for a single rat brain in three orthogonal planes is shown in Figure 6.10, with Figures 6.12-6.14 showing single-plane $\chi_I(\vec{r})$ maps for all datasets. Over all the examined datasets, the minimisation returned relres = $0.68 \pm 0.06$ (defined in Equation 5.42) where $\pm$ indicates the standard deviation.

## 6.6 Discussion and Future work

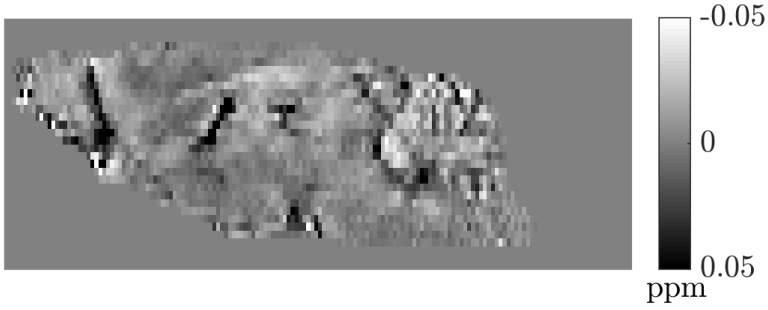
The generated $R_2^*(\vec{r})$ and $\chi_I(\vec{r})$ maps have been sent to the Department of Neurobiology in Tel-Aviv University and CUBRIC for analysis to investigate neuroplastic changes in the rat brain produced by the water-maze task. This will be achieved via examination of $R_2^*(\vec{r})$ and $\chi_I(\vec{r})$ values in white matter, along with data from the numerous other imaging modalities employed. At present, the data from the multi-modal acquisitions are being coregistered to a rat atlas and voxelwise comparisons are being performed for rats pre- and post-water maze task within white matter tissue. In addition, a tractography based analysis is being performed within the corpus callosum and the fornix of the individual rat brains between the different experimental groups. However, there are limitations that must be considered when performing this analysis for the $R_2^*(\vec{r})$ and $\chi_I(\vec{r})$ data.
Due to the challenges in scanning rodents *in-vivo* and the numerous imaging protocols being implemented, there were time limitations on the multi-echo GE scan, which restricted the accessible spatial resolution and SNR. As $R_2^*(\vec{r})$ maps are generated via a voxelwise inversion, lower resolution is not problematic beyond contrast limitations and partial volume effects. However, QSM is not a voxelwise process and currently ongoing work [23] indicates that increasing slice thickness can have a substantial impact on the root-mean-square error (RMSE) of $\chi_I$ values,




(a) $\chi_I(\vec{r})$



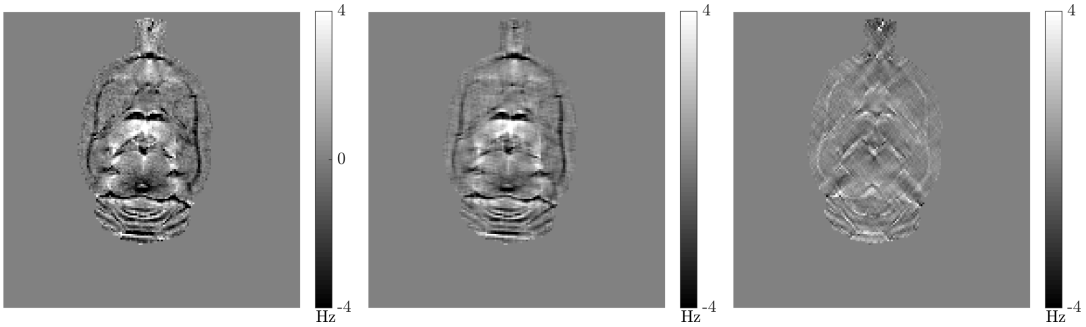

(b) $\chi_I(\vec{r})$




(c) $\chi_I(\vec{r})$

Figure 6.10: Obtained isotropic quantitative susceptibility maps for a single rat brain, shown in three orthogonal planes. Protocol outlined in Section 6.5.3. Experimental $\Delta f_{\text{filt}}(\vec{r})$ maps for this data set shown in Figure 6.8. Note that susceptibility scale is flipped so that more diamagnetic tissues appear bright.

with a higher RMSE on smaller susceptibility sources. In addition, an increased sensitivity to post-processing artefacts will exist within low-resolution, lower SNR




(a) $\Delta B(\vec{r})$ (b) $\Delta B_{\text{recon}}(\vec{r})$ (c) $\Delta B(\vec{r})$-$\Delta B_{\text{recon}}(\vec{r})$

Figure 6.11: Comparison of an experimentally generated $\Delta B(\vec{r})$ map (Figure 6.11a) with the reconstructed $\Delta B(\vec{r})$ map from the determined $\chi_I(\vec{r})$ distribution (Figure 6.11b) and subsequent difference (Figure 6.11c).

datasets, due to greater partial volume effects at the boundary of the ROI (discussed in Section 5.3.3) and a greater noise contribution.

Furthermore, $\chi_I(\vec{r})$ and $R_2^*(\vec{r})$ maps are being generated in this project without consideration of other potential sources of signal contrast. In white matter there is significant evidence that susceptibility is anisotropic [24, 25] (discussed in detail in Section 7.1), which implies that the white matter susceptibility has an orientation dependence. Evidence also exists for $R_2^*$ anisotropy in white matter [26, 27]. Additionally, chemical exchange contributions, hypothesised to exist within white matter [28, 29] can modify the phase contrast (discussed in detail in Section 7.2). Current arguments about microstructure content indicate that the non-spherical susceptibility inclusions in white matter will require greater consideration when describing the underlying susceptibility distribution [30, 31] (discussed in detail in Section 7.3). Finally, non-linear phase evolution due to signal compartmentalisation [32, 33] can modify the observed magnetic properties of tissue as TE is varies (discussed in detail in Section 7.4), though this was not observed within the experimental multi-echo GE data (hence fitting was restricted to a single-exponential model of signal evolution). Incorrect values of $\chi_I(\vec{r})$ may be obtained due to the impact of these additional phase contributions. Examination of the residual of the reconstructed $\Delta B(\vec{r})$ maps from the determined $\chi_I(\vec{r})$ distributions, $\Delta B_{\text{recon}}(\vec{r})$ (example in Figure 6.11), reveals residuals and reconstruction artefacts surrounding white matter tracts. This combined with the large relres value obtained from the least-squares minimisation is suggestive of additional sources of field perturbations that cannot be described with a model of $\chi_I(\vec{r})$.

Finally, consideration of a reference susceptibility value, $\chi_{I_{\text{ref}}}$ has not been applied within this data analysis. The question of susceptibility referencing is an ongoing debate in the field of QSM. Due to contrast limitations, it would be challenging

here to select a clearly defined region to act as a susceptibility reference. In this work, $\chi_{I_{\text{ref}}}$ has been taken as the average susceptibility value within the entire tissue. Therefore when comparing experimental datasets, it must be ensured that apparent susceptibility variations are not being induced by changes in the value of $\chi_{I_{\text{ref}}}$.

Knowledge of these limitations requires careful consideration when analysing the susceptibility data for this study. To define the susceptibility values in this project as 'quantitative' and to interpret susceptibility changes in white matter tracts before and after the water maze task as evidence of neuroplasticity must be questioned thoroughly. With further discussion with collaborators and careful future analysis, work will continue to quantify the results appropriately.

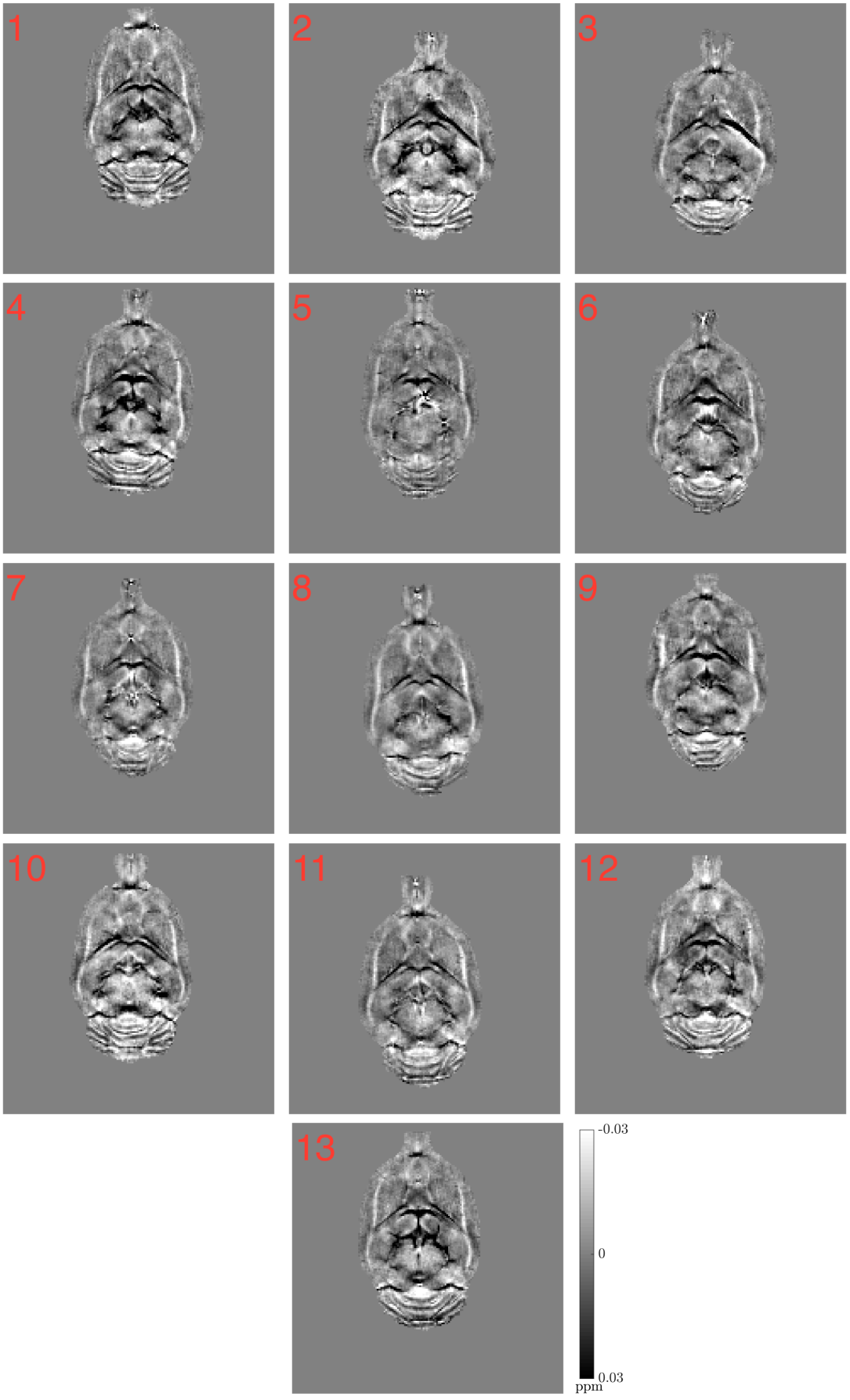



Figure 6.12: Isotropic quantitative susceptibility maps for all rat brains pre-water-maze task. Numbers correspond to matching animals.

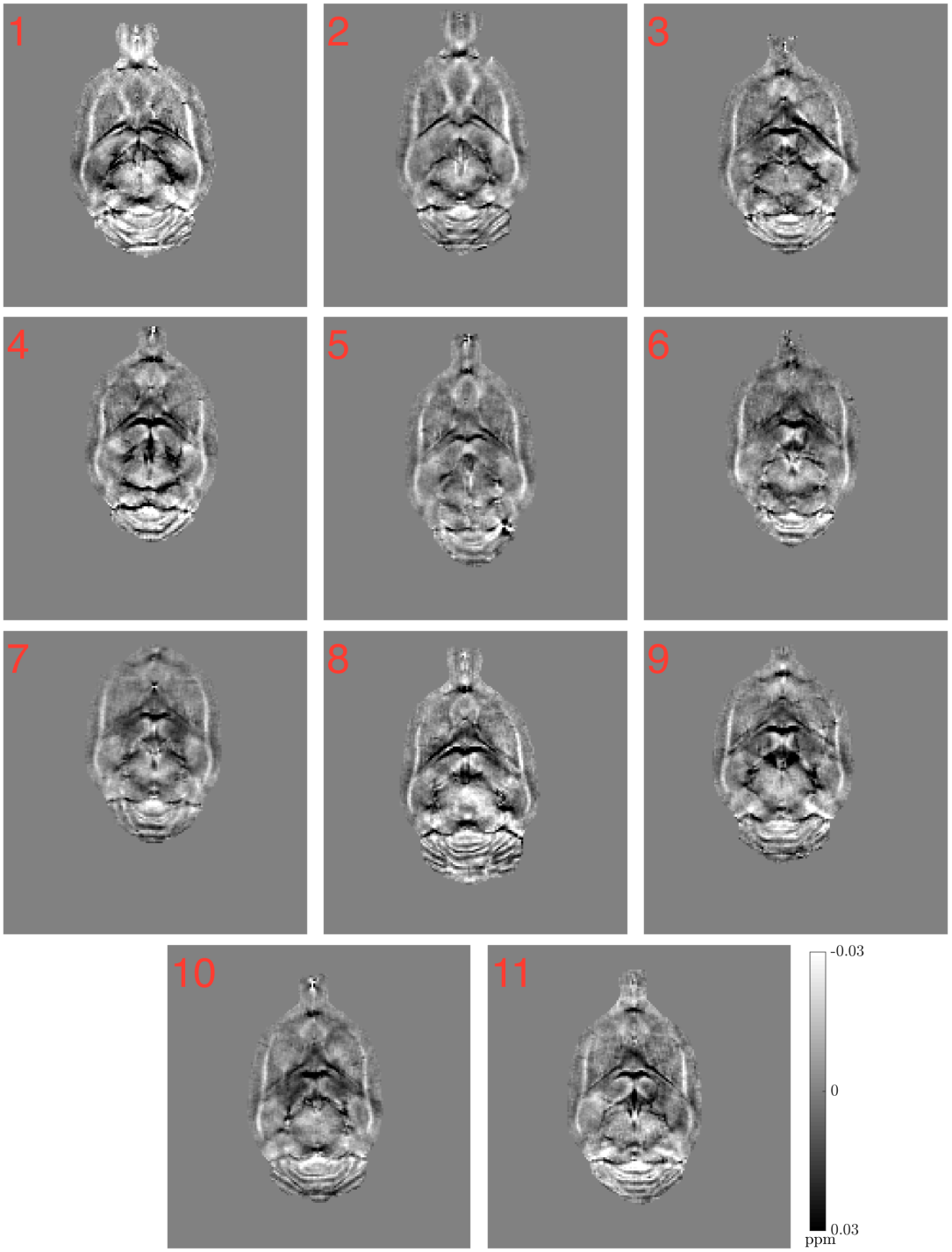



Figure 6.13: Isotropic quantitative susceptibility maps for all rat brains post-water-maze task. Numbers correspond to matching animals.

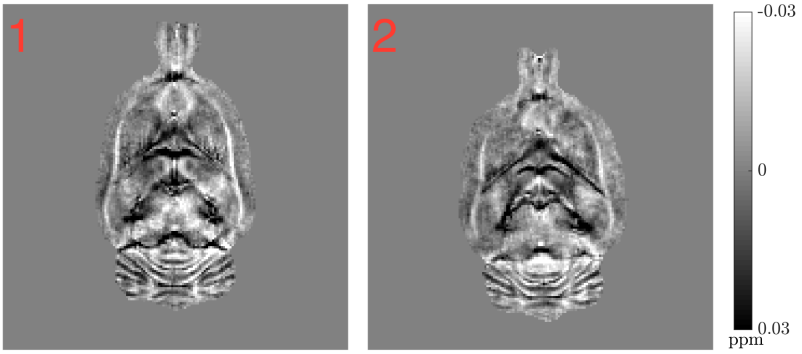



Figure 6.14: Isotropic quantitative susceptibility maps for all rat brains two-weeks post-water-maze task. Numbers correspond to matching animals.

# Bibliography


[1] Boreom Lee, Ji-Young Park, Wi Hoon Jung, Hee Sun Kim, Jungsu S Oh, Chi-Hoon Choi, Joon Hwan Jang, Do-Hyung Kang, and Jun Soo Kwon. White matter neuroplastic changes in long-term trained players of the game of "Baduk"(GO): a voxel-based diffusion-tensor imaging study. *Neuroimage*, 52(1):9–19, 2010.

[2] Timothy H Murphy and Dale Corbett. Plasticity during stroke recovery: from synapse to behaviour. *Nature Reviews Neuroscience*, 10(12):861–872, 2009.

[3] Lotfi B Merabet and Alvaro Pascual-Leone. Neural reorganization following sensory loss: the opportunity of change. *Nature Reviews Neuroscience*, 11(1):44–52, 2010.

[4] Sara N Burke and Carol A Barnes. Neural plasticity in the ageing brain. *Nature Reviews Neuroscience*, 7(1):30–40, 2006.

[5] Denis Le Bihan, Jean-François Mangin, Cyril Poupon, Chris A Clark, Sabina Pappata, Nicolas Molko, and Hughes Chabriat. Diffusion tensor imaging: concepts and applications. *Journal of magnetic resonance imaging*, 13(4):534–546, 2001.

[6] Shir Hofstetter, Ido Tavor, Shimrit Tzur Moryosef, and Yaniv Assaf. Short-term learning induces white matter plasticity in the fornix. *Journal of Neuroscience*, 33(31):12844–12850, 2013.

[7] Tamar Blumenfeld-Katzir, Ofer Pasternak, Michael Dagan, and Yaniv Assaf. Diffusion MRI of structural brain plasticity induced by a learning and memory task. *PloS one*, 6(6):e20678, 2011.

[8] Richard Morris. Developments of a water-maze procedure for studying spatial learning in the rat. *Journal of neuroscience methods*, 11(1):47–60, 1984.

[9] Yaniv Assaf and Peter J Basser. Composite hindered and restricted model of diffusion (CHARMED) MR imaging of the human brain. *Neuroimage*, 27(1):48–58, 2005.

[10] RM Henkelman, GJ Stanisz, and SJ Graham. Magnetization transfer in MRI: a review. *NMR in Biomedicine*, 14(2):57–64, 2001.

[11] Robert J Zatorre, R Douglas Fields, and Heidi Johansen-Berg. Plasticity in gray and white: neuroimaging changes in brain structure during learning. *Nature neuroscience*, 15(4):528–536, 2012.

[12] Wei Li, Bing Wu, Alexandru V Avram, and Chunlei Liu. Magnetic susceptibility anisotropy of human brain *in-vivo* and its molecular underpinnings. *Neuroimage*, 59(3):2088–2097, 2012.

[13] Chunlei Liu, Wei Li, G Allan Johnson, and Bing Wu. High-field (9.4 T) MRI of brain dysmyelination by quantitative mapping of magnetic susceptibility. *Neuroimage*, 56(3):930–938, 2011.

[14] Tian Liu, Cynthia Wisnieff, Min Lou, Weiwei Chen, Pascal Spincemaille, and Yi Wang. Nonlinear formulation of the magnetic field to source relationship for robust quantitative susceptibility mapping. *Magnetic resonance in medicine*, 69(2):467–476, 2013.

[15] Hussein S. Abdul-Rahman, Munther A. Gdeisat, David R. Burton, Michael J. Lalor, Francis Lilley, and Christopher J. Moore. Fast and robust three-dimensional best path phase unwrapping algorithm. *Appl. Opt.*, 46(26):6623–6635, Sep 2007.

[16] Hákon Gudbjartsson and Samuel Patz. The Rician distribution of noisy MRI data. *Magnetic resonance in medicine*, 34(6):910–914, 1995.

[17] E Mark Haacke, Robert W Brown, Michael R Thompson, Ramesh Venkatesan, et al. *Magnetic resonance imaging: physical principles and sequence design*, volume 82. Wiley-Liss New York:, 1999.

[18] Pinar Senay Özbay, Andreas Deistung, Xiang Feng, Daniel Nanz, Jürgen Rainer Reichenbach, and Ferdinand Schweser. A comprehensive numerical analysis of background phase correction with V-SHARP. *NMR in Biomedicine*, 2016.

[19] Paul A. Yushkevich, Joseph Piven, Heather Cody Hazlett, Rachel Gimpel Smith, Sean Ho, James C. Gee, and Guido Gerig. User-Guided 3D Active Contour Segmentation of Anatomical Structures: Significantly Improved Efficiency and Reliability. *Neuroimage*, 31(3):1116–1128, 2006.

[20] Ferdinand Schweser, Andreas Deistung, Berengar Wendel Lehr, and Jürgen Rainer Reichenbach. Quantitative imaging of intrinsic magnetic tissue properties using MRI signal phase: an approach to *in-vivo* brain iron metabolism? *Neuroimage*, 54(4):2789–2807, 2011.

[21] Tian Liu, Jing Liu, Ludovic de Rochefort, Pascal Spincemaille, Ildar Khalidov, James Robert Ledoux, and Yi Wang. Morphology enabled dipole inversion (MEDI) from a single-angle acquisition: comparison with COSMOS in human brain imaging. *Magnetic resonance in medicine*, 66(3):777–783, 2011.

[22] Wei Li, Nian Wang, Fang Yu, Hui Han, Wei Cao, Rebecca Romero, Bundhit Tantiwongkosi, Timothy Q Duong, and Chunlei Liu. A method for estimating and removing streaking artifacts in quantitative susceptibility mapping. *Neuroimage*, 108:111–122, 2015.

[23] Anita Karsa, Emma Biondetti, Shonit Punwani, and Karin Shmueli. The effect of large slice thickness and spacing and low coverage on the accuracy of susceptibility mapping. In *Proceedings of the 24$^{th}$ Annual Meeting of the ISMRM, Singapore*, page 1555, 2016.

[24] Jongho Lee, Karin Shmueli, Masaki Fukunaga, Peter van Gelderen, Hellmut Merkle, Afonso C Silva, and Jeff H Duyn. Sensitivity of MRI resonance frequency to the orientation of brain tissue microstructure. *Proceedings of the National Academy of Sciences*, 107(11):5130–5135, 2010.

[25] Chunlei Liu. Susceptibility tensor imaging. *Magnetic resonance in medicine*, 63(6):1471–1477, 2010.

[26] B Bender and U Klose. The *in-vivo* influence of white matter fiber orientation towards $B_0$ on $T_2^*$ in the human brain. *NMR in biomedicine*, 23(9):1071–1076, 2010.

[27] Samuel Wharton and Richard Bowtell. Gradient echo based fiber orientation mapping using $R_2^*$ and frequency difference measurements. *Neuroimage*, 83:1011–1023, 2013.

[28] Karin Shmueli, Stephen J Dodd, Tie-Qiang Li, and Jeff H Duyn. The contribution of chemical exchange to MRI frequency shifts in brain tissue. *Magnetic resonance in medicine*, 65(1):35–43, 2011.

[29] Kai Zhong, Jochen Leupold, Dominik von Elverfeldt, and Oliver Speck. The molecular basis for gray and white matter contrast in phase imaging. *Neuroimage*, 40(4):1561–1566, 2008.

[30] J Luo, X He, and DA Yablonskiy. Magnetic susceptibility induced white matter MR signal frequency shifts—experimental comparison between Lorentzian sphere and generalized Lorentzian approaches. *Magnetic resonance in medicine*, 71(3):1251–1263, 2014.

[31] Dmitriy A Yablonskiy and Alexander L Sukstanskii. Generalized Lorentzian Tensor Approach (GLTA) as a biophysical background for quantitative susceptibility mapping. *Magnetic resonance in medicine*, 73(2):757–764, 2015.

[32] Peter van Gelderen, Jacco A de Zwart, Jongho Lee, Pascal Sati, Daniel S Reich, and Jeff H Duyn. Nonexponential $T_2^*$ decay in white matter. *Magnetic resonance in medicine*, 67(1):110–117, 2012.

[33] Pascal Sati, Peter van Gelderen, Afonso C Silva, Daniel S Reich, Hellmut Merkle, Jacco A de Zwart, and Jeff H Duyn. Micro-compartment specific $T_2^*$ relaxation in the brain. *Neuroimage*, 77:268–278, 2013.

# Chapter 7

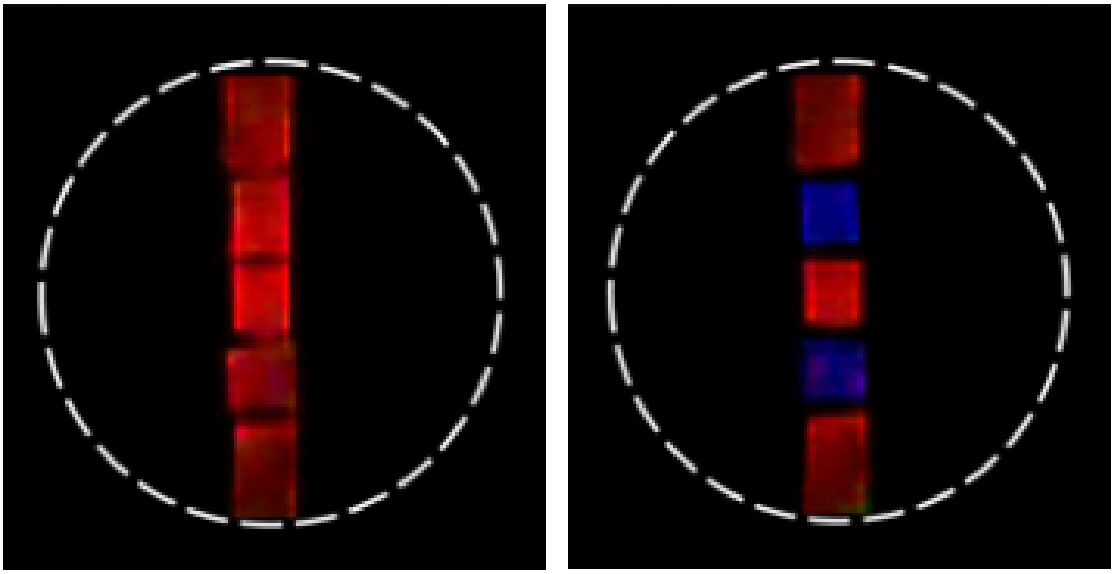
# Beyond Isotropic Susceptibility

## 7.1 Anisotropic Susceptibility

### 7.1.1 Motivation

It was initially considered [1] that under 'ordinary' experimental circumstances for biomedical MRI, magnetic susceptibility could be appropriately defined as an isotropic, scalar constant, $\chi_I$. However, with increases in field strength and the ability to robustly obtain information about both field perturbations and susceptibility in tissue [2], this view has been challenged. In 2010, evidence emerged of orientation-dependent field perturbations existing within tissue [3, 4] that cannot be explained by a model of isotropic susceptibility alone. The concept of orientation-dependent field perturbations should not be considered surprising, since previous work in this thesis (Section 4.2) has explicitly described how observed field perturbations depend on both the shape and orientation of an object with respect to the static magnetic field. However in some tissues, orientation-dependent field perturbations have been found to exist independently of the macroscopic tissue structure [3], or with a form that cannot be described using isotropic susceptibility [5]. This phenomenon has been well documented in white matter [3, 4], where anisotropy is hypothesised to be due to highly ordered, radially oriented lipid bilayers within the myelin sheath [6] (experimental example shown in Figure 7.1).

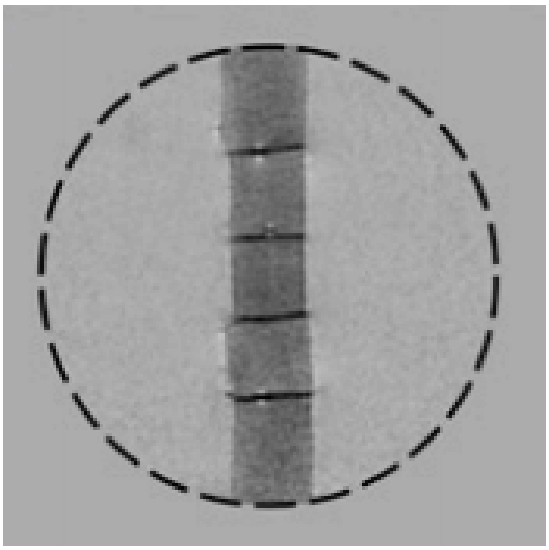
The ability to quantify susceptibility anisotropy provides the opportunity to examine the sub-voxel structure of tissue. QSM provides an experimenter with a single $\chi_I$ value, an incredibly valuable piece of information in quantifying tissue composition within a voxel. However, evidence of anisotropy would imply the existence of an ordered molecular structure within the tissue. Furthermore, if susceptibility anisotropy is found to be significant in some tissue types, QSM based on a



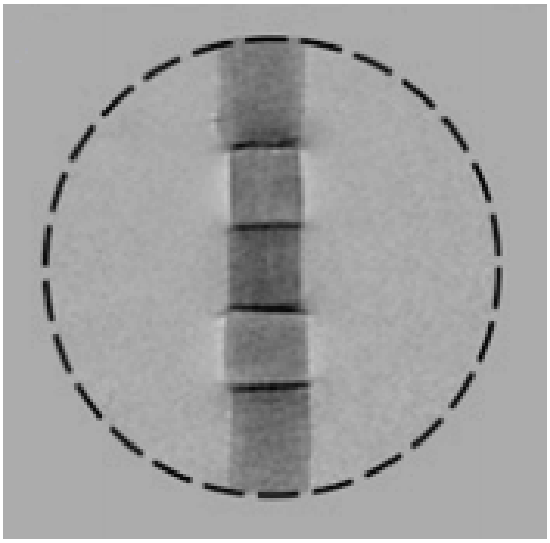
(a) DTI



(b) DTI



(c) $\Delta B(\vec{r})$



(d) $\Delta B(\vec{r})$

Figure 7.1: Example of the orientation dependence of frequency perturbations in white matter. An *ex-vivo* sample of human corpus callosum was cut into 5 pieces and placed in a saline solution. Figure 7.1a shows the DTI of the corpus callosum (indicating the fibres are pointing in the same direction), with Figure 7.1c showing the resulting field perturbations. In Figures 7.1b and 7.1d, the second and fourth section of the corpus callosum are rotated. Though the macrostructural shape of the corpus callosum section is near-identical (a rectangular cube of white matter), the field perturbations are significantly different, both internally and externally to the white matter. Images adapted from [3].

model of isotropic susceptibility would not be as robust as previously considered, since similarly to $\Delta B(\vec{r})$ maps, calculated $\chi_I(\vec{r})$ maps would then be dependent on tissue orientation with respect to the $\vec{B}_0$ field, creating challenges in comparing $\chi_I$ values between tissue types and subjects. The ability to quantify susceptibility anisotropy provides both a further insight into underlying properties of tissue

and allows the potential of QSM to provide reliable, repeatable information about susceptibility distributions to be scrutinised.

### 7.1.2 Theory

To describe the anisotropic properties of tissue susceptibility, the model of susceptibility within a single voxel is extended from a scalar constant, $\chi_I$, to a 3×3 susceptibility tensor, $\underline{\underline{\chi}}$:

$$\underline{\underline{\chi}} = \begin{bmatrix} \chi_{11} & \chi_{12} & \chi_{13} \\ \chi_{21} & \chi_{22} & \chi_{23} \\ \chi_{31} & \chi_{32} & \chi_{33} \end{bmatrix} \tag{7.1}$$

where $\underline{\underline{\chi}}$ is a symmetric tensor [1] with six independent components. In isotropic systems, $\underline{\underline{\chi}}$ reduces to a 3×3 scaled multiple of the identity matrix:

$$\underline{\underline{\chi}} = \begin{bmatrix} \chi_I & 0 & 0 \\ 0 & \chi_I & 0 \\ 0 & 0 & \chi_I \end{bmatrix} \tag{7.2}$$

identical to the previous discussion of $\underline{\underline{\chi_I}}$ in Equation 4.2.
From the previous discussion in Section 4.3, in isotropic systems $\underline{\underline{\chi}}$ can be theoretically determined from a single orientation scan, independent of the orientation of the tissue with respect to the $\vec{B}_0$ field (directed along the $\hat{z}$-dimension):

$$\Delta B_{\text{spin}_z}(\vec{r}) = B_0 \cdot \mathcal{F}^{-1}\left[\left(\frac{1}{3} - \frac{k_z^2}{k^2}\right)\mathcal{F}\left[\chi_I(\vec{r})\right]\right] \tag{7.3}$$

where $\chi_I(\vec{r})$ represents $\chi_{33}(\vec{r})$. This can be generalised for an arbitrarily oriented $\vec{B}_0$ field:

$$\Delta B_{\text{spin}_{B_0}}(\vec{r}) = B_0 \cdot \mathcal{F}^{-1}\left[\left(\frac{1}{3} - \frac{\left(\vec{k}\cdot\hat{B}_0\right)^2}{k^2}\right)\mathcal{F}\left[\chi_I(\vec{r})\right]\right] \tag{7.4}$$

obtained by repeating the derivation in Section 4.3.1, replacing $\vec{H}_0 = H_0 \cdot \hat{z}$ with $H_0 \cdot \hat{H}_0$, where $\hat{H}_0$ is a unit vector along the field direction. Repeating this derivation for an arbitrary 3×3 $\underline{\underline{\chi}}$ tensor [4, 7]:

$$\Delta B_{\text{spin}_{B_0}}(\vec{r}) = B_0 \cdot \mathcal{F}^{-1}\left[\frac{1}{3}\hat{B}_0 \cdot \mathcal{F}\left[\underline{\underline{\chi}}(\vec{r})\right] \cdot \hat{B}_0 - \frac{\left(\vec{k}\cdot\hat{B}_0\right)\vec{k}\cdot\mathcal{F}\left[\underline{\underline{\chi}}(\vec{r})\right]\cdot\hat{B}_0}{k^2}\right]. \tag{7.5}$$

### 7.1.3 Properties of the Susceptibility Tensor

As $\underline{\underline{\chi}}$ is a symmetric matrix, it is normal and diagonalisable via eigenvalue/vector decomposition:

$$\underline{\underline{\chi}} = \begin{bmatrix} \lambda_1 & 0 & 0 \\ 0 & \lambda_2 & 0 \\ 0 & 0 & \lambda_3 \end{bmatrix} \tag{7.6}$$

where $\lambda_{1,2,3}$ are the eigenvalues of $\underline{\underline{\chi}}$ and the three orthogonal eigenvectors are written as $\hat{v}_{1,2,3}$. The mean magnetic susceptibility (MMS) [8] of $\underline{\underline{\chi}}$ is defined as:

$$\text{MMS} = \frac{1}{3}\left(\lambda_1 + \lambda_2 + \lambda_3\right). \tag{7.7}$$

This can be interpreted as the equivalent of $\chi_I$ for any 3×3 $\underline{\underline{\chi}}$ tensor. However, as the trace of $\underline{\underline{\chi}}$ is rotationally invariant:

$$\begin{aligned} \text{tr}\ \underline{\underline{\chi}} &= \chi_{11} + \chi_{22} + \chi_{33} \\ &= \text{tr}\ \underline{\underline{R\chi}} \end{aligned} \tag{7.8}$$

where tr defines the trace operator and $\underline{\underline{R}}$ is a general rotation matrix, Equation 7.7 can be generalised for $\underline{\underline{\chi}}$ in *any* reference frame, defining [8]:

$$\text{MMS} = \frac{1}{3}\left(\chi_{11} + \chi_{22} + \chi_{33}\right) \tag{7.9}$$

for *all* $\underline{\underline{\chi}}$. In white matter, assuming that cylindrical symmetry is present and that the most paramagnetic (positive) eigenvalue corresponds to the direction of the nerve fibre [7], the magnetic susceptibility anisotropy (MSA) is defined as [7, 8]:

$$\text{MSA} = \lambda_1 - \frac{\lambda_2 + \lambda_3}{2} \tag{7.10}$$

where $\lambda_1$ is defined as the most positive eigenvalue. However, in other tissues without cylindrical symmetry or with different susceptibility properties, a more complex definition of MSA is required.

### 7.1.4 Susceptibility Tensor Imaging

Equation 7.5 forms the foundation of Susceptibility Tensor Imaging (STI) [2]. The first publication on STI was in 2010, when Liu [4] first derived Equation 7.5 and experimentally mapped the full 3×3 $\underline{\underline{\chi}}(\vec{r})$ tensor in an *ex-vivo* mouse brain by scanning the sample at multiple orientations to $\vec{B}_0$. Liu's groundbreaking paper provided a novel technique to quantify susceptibility anisotropy within tissue.
Equation 7.5 can be redefined as a forward problem, $\Delta\text{B} = \underline{\underline{A}}\chi$, where:

$$\underline{\underline{A}} = \underline{\underline{\text{B}_0\mathcal{F}^{-1}\text{D}_{\text{STI}}\mathcal{F}}} \tag{7.11}$$

defining $\underline{\underline{\mathrm{B}_0}}$ as the identity matrix scaled by $B_0$, $\underline{\underline{\mathcal{F}}}/\underline{\underline{\mathcal{F}}}^{-1}$ are the Fourier/inverse Fourier transform matrices respectively and $\underline{\underline{\mathrm{D}_{\mathrm{STI}}}}$ is comprised of the $k$-space dipole field kernels for the individual components of $\chi$. When considering an individual voxel in $k$-space [4]:

$$\underline{\underline{\mathrm{D}_{\mathrm{STI}}}} = \begin{bmatrix} f(B_x^2) & g(B_xB_y) & f(B_y^2) & g(B_xB_z) & g(B_yB_z) & f(B_z^2) \end{bmatrix} \tag{7.12}$$

where $B_{x,y,z}$ are the individual components of $\vec{B}_0$, defining:

$$\begin{aligned} f(B_i^2) &= \frac{1}{3}B_i^2 - \vec{k}\cdot\vec{B}_0\frac{k_iB_i}{k^2} \\ g(B_iB_j) &= \frac{2}{3}B_iB_j - \vec{k}\cdot\vec{B}_0\frac{k_iB_j + k_jB_i}{k^2} \end{aligned} \tag{7.13}$$

where $B_i = \frac{\vec{B}\cdot\hat{r}_i}{|B_0|}$. To reflect the symmetry of $\underline{\underline{\chi}}$, the forward problem vector $\chi$ is composed of six components per voxel per orientation, with the repeated sampling of the off-diagonal components of $\chi$ contained within $\underline{\underline{\mathrm{D}_{\mathrm{STI}_{\mathrm{voxel}}}}}$, as can be seen in Equation 7.13. For an N×N×N dataset:

$$\underline{\underline{\mathrm{D}_{\mathrm{STI}}}} = \begin{bmatrix} \underline{\underline{\mathrm{D}_{\mathrm{STI}_{1,1,1}}}} & 0 & 0 & \cdots & 0 \\ 0 & \underline{\underline{\mathrm{D}_{\mathrm{STI}_{1,1,2}}}} & 0 & \cdots & 0 \\ 0 & 0 & \underline{\underline{\mathrm{D}_{\mathrm{STI}_{1,1,3}}}} & \cdots & 0 \\ \vdots & \vdots & \vdots & \ddots & \vdots \\ 0 & 0 & 0 & \cdots & \underline{\underline{\mathrm{D}_{\mathrm{STI}_{\mathrm{N,N,N}}}}} \end{bmatrix}. \tag{7.14}$$

Provided that the system is scanned at multiple orientations to $\vec{B}_0$, with sufficient orientations the inversion is well posed (properties of well-posedness and multiple orientation scanning are discussed in Sections 5.4.2 and 5.4.4 respectively) and $\chi$ can be solved via the direct inversion of $\underline{\underline{A}}$ (discussed in Section 5.4.5). As $\underline{\underline{A}}$ is too large to be stored computationally, this operation can be completed on a $k$-space voxelwise basis, defining:

$$\underline{\underline{\mathrm{D}_{\mathrm{STI}}}} = \begin{bmatrix} f(B_x^2)_1 & g(B_xB_y)_1 & f(B_y^2)_1 & g(B_xB_z)_1 & g(B_yB_z)_1 & f(B_z^2)_1 \\ f(B_x^2)_2 & g(B_xB_y)_2 & f(B_y^2)_2 & g(B_xB_z)_2 & g(B_yB_z)_2 & f(B_z^2)_2 \\ \vdots & \vdots & \vdots & \vdots & \vdots & \vdots \\ f(B_x^2)_S & g(B_xB_y)_S & f(B_y^2)_S & g(B_xB_z)_S & g(B_yB_z)_S & f(B_z^2)_S \end{bmatrix} \tag{7.15}$$

where $S$ is the number of sampling orientations. In practice, STI is commonly implemented as an iterative least squares minimisation (discussed in Section 5.4.5), which involves solving the following problem [8]:

$$\min_{\underline{\underline{\chi}}(\vec{r})} \left\{ \|O_1\|_2^2 + \|O_2\|_2^2 + \cdots + \|O_S\|_2^2 \right\} \tag{7.16}$$

where $O_i = \underline{\underline{A_i}}\chi - \Delta \mathrm{B}_i$, with the subscript $i$ defining a single orientation dataset. The condition number, $C$ (discussed in Section 5.4.2) of $\underline{\underline{\mathrm{D_{STI}}}}$ is defined as:

$$C = \frac{\max \sqrt{\mathrm{eig}\left(\underline{\underline{\mathrm{D^*_{STI}}}} \cdot \underline{\underline{\mathrm{D_{STI}}}}\right)}}{\min \sqrt{\mathrm{eig}\left(\underline{\underline{\mathrm{D^*_{STI}}}} \cdot \underline{\underline{\mathrm{D_{STI}}}}\right)}} \tag{7.17}$$

where eig is the eigenvalue operator. As $\underline{\underline{\mathrm{D_{STI}}}}$ is a *block diagonal* matrix, the eigenvalues will be identical to those of the individual voxel matrices: $\underline{\underline{\mathrm{D_{STI_{voxel}}}}}$. Therefore eigenvalue decomposition can be performed without generating $\underline{\underline{\mathrm{D_{STI}}}}$ directly:

$$\mathrm{eig}\left(\underline{\underline{\mathrm{D^*_{STI}}}} \cdot \underline{\underline{\mathrm{D_{STI}}}}\right) = \left[\mathrm{eig}\left(\underline{\underline{\mathrm{D^*STI}_{1,1,1}}} \cdot \underline{\underline{\mathrm{D_{STI}}_{1,1,1}}}\right), \mathrm{eig}\left(\underline{\underline{\mathrm{D^*STI}_{1,1,2}}} \cdot \underline{\underline{\mathrm{D_{STI}}_{1,1,2}}}\right), \ldots, \mathrm{eig}\left(\underline{\underline{\mathrm{D^*STI}_{N,N,N}}} \cdot \underline{\underline{\mathrm{D_{STI}}_{N,N,N}}}\right)\right] \tag{7.18}$$

In STI, rather than considering the $\vec{B}_0$ field as static and the tissue sample as rotating (field frame of reference), the sample frame of reference is used, i.e. a rotating $\vec{B}_0$ field and a static tissue sample is assumed. When considering the field frame of reference, a quantitative susceptibility map is required for each individual orientation [4], and this approach is prone to errors due to the ill-posedness of single orientation QSM (discussed in detail in Section 5.4). When utilising the sample frame of reference, this is no longer required. In addition, use of the sample frame of reference makes comparisons between different samples easier, e.g comparisons between subjects in an *in-vivo* brain study [7].

Similar to the issues presented in the discussion of COSMOS in Section 5.4.4, STI's potential as a research tool is limited due to the requirement for scanning samples at multiple orientations to $\vec{B}_0$, due to both physical restrictions and time constraints. As $\underline{\underline{\chi}}$ has six independent components, a theoretical minimum of six well-defined orientations are required to fully resolve $\underline{\underline{\chi}}$ without additional approximations and regularisation (discussed in following section). Previous research [8] suggests that an increased rotation range is the key factor for improving STI performance, rather than an increased number of scanning orientations. Though this is advantageous for reducing total scanning time, it severely limits what is possible *in-vivo*, where bore size restrictions and physical limitations prevent ROI rotation, in addition to increased motion artefacts if subjects are uncomfortable. Furthermore, six orientations will still require a subject to remain in the scanner bore for an extensive period of time. However, despite these restrictions, *in-vivo* STI studies have been performed over the human brain [6]. For *ex-vivo* studies where these limitations are not present, STI protocols can be readily applied to further examine the anisotropic properties of tissue samples.

### 7.1.5 Approximation and Regularisation

If data are acquired at a sufficient number of well defined orientations in an STI protocol (ideally uniformly distributed over a spherical surface [7]), the matrix inversion should be well-posed and regularisation methods similar to those used for QSM (Section 5.4.5) should not be necessary. However, the *in-vivo* feasibility of STI can prevent the inversion being well-posed, including limitations in the accessible range of sample rotation, number of orientations sampled, errors generated due to imperfect dataset co-registration and noise, induced both experimentally and through processing phase data in unwrapping and background field removal (discussed in Sections 5.2 and 5.3). In experimental conditions where these limitations are apparent, regularisation, in addition to using approximations to simplify the form of the underlying anisotropy distribution can assist in determining $\underline{\underline{\chi}}(\vec{r})$. Li et al. [7] simplified the STI protocol in white matter by approximating nerve fibres as cylindrically symmetric, reducing the number of unique eigenvalues to two. Furthermore, the principal eigenvector (defined as the eigenvector corresponding to the most positive eigenvalue) was assumed to coincide with the fibre orientation obtained from Diffusion Tensor Imaging (DTI) [9]. By obtaining an initial DTI reference scan and utilising the resulting information in an STI protocol, the number of unknowns is reduced from six to two.

In a second paper, Li et al. [8] regularised the STI inversion by including known spatial priors about the underlying $\underline{\underline{\chi}}(\vec{r})$ distribution. In this regularisation, areas of 'known' isotropy are forced to have isotropic $\underline{\underline{\chi}}(\vec{r})$, by enforcing $\underline{\underline{\chi}}$ to be a scaled version of the identity matrix (as defined in Equation 7.2). In addition, a gradient regularisation mask (described in Section 6.5.3) was generated from a QSM protocol and included in the STI regularisation. This led to the minimisation problem being defined as:

$$\min_{\underline{\underline{\chi}}} \left\{ \|O_1\|_2^2 + \|O_2\|_2^2 + \cdots + \|O_S\|_2^2 + \sum_{l=1}^{3} \beta_1^2 \left\| M_{1l} \frac{\partial \chi_I}{\partial l} \right\|_2^2 + \sum_{m=1}^{3} \sum_{n=m+1}^{3} \beta_2^2 \left( \|M_2 \chi_{mn}\|_2^2 + \left\| M_2 \left( \chi_{mm} - \chi_{nn} \right) \right\|_2^2 \right) \right\} \tag{7.19}$$

where $M_{1l}$ are the gradient regularisation masks ($l = 1, 2, 3$ corresponds to the $\hat{x}, \hat{y}$ and $\hat{z}$ directions respectively), $M_2$ is a mask defining regions where $\underline{\underline{\chi}} = \chi_I \underline{\underline{I}}$ and $\beta_{1,2}$ are regularisation weighting coefficients. This method is known as Mean Magnetic Susceptibility Regularised Susceptibility Tensor Imaging (MMSR-STI). Both these techniques have produced significantly improved $\underline{\underline{\chi}}(\vec{r})$ maps in regions of white matter *in-vivo*. However, limitations exist in the appropriateness of these extensions to the original STI technique. In the MMSR-STI paper [8], isotropic

regularisation was performed everywhere apart from white matter tissue, excluding the iron rich deep nuclei. This prevents any assessment of susceptibility anisotropy beyond the white matter boundary. Similar issues exist when approximating the $\underline{\underline{\chi}}$ tensor as cylindrically symmetric [7], as this prevents accurate assessment of anisotropy in regions without this property. Current evidence suggests that the principal eigenvector is aligned with the fibre direction obtained from DTI [6]. However, susceptibility contrast appears to originate from a different source to DTI [10] and further work is required to ensure that the co-alignment of DTI and STI tensors is a suitable assumption when obtaining $\underline{\underline{\chi}}(\vec{r})$ maps.

## 7.2 Chemical Exchange

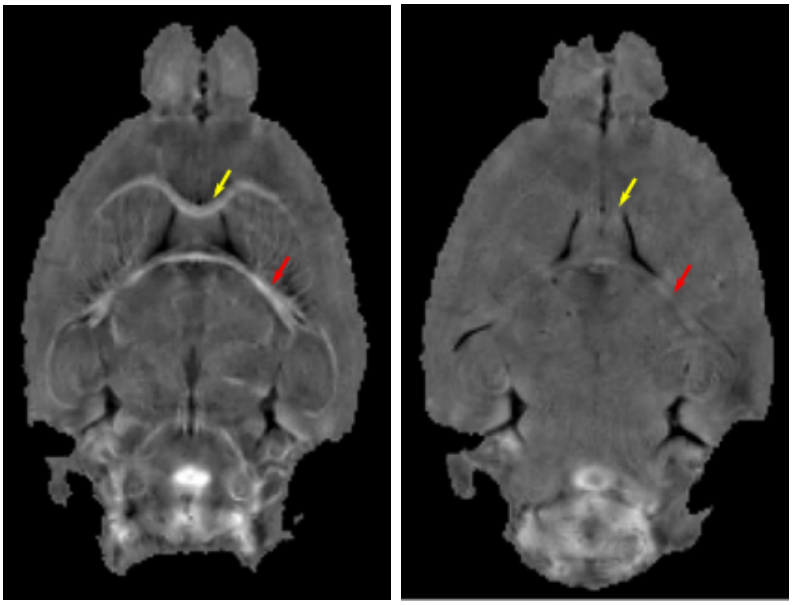
In 2011, Shmueli et al. [11] experimentally determined that a significant source of contrast between grey and white matter in field perturbation maps is induced by chemical exchange effects, $E$, observed as an orientation-independent local field offset within tissue:

$$\Delta B_{\text{exc}} = B_0 \cdot E. \tag{7.20}$$

Shmueli et al. [11] further concluded that ignoring chemical exchange effects when examining field perturbation maps could lead to incorrect estimations of susceptibility properties within tissue.

Similar to susceptibility anisotropy, quantifying the properties of chemical exchange *in-vivo* could provide a further insight into the sub-voxel mechanisms of tissue. Chemical exchange effects have been hypothesised to originate from the exchange of water protons and macromolecules [12] found within myelin [13], with recent work additionally investigating the contribution of white matter lipids [14]. The lack of contrast between grey and white matter in $\Delta B(\vec{r})$ maps [10] acquired from shiverer mice is consistent with the hypothesis that chemical exchange effects observed in white matter originate within myelin (example in Figure 7.2).

In several studies, the inclusion of orientation-independent local field offsets has been considered essential in explaining the observed field perturbations in white matter [15–18]. In a recent study, Wharton and Bowtell [15] isolated the local effects of chemical exchange from susceptibility in an *ex-vivo* pig optic nerve and observed a significant orientation-independent local field offset. Luo et al. [16] additionally required a constant offset term within their experimental fitting to describe the field perturbations from an *ex-vivo* rat optic nerve. Luo et al. [16] hypothesised that the observed shift does not necessarily originate from the optic nerve itself, due to the possibility of induced exchange effects from chemicals introduced in the experimental set-up (formalin and phosphate-buffered saline). Whar-



(a) Control mouse (b) Shiverer mouse

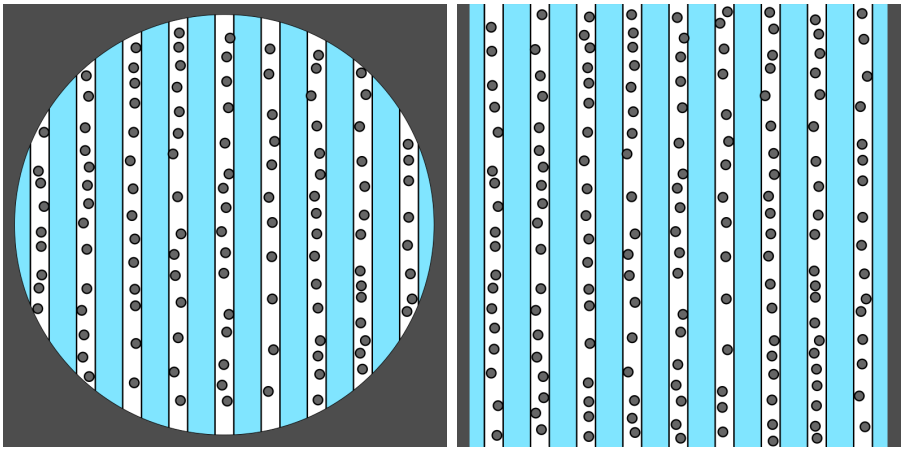
Figure 7.2: $\Delta B(\vec{r})$ of an *ex-vivo* healthy, control mouse (Figure 7.2a) vs. an *ex-vivo* shiverer mouse (Figure 7.2b). Note the loss of white matter/grey matter contrast in the corpus callosum (yellow arrow) and hippocampal commissure (red arrow). Images adapted from [10].

ton and Bowtell [15] hypothesised that exchange effects may have been manifested within the agarose gel surrounding the optic nerve. However, even if chemical exchange in external agents is the cause of the observed field offset, the implications could have significant repercussions in how *ex-vivo* phase imaging studies are performed.

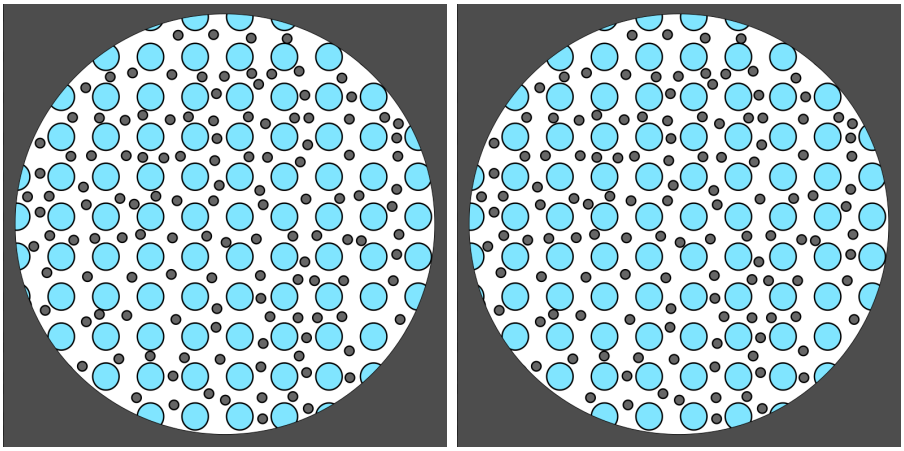
## 7.3 Non-Spherical Microstructural Susceptibility Inclusions

### 7.3.1 Introduction

In addition to susceptibility anisotropy and exchange, sub-voxel compartmentalisation due to the presence of microstructural susceptibility inclusions can further complicate the relationship between tissue composition and observed field perturbations. Within this thesis thus far, susceptibility inclusions in tissue have been considered as spherically symmetric point sources, producing field perturbations that are appropriately characterised by using the sphere of Lorentz (SOL) correction (introduced in Section 4.2.3). This assumption has continued into the discussion of susceptibility anisotropy, with the left-hand-side term in Equation 7.5 introducing the SOL correction for STI [6]. However, the existence of



(a) Sphere of Lorentz ⊥ (b) 'Cylinder of Lorentz' ⊥



(c) Sphere of Lorentz ∥ (d) 'Cylinder of Lorentz' ∥

Figure 7.3: The existence of cylindrically symmetric tissue microstructure (here denoted by blue cylinders) would prevent spherical averaging of the field perturbations sampled by spins (grey spheres) at the length scale of the volumes shown here, due to non-spherical compartmentalisation induced by the tissue architecture. He et al. [20] argued that the sphere of Lorentz approximation would no longer be valid and a more suitable 'cylinder of Lorentz' could be utilised instead. Images for visualisation purposes only.

anisotropic susceptibility implies that the microstructure within the tissue must also be anisotropic [19], reflective of the symmetry of the anisotropy distribution. In 2009, He et al. [20] provided evidence that the existence of non-spherical susceptibility inclusions at the cellular/subcellular level could explain the lack of observed contrast in $\Delta B(\vec{r})$ maps between white matter and cerebrospinal fluid (CSF). He et al. [20] argued that the cylindrically symmetric microstructural tissue architecture in white matter contains cylindrical susceptibility inclusions that are incorrectly accounted for when using the form of the SOL introduced in QSM. To correct for this, the 'generalised Lorentzian approximation' (GLA) was introduced, by implementing a 'cylinder of Lorentz' correction (visualised in Figure 7.3) to account for the symmetry of the tissue architecture.

In recent years, there has been a significant amount of debate regarding the GLA and its relevance to field perturbations in white matter [21, 22]. Within this section, to explain the concept of the GLA clearly, simulations of model structures will be used to visualise the impact of cylindrically symmetric tissue architecture. Beyond this, its relevance in white matter will be discussed.

### 7.3.2 Simulated Example of the Impact of Cylindrically Symmetric Tissue Architecture

To examine the effect of cylindrically symmetric tissue architecture on $\Delta B(\vec{r})$ maps, two simulated susceptibility distributions (composition and properties detailed in Figure 7.4) were generated to investigate the impact of spherical and cylindrical susceptibility inclusions within a cylindrical body. $\Delta B(\vec{r})$ maps were generated from the $\chi_I(\vec{r})$ distributions, with the cylindrical axis of symmetry oriented at five different angles to $\vec{B}_0$ ($\theta = 0°$, 22.5°, 45°, 67.5° and 90°). Figure 7.5 shows the $\Delta B(\vec{r})$ maps generated from the $\chi_I(\vec{r})$ distributions at 0° and 90° to $\vec{B}_0$.

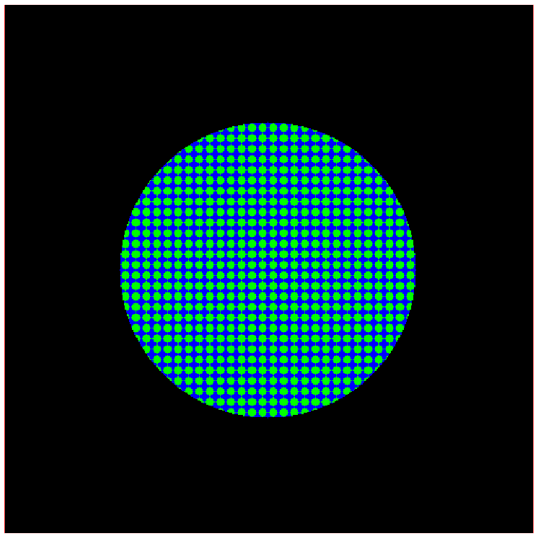
Externally to the large cylindrical body, the field perturbations, $\Delta B_{\text{ext}}(\vec{r})$, should be independent of the shape of the internal susceptibility inclusions and depend only on the volume susceptibility, $\chi_{I_{\text{vol}}}$ (here defined as the average susceptibility per voxel) within the cylindrical body [16]:

$$\chi_{I_{\text{vol}}} = \frac{\chi_{I_{\text{med}}} \cdot V_{\text{med}} + \chi_{I_{\text{sph/cyl}}} \cdot V_{\text{sph/cyl}}}{V_{\text{med}} + V_{\text{sph/cyl}}} \tag{7.21}$$

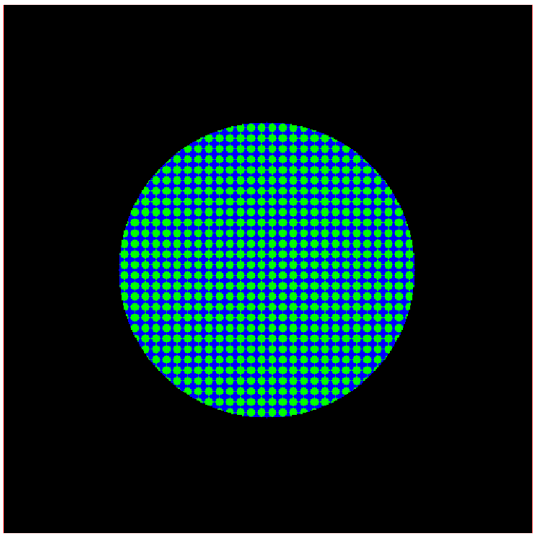
where $V_i$ defines the volume of $i$, $\chi_{I_{\text{sph/cyl}}}$ is the susceptibility of the spherical/cylindrical inclusions and $\chi_{I_{\text{med}}}$ is the susceptibility of the medium surrounding the inclusions within the cylindrical body. From the analytical solution of $\Delta B_{\text{ext}}(\rho, \phi, \theta)$ for an infinite cylinder surrounded by an external medium of $\chi_I = 0$ (Table 4.4 and visualised in Figure 4.7):

$$\Delta B_{\text{ext}}(\rho, \phi, \theta) = B_0 \cdot \frac{\chi_{I_{\text{vol}}}}{2} \cdot \left(\frac{a}{\rho}\right)^2 \cos 2\phi \sin^2 \theta \tag{7.22}$$

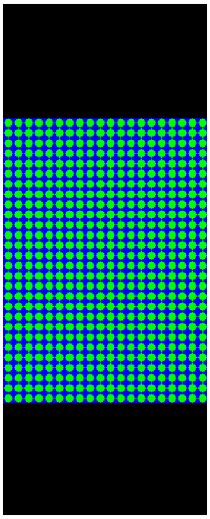
where $a$ defines the radius of the cylinder, $\rho$ describes the radial cylindrical polar coordinate, $\phi$ defines the angle between the $\vec{B}_0$ field and $\vec{\rho}$, and $\theta$ defines the angle between the component of the $\vec{B}_0$ field that is perpendicular to the cylinder's axis and the cylindrical axis of symmetry. In the simulations presented here, the susceptibility properties of the spherical and cylindrical inclusions were modified to ensure $\chi_{I_{\text{vol}}} = 50\,\text{ppm}$ for both models, setting $\chi_{I_{\text{sph}}} = 191.1\,\text{ppm}$ and $\chi_{I_{\text{cyl}}} = 100.7\,\text{ppm}$ to account for relative volume fractions of the susceptibility inclusions. Therefore, the form of $\Delta B_{\text{ext}}(\vec{r})$ should be identical in both cases. This was verified



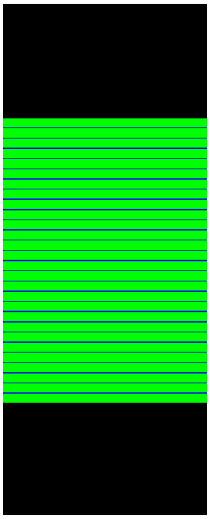
(a) $\chi_I(\vec{r})$ with spherical inclusions $\perp$



(b) $\chi_I(\vec{r})$ with cylindrical inclusions $\perp$



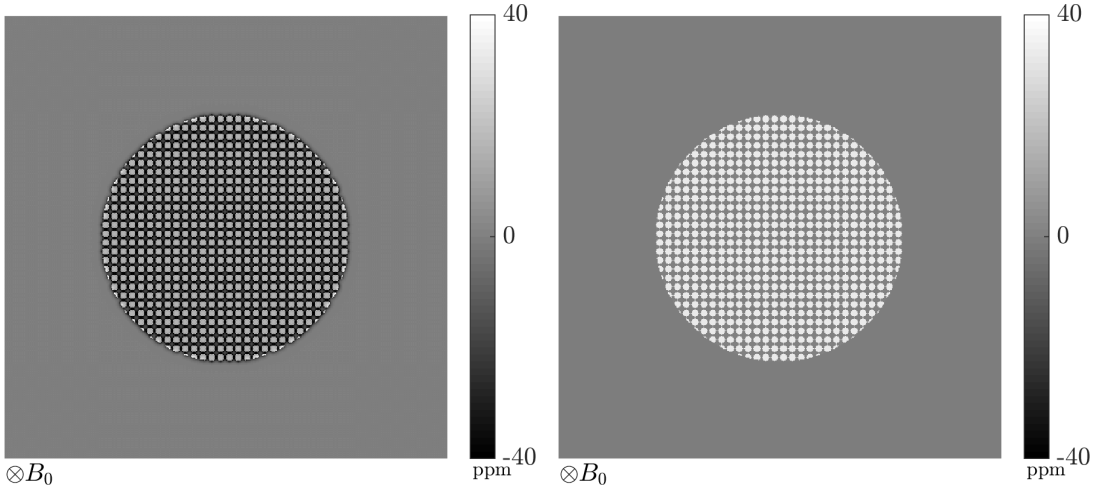
(c) $\chi_I(\vec{r})$ with spherical inclusions $\parallel$



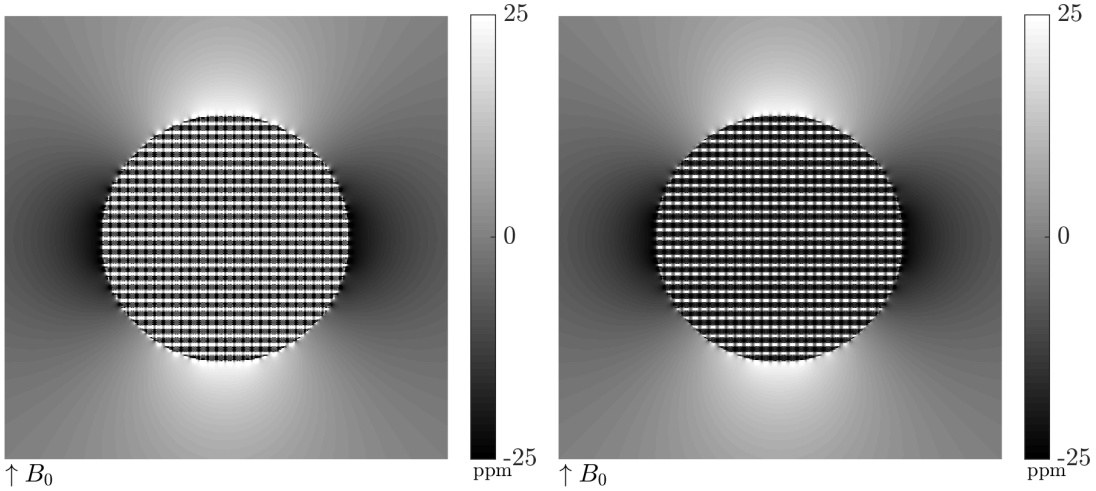
(d) $\chi_I(\vec{r})$ with cylindrical inclusions $\parallel$

Figure 7.4: Two $\chi_I(\vec{r})$ distributions confined to a cylindrical volume were simulated containing either spherical $\chi_I$ sources, $\chi_{I_{\text{sph}}}$ (Figures 7.4a and 7.4c), or cylindrical $\chi_I$ sources, $\chi_{I_{\text{cyl}}}$ (Figures 7.4b and 7.4d), surrounded by an isotropic medium, $\chi_{I_{\text{med}}}$. Here the spherical/cylindrical susceptibility inclusions are displayed in green, with the surrounding isotropic medium displayed in blue. In both cases, the average volume susceptibility, $\chi_{I_{\text{vol}}} = 50\,\text{ppm}$ within the cylindrical body, setting $\chi_{I_{\text{sph}}} = 191.1\,\text{ppm}$ and $\chi_{I_{\text{cyl}}} = 100.7\,\text{ppm}$ to account for relative volume fractions of the susceptibility inclusions. In the isotropic medium surrounding the $\chi_{I_{\text{sph/cyl}}}$ sources (blue region), $\chi_{I_{\text{med}}} = 1\,\text{ppm}$. Surrounding the cylinders (black region), $\chi_{I_{\text{ext}}} = 0\,\text{ppm}$.

in our simulations, with comparisons to a solid cylinder presented in Figure 7.6. Assuming that the susceptibility inclusions *contribute* to the sampled signal, in addition to $\Delta B_{\text{ext}}(\vec{r})$, the average internal field perturbation within the cylindrical body, $B_{\text{int}_{\text{av}}}$ should be independent of the shape of the susceptibility inclusions and




(a) $\Delta B(\vec{r})$ with spherical inclusions (b) $\Delta B(\vec{r})$ with cylindrical inclusions




(c) $\Delta B(\vec{r})$ with spherical inclusions (d) $\Delta B(\vec{r})$ with cylindrical inclusions

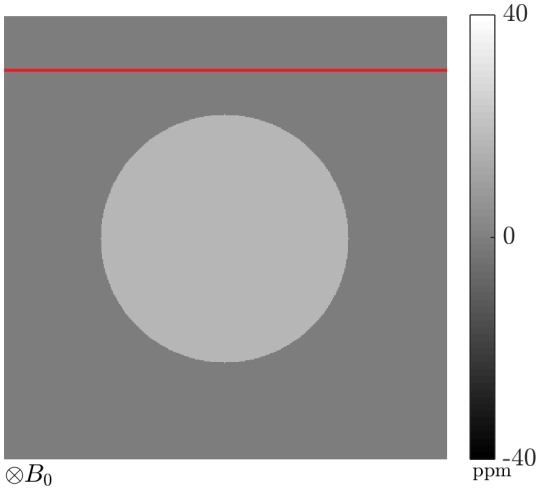
Figure 7.5: $\Delta B(\vec{r})$ maps from the $\chi_I(\vec{r})$ maps in Figure 7.4, with the axis of symmetry parallel (Figures 7.5a and 7.5b) and perpendicular (Figures 7.5c and 7.5d) to $\vec{B}_0$. To compare directly to the $\chi_I(\vec{r})$ maps, units were kept in ppm. Simulated using the $k$-space forward model (described in Section 4.3) on a 2100×2100×200 matrix using MATLAB (Release 2015a, The MathWorks Inc., Natick, MA, United States).

depend only on $\chi_{I_{\text{vol}}}$:

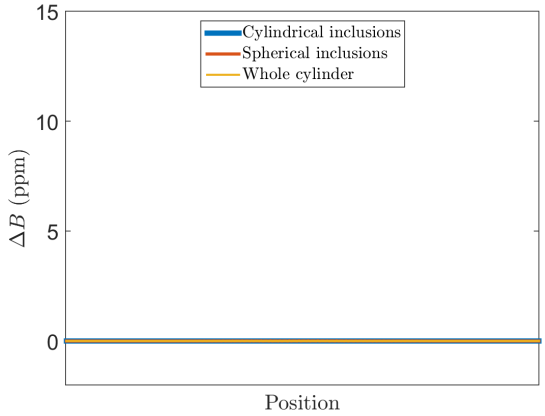
$$\Delta B_{\text{int}_{\text{av}}} = \frac{\chi_{I_{\text{vol}}}}{3} - \frac{\chi_{I_{\text{vol}}}}{2} \sin^2 \theta \tag{7.23}$$

obtaining the same results as an infinite, homogeneous cylinder with SOL correction as outlined in Table 4.5. This was confirmed using the simulated $\Delta B(\vec{r})$ maps, with results shown in Figure 7.7.

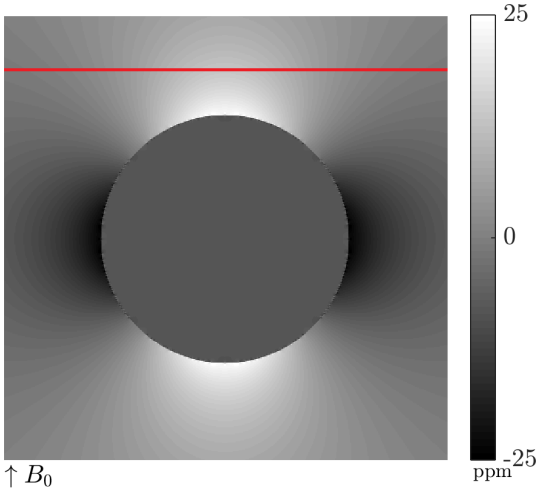
Repeating the above simulation, it is now assumed that the susceptibility inclusions *do not contribute* to the sampled signal. For interpretation purposes, the susceptibility inclusions can be considered as non-hydrogen containing regions, surrounded by water. External to the susceptibility inclusions, field perturba-



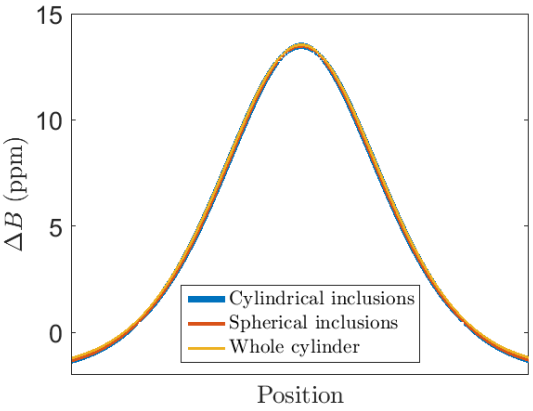

(a) $\Delta B(\vec{r})$ - solid cylinder




(b) line profile




(c) $\Delta B(\vec{r})$ - solid cylinder



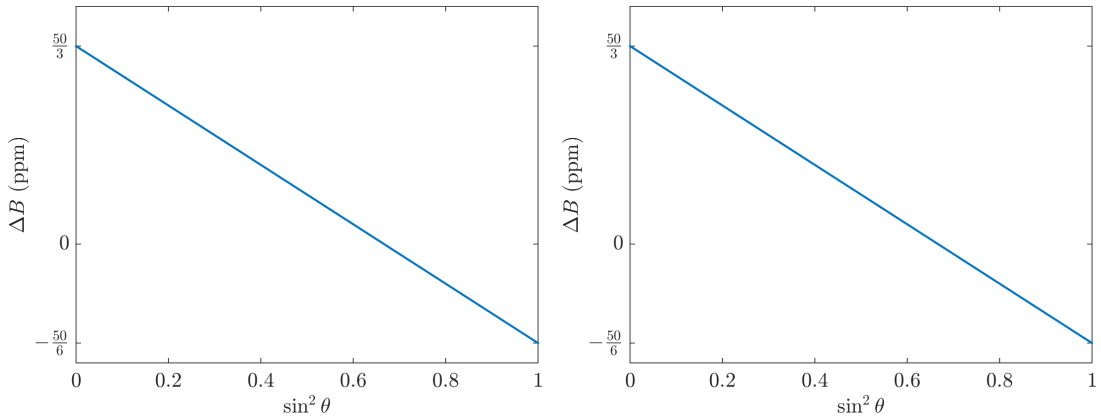

(d) line profile

Figure 7.6: $\Delta B(\vec{r})$ maps for a solid cylinder (Figures 7.6a and 7.6c) with $\chi_{I_{\text{vol}}} = 50\,\text{ppm}$. Comparisons of the line profiles (red line) of $\Delta B(\vec{r})$ over the solid cylinder parallel (Figure 7.6b) and perpendicular (Figure 7.6d) to $\vec{B}_0$ show a near identical form to the susceptibility inclusion cases (Figure 7.5), with small errors generated from the discrete nature of the Fourier transform operations and the susceptibility inclusions. Figures 7.6a and 7.6c simulated using the $k$-space forward model (described in Section 4.3) on a 2100×2100×200 matrix using MATLAB (Release 2015a, The MathWorks Inc., Natick, MA, United States).

tions are generated which impact the signal from the surrounding medium. For cylindrical susceptibility inclusions, it can be determined that averaging the field generated outside a single infinite cylindrical susceptibility inclusion of radius $a$ centred in a cylindrical volume of length $2z$ and radius $\rho$ (from Equation 7.22):

$$\int_{-z}^{z} dz \int_{a}^{\rho} d\rho \int_{0}^{2\pi} \rho d\phi \, \Delta B_{\text{ext}_{\text{cyl}}}(\rho, \phi, \theta) = 0 \tag{7.24}$$

for any choice of integral length, $z$, integral radius $\rho$ or angle between the $\vec{B}_0$ field and the principal axis of the cylinder, $\theta$. This concept can be expanded when




(a) $\Delta B_{\text{int}_{\text{av}}}$ for spherical inclusions (b) $\Delta B_{\text{int}_{\text{av}}}$ for cylindrical inclusions

Figure 7.7: Comparison of $\Delta B_{\text{int}_{\text{av}}}$ for spherical susceptibility inclusions (Figure 7.7a) and cylindrical susceptibility inclusions (Figure 7.7b) as a function of $\sin^2\theta$, with the assumption that the susceptibility inclusions contribute to the sampled signal ($\chi_{I_{\text{med}}} = 1\,\text{ppm}$ and $\chi_{I_{\text{vol}}} = 50\,\text{ppm}$). Here $\Delta B_{\text{int}_{\text{av}}}$ is taken over the entire cylindrical body (blue and green region in Figure 7.4). From the simulations it is apparent that $\Delta B_{\text{int}_{\text{av}}}$ is independent of the form of the internal susceptibility inclusions and only depends on the volume susceptibility, $\chi_{I_{\text{vol}}} = 50\,\text{ppm}$.

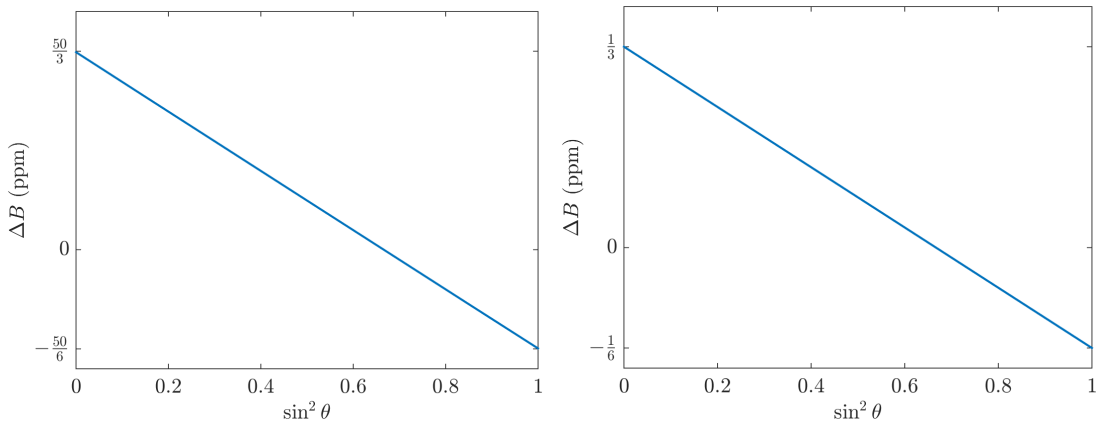
averaging the fields generated from a set of cylinders evenly distributed over a cylindrical volume (as visualised in Figures 7.4b and 7.4d), as the cylindrical symmetry of the system will lead to cylindrically symmetric averaging of the external field perturbations. Therefore when considering cylindrical susceptibility inclusions within a cylindrical volume, the signal sampled will only depend on $\chi_{I_{\text{med}}}$ and is independent of $\chi_{I_{\text{cyl}}}$, defining:

$$\Delta B_{\text{int}_{\text{av-cyl}}} = \frac{\chi_{I_{\text{med}}}}{3} - \frac{\chi_{I_{\text{med}}}}{2}\sin^2\theta. \tag{7.25}$$

However, the field generated from a single spherical susceptibility inclusion of radius $a$ centred within a cylindrical volume is equivalent to the internal field perturbations generated within an infinite cylinder, defining:

$$\int_{-z}^{z} dz \int_{0}^{\rho} d\rho \int_{0}^{2\pi} \rho d\phi\, \Delta B_{\text{ext}_{\text{sph}}}(\varrho, \Theta) = \frac{\chi_{I_{\text{vol-cyl}}}(\rho, z)}{3} - \frac{\chi_{I_{\text{vol-cyl}}}(\rho, z)}{2}\sin^2\theta \tag{7.26}$$

where $\varrho$ is the radial spherical coordinate measured relative to the centre of the sphere, $\Theta$ defines the angle between the $\vec{B}_0$ field and $\vec{\varrho}$ respectively and $\chi_{I_{\text{vol-cyl}}}(\rho, z)$ is the volume susceptibility of the cylinder (dependent on both the radius and length of the cylindrical integral). The cylindrical surface must encompass the entire spherical volume (with $z$ significantly greater than $a$ to simulate the infinite cylinder condition). As with the cylindrical inclusion case, this concept can be expanded when averaging the fields generated from a set of spheres evenly distributed over a cylindrical volume (as visualised in Figures 7.4a and 7.4c), as the cylindrical symmetry of the system will lead to cylindrically symmetric averaging




(a) $\Delta B_{\text{int}_{\text{av}}}$ for spherical inclusions (b) $\Delta B_{\text{int}_{\text{av}}}$ for cylindrical inclusions

Figure 7.8: Simulation results comparing $\Delta B_{\text{int}_{\text{av}}}$ for spherical susceptibility inclusions (Figure 7.7a) and cylindrical susceptibility inclusions (Figure 7.7b) as a function of $\sin^2\theta$, with the assumption that the susceptibility inclusions *do not* contribute to the sampled signal ($\chi_{I_{\text{med}}} = 1\,\text{ppm}$ and $\chi_{I_{\text{vol}}} = 50\,\text{ppm}$). Here $\Delta B_{\text{int}_{\text{av}}}$ is taken over the cylindrical body external to the susceptibility inclusions (blue region in Figure 7.4) With cylindrical susceptibility inclusions, $\Delta B_{\text{int}_{\text{av}}}$ is independent of $\chi_{I_{\text{cyl}}}$, depending only on $\chi_{I_{\text{med}}}$ (Figure 7.8b). This is unlike the case for spherical susceptibility inclusions (Figure 7.8a).

of the external field perturbations. As $\Delta B_{\text{int}_{\text{sph}}} = 0$ (Table 4.5), the integral is independent of the internal field perturbations of the sphere. Therefore when considering spherical susceptibility inclusions within a cylindrical volume, the sampled signal depends on both $\chi_{I_{\text{med}}}$ and $\chi_{I_{\text{sph}}}$, defining:

$$\Delta B_{\text{int}_{\text{av-sph}}} = \frac{\chi_{I_{\text{vol}}}}{3} - \frac{\chi_{I_{\text{vol}}}}{2}\sin^2\theta \tag{7.27}$$

identical to the form in Equation 7.25. This was confirmed using the simulated $\Delta B(\vec{r})$ maps, with results shown in Figure 7.8.

Returning to the $\chi_I(\vec{r})$ distribution in Figure 7.4, shrinking the cylindrical susceptibility inclusions to a microstructural size, though the individual cylinders cannot be directly imaged, they will still have an impact on the field perturbations within each voxel. External to the cylindrical body, Equation 7.22 will remain valid and external susceptibility inclusions will depend on $\chi_{\text{vol}}$. However, internally:

$$\vec{B}_{\text{int}_{\text{cyl}}} = \vec{B}_0 + \vec{B}_0\left(\frac{1}{3} - \frac{1}{2}\sin^2\theta\right)\chi_{I_{\text{med}}}. \tag{7.28}$$

This can be extended for arbitrary spin distributions, generating the SOL expression in Equation 4.28:

$$\vec{B}_{\text{spin}}(\vec{r}) = \vec{B}_0 + \vec{B}_0\left(\frac{1}{3} - \frac{1}{2}\sin^2\theta(\vec{r})\right)\chi_{I_{\text{med}}}(\vec{r}) + \vec{B}_d(\vec{r}). \tag{7.29}$$

### 7.3.3 Evidence in White matter

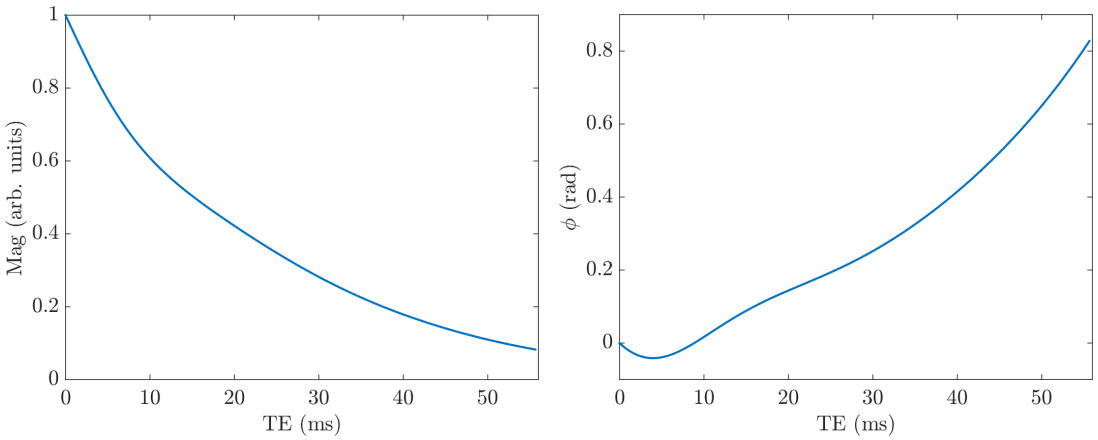
In 2014, Luo et al. [16] experimentally validated the GLA by examining the field perturbations induced inside and outside an *ex-vivo* rat optic nerve as a function of $\theta$, the angle between the $\vec{B}_0$ field and the principal axis of the optic nerve, hypothesising that differences in the susceptibility properties of field perturbations internal and external to the optic nerve provided evidence of microstructural cylindrical susceptibility inclusions. In 2015, Wharton and Bowtell [15] provided further evidence, observing a $\sin^2\theta$ dependence of field perturbations within a porcine optic nerve, after independently calculating and removing the field perturbations evaluated using the average susceptibility values derived from analysis of the externally measured field perturbations. Simulation work has also been used [23] to support the use of the GLA model to explain the changes in phase contrast in multiple sclerosis lesions in white matter.
However, Lee et al. [3] provided evidence that anisotropic susceptibility (discussed in Section 7.1) was more suited to explain the observed field perturbations in white matter. By segmenting an *ex-vivo* corpus callosum sample and rotating sections to $\vec{B}_0$ while maintaining the macroscopic structure, observed changes in external field perturbations (results shown in Figure 7.1) do not agree with the GLA proposition that external field perturbations should only depend on the volume susceptibility of the sample. Further work on the GLA [19] acknowledged the importance of susceptibility anisotropy and proposed a model consisting of anisotropic cylindrical susceptibility inclusions within an isotropic susceptibility medium. This bridges the gap between anisotropic susceptibility and the GLA, while maintaining the hypothesis that tissue microstructure must reflect the symmetry of the anisotropy distribution. Despite this, continued discussion on the mathematical basis of the GLA is still apparent, with alternative mechanisms proposed to explain the observed field perturbations in white matter [24].

## 7.4 Compartmentalisation

### 7.4.1 What is Compartmentalisation?

Previous work in this chapter has described how anisotropic susceptibility, chemical exchange and non-spherical susceptibility inclusions which do not generate an NMR signal can generate field perturbations that cannot be effectively described using a model of isotropic susceptibility alone. The theory outlined in this chapter (and previous chapters) has been presented assuming either [25, 26]:

1. Magnetic inclusions within tissue are well mixed and GE signal evolution




(a) Mag(TE) (b) $\phi$(TE)

Figure 7.9: Example of multi-exponential magnitude decay and non-linear phase evolution for a three compartment system. Signal evolution of this form provides evidence of signal compartmentalisation. Here $S_{0,1/2/3} = 0.126/0.501/0.373$, $T^*_{2,1/2/3} = 6.1/25.3/41.5\,\text{ms}$ and $\Delta f_{1/2/3} = 31.8/2.0/-4.1\,\text{Hz}$. Values taken from experimentally determined results over the *in-vivo* human splenium at 7T [28].

from a single voxel follows the monoexponential form in Equation 3.33.

2. Molecular mixing rates between compartments within a single voxel is fast compared to the relaxation times within compartments, leading to signal averaging within a voxel and GE signal evolution from a single voxel following the form in Equation 3.33.

However, these assumptions are not valid in all experimental circumstances and the signal from a single voxel can consist of the combined signal from separate compartments (also known as 'pools') with unique magnetic properties, generalising Equation 3.33 for GE sequences as follows [27, 28] :

$$S(t) = \sum_{n=1}^{N} S_{0,n} e^{-\frac{t}{T^*_{2,n}}} e^{-i\cdot 2\pi \Delta f_n t} \tag{7.30}$$

where $n$ is the compartment number and $N$ is the total number of compartments, with the notation $2\pi\Delta f$ used rather than $\Delta\omega$ to remain consistent with literature on compartmentalised signal. When examining the magnitude signal from a multi-echo GE or spin-echo (SE) [29] sequence, deviations of the signal from a mono-exponential decay is indicative of compartmentalisation of the tissue. For multi-echo GE phase signal, tissue compartmentalisation can lead to non-linear phase evolution (example shown in Figure 7.9).
It is worth noting that the classification of a multi-compartmental signal would not be necessary if it would be possible to improve spatial resolution to discriminate

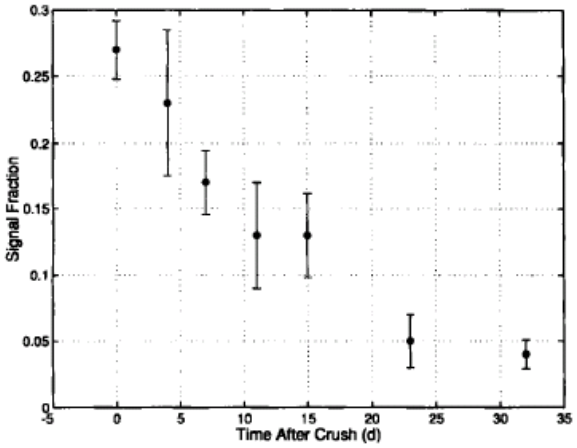
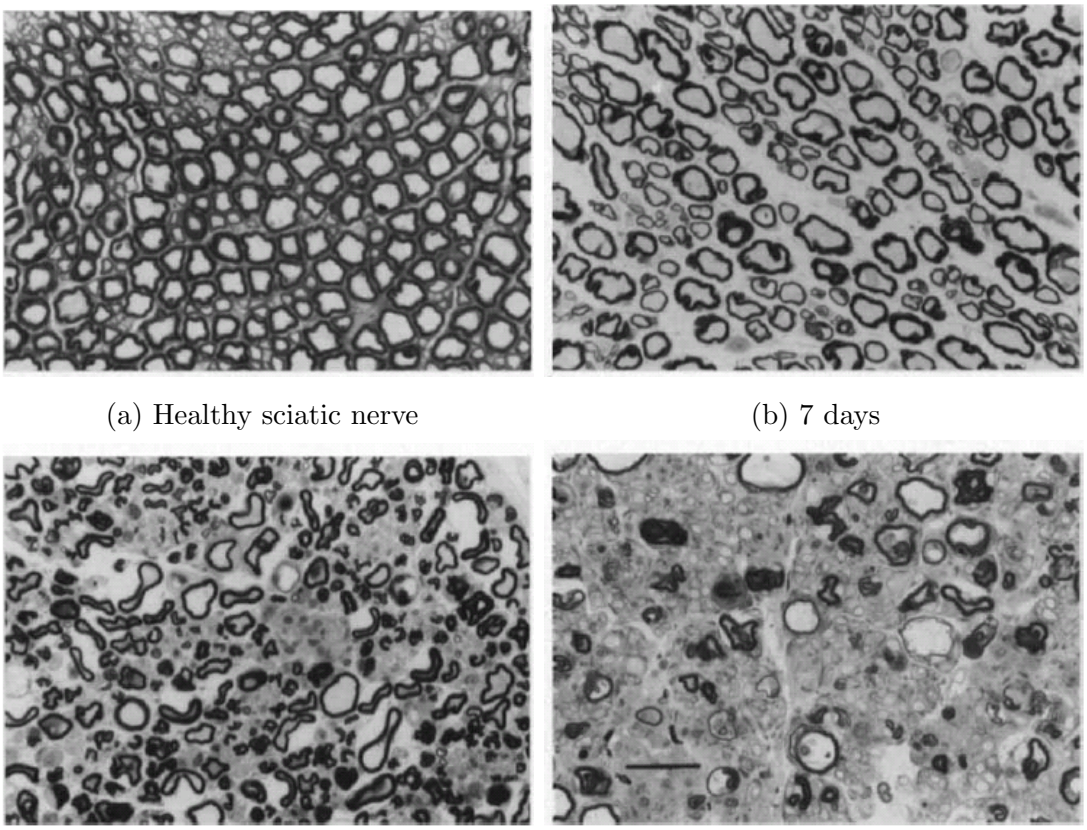



Figure 7.10: Decrease in the fractional content of the short $T_2$ component (associated with myelin) with increased time after damage to sciatic nerve. Figure taken from [32].

between the different compartments, in a similar fashion to how current MRI resolution allows us to discriminate between different regions of the brain. However, tissue structures leading to compartmentalisation in white matter are typically of the order of $\mu$ m [30, 31] or less in size, which far exceeds the current resolution possibilities of *in-vivo*, *ex-vivo*, pre-clinical and clinical scanner resolutions. Therefore multi-echo GE datasets, combined with modelling and confirmation with histology are essential in classifying these microstructural effects in tissue.

### 7.4.2 $T_2$ Compartmentalisation of White Matter

The first paper providing evidence of *in-vivo* signal compartmentalisation in the human brain was published in 1994, when MacKay et al. [33] distinguished three distinct compartments with unique $T_2$ properties within individual white matter voxels. MacKay et al. [33] combined multi-echo SE experimental data over the human brain with non-negative, voxelwise least squares fitting of an arbitrary number of exponential components to the experimentally measured signal evolution. Here, a short $T_2$ component ($10\,\text{ms} < T_2 < 55\,\text{ms}$) was observed and assigned to the myelin compartment, with a second, longer $T_2$ component ($70\,\text{ms} < T_2 < 90\,\text{ms}$) assigned to water in axonal/extracellular spaces and a third, long $T_2$ component ($T_2 \geq 1\,\text{s}$) assigned to cerebrospinal fluid. Further work [25] improved on the least squares fitting to quantify a smooth $T_2$ distribution curve over different brain regions *in-vivo*, repeating the observation of a short $T_2$ myelin compartment, in addition to providing evidence of distinct separation of axonal and extracellular compartments in some white matter regions, observing three peaks with $T_2 < 1\,\text{s}$. Strong evidence to further associate the short $T_2$ component with the myelin compartment, in addition to quantification and separation of the axonal and extracel-



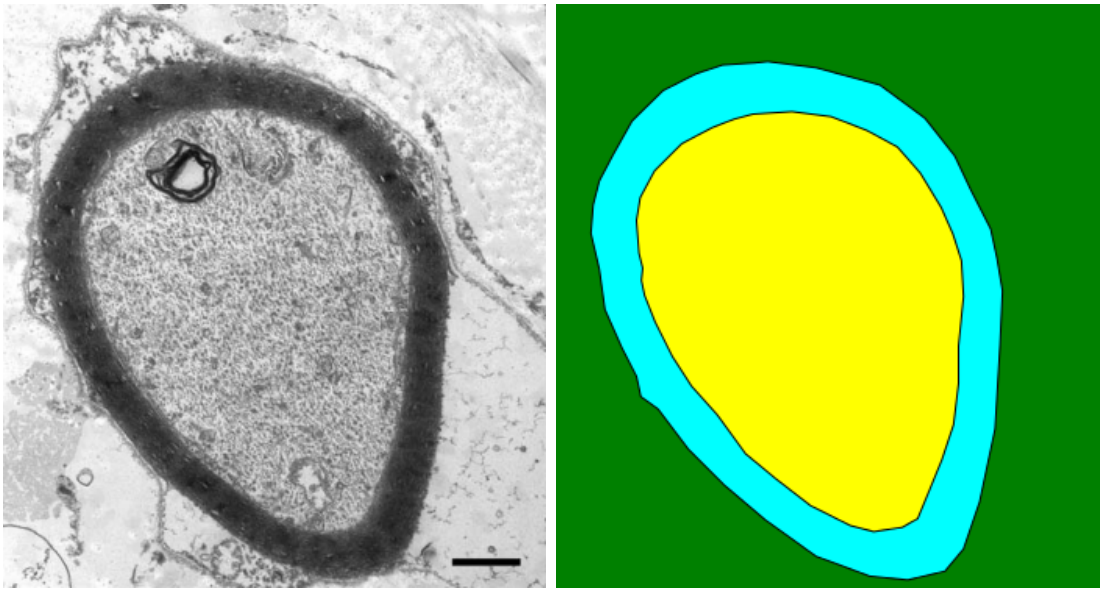
(a) Healthy sciatic nerve (b) 7 days

(c) 14 days (d) 28 days

Figure 7.11: Histology showing increased damage to the healthy sciatic nerve (Figure 7.11a 7 days (Figure 7.11b), 14 days (Figure 7.11c) and 28 days (Figure 7.11d) postinjury. Images adapted from [32].

lular compartments was provided with an *in-vitro* study of the frog sciatic nerve undergoing degeneration after injury [32]. In the healthy sciatic nerve, three separate compartments, with $T_2 < 250\,\text{ms}$ were observed, associated with the axonal, myelin and extracellular spaces. As the sciatic nerve deteriorated, the initial three-compartment, triple-exponential signal evolution of the sciatic nerve transformed into a one-compartment, mono-exponential signal evolution, with an observed decrease in the fraction of the short $T_2$ component associated with myelin (Figure 7.10). Utilising histology of the degenerating sciatic nerve (Figure 7.11), Does et al. [32] were able to associate the decrease in signal compartmentalisation with a decrease in the myelin fractional content and breakdown in the myelin compartment (Figure 7.10), observing an initial swelling of the extracellular space followed by myelin breakdown. Additionally, this provided direct evidence that myelin acts as a diffusion barrier between the axonal and extracellular space, forming the three separate compartments with distinct magnetic properties.

In 2003, Lancaster et al. [31] utilised the repeated observation of three-compartments within white matter to improve quantification of myelin content *in-vivo*. Rather



(a) Optic nerve fibre (b) Three compartment model

Figure 7.12: Example of a through-plane slice of human optic nerve (Figure 7.12a) obtained via transmission electron microscopy. Figure 7.12b shows the interpretation of the nerve fibre in the three compartment model, indicating contributions from the axonal (yellow), myelin (blue) and extracellular (green) compartments. Bar in Figure 7.12a indicates 1 $\mu$m on scale. Figure 7.12a adapted from [34].

than fitting to an arbitrary number of exponential components [25, 32, 33], Lancaster et al. [31] restricted fitting to three exponential components, known as the 'three-pool' model:

$$S(t) = S_0 \left[ A_a e^{-\frac{t}{T_{2,a}}} + A_m e^{-\frac{t}{T_{2,m}}} + A_e e^{-\frac{t}{T_{2,e}}} \right]. \tag{7.31}$$

Here $a$, $m$ and $e$ refer to the axonal, myelin and extracellular compartment and $A_i$ are the relative amplitudes of each compartment ($A_a + A_m + A_e = 1$). A physical interpretation of this model is displayed in Figure 7.12. Utilising SE sequences to obtain a single $T_1$ weighted image and a dual-echo $T_2$ weighted image, with the assumption that $T_1$ decay is monoexponential and assigning $T_2$ values to the three pools, Lancaster et al. [31] calculated the relative amplitudes of the axonal, myelin and extracellular compartments, using the relative amplitude of the myelin water signal to quantify myelination changes within children. Andrews et al. [35] further verified the robustness of fitting with the three-pool model compared to an arbitrary number of exponential components, obtaining an improved three-compartment fit for the three-pool model in low SNR conditions in *in-vitro* optic nerve samples.

### 7.4.3 $T_2^*$ and $\Delta f$ Compartmentalisation in White Matter

The model of $T_2$ compartmentalisation in Equation 7.31 lays the foundation for the examination of the effects of signal compartmentalisation on GE ($T_2^*$ weighted) sequences (underlying theory of GE sequences discussed in Section 3.4). The GE sequence can provide significant advantages when examining compartmentalised signal, utilising short echo times and small echo spacings to sample the rapidly relaxing signal from the myelin compartment [36]. Furthermore, GE sequences are fast, have a low specific absorption rate (SAR) and are advantageous at higher field strengths [36].

In white matter, the average $T_2^*$ relaxation time is significantly shorter than the corresponding $T_2$ (values given in Table 3.2). Therefore $T_2^*$ weighting provides the possibility to examine the signal evolution with a smaller contribution of molecular mixing between the compartments [27]. Furthermore, GE acquisitions provide phase information, which can additionally be examined for compartmentalisation. For a GE sequence, Equation 7.31 is written as follows [27, 28]:

$$S(t) = S_0 \left[ A_a e^{-\frac{t}{T_{2,a}^*}} e^{-i\cdot 2\pi \Delta f_a t} + A_m e^{-\frac{t}{T_{2,m}^*}} e^{-i\cdot 2\pi \Delta f_m t} + A_e e^{-\frac{t}{T_{2,e}^*}} e^{-i\cdot 2\pi \Delta f_e t} \right]. \quad (7.32)$$

This equation leads to a complex relationship when examining multi-echo GE signal evolution and the magnitude of Equation 7.32 will not provide a purely $T_2^*$ weighted three-compartment signal:

$$\begin{aligned} \mathrm{Mag}(t) &= S_0 \left[ \sum_{\substack{k= \\ a,m,e}} \sum_{\substack{l= \\ a,m,e}} A_k A_l e^{-t\left(\frac{1}{T_{2,k}^*}+\frac{1}{T_{2,l}^*}\right)} e^{-i\cdot 2\pi(\Delta f_k - \Delta f_l)t} \right]^{\frac{1}{2}} \\ &\neq S_0 \left[ \sum_{\substack{k= \\ a,m,e}} \sum_{\substack{l= \\ a,m,e}} A_k A_l e^{-t\left(\frac{1}{T_{2,k}^*}+\frac{1}{T_{2,l}^*}\right)} \right]^{\frac{1}{2}}. \end{aligned} \quad (7.33)$$

When $k = l$, the complex terms cancel. However when $k \neq l$, the complex terms lead to additional cosine modulation (example in Figure 7.13). For example, the interference between the signals from the axonal and myelin pool is as follows:

$$\begin{aligned} \mathrm{Mag}_{a,m}(t) &= S_0 \left[ A_a A_m e^{-t\left(\frac{1}{T_{2,a}^*}+\frac{1}{T_{2,m}^*}\right)} \left( e^{-i\cdot 2\pi(\Delta f_a - \Delta f_m)t} + e^{-i\cdot 2\pi(\Delta f_m - \Delta f_a)t} \right) \right]^{\frac{1}{2}} \\ &= S_0 \left[ 2A_a A_m e^{-t\left(\frac{1}{T_{2,a}^*}+\frac{1}{T_{2,m}^*}\right)} \cos\left(2\pi \Delta f_m t - 2\pi \Delta f_a t\right) \right]^{\frac{1}{2}}. \end{aligned} \quad (7.34)$$

As previously shown in Figure 7.9b, GE signal phase will not evolve linearly with time in compartmentalised tissue. For the three-pool model, taking the phase

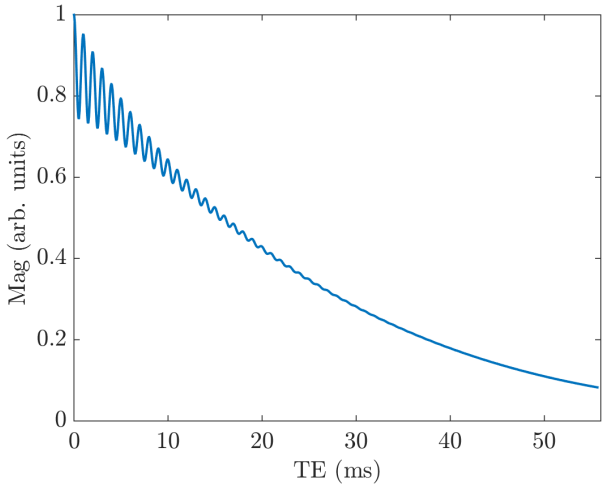



Figure 7.13: Visualisation of how the interaction between three compartments with unique $\Delta f$ properties can lead to cosine modulation of the magnitude signal. Parameters equal to those used in Figure 7.9, setting $\Delta f_1 = 1000\,\text{Hz}$ to visualise the modulation more clearly.

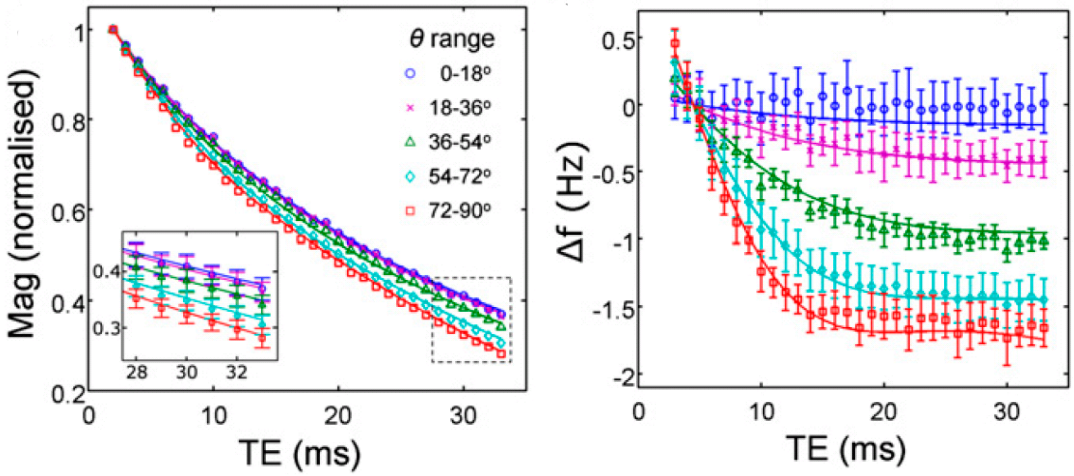
component of Equation 7.32:

$$\phi(t) = \arctan\left(-\frac{A_a e^{-\frac{t}{T^*_{2,a}}}\sin(2\pi\Delta f_a t) + A_m e^{-\frac{t}{T^*_{2,m}}}\sin(2\pi\Delta f_m t) + A_e e^{-\frac{t}{T^*_{2,e}}}\sin(2\pi\Delta f_e t)}{A_a e^{-\frac{t}{T^*_{2,a}}}\cos(2\pi\Delta f_a t) + A_m e^{-\frac{t}{T^*_{2,m}}}\cos(2\pi\Delta f_m t) + A_e e^{-\frac{t}{T^*_{2,e}}}\cos(2\pi\Delta f_e t)}\right). \tag{7.35}$$

Unlike the single compartment case, this formula will not reduce significantly and phase evolution is weighted by $A_{a,m,e}$ and $T^*_{2,a,m,e}$.

In 2010, Hwang et al [36] provided the first experimental example of *in-vivo* voxelwise fitting of multi-exponential GE magnitude data to the three-pool model, without accounting for the contribution of $\Delta f$, based on a preliminary study in post-mortem brain samples [37]. Similarly to the $T_2$ studies discussed in Section 7.4.2, Hwang et al [36] observed three distinct compartments and associated the shortest $T_2^*$ compartment with myelin. In 2012, Van Gelderen et al. [27] accounted for the additional phase modulation, utilising the full form of Equation 7.33 to improve fitting to multi-echo GE experimental magnitude data. Furthermore, Van Gelderen et al. [27] noted significant differences in the frequency offsets of the three compartments, observing a 'substantial' [27] positive frequency perturbation ($35.8 \pm 2.9$Hz at 7T and $19.4 \pm 2.6$Hz at 3T [27] in the *in-vivo* human splenium) of the short $T_2^*$ (myelin) compartment relative to extracellular compartment in white matter.

Further studies [17, 28] (experimental results from [28] over the *in-vivo* human splenium at 7T shown in Figure 7.9) examining the compartmentalisation of magnitude and phase data attested to the observation of the distinctive magnetic properties of the myelin pool, in addition to observing a significant orientation dependence of signal evolution in white matter (example in Figure 7.14).




(a) Mag(TE)

(b) Change in frequency (Hz)

Figure 7.14: Observation of orientation dependence of magnitude (Figure 7.14a) and frequency difference evolution (Figure 7.14b) *in-vivo* over white matter regions. Here $\theta$ defines the orientation of the nerve fibres relative to $\vec{B}_0$. Details of frequency difference evolution (and frequency difference mapping) discussed in Section 8.2. Images adapted from [17].

### 7.4.4 $T_1$ Compartmentalisation in White Matter

In addition to compartmentalisation of the transverse relaxation components, previous research has observed $T_1$ compartmentalisation within white matter [38], with the shortest $T_1$ component associated with the myelin compartment. From Equation 3.34, it can be determined that $T_1$ compartmentalisation will induce a dependence of the relative amplitudes of each compartment, $A_{a,m,e}$, on the flip angle, $\alpha$, and the TR:

$$A_{a,m,e} \propto \frac{1 - e^{-\frac{\mathrm{TR}}{T_{1,a,m,e}}}}{1 - e^{-\frac{\mathrm{TR}}{T_{1,a,m,e}}} \cos\alpha} \tag{7.36}$$

indicating that the determined amplitudes of the white matter compartments will vary with $\alpha$ and TR. A thorough investigation of the impact of this effect is beyond the scope of this Thesis. However, it can be noted that by varying $\alpha$ over multiple acquisitions, $T_1$ estimates for the individual compartments can be determined. Research into this is ongoing [39].

### 7.4.5 Considerations of Compartmentalisation

The existence of a significant frequency perturbation in the myelin compartment agrees with previous discussions on the role of myelin in susceptibility (Section 6.2) and chemical exchange (Section 7.2). Examination of the properties of GE signal evolution in white matter at different orientations to $\vec{B}_0$ was utilised to transform the three-pool model into a physical model describing the underlying

magnetic properties of white matter [17]. This model is introduced and discussed in detail in Section 8.3.

Compartmentalisation challenges the assumption of linear phase evolution and implies a TE dependence on the observed magnetic properties of tissue. Two recent papers [40, 41] have attested to the possibility of an observed TE-dependence of $\chi_I(\vec{r})$ maps derived from QSM. Yablonskiy and Sukstanskii [19] additionally modified the GLA to account for tissue compartmentalisation and it can be hypothesised that the increased contribution from myelin at lower TE would have an impact on the observed susceptibility anisotropy in white matter.

Due to the large number of individual components in the three-pool model (nine components - $A_{a,m,e}$, $T^*_{2,a,m,e}$ and $\Delta f_{a,m,e}$), fitting is an inherently ill-posed problem [27] and a low number of sampled echoes or low SNR restricts the possibility of obtaining unique values for the three-pool model components. This is particularly problematic for voxelwise analysis and typically assessment over ROIs is performed to obtain robust results in tissue [42]. In addition, examination of phase data for compartment fitting still requires filtering of the data via unwrapping and background field removal (previously discussed in Sections 5.2 and 5.3). Recent work by Nam et al. [42] incorporated background fields into fitting over the complex signal, avoiding the requirement of unwrapping and background field removal, reducing artefacts induced by processing errors in the results. However, any analysis utilising the three-pool method remains time consuming and prone to noise-induced fitting errors, preventing its practical use as both a robust research tool and use in clinic. In Chapter 8, a novel processing technique known as Frequency Difference Mapping (FDM) is introduced, which can rapidly provide information about signal compartmentalisation in tissue without the initial requirement of fitting to a multi-variable model. The chapter continues to describe a novel FDM algorithm which does not require the use of phase unwrapping or background field removal, in addition to a detailed discussion of an experiment performed using the technique over the *in-vivo* corpus callosum at 7T.

# Bibliography


[1] John Schenck. The role of magnetic susceptibility in magnetic resonance imaging: MRI magnetic compatibility of the first and second kinds. *Med. Phys.*, 23(6):815–850, 1996.

[2] Wei Li, Chunlei Liu, Timothy Q Duong, Peter Zijl, and Xu Li. Susceptibility tensor imaging (STI) of the brain. *NMR in Biomedicine*, 2016.

[3] Jongho Lee, Karin Shmueli, Masaki Fukunaga, Peter van Gelderen, Hellmut Merkle, Afonso C Silva, and Jeff H Duyn. Sensitivity of MRI resonance frequency to the orientation of brain tissue microstructure. *Proceedings of the National Academy of Sciences*, 107(11):5130–5135, 2010.

[4] Chunlei Liu. Susceptibility tensor imaging. *Magnetic resonance in medicine*, 63(6):1471–1477, 2010.

[5] Christian Denk, Enedino Hernandez Torres, Alex MacKay, and Alexander Rauscher. The influence of white matter fibre orientation on MR signal phase and decay. *NMR in Biomedicine*, 24(3):246–252, 2011.

[6] Wei Li, Bing Wu, Alexandru V Avram, and Chunlei Liu. Magnetic susceptibility anisotropy of human brain *in-vivo* and its molecular underpinnings. *Neuroimage*, 59(3):2088–2097, 2012.

[7] Xu Li, Deepti S Vikram, Issel Anne L Lim, Craig K Jones, Jonathan AD Farrell, and Peter CM van Zijl. Mapping magnetic susceptibility anisotropies of white matter *in-vivo* in the human brain at 7 T. *Neuroimage*, 62(1):314–330, 2012.

[8] Xu Li and Peter Zijl. Mean magnetic susceptibility regularized susceptibility tensor imaging (MMSR-STI) for estimating orientations of white matter fibers in human brain. *Magnetic resonance in medicine*, 72(3):610–619, 2014.

[9] Denis Le Bihan, Jean-François Mangin, Cyril Poupon, Chris A Clark, Sabina Pappata, Nicolas Molko, and Hughes Chabriat. Diffusion tensor imaging:

concepts and applications. *Journal of magnetic resonance imaging*, 13(4):534–546, 2001.

[10] Chunlei Liu, Wei Li, G Allan Johnson, and Bing Wu. High-field (9.4 T) MRI of brain dysmyelination by quantitative mapping of magnetic susceptibility. *Neuroimage*, 56(3):930–938, 2011.

[11] Karin Shmueli, Stephen J Dodd, Tie-Qiang Li, and Jeff H Duyn. The contribution of chemical exchange to MRI frequency shifts in brain tissue. *Magnetic resonance in medicine*, 65(1):35–43, 2011.

[12] Kai Zhong, Jochen Leupold, Dominik von Elverfeldt, and Oliver Speck. The molecular basis for gray and white matter contrast in phase imaging. *Neuroimage*, 40(4):1561–1566, 2008.

[13] M De Felici, R Felici, C Ferrero, A Tartari, M Gambaccini, and S Finet. Structural characterization of the human cerebral myelin sheath by small angle x-ray scattering. *Physics in medicine and biology*, 53(20):5675, 2008.

[14] K Shmueli, SJ Dodd, P Gelderen, and JH Duyn. Investigating lipids as a source of chemical exchange-induced MRI frequency shifts. *NMR in Biomedicine*, 2016.

[15] Samuel Wharton and Richard Bowtell. Effects of white matter microstructure on phase and susceptibility maps. *Magnetic resonance in medicine*, 73(3):1258–1269, 2015.

[16] J Luo, X He, and DA Yablonskiy. Magnetic susceptibility induced white matter MR signal frequency shifts—experimental comparison between Lorentzian sphere and generalized Lorentzian approaches. *Magnetic resonance in medicine*, 71(3):1251–1263, 2014.

[17] Samuel Wharton and Richard Bowtell. Fiber orientation-dependent white matter contrast in gradient echo MRI. *Proceedings of the National Academy of Sciences*, 109(45):18559–18564, 2012.

[18] Samuel Wharton and Richard Bowtell. Gradient echo based fiber orientation mapping using $R_2^*$ and frequency difference measurements. *Neuroimage*, 83:1011–1023, 2013.

[19] Dmitriy A Yablonskiy and Alexander L Sukstanskii. Generalized Lorentzian Tensor Approach (GLTA) as a biophysical background for quantitative susceptibility mapping. *Magnetic resonance in medicine*, 73(2):757–764, 2015.

[20] Xiang He and Dmitriy A Yablonskiy. Biophysical mechanisms of phase contrast in gradient echo MRI. *Proceedings of the National Academy of Sciences*, 106(32):13558–13563, 2009.

[21] Jeff H Duyn and Thomas M Barbara. The sphere of Lorentz and demagnetization factors in white matter. *Magnetic resonance in medicine: official journal of the Society of Magnetic Resonance in Medicine/Society of Magnetic Resonance in Medicine*, 72(1):1, 2014.

[22] Dmitriy A Yablonskiy, Xiang He, Jie Luo, and Alexander L Sukstanskii. Lorentz sphere versus generalized Lorentzian approach: What would lorentz say about it? *Magnetic resonance in medicine*, 72(1):4–7, 2014.

[23] Dmitriy A Yablonskiy, Jie Luo, Alexander L Sukstanskii, Aditi Iyer, and Anne H Cross. Biophysical mechanisms of MRI signal frequency contrast in multiple sclerosis. *Proceedings of the National Academy of Sciences*, 109(35):14212–14217, 2012.

[24] Thomas M Barbara. White matter shifts in MRI: Rehabilitating the Lorentz sphere in magnetic resonance. *Journal of Magnetic Resonance*, 270:40–46, 2016.

[25] Kenneth P Whittall, Alex L Mackay, Douglas A Graeb, Robert A Nugent, David KB Li, and Donald W Paty. *In-vivo* measurement of $T_2$ distributions and water contents in normal human brain. *Magnetic Resonance in Medicine*, 37(1):34–43, 1997.

[26] Mark D Does and John C Gore. Compartmental study of $T_1$ and $T_2$ in rat brain and trigeminal nerve *in-vivo*. *Magnetic resonance in medicine*, 47(2):274–283, 2002.

[27] Peter van Gelderen, Jacco A de Zwart, Jongho Lee, Pascal Sati, Daniel S Reich, and Jeff H Duyn. Nonexponential $T_2^*$ decay in white matter. *Magnetic resonance in medicine*, 67(1):110–117, 2012.

[28] Pascal Sati, Peter van Gelderen, Afonso C Silva, Daniel S Reich, Hellmut Merkle, Jacco A de Zwart, and Jeff H Duyn. Micro-compartment specific $T_2^*$ relaxation in the brain. *Neuroimage*, 77:268–278, 2013.

[29] E Mark Haacke, Robert W Brown, Michael R Thompson, Ramesh Venkatesan, et al. *Magnetic resonance imaging: physical principles and sequence design*, volume 82. Wiley-Liss New York:, 1999.

[30] Francisco Aboitiz, Arnold B Scheibel, Robin S Fisher, and Eran Zaidel. Fiber composition of the human corpus callosum. *Brain research*, 598(1):143–153, 1992.

[31] Jack L Lancaster, Trevor Andrews, L Jean Hardies, Stephen Dodd, and Peter T Fox. Three-pool model of white matter. *Journal of Magnetic Resonance Imaging*, 17(1):1–10, 2003.

[32] Mark D Does and Richard E Snyder. Multiexponential $T_2$ relaxation in degenerating peripheral nerve. *Magnetic resonance in medicine*, 35(2):207–213, 1996.

[33] Alex Mackay, Kenneth Whittall, Julian Adler, David Li, Donald Paty, and Douglas Graeb. *In-vivo* visualization of myelin water in brain by magnetic resonance. *Magnetic Resonance in Medicine*, 31(6):673–677, 1994.

[34] Valerio Carelli, Fred N Ross-Cisneros, and Alfredo A Sadun. Mitochondrial dysfunction as a cause of optic neuropathies. *Progress in retinal and eye research*, 23(1):53–89, 2004.

[35] Trevor Andrews, Jack L Lancaster, Stephen J Dodd, Carmen Contreras-Sesvold, and Peter T Fox. Testing the three-pool white matter model adapted for use with $T_2$ relaxometry. *Magnetic resonance in medicine*, 54(2):449–454, 2005.

[36] Dosik Hwang, Dong-Hyun Kim, and Yiping P Du. *In-vivo* multi-slice mapping of myelin water content using $T_2^*$ decay. *Neuroimage*, 52(1):198–204, 2010.

[37] Yiping P Du, Renxin Chu, Dosik Hwang, Mark S Brown, Bette K Kleinschmidt-DeMasters, Debra Singel, and Jack H Simon. Fast multislice mapping of the myelin water fraction using multicompartment analysis of $T_2^*$ decay at 3 T: a preliminary postmortem study. *Magnetic resonance in medicine*, 58(5):865–870, 2007.

[38] Daeun Kim, Hyo Min Lee, Se-Hong Oh, and Jongho Lee. Probing signal phase in direct visualization of short transverse relaxation time component (ViSTa). *Magnetic resonance in medicine*, 74(2):499–505, 2015.

[39] Elena Kleban, Benjamin Tendler, Penny Gowland, and Richard Bowtell. Probing the myelin water compartment with saturation recovery, multi-echo GE imaging at 7T. In *Proceedings of the 24$^{th}$ Annual Meeting of the ISMRM, Singapore*, page 1554, 2016.

[40] Surabhi Sood, Javier Urriola, David Reutens, Kieran O'Brien, Steffen Bollmann, Markus Barth, and Viktor Vegh. Echo time-dependent quantitative susceptibility mapping contains information on tissue properties. *Magnetic resonance in medicine*, 2016.

[41] Matthew J Cronin, Nian Wang, Kyle S Decker, Hongjiang Wei, Wen-Zhen Zhu, and Chunlei Liu. Exploring the origins of echo-time-dependent quantitative susceptibility mapping (QSM) measurements in healthy tissue and cerebral microbleeds. *NeuroImage*, 149:98–113, 2017.

[42] Yoonho Nam, Jongho Lee, Dosik Hwang, and Dong-Hyun Kim. Improved estimation of myelin water fraction using complex model fitting. *NeuroImage*, 116:214–221, 2015.

# Chapter 8

# Frequency Difference Mapping Applied to the Corpus Callosum at 7T

## 8.1 Introduction

White matter contrast in GE MRI has been attributed to the presence of myelin and its complex susceptibility (Section 6.2), chemical exchange (Section 7.2), structural (Section 7.3) and compartmentalisation (Section 7.4) properties relative to the surrounding tissue. The distinctive magnetic properties of myelin are characterised by short $T_2$ and $T_2^*$ relaxation times [1–12], in addition to a significant, orientation dependent frequency offset [5, 6, 13]. This chapter describes a project undertaken at the SPMIC examining the compartmentalisation properties of white matter to reveal information about its micro- (sub-voxel) structural properties.

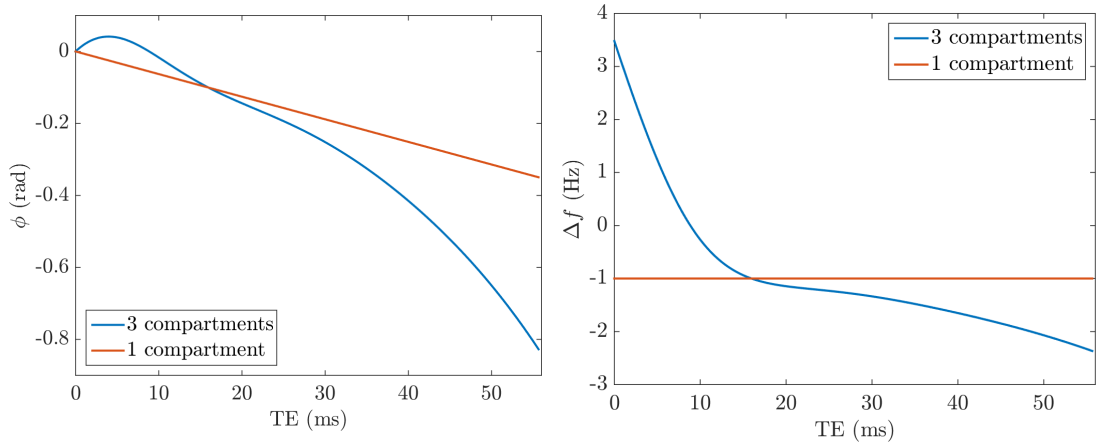
Previous work in this thesis (Section 7.4) discussed how tissue compartmentalisation is characterised by deviations of multi-echo GE magnitude signals from monoexponential decay, along with non-linear phase evolution. Frequency difference mapping (FDM) is a phase processing technique which characterises non-linear temporal phase evolution to probe signal compartmentalisation and reveal information about microstructure properties. The research described in this chapter introduces a novel FDM algorithm and demonstrates the sensitivity of FDM to white matter microstructure. To achieve this, frequency difference maps generated from multi-echo GE phase data via the novel FDM algorithm were combined with magnitude data to examine the temporal signal evolution in regions of the corpus callosum. The temporal signal evolution was then combined with a physical three-pool model of nerve fibres (three-pool model discussed in Section 7.4.3, physical model discussed in Section 8.3) to classify the underlying white matter distribu-

tion and indicate what properties give rise to signal variation across regions of the corpus callosum.
In this chapter, field perturbations are described using the notation $\Delta f$ in units of Hz, defined as evolving *positively* for a positive phase evolution as per the Philips convention ($\phi = +2\pi\Delta f t$). Conversions can be performed using the information in Table 3.3.

## 8.2 Frequency Difference Mapping

### 8.2.1 Introduction

Frequency difference mapping (FDM) is a recently developed phase-based technique [6, 13, 14] that takes advantage of the non-linear temporal evolution of the phase in GE sequences to obtain images that carry information about white matter microstructure. FDM is based on a simple concept - *in a voxel consisting of a single, well mixed compartment, phase will evolve at a constant rate, corresponding to a constant frequency. In voxels where the sub-voxel signal is compartmentalised into regions of distinct magnetic properties, phase will evolve at a changing rate, corresponding to a varying frequency.* This is visualised in Figure 8.1.
In previous work [6, 13, 14] FDM has been performed by filtering multi-echo GE phase data via unwrapping and background field removal (discussed in Sections 5.2 and 5.3) before converting individual echoes into frequency maps via scaling by $\frac{1}{2\pi\mathrm{TE}}$ (Equation 5.3). By comparing frequency images at different TE via subtraction (or some other comparative means), remaining contrast is indicative of compartmentalisation and therefore microstructure. Frequency difference measurements in white matter obtained by Wharton and Bowtell [6] are shown in Figure 7.14b, indicating the orientation dependence of the frequency difference in white matter.
The protocol below describes a novel FDM processing algorithm, hypothesised to reveal information about white matter microstructure and to be sensitive to small changes in microstructural content. Unlike other FDM and phase processing techniques, the algorithm introduced in this chapter does not require the use of sophisticated phase unwrapping and image filtering (discussed in Sections 5.2 and 5.3), which can induce artefacts in experimental data [15–17], as phase unwrapping and background field removal are indirectly performed as a direct consequence of the FDM protocol.




(a) $\phi$(TE)

(b) $\Delta f$(TE)

Figure 8.1: Comparison of phase (Figure 8.1a) and frequency (Figure 8.1b) evolution for a voxel consisting of a single compartment (red lines) and three compartments (blue lines), each with distinct magnetic properties. The single compartment voxel shows a linear evolution of phase with time, corresponding to a constant frequency. However, in the three compartment case, phase evolution is non-linear, corresponding to a frequency that varies with time. Parameters for the three-compartment model are those found in the splenium of the human corpus callosum *in-vivo* at 7T by Sati et al. [5] (parameters given in Figure 7.9), with a flip in the sign of the phase evolution to remain consistent with the Philips sign convention used throughout this chapter. Single compartment model simulated defining $\Delta f = -1\,\text{Hz}$ (amplitude and $T_2^*$ properties do not impact single-compartment phase evolution).

### 8.2.2 FDM Protocol

Unprocessed GE data obtained from the scanner shows phase variations due to non-local field sources (Section 5.3.1), $\Omega$, as well as time-independent phase offsets (Sections 5.2.2 and 6.5.1), $\phi_0$, due to RF transmit phase variation and sequence imperfections. The measured signal obtained from the scanner consequently takes the form:

$$S(t) = S_0 e^{i\Omega t} e^{i\phi_0} F(t) \tag{8.1}$$

where $F(t)$ is the contribution from local tissue content. In white matter, $F(t)$ can be described by the three-pool model (discussed in Section 7.4.3):

$$F(t) = A_a e^{-\frac{t}{T_{2,a}^*}} e^{i\cdot 2\pi\Delta f_a t} + A_m e^{-\frac{t}{T_{2,m}^*}} e^{i\cdot 2\pi\Delta f_m t} + A_e e^{-\frac{t}{T_{2,e}^*}} e^{i\cdot 2\pi\Delta f_e t}. \tag{8.2}$$

To observe the non-linear phase evolution over white matter, it is necessary to unwrap the experimental phase data and then remove the dependence on $\Omega$ and $\phi_0$ to reveal the non-linear phase evolution resulting from the the three-pool model. In previous FDM methods [6, 13, 14], this was achieved via spatial unwrapping and background field removal (discussed in Sections 5.2 and 5.3). However, if the signal evolution is measured using a multi-echo GE sequence, with initial

echo time, $\mathrm{TE}_1$, and an inter-echo spacing, $\Delta\mathrm{TE}$, such that the $\mathrm{n}^{\mathrm{th}}$ echo time is $\mathrm{TE}_1 + (\mathrm{n}-1)\Delta\mathrm{TE}$, then $\phi_0$ can be eliminated by dividing the complex signal at the $\mathrm{n}^{\mathrm{th}}$ echo time, $\mathrm{TE}_\mathrm{n}$, by $S(\mathrm{TE}_1)$

$$\begin{aligned} S'(\mathrm{TE}_\mathrm{n}) &= \frac{S(\mathrm{TE}_\mathrm{n})}{S(\mathrm{TE}_1)} \\ &= e^{i\cdot 2\pi\Omega(\mathrm{n}-1)\Delta\mathrm{TE}} \cdot \frac{F(\mathrm{TE}_\mathrm{n})}{F(\mathrm{TE}_1)}. \end{aligned} \tag{8.3}$$

The effects of the non-local field perturbations (described by $\Omega$) can then be removed by dividing $S'(\mathrm{TE}_\mathrm{n})$ by $(S'(\mathrm{TE}_2))^{\mathrm{n}-1}$

$$\begin{aligned} S''(\mathrm{TE}_\mathrm{n}) &= \frac{S'(\mathrm{TE}_\mathrm{n})}{\left(S'(\mathrm{TE}_2)\right)^{\mathrm{n}-1}} \\ &= \frac{F(\mathrm{TE}_\mathrm{n})}{F(\mathrm{TE}_1)} \cdot \left(\frac{F(\mathrm{TE}_1)}{F(\mathrm{TE}_2)}\right)^{\mathrm{n}-1} \end{aligned} \tag{8.4}$$

yielding a signal which is predominantly sensitive to myelin, due to the form of $\left(\frac{F(\mathrm{TE}_1)}{F(\mathrm{TE}_2)}\right)^{\mathrm{n}-1}$ which enhances sensitivity to signals with short $T_2^*$. The argument of $S''(\mathrm{TE}_\mathrm{n})$ is then scaled:

$$\phi''_{\mathrm{Hz}}(\mathrm{TE}_\mathrm{n}) = \frac{\arg\left[S''(\mathrm{TE}_\mathrm{n})\right]}{2\pi\cdot(\mathrm{TE}_\mathrm{n} - \mathrm{TE}_2)} \tag{8.5}$$

to yield the frequency difference at the $\mathrm{n}^{\mathrm{th}}$ echo measured in Hz (protocol visualised in Figure 8.2). This can also be performed on the unprocessed phase data alone, $\phi(\mathrm{TE})$, replacing $S(\mathrm{TE})$ with the complex exponential $e^{i\cdot\phi(\mathrm{TE})}$, defining:

$$\phi(\mathrm{TE}_\mathrm{n}) = \arg\left[e^{i\cdot S(\mathrm{TE}_\mathrm{n})}\right] \tag{8.6}$$

$$\phi'(\mathrm{TE}_\mathrm{n}) = \arg\left[\frac{e^{i\cdot\phi(\mathrm{TE}_\mathrm{n})}}{e^{i\cdot\phi(\mathrm{TE}_1)}}\right] \tag{8.7}$$

$$\phi''(\mathrm{TE}_\mathrm{n}) = \arg\left[\frac{e^{i\cdot\phi'(\mathrm{TE}_\mathrm{n})}}{\left(e^{i\cdot\phi'(\mathrm{TE}_2)}\right)^{\mathrm{n}-1}}\right] \tag{8.8}$$

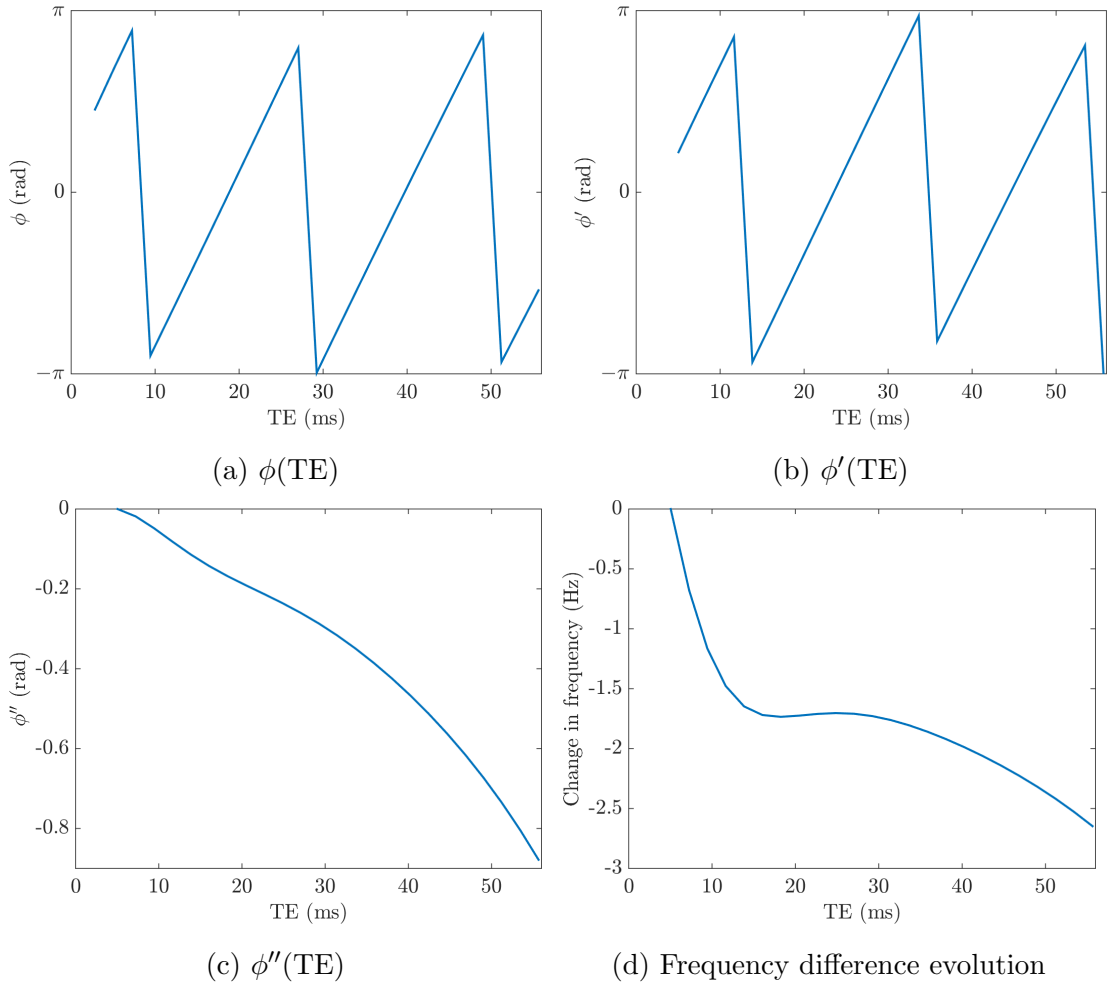
$$\phi''_{\mathrm{Hz}}(\mathrm{TE}_\mathrm{n}) = \frac{\phi''(\mathrm{TE}_\mathrm{n})}{2\pi\cdot(\mathrm{TE}_\mathrm{n} - \mathrm{TE}_2)}. \tag{8.9}$$

Defining noise in the argument of $S$ as scaling inversely with the magnitude data's SNR:

$$\mathrm{noise}_{\arg[S]} = \frac{\mathrm{noise}_{\mathrm{mag}}}{|S|}, \tag{8.10}$$

where $\mathrm{noise}_{\mathrm{mag}}$ is echo-time independent, it can be determined from Equation 8.5 that:

$$\mathrm{noise}_{\phi''_{\mathrm{Hz}}} = \sqrt{\frac{1}{|S_{\mathrm{n}|^2}} + \frac{(\mathrm{n}-2)^2}{|S_1|^2} + \frac{(\mathrm{n}-1)^2}{|S_2|^2}} \cdot \frac{\mathrm{noise}_{\mathrm{mag}}}{2\pi\cdot(\mathrm{TE}_\mathrm{n} - \mathrm{TE}_2)}. \tag{8.11}$$




(a) $\phi$(TE) (b) $\phi'$(TE)

(c) $\phi''$(TE) (d) Frequency difference evolution

Figure 8.2: Visualisation of FDM processing steps for the single-voxel phase evolution of a triple exponential signal with an additional non-local field source term, $\Omega = 50\,\text{Hz}$ and time-independent phase offset, $\phi_0 = 0.5\,\text{rad}$. Starting with the unprocessed wrapped phase (Figure 8.2a), the dataset is divided by the complex exponential of the first echo (Figure 8.2b and Equation 8.7) to remove any dependency on $\phi_0$. The dataset is then divided by the complex exponential of the scaled second echo (Figure 8.2c and Equation 8.8) to remove any dependency on $\Omega$ and subsequently scaled by the echo time difference times $2\pi$ to yield a frequency difference in Hz (Figure 8.2d and Equation 8.9). Parameters for the three-pool model defined as those found in the splenium of the human corpus callosum *in-vivo* at 7T by Sati et al. [5]. Parameters defined in Figure 7.9, with 25 echoes ($\text{TE}_1 = 2.84\,\text{ms}$, $\Delta\text{TE} = 2.2\,\text{ms}$, $\text{TE}_{25} = 55.6\,\text{ms}$). Results plotted against TE of the original signal, as with all future results presented within this chapter.

It is important to note that the form of $\phi''$(TE) does not yield information relating to the raw phase of the signal defined by $\phi$(TE). It reveals information about changes, or differences in measured frequency. The local phase, $\phi$(TE), described by a single compartment yields $\phi''(\text{TE}) = 0$ for all values of TE. This is made apparent when performing the scaled second echo division (Equation 8.8), as all linear variations of phase with time are removed (in a single-compartment signal, phase varies linearly with time). Any non-zero values of phase/frequency obtained

after generating images via FDM are indicative of non-linear phase evolution.

### 8.2.3 Advantages of FDM

In contrast to other phase-based approaches for probing white matter properties such as QSM (discussed in Section 5.4) and STI (discussed in Section 7.1), FDM can yield local contrast that is sensitive to microstructure without requiring the solution of a complex inverse problem. For example, QSM requires the implementation of sophisticated methods for inversion of the dipole field (discussed in Sections 5.4.3-5.4.5). Advancement of techniques to invert the dipole field have produced more accurate susceptibility maps, but all have been based on the requirement of solving the ill-conditioned dipole field inversion. Susceptibility tensor imaging is an even more complex inverse problem, and although it can be made well-conditioned with a sufficient number of well defined scanning orientations [18, 19], it is based on a scanning protocol which is time consuming, prone to error and impractical *in-vivo* considering the bore size of the scanner and requirements of subjects to remain still for long periods of time in uncomfortable positions (as discussed in Section 7.1.5).

The previous discussion on signal compartmentalisation (Section 7.4) focused on revealing white matter microstructure properties via fitting a three-pool model to experimental data. This poses the question as to what benefits FDM can provide a user over three-pool model fitting - both methods require the same set of initial multi-echo GE data. When performing FDM, contrast in frequency difference maps is indicative of microstructural content. Frequency difference maps can be obtained in a few simple steps and do not require fitting to the three-pool model to indicate the existence of microstructure. This is beneficial for rapid analysis of tissue properties. Once frequency difference maps have been obtained, fitting to the three-pool model can be performed to provide a more 'quantitative' analysis, but the contrast from FDM alone should be sufficient to observe both microstructure content and changes in microstructure content. The potential adaptability of this technique is significant - in this chapter a FDM protocol is introduced that is sensitive to the rapidly-decaying myelin pool in white matter, but it can be hypothesised that the FDM protocol could be adjusted to provide sensitivity to other sources of microstructural contrast.

## 8.3 Creating a Model of Myelinated Nerve Fibres

### 8.3.1 Requirements

From the previous discussions of white matter in this thesis, requirements for a model of myelinated nerve fibres can be considered as follows:

1. The model must be geometrically consistent with the underlying anatomical structure observed within myelinated nerve fibres, as per Figure 7.12a.
2. The model must consist of three separate compartments; the axonal, myelin and external compartments (Sections 7.4.2 and 7.4.3).
3. The susceptibility contrast will originate from the myelin compartment of the nerve fibre model (Section 6.2).
4. Susceptibility anisotropy must be present in the model and originate from radially-oriented lipid bilayers in the myelin (Section 6.2).
5. Chemical exchange must be present in the model and originate in the myelin (Section 7.2).
6. The contributions of fibre geometry, susceptibility, exchange and compartmentalisation must be able to effectively explain the observed orientation dependence of frequency perturbations, in addition to the experimentally observed evolution of multi-exponential magnitude signal and non-linear phase with time (Sections 7.4.2 and 7.4.3).

### 8.3.2 Geometric Structure of Myelinated Nerve Fibre Model

Examination of the structure of myelinated nerve fibres, as per Figure 7.12a indicates that they possess geometric similarities to a cylinder. Myelinated nerve fibres contain very long, continuous axons surrounded by myelin, with a through-plane geometry that possesses a high degree of cylindrical symmetry. A first approximation would be to model myelinated nerve fibres as infinite nested cylinders, with different radii corresponding to the axonal, myelin and external pools.
This model is a simplification of the distorted cylindrical structure that is observed experimentally. However it is a good first approximation for creating a model, as the susceptibility properties of cylinders are well understood and can be defined analytically and in the presence of a large number of near-cylindrical nerve fibres,

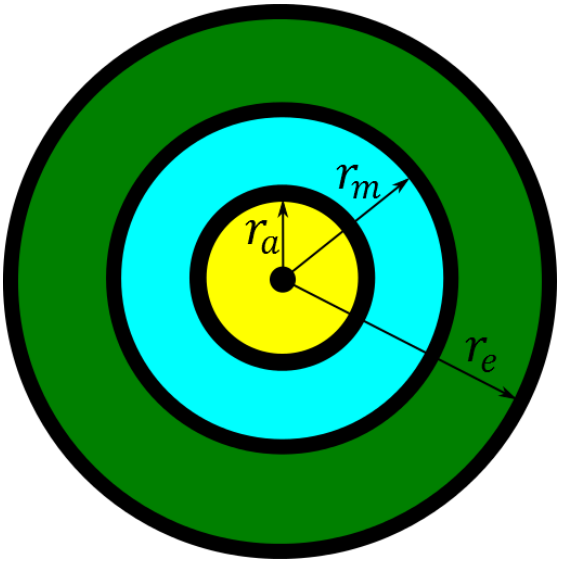



Figure 8.3: Visualisation of the 2D myelinated nerve fibre model containing the axonal (yellow), myelin (blue) and extracellular (green) compartments with radii $r_a$, $r_m$ and $r_e$ respectively. The external compartment is modelled as a cylinder to simplify the geometrical properties further.

the cylindrical approximation will be representative of the average underlying geometry. As the length of nerve fibres is significantly greater than the diameter, the infinite cylinder approximation is appropriate and a 2D model will be sufficient to explain the frequency properties. This is visualised in Figure 8.3.
From Figure 8.3, the fibre volume fraction (FVF) and g-ratio of nerve fibres can be defined as follows:

$$\begin{aligned} \text{FVF} &= \left(\frac{r_m}{r_e}\right)^2 \\ \text{g} &= \frac{r_a}{r_m} \end{aligned} \tag{8.12}$$

where $g$ is the g-ratio and $r_{a,m,e}$ are the radii of the axonal, myelin and extracellular compartments respectively. The FVF takes a value of between 0 and 1 which indicates the volume fraction of myelinated nerve fibres within a region. The g-ratio takes a value of between 0 and 1 that indicates the ratio of the radius of the axonal compartment to the radius of the nerve fibre. The relative thickness of the myelin sheath, $\frac{r_m - r_a}{r_m}$, scales as $1 - \text{g}$, so higher g-values corresponds to thinner sheaths. These two parameters are of great interest in neuroscience due to their relationship with brain function and disease.
From the physical description of the geometric fibre model, the values of $A_{a,m,e}$ in Equation 8.2 can be written in terms of the FVF and g-ratio of nerve fibres by

calculating the relative volumes of the different compartments [13]:

$$\begin{aligned} A_a &= \mathrm{FVF} \times g^2 \\ A_m &= \rho \times \mathrm{FVF}\left(1 - g^2\right) \\ A_e &= 1 - \mathrm{FVF} \end{aligned} \tag{8.13}$$

where $\rho$ is the relative water concentration of the myelin compartment, which has been reported as lower than the axonal and external compartments [6]. The form of Equation 8.13 means that:

$$A_a + \frac{A_m}{\rho} + A_e = 1. \tag{8.14}$$

### 8.3.3 Modelling Susceptibility in Myelin

As all of the susceptibility contrast in this model is assumed to originate from myelin, myelin can be defined with an isotropic/anisotropic susceptibility value, $\chi_{I/A}$, with the axonal and external compartments' susceptibility set to zero. Previous work by Wharton and Bowtell [6, 13] has produced analytical solutions for the average field perturbation induced by a nerve fibre model in which the myelin compartment has isotropic susceptibility $\chi_I$ and radially oriented anisotropic susceptibility, $\chi_A$, This gives for each of the three compartments:

$$\begin{aligned} \Delta B_{a-\chi} &= -B_0 \frac{3\chi_A \sin^2\theta}{4} \ln g \\ \Delta B_{m-\chi} &= B_0 \left[ \frac{\chi_I}{2}\left(\frac{2}{3} - \sin^2\theta\right) + \frac{\chi_A}{2}\left(\left(\frac{1}{4} + \frac{3}{2}\left(\frac{g^2}{1-g^2}\right)\ln g\right)\sin^2\theta - \frac{1}{3}\right)\right] \\ \Delta B_{e-\chi} &= 0 \end{aligned} \tag{8.15}$$

where $\theta$ defines the orientation of the nerve fibre with respect to the applied magnetic field.

### 8.3.4 Modelling Chemical Exchange in Myelin

From the previous discussion of chemical exchange in Section 7.2, chemical exchange is observed as an orientation-independent local frequency offset within tissue [20]. From this description, the average chemical exchange contribution in the myelinated nerve fibre model is defined as:

$$\begin{aligned} \Delta B_{a-E} &= 0 \\ \Delta B_{m-E} &= B_0 \cdot E \\ \Delta B_{e-E} &= 0. \end{aligned} \tag{8.16}$$

Combining this with the field perturbations induced by $\chi_I$ and $\chi_A$, the average total field perturbation per compartment, $\Delta B_{a,m,e}$:

$$\begin{aligned}
\Delta B_a &= -B_0 \frac{3\chi_A \sin^2\theta}{4} \ln g \\
\Delta B_m &= B_0 \left[ \frac{\chi_I}{2}\left(\frac{2}{3} - \sin^2\theta\right) + \frac{\chi_A}{2}\left(\left(\frac{1}{4} + \frac{3}{2}\left(\frac{g^2}{1-g^2}\right)\ln g\right)\sin^2\theta - \frac{1}{3}\right) + E \right] \\
\Delta B_e &= 0.
\end{aligned} \tag{8.17}$$

### 8.3.5 Application to the Three-Pool Model

From Equation 8.13, the geometric properties of nerve fibres can be obtained by fitting FDM data to the FDM modified three-pool model in Equation 8.5 to obtain $A_{a,m,e}$, $\Delta f_{a,m,e}$ and $T^*_{2,a,m,e}$. The FVF and g-ratio can be defined in terms of $A_{a,m,e}$ as:

$$\begin{aligned}
\text{FVF} &= \frac{A_m}{\rho} + A_a \\
g &= \sqrt{\frac{A_a}{\frac{A_m}{\rho} + A_a}}
\end{aligned} \tag{8.18}$$

and determined using the constraint in Equation 8.14 with a known value of $\rho$. $\chi_A$ can be determined by rearranging the axonal component of Equation 8.17 and inserting the determined values for $\Delta B_a$ (where $\Delta B_a = \frac{2\pi\Delta f_a}{\gamma}$ from Table 3.3) and $g$, with prior knowledge of $\theta$:

$$\chi_A = -\frac{4 \cdot \Delta B_a}{3\sin^2\theta \cdot \ln g \cdot B_0} \tag{8.19}$$

and with the determined value for $\Delta f_m$, $\chi_A$ and $g$, an expression for $\chi_I$ and $E$ can be obtained:

$$\frac{\chi_I}{2}\left(\frac{2}{3} - \sin^2\theta\right) + E = \frac{\Delta B_m}{B_0} - \frac{\chi_A}{2}\left(\left(\frac{1}{4} + \frac{3}{2}\left(\frac{g^2}{1-g^2}\right)\ln g\right)\sin^2\theta - \frac{1}{3}\right). \tag{8.20}$$

## 8.4 Method

Magnitude and phase data were collected from a single, sagittal slice of the *in-vivo* human brain in 10 healthy subjects via a multi-echo GE scan on a Philips Achieva 7T MR scanner. Each scan consisted of 20 echoes ($\text{TE}_1 = 2.4\,\text{ms}$, $\Delta\text{TE} = 2.4\,\text{ms}$,

$TE_{20}$ = 48 ms). The sagittal slice was positioned on the mid-line, thus spanning a portion of the corpus callosum where the fibres are oriented perpendicular to $\vec{B}_0$ (resolution = 1 $mm^2$, slice thickness = 5 mm, FOV = 224×224 $mm^2$), with TR = 140 ms, flip angle = 25°, no. of averages = 10, acquisition time = 314 s. A unipolar readout gradient was utilised by enabling 'flyback' gradients, to prevent discrepancies between odd and even echoes [21] at the cost of an increased minimum echo spacing, ΔTE. No flow compensation was utilised within this sequence, allowing a reduced first TE, $TE_1$, due to the introduction of additional gradients [22], but increasing sensitivity to flow artefacts from vessels surrounding the corpus callosum. Scanning was approved by the local ethics committee and all subjects gave informed consent.

Six scans were acquired per subject with subjects moved out and back into the scanner after the third scan to allow testing for repeatability between scans and scanning sessions. Phase data was processed as detailed in Section 8.2.2 to generate frequency difference maps. Co-registration was applied to each set of three images using FSL FLIRT [23–25] and involved co-registering the magnitude data and then applying the transformation matrix to subsequent frequency difference maps.

After each set of three scans, phase sensitive inversion recovery (PSIR), $T_1$-weighted images [26], were also acquired at the same orientation as the GE scans to distinguish the corpus callosum (resolution = 1 $mm^2$, slice thickness = 5 mm, no. of slices = 5, FOV = 224×224×25 $mm^3$, TE = 3.7 ms, no. of echoes = 1, TR = 12.9 ms, flip angle = 8°, no. of averages = 1, acquisition time = 40 s).

To examine the potential of using FDM as a method of classifying white matter tissue properties, the corpus callosum was manually masked in the PSIR image using MRIcron [27]. The corpus callosum was then split into five regions of interest (ROI) corresponding to the genu, anterior body, middle body, posterior body and splenium, by dividing the length of the corpus callosum into five distinct sections as defined in Aboitiz et al. [28] (splitting visualised in Figure 8.10). These five ROI were utilised to examine the signal evolution in the GE magnitude data and frequency difference maps, with signals summed and averaged over voxels in each ROI for the six repeats on each subject, to classify how signal magnitude and frequency difference developed with echo time for individual subjects. Additionally, ROI were taken over the superior cerebral peduncle and a grey matter region for further analysis (ROIs visualised in Figure 8.10).

Frequency difference data for all five ROI in the corpus callosum were then fitted to determine the individual components of the three-pool model for each subject. This was achieved by taking the phase component of the three-pool model, $F(TE)$

(Equation 8.2), running the FDM protocol (Equations 8.6-8.9) and fitting to the experimental data. Magnitude data was fitted to the absolute value of $F(t)$. This was performed using the 'lsqnonlin' function in MATLAB (Release 2013a, The MathWorks Inc., Natick, MA, United States) by simultaneously simulating the magnitude and frequency difference evolution for each experimental pair of magnitude and frequency difference data. Initial values of variables were set as shown in Table 8.1. $\Delta f_e$ was set equal to 0 in agreement with Equation 8.17 to reduce the number of fitting parameters, thus defining calculated $\Delta f_{a,m}$ values relative to $\Delta f_e$.

From the determined values of $A_{a,m,e}$, $\Delta f_{a,m,e}$ and $T^*_{2,a,m,e}$ for the different regions of the corpus callosum in individual subjects, Equations 8.18-8.20 were utilised to determine values for the FVF, g-ratio, $\chi_I$ and $\chi_A$. It is not possible to separate the contributions of $A_m/\rho$ or $\chi_I/E$ so values were determined with the assumption that $\rho = 0.7$ and $E = 20\,\text{ppb}$ as determined in previous literature [6]. In addition, $\theta$ was set to 90° based on the assumption that nerve fibres in the corpus callosum run perpendicular to the magnetic field with the head in standard orientation within the scanner.

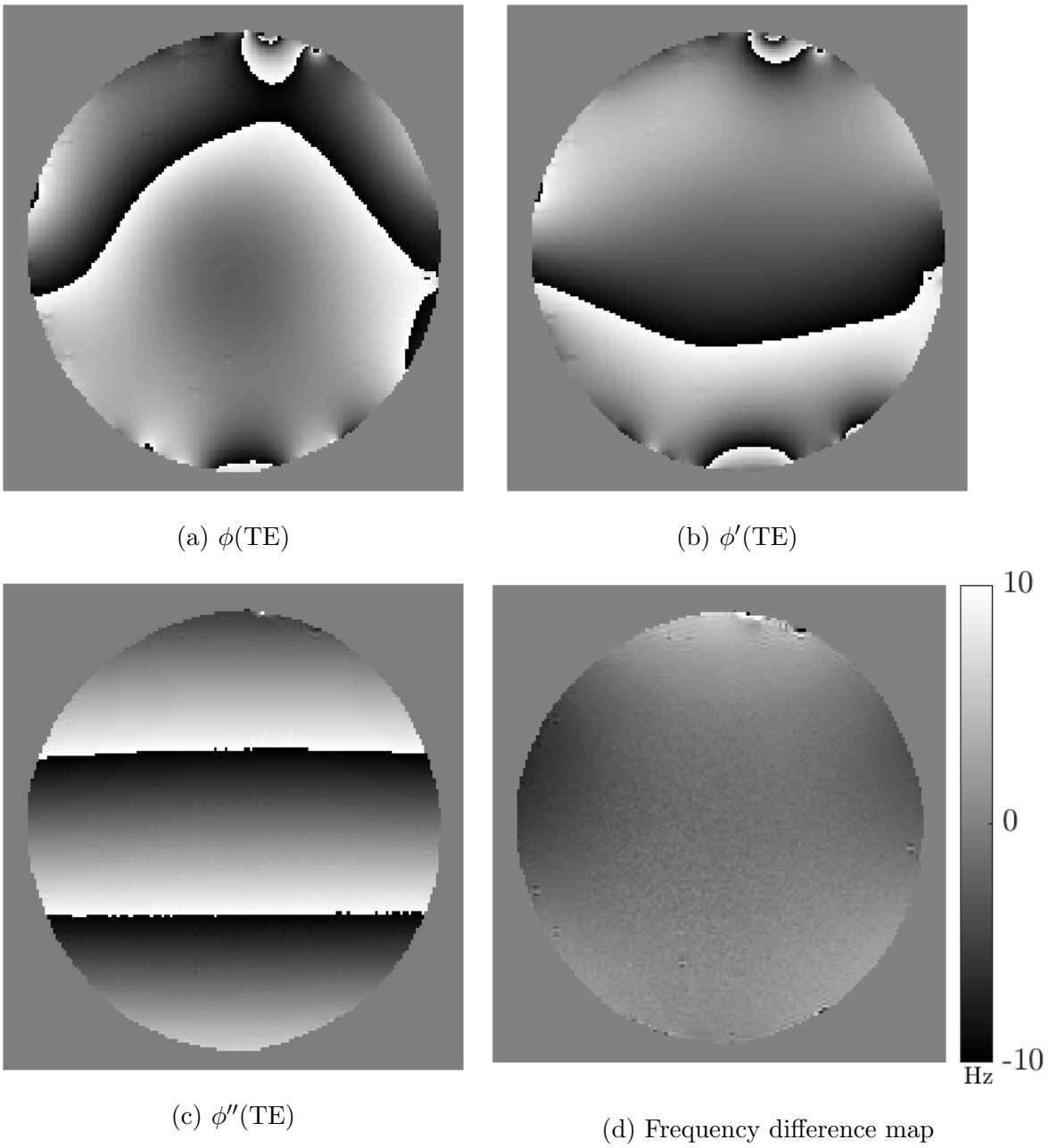
To test the robustness of the parameter values obtained from the model fit, simulated frequency difference data were generated from the parameters obtained from the middle body of the corpus callosum and normally distributed random noise was added to the real and imaginary simulated signal components of $F(\text{TE})$ (as a percentage of $F(\text{TE}_1)$). Magnitude and frequency difference evolution curves were then simulated as outlined in the theory section. These simulations were fitted to the model starting with parameters defined in Table 8.1 using the 'lsqnonlin' function in MATLAB (Release 2013a, The MathWorks Inc., Natick, MA, United States).

## 8.5 Applying FDM to Phantom and Brain Data

In a phantom consisting of a single homogeneous material, phase variation is expected to show a linear relationship with time due to the existence of only a

| **Parameter** | $T^*_{2a}$(ms) | $T^*_{2m}$(ms) | $T^*_{2e}$(ms) | $A_a$ | $A_m$ | $A_e$ | $\Delta f_a$(Hz) | $\Delta f_m$(Hz) |
|---|---|---|---|---|---|---|---|---|
| **Init. value** | 36 | 8 | 36 | 0.5 | 0.5 | 0.5 | 0 | 0 |
| **Min. value** | 0 | 0 | 0 | 0 | 0 | 0 | -100 | -100 |
| **Max. value** | 100 | 100 | 100 | 1 | 1 | 1 | 100 | 100 |

Table 8.1: Parameter values (initial and range) used in fit of experimental data to FDM and magnitude modified forms of Equation 8.2.




(a) $\phi$(TE) (b) $\phi'$(TE)

(c) $\phi''$(TE) (d) Frequency difference map

Figure 8.4: Visualisation of FDM processing steps for a sagittal slice, multi-echo GE scan over a homogeneous agar phantom at TE = 14.4 ms ($6^{\text{th}}$ echo). (a): Original unprocessed phase data (b): After division by first echo dataset to remove $\phi_0$ (c): After second scaled echo division to remove $\Omega$ (d): Filtered using a 1D complex filter and converted to Hz. The read gradient direction is vertical in the figure.

single compartment in each voxel. Therefore the frequency variation along the echo train is expected to remain at 0 Hz. To test this, a single-slice, sagittal, multi-echo GE scan was performed on an oblate spheroidal phantom consisting of a homogeneous agar solution (recipe outlined in [29]) at 7T (parameters identical for the single-slice *in-vivo* protocol outlined in Section 8.4). Processing steps are visualised in Figure 8.4. From the data it became apparent that when applying

FDM to experimental data, after the division by a scaled second echo to remove $\Omega$, an additional step is required, involving fitting and subtraction of a term describing linear phase variation in the read direction (foot-head), resulting from a phase correction step applied to individual echoes in the scanning protocol, referencing to the central line of $k$-space (Figure 8.4c). The complex data:

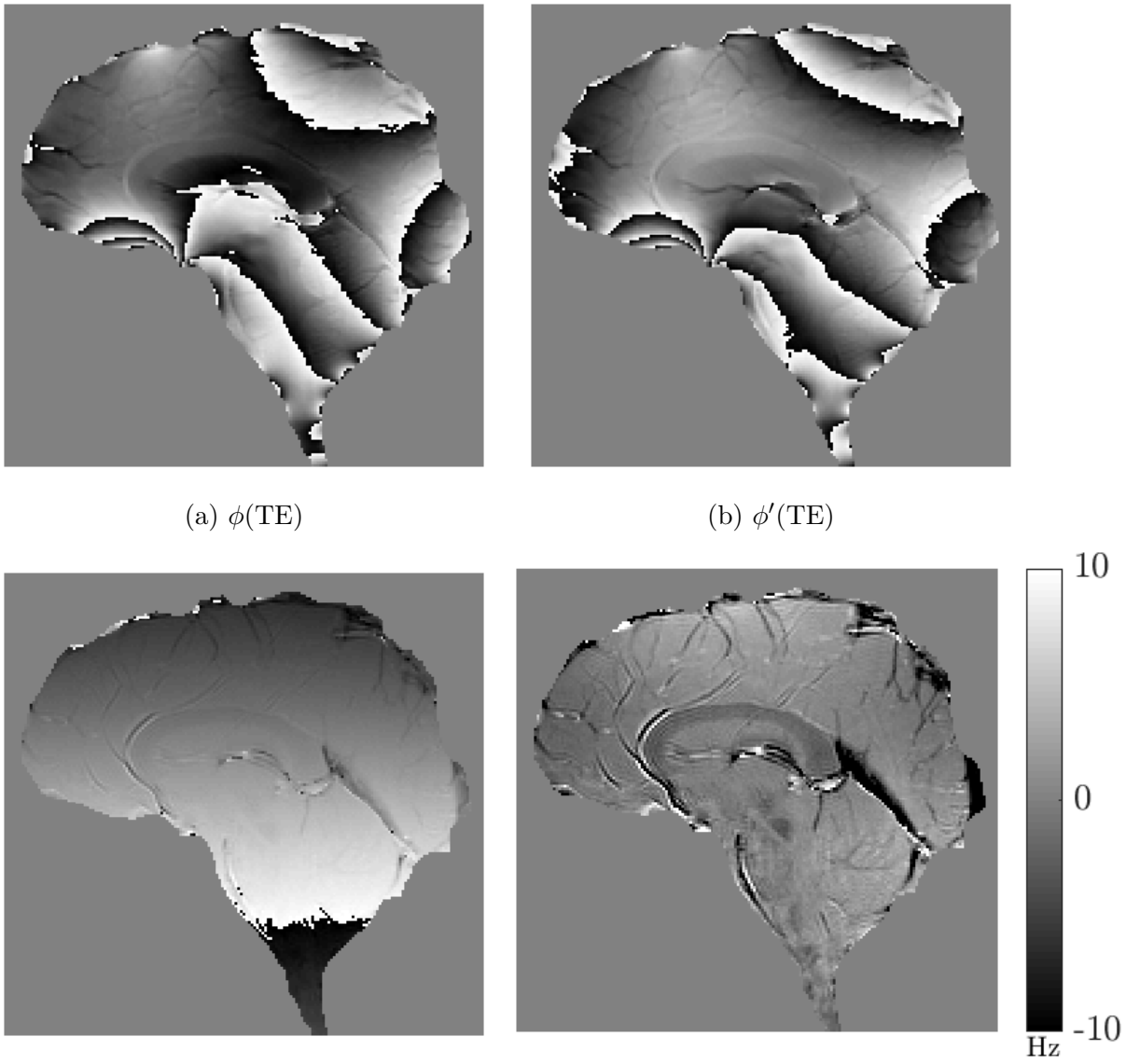
$$z(\mathrm{TE}_n) = \mathrm{Mag}(\mathrm{TE}_n) \cdot e^{i \arg \phi''(\mathrm{TE}_n)} \tag{8.21}$$

was summed in each individual echo along the phase encoding direction to yield a 1D profile which reveals coherent phase variation along the read direction. The phase variation along this profile was unwrapped and a $1^{\mathrm{st}}$ order polynomial fitted to the *in-vivo* phase, expanded into a 2D matrix and removed from $\phi''(\mathrm{TE})$ via complex division. This technique was applied to the masked brain, with steps visualised in Figure 8.5

Closer inspection of both the phantom and brain data yielded a distinctive pattern of small residual large-length-scale variation of the frequency data in both sets of images consisting of positive and negative lobes. These lobes are visualised in Figures 8.6a and 8.6b obtained by thresholding Figures 8.4d and 8.5d over a narrow frequency difference range ($\pm 1$ Hz). This pattern of frequency variation, which was found to be stable over repeated experiments, is most likely to due to short-lived eddy currents which produce small time-varying magnetic fields that contribute to non-linear phase evolution. In contrast to the frequency difference variation due to the anatomical distribution of myelinated structures, this contribution to the frequency difference has a low spatial frequency and varies smoothly with spatial position. It could therefore be removed from the data by subtracting a $6^{\mathrm{th}}$ order polynomial fit to the frequency difference data in which regions of anatomical contrast (white matter and blood vessels) had been masked out. This masking was performed by thresholding the frequency difference map to remove all voxels below $-3.5$ Hz and masking the whole corpus callosum with the manually generated ROI (Figure 8.6c). Results produced by using the eddy current removal procedure are shown in Figure 8.6d.

## 8.6 Results

Frequency difference maps obtained at TE = 14.4 ms ($6^{\mathrm{th}}$ echo) from all subjects are displayed in Figure 8.7, with corresponding PSIR and magnitude images shown in Figures 8.8 and 8.9. Figure 8.10 shows how the frequency difference maps develop with TE for a single subject, with corresponding magnitude images shown in Figure 8.11. Due to the nature of FDM processing, there is one less frequency difference map than the number of acquired phase images (Equation




(a) $\phi$(TE)

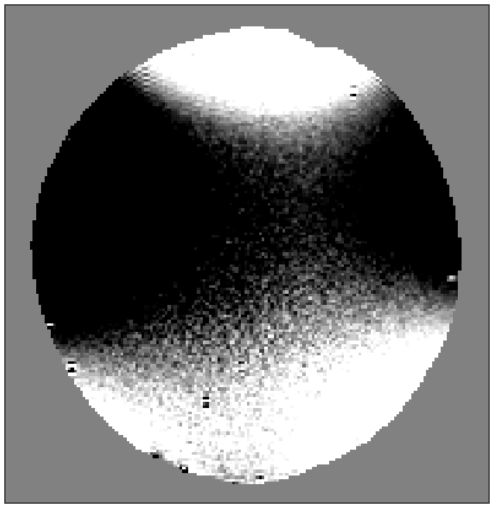
(b) $\phi'$(TE)

(c) $\phi''$(TE)

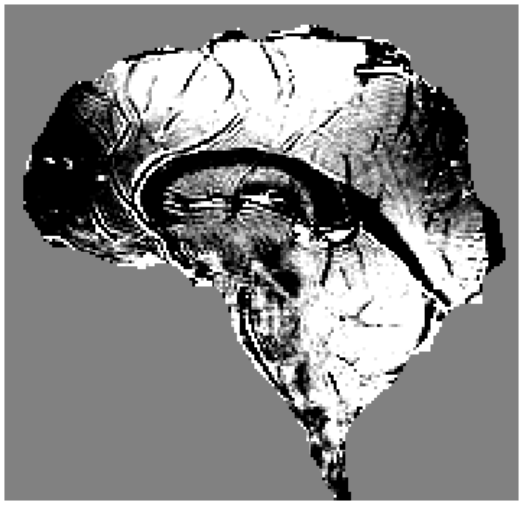
(d) Frequency difference map

Figure 8.5: Visualisation of FDM processing steps for a sagittal slice, multi-echo GE scan over the corpus callosum of an *in-vivo* human brain at TE = 14.4 ms ($6^{\text{th}}$ echo). (a): Original unprocessed phase data (b): After division by first echo dataset to remove $\phi_0$ (c): After second scaled echo division to remove $\Omega$ (d): Filtered using a 1D complex filter and converted to Hz. The read gradient direction is vertical in the figure.

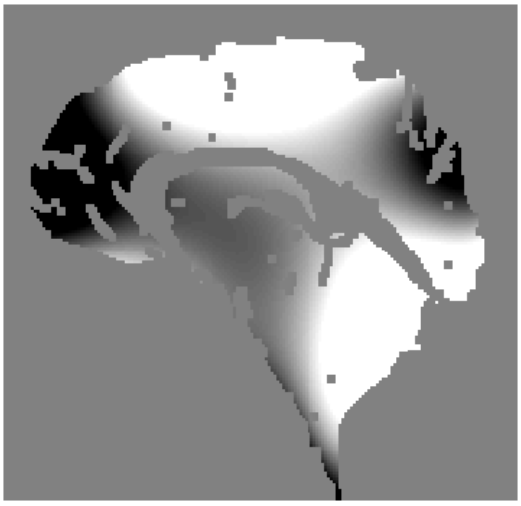
8.3) and all data values in the first image are equal to zero (Equation 8.4). The effects of $\phi_0$ and $\Omega$ have evidently been removed in the FDM processed images and anatomical structure is consistently depicted in these frequency difference maps, with white matter and blood vessels providing the dominant source of contrast. The corpus callosum in which the nerve fibres are oriented perpendicular to $B_0$ is clearly depicted as hypointense compared with the surrounding tissue, with the signal becoming more negative with increasing TE at the low echo times. Other



(a) Frequency difference map (±1 Hz)



(b) Frequency difference map (±1 Hz)



(c) Eddy current simulation



(d) Frequency difference map (±1 Hz)

Figure 8.6: (a) and (b): Distinctive lobe patterns observed in phantom and brain data scanned at the same orientation (TE = 14.4 ms). (c): simulation of large-scale field perturbations over the *in-vivo* brain via the use of a $6^{\text{th}}$ order polynomial fit over masked data (d): After removal of $6^{\text{th}}$ order polynomial fit. All images scaled between ±1 Hz.

structures, such as the superior cerebellar peduncle, the pons and medulla oblongata (highlighted in Figure 8.10), which contain white matter fibre bundles oriented perpendicular to the field also show similar behaviour. Veins also generally appear with low intensity in the frequency difference maps as a result of the significant frequency offset and rapid decay of the signal from venous blood, which will give rise to non-linear phase evolution. There is an increase in signal around arteries most likely resulting from flow effects.

Figures 8.12a and 8.12b compare a frequency difference map with the voxelwise standard deviation of three repeats from the same subject, to indicate the re-

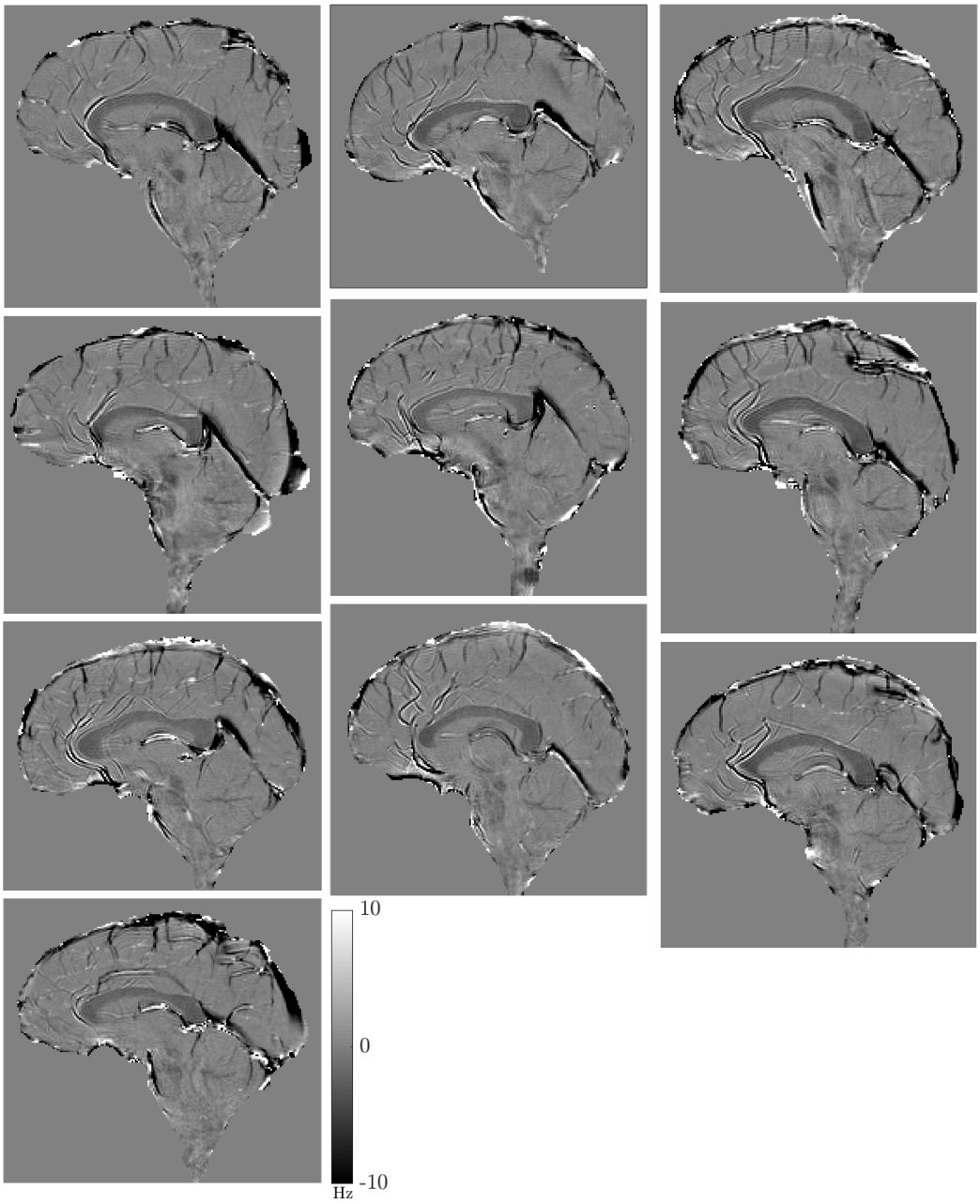



Figure 8.7: Individual frequency difference maps generated at TE = 14.4 ms for 10 subjects undergoing a single slice sagittal scan over the midline of the corpus callosum (parameters outlined in Section 8.4). All frequency difference maps scaled between ±10 Hz.

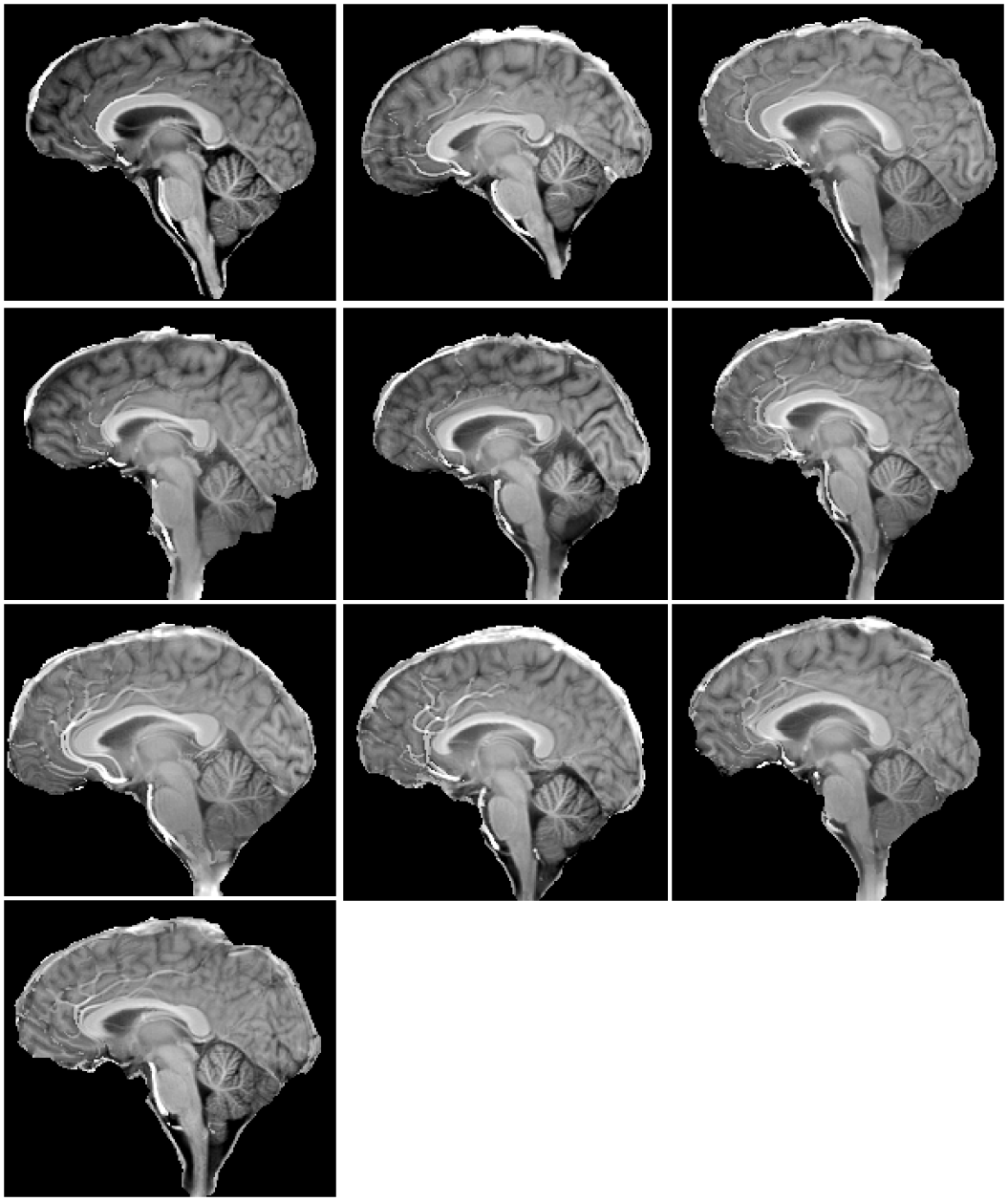


Figure 8.8: PSIR images of the mid-slice over all 10 subjects. Acquisition parameters given in Section 8.4.

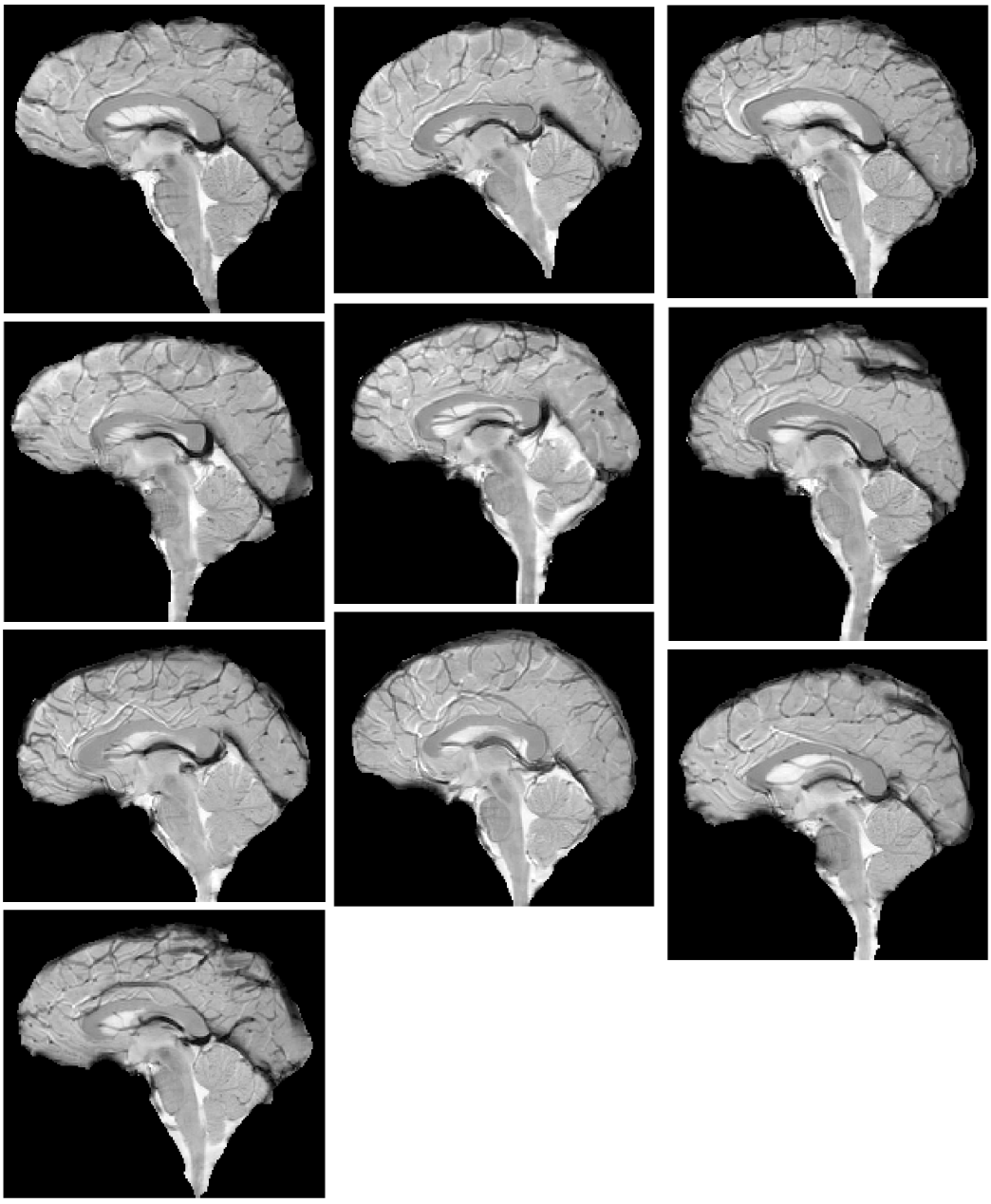


Figure 8.9: Magnitude images for the corresponding frequency difference maps over all 10 subjects as displayed in Figure 8.7. All echoes normalised to first echo image (TE = 2.4 ms) to show relative signal amplitude. TE = 14.4 ms displayed.

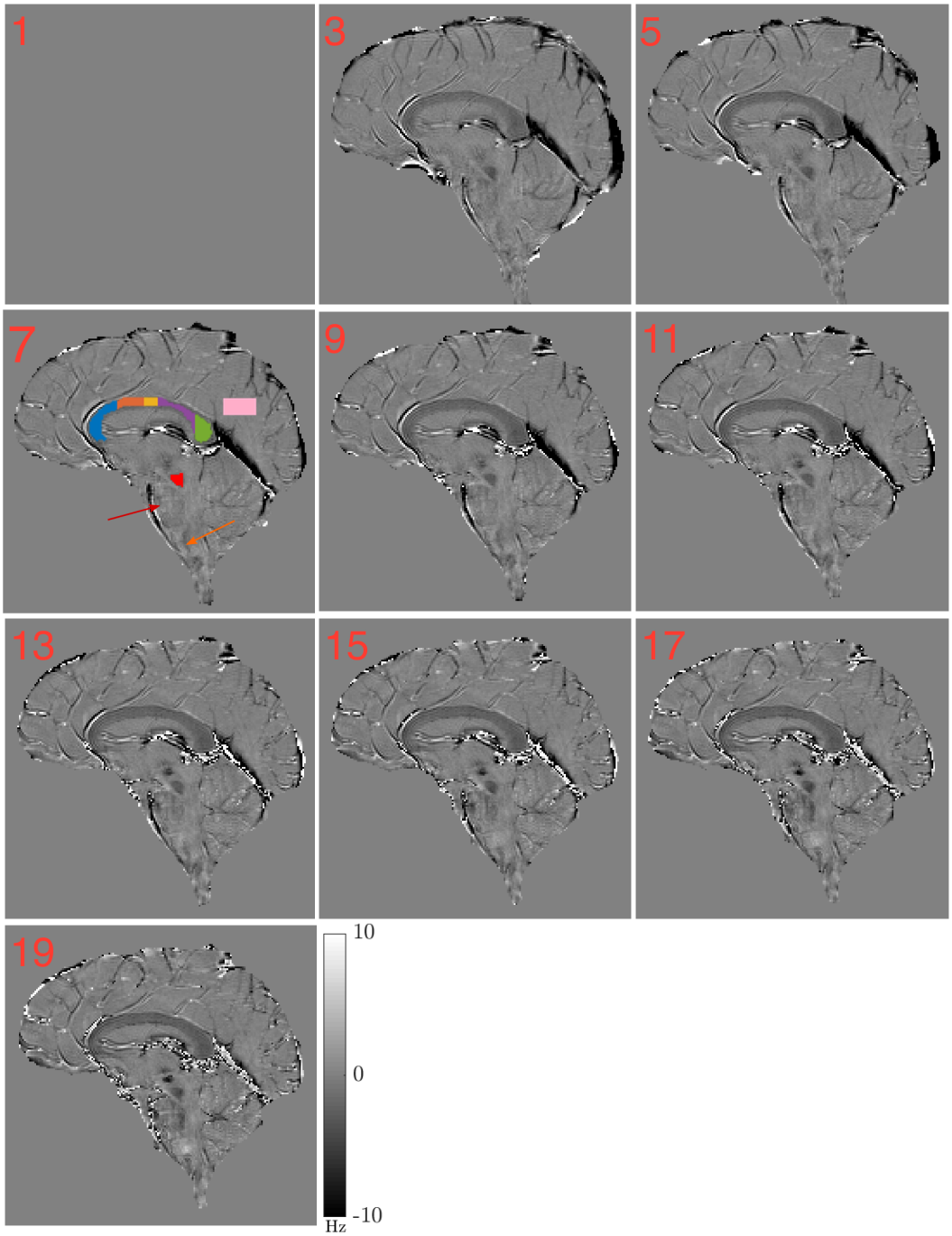



Figure 8.10: Development of frequency difference maps over a single subject undergoing a single slice sagittal scan over the midline of the corpus callosum (parameters outlined in Section 8.4). 19 echo times (TE = 4.8-48 ms), with every 2$^{nd}$ echo shown in this figure (numbered) from top left to bottom right (1$^{st}$, 3$^{rd}$ etc...). ROIs used in analysis for this subject shown on the 7$^{th}$ echo. Here the red arrow - pons, orange arrow - medulla oblongata. The highlighted corpus callosum shows splitting into 5 regions - genu (blue), anterior body (orange), middle body (yellow), posterior body (purple) and splenium (green). The red and pink ROI indicates the superior cerebral peduncle and grey matter region used in further analysis. All frequency difference maps scaled between ±10 Hz.

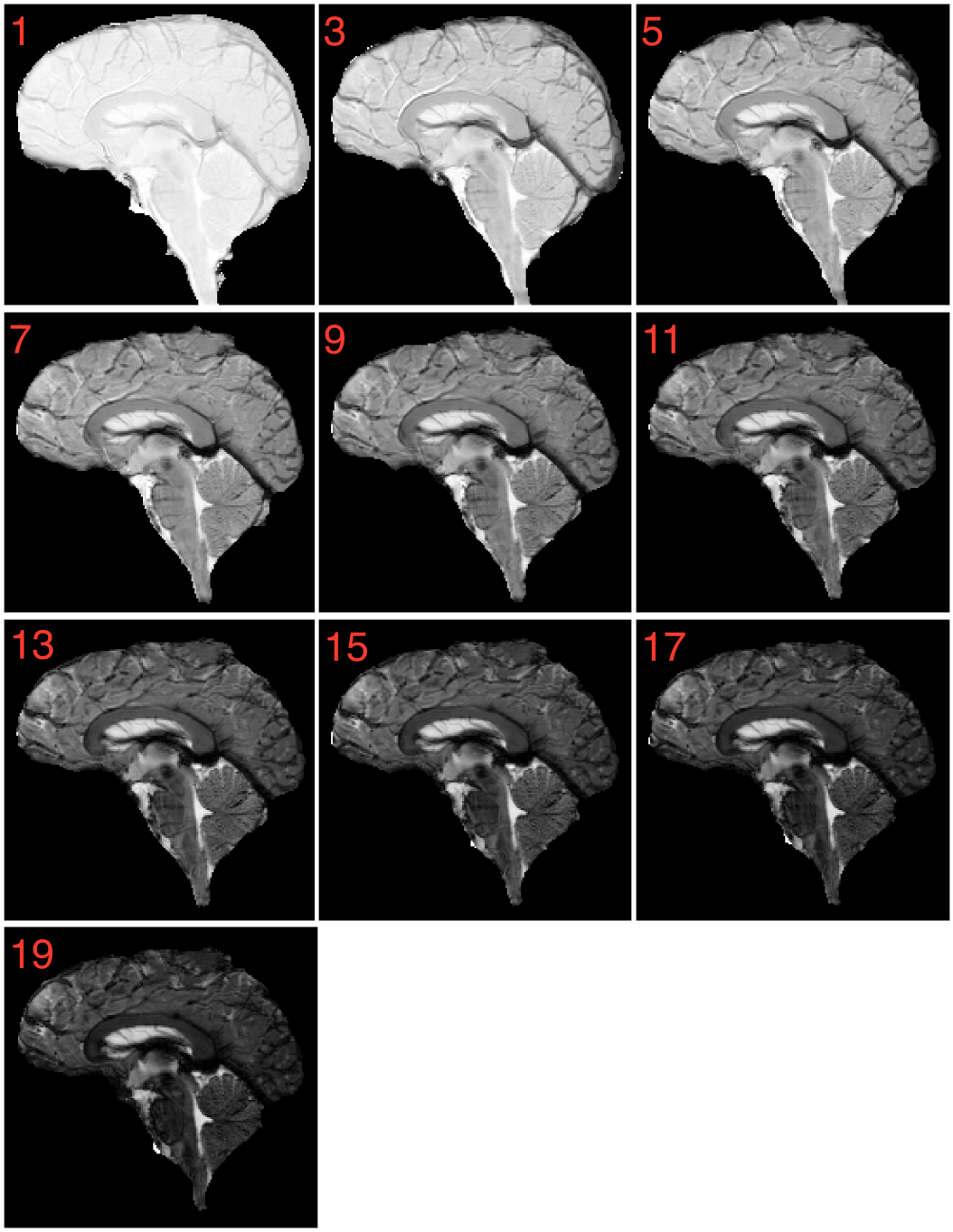
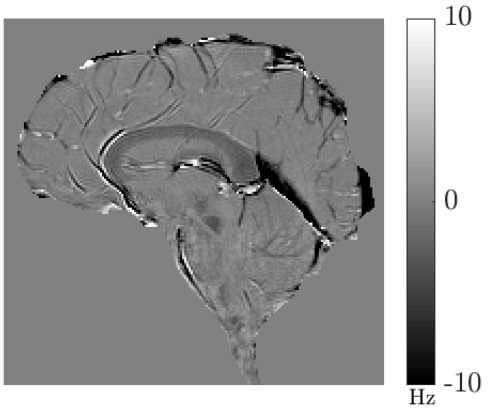
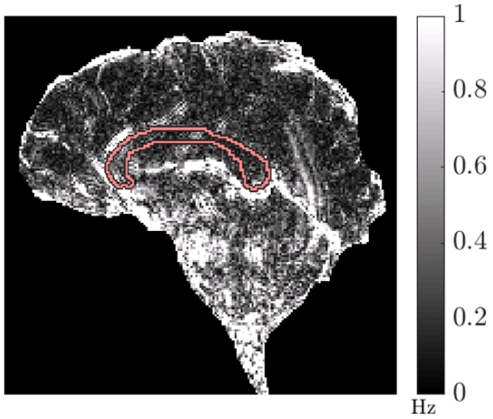


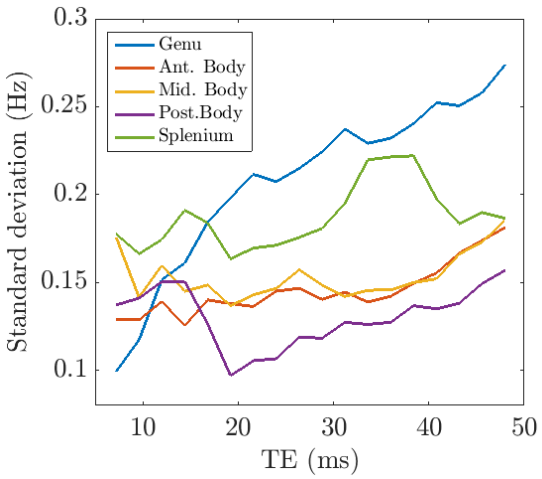

Figure 8.11: Magnitude images for the corresponding frequency difference maps over a single subject as displayed in Figure 8.10. All echoes normalised to first echo image to show relative signal amplitude (TE = 2.4 ms), setting Mag(TE = 2.4 ms) equal to one for all voxels. 19 echo times (after removing normalised first echo) with every 2$^{nd}$ echo shown in this figure (numbered) from top left to bottom right (1$^{st}$, 3$^{rd}$ etc...).



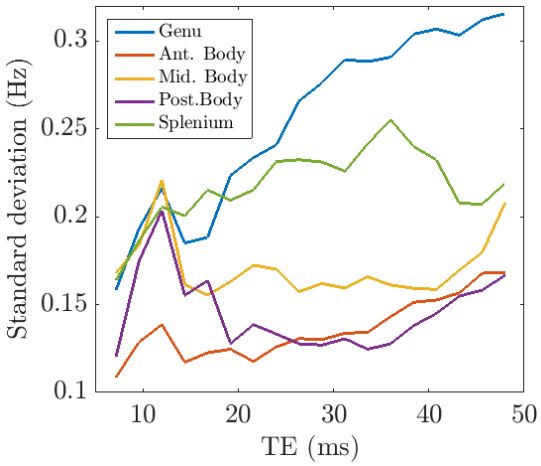

(a) Frequency difference map



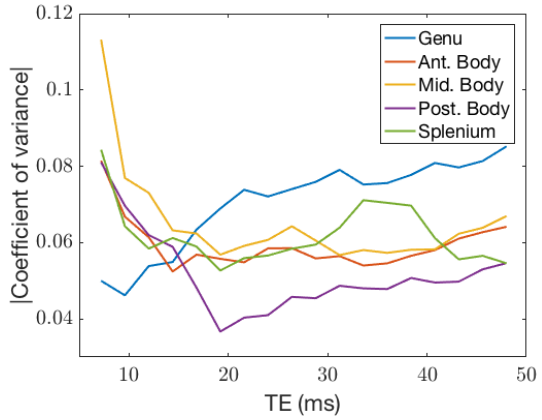

(b) Standard deviation map



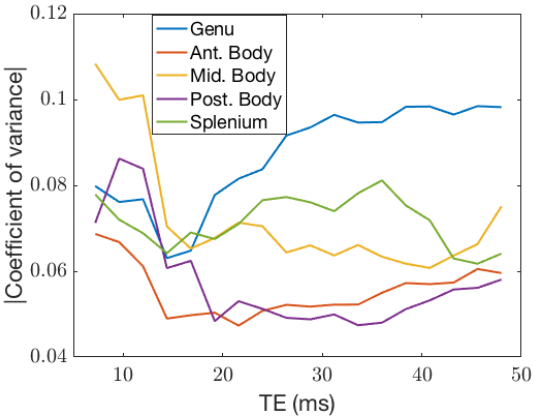

(c) Standard deviation between repeats




(d) Standard deviation between sessions




(e) Coefficient of variance between repeats




(f) Coefficient of variance between sessions

Figure 8.12: (a) and (b): Comparison of frequency difference map for a single scan and the standard deviation map for three repeats of the same subject in a single scanning session ($6^{\text{th}}$ echo, TE = 14.4 ms). Red line shows the corpus callosum region selected for analysis. (c) and (d): Standard deviation across average value in ROI between repeats inside the scanner and between scanning sessions. (e) and (f): |coefficient of variance| = $\left|\frac{\text{standard deviation}}{\text{change in frequency}}\right|$ across average value in ROI between repeats inside the scanner and between scanning sessions.

peatability of the FDM measurements while also highlighting regions affected by variable artefacts. A large standard deviation is observed in the proximity of large arteries, most notably at the front of the corpus callosum where Gibbs ringing is also apparent. The variation with TE of the standard deviation of the average value of the 5 ROI in the corpus callosum is additionally shown in Figure 8.12, with Figure 8.12c displaying the average over subjects of the standard deviation over the sets of three measurements made without moving the subject out of the scanner, while Figure 8.12d shows the standard deviation between scanning sessions. Figure 8.12c was formed by calculating the mean standard deviation of each ROI across all 10 subjects for each set of three scans acquired without moving subjects out of the scanner; Figure 8.12d was formed by calculating the mean of the standard deviation between subsequent scan sets (three scans per set, two sets per subject) for each subject. Examination of these figures indicates that the standard deviation of the genu rises with increased echo time, likely due to the impact of the surrounding arteries, but that for other regions a consistent trend is not observed. Figures 8.12e and 8.12f display the subsequent coefficient of variance ($|\text{coefficient of variance}| = \left|\frac{\text{standard deviation}}{\text{change in frequency}}\right|$) for Figures 8.12c and 8.12d. In these plots (and subsequent graphs), the range of TE values shown starts at the third echo TE = 7.2 ms because the FDM processing does not yield a value of the FDM at the first echo and forces the value to zero at the 2$^{\text{nd}}$ echo.

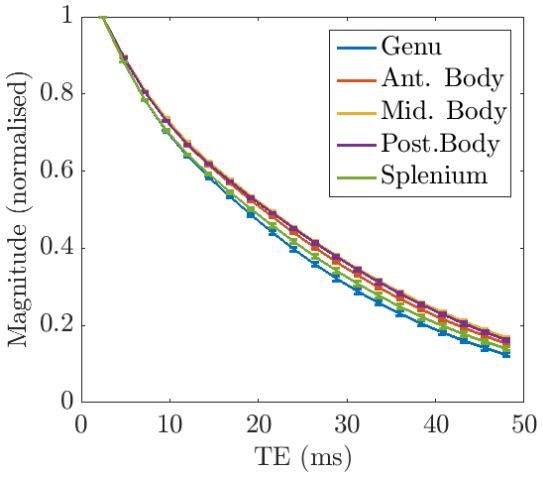
Figure 8.13 shows the mean magnitude and frequency difference curves across all subjects in the 5 ROI of the corpus callosum (Figures 8.13a and 8.13b), in addition to the superior cerebral peduncle and a region of grey matter (Figures 8.13c and 8.13d). The genu and splenium display a more rapid magnitude decay compared to the central regions of the corpus callosum, along with an increased change in frequency.

Figure 8.14 displays the variation over the corpus callosum of the parameters used in the experimental fitting, while Figure 8.15 displays the average residual remaining when subtracting the model fit to experimental data. Figure 8.16 shows the values for the FVF, g-ratio, $\chi_I$ and $\chi_A$, calculated from applying Equations 8.18 8.19 and 8.20 to the parameter results.

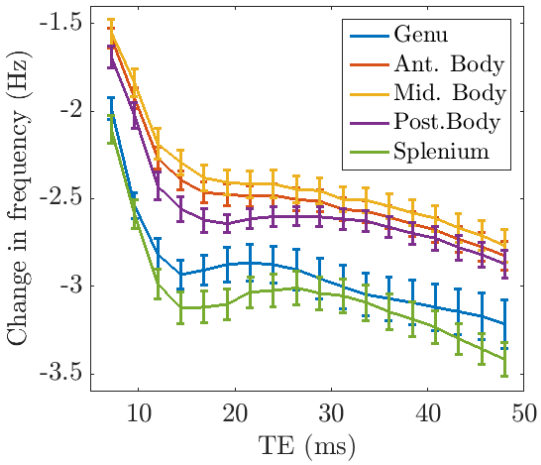
Table 8.2 indicates how parameter values vary over simulations of the middle body of the corpus callosum with added normally distributed random noise as outlined in Section 8.4 (results discussed in the following section).

| **Parameter** | $T^*_{2a}$(ms) | $T^*_{2m}$(ms) | $T^*_{2e}$(ms) | $A_a$ | $A_m$ | $A_e$ | $\Delta f_a$(Hz) | $\Delta f_m$(Hz) |
|---|---|---|---|---|---|---|---|---|
| **Mid.CC value** | $57 \pm 7$ | $7.2 \pm 0.4$ | $33 \pm 3$ | $0.40 \pm 0.07$ | $0.14 \pm 0.02$ | $0.46 \pm 0.07$ | $-6.9 \pm 0.3$ | $24 \pm 2$ |
| **0% noise** | 57 | 7.2 | 33 | 0.40 | 0.14 | 0.46 | $-6.9$ | 24 |
| **0.05% noise** | $58 \pm 4$ | $7.2 \pm 0.1$ | $33 \pm 1$ | $0.40 \pm 0.04$ | $0.142 \pm 0.005$ | $0.46 \pm 0.04$ | $-6.9 \pm 0.2$ | $23.7 \pm 0.8$ |
| **0.1% noise** | $60 \pm 10$ | $7.2 \pm 0.1$ | $33 \pm 2$ | $0.40 \pm 0.07$ | $0.14 \pm 0.01$ | $0.46 \pm 0.08$ | $-6.9 \pm 0.3$ | $20 \pm 10$ |
| **0.5% noise** | $60 \pm 20$ | $7.2 \pm 0.6$ | $40 \pm 20$ | $0.4 \pm 0.2$ | $0.16 \pm 0.05$ | $0.3 \pm 0.2$ | $-8 \pm 1$ | $21 \pm 4$ |
| **1% noise** | $60 \pm 30$ | $7 \pm 1$ | $60 \pm 30$ | $0.6 \pm 0.2$ | $0.18 \pm 0.07$ | $0.3 \pm 0.2$ | $-9 \pm 2$ | $19 \pm 5$ |
| **2% noise** | $60 \pm 30$ | $9 \pm 7$ | $70 \pm 30$ | $0.6 \pm 0.2$ | $0.17 \pm 0.09$ | $0.3 \pm 0.2$ | $-10 \pm 3$ | $19 \pm 8$ |

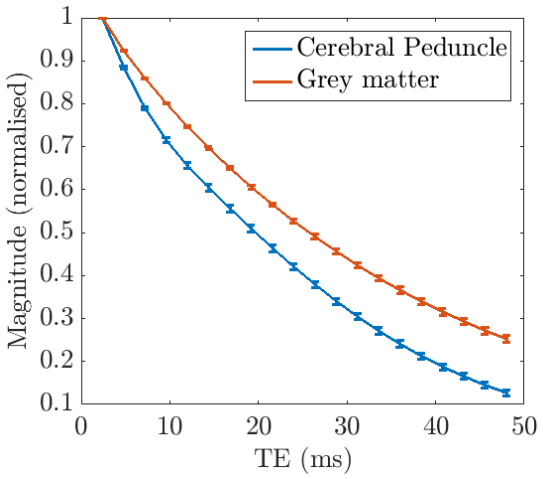
Table 8.2: Results obtained by fitting a simulated model of signal evolution with added normally distributed random noise to the three-pool model. Initial parameters defined from the mean experimentally determined parameter values of the middle body of the corpus callosum (Figure 8.14), with errors reflecting the average standard deviation from repeats on individual subjects. Simulated values and errors reflect the mean and standard deviation over 1000 simulated repeats. Initial fitting parameters as defined in Table 8.1.



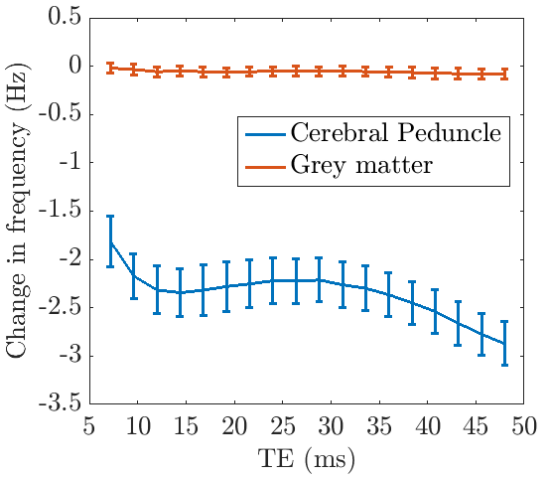

(a) Mag(TE)




(b) Frequency difference evolution




(c) Mag(TE)




(d) Frequency difference evolution

Figure 8.13: Average magnitude and frequency difference evolution for 60 scans over 10 subjects in the five corpus callosum ROI (Figures 8.13a and 8.13b), in addition to the superior cerebral peduncle and a region of grey matter (Figures 8.13c and 8.13d). ROIs for a single subject highlighted in Figure 8.10. Error bars represent the standard error of the mean.

## 8.7 Discussion

The processing steps of FDM eliminate the effects of non-local field sources $\Omega$ and $\phi_0$, yielding frequency difference maps which reveal contrast in areas containing microstructure, suitable for further analysis to obtain information about the properties of white matter. Figures 8.13a and 8.13b reveal an ordered variation of signal behaviour across the corpus callosum, with the splenium and genu displaying faster magnitude decay and a larger change in frequency with TE than is found in the mid-regions of the corpus callosum. The superior cerebral peduncle, a white matter region clearly indicated in frequency difference maps (highlighted in Figure 8.10) shows similar signal evolution to the corpus callosum (Figures 8.13c

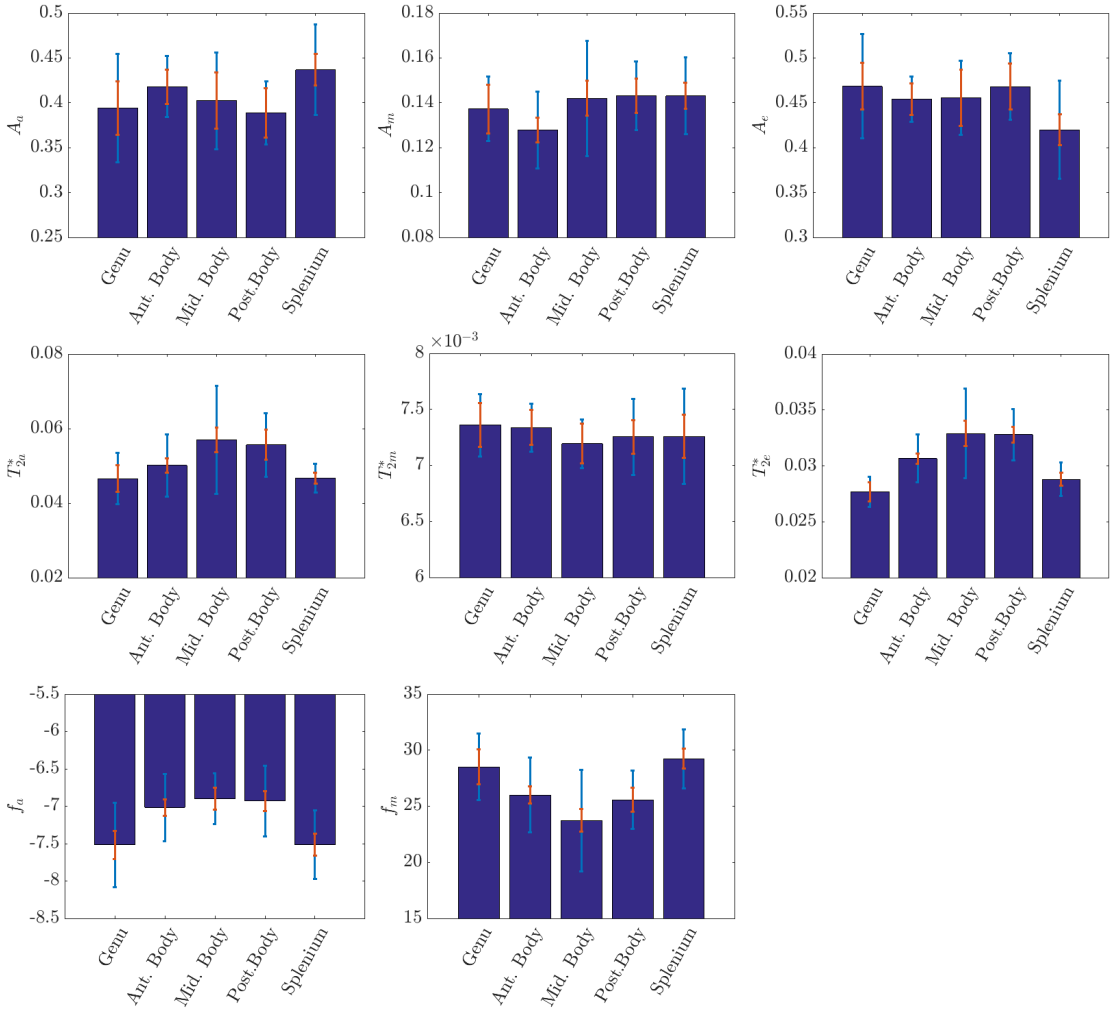
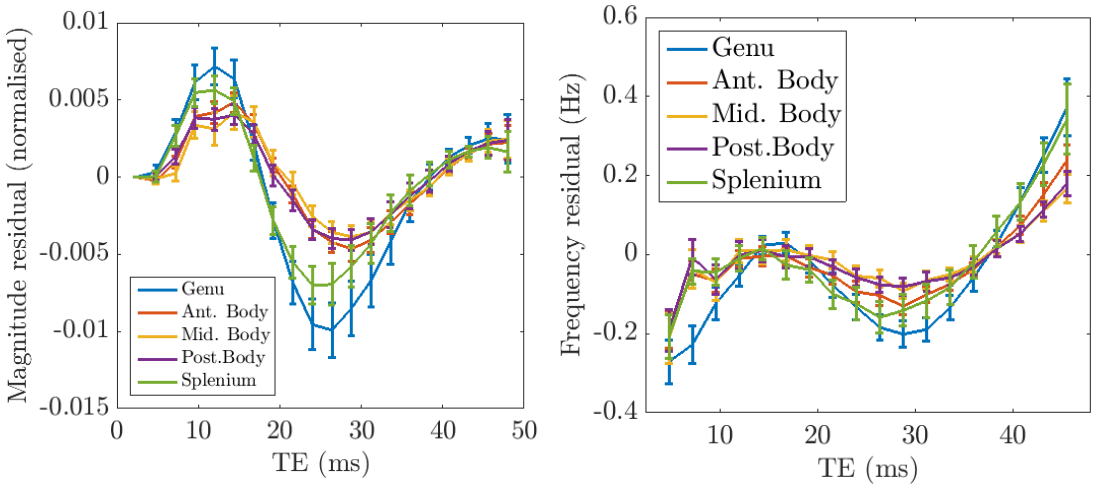



Figure 8.14: Results for fitting the magnitude signal (absolute value of Equation 8.2) and FDM (Equation 8.5) to the three-pool model to experimental data. Here the orange line represents the average standard error per subject and the blue line represents the standard deviation between subjects.

and 8.13d). Signal evolution over a region of grey matter (ROI highlighted in Figure 8.10) displayed in Figures 8.13c and 8.13d shows no significant change in frequency, giving a further indication of the sensitivity of this technique to the three compartment signal from white matter.

Examination of Figure 8.12 indicates that the standard deviation and subsequent coefficient of variance determined is small enough that this protocol can be repeated reliably over an ROI. However, it is apparent from Figure 8.12b that the standard deviation varies substantially within different regions of the dataset, particularly surrounding blood vessels. The use of flow compensation could help mitigate these artefacts and is left as future work.

Furthermore, it is apparent that the FDM processing protocol presented within this chapter has an inherent sensitivity to noise, due to the division of the unpro-



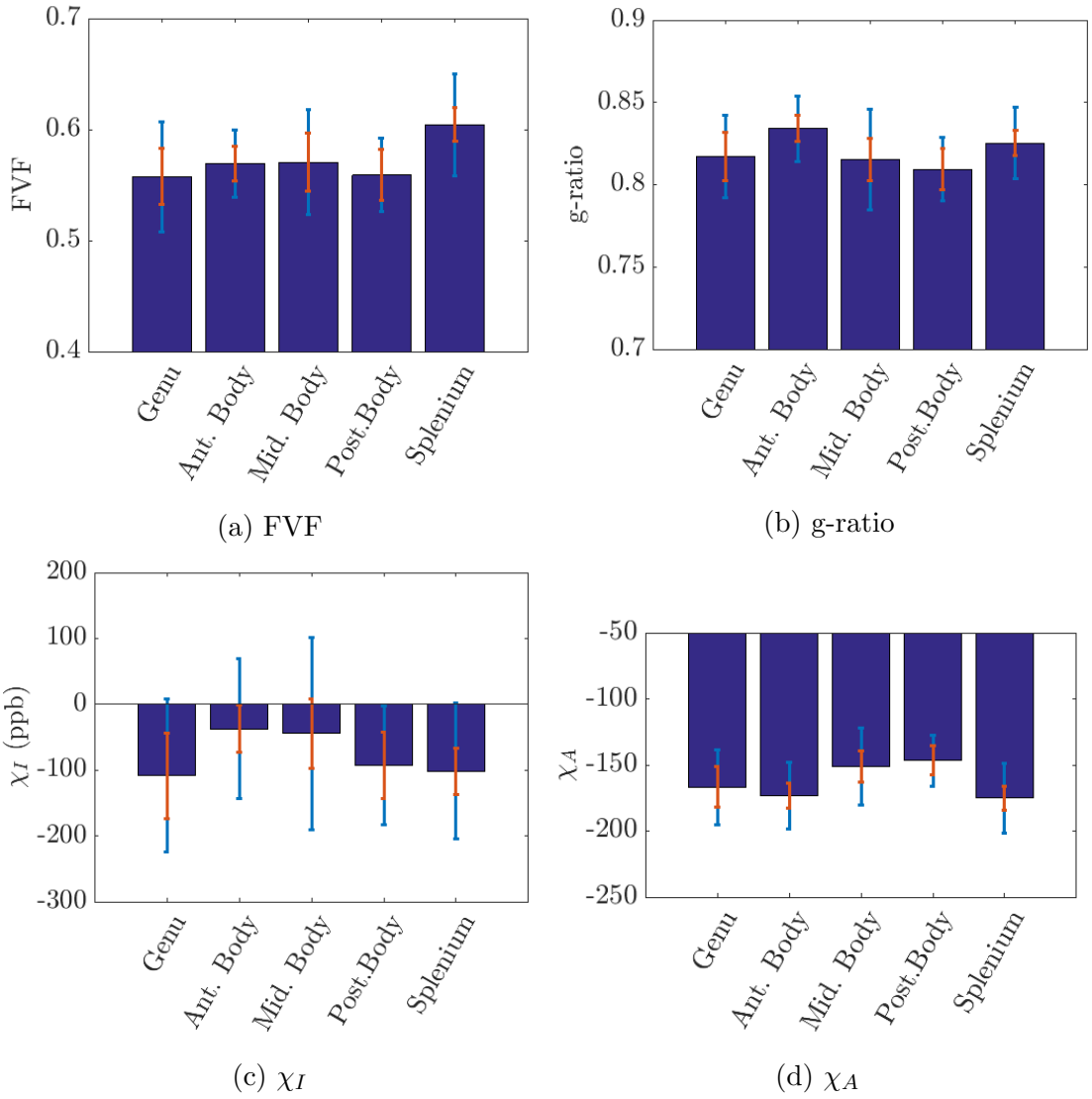

(a) Magnitude residual

(b) Frequency difference residual

Figure 8.15: (a): Residual value for magnitude comparison to model fit. (b): Residual value for frequency comparison to model fit. Residuals were calculated from each individual data set (6 per subject for 10 subjects) with errors formed from the standard error of the mean.

cessed phase data by the complex exponential of the first echo, followed by the subsequent division by the complex exponential of the scaled second echo. The complex divisions within this FDM protocol lead to a significant propagation of noise within the frequency difference maps and further work will be required to assess whether an improved processing protocol, using phase data collected at different echo times to perform the complex exponential divisions could improve the SNR of the obtained frequency difference maps. In addition, an improved method of estimating the phase offset, $\phi_0$, could eliminate the requirement of complex exponential division and increase the usability of FDM for 3D applications.

Assessment of the frequency difference curves led to numerous questions as to what was causing the differences in contrast between the different regions in the corpus callosum. Is what we are seeing due to differences in microstructure properties, or propagation from artefacts? From examination of the FDM images and standard deviation maps within single subjects, artefacts seem most apparent in the genu of the corpus callosum, developing from nearby arteries. Examination of subjects with little interaction between the corpus callosum ROI and observed artefacts still showed these trends. Artefacts were not observed over the splenium of the corpus callosum which also displays an increased change in frequency. Due to the position of the genu/splenium being lower in the foot-head direction relative to the mid-regions, a further attempt to regress out the differences between the genu/splenium and mid-regions through the application of an additional linear filter along the foot-head direction was carried out, but this did not remove the larger change in frequency observed in the genu/splenium.




(a) FVF (b) g-ratio

(c) $\chi_I$ (d) $\chi_A$

Figure 8.16: Variation of the FVF, g-ratio $\chi_I$ and $\chi_A$ over the corpus callosum averaged in all subjects. Calculated from Equations 8.18 - 8.20, setting $\rho = 0.7$ and $E = 20\,\text{ppb}$ as defined in [6]. Here the orange line represents the average standard error per subject and the blue line represents the standard deviation between subjects.

Parameter results in Figures 8.14 and 8.16 indicate the potential sensitivity of the FDM technique to variations in nerve fibre parameters. Results in Figure 8.14 are in strong agreement with previously reported values [5] obtained from fitting a triple-exponential model to magnitude and phase data over the splenium of the corpus callosum and recent work [17] calculating the myelin water fraction ($A_m$) over the optic radiations.The measured $T_2^*$ values show that, as expected, the myelin water has a short $T_2^*$ compared to the axonal and external pools. When examining the signal evolution over the corpus callosum, the calculated frequency offset within the myelin pool, $\Delta f_m$, agrees with the hypothesis that the early decrease of frequency with TE result from the rapid decay of the myelin signal

contribution, which has a positive frequency offset relative to the signals from the axonal and external pools for fibres that are perpendicular to $B_0$ [5, 17]. Figure 8.16 indicates the potential sensitivity to the properties of nerve fibres using the geometric three-pool model [6], explaining signal variation as a consequence of the physical properties of nerve fibres, obtaining similar values for the FVF, g-ratio, $\chi_I$ and $\chi_A$ as in [6] (where FVF = 0.5, $g = 0.8$, $\chi_I = -100\,\text{ppb}$ and $\chi_A = -100\,\text{ppb}$) but further examination is beyond the scope of this chapter. Interplay between the signals from the axonal and external pools is hypothesised to contribute to the continuing reduction in frequency at larger TE values.

Simulated results in Table 8.2 give an indication to the robustness of the fitting algorithm used. With no noise present, the fitting function produced exact results for $A_{a,m,e}$, $T^*_{2,a,m,e}$ and $\Delta f_{a,m}$ starting from initial parameters defined in Table 8.1. Increased noise leads to an increase in standard deviation, but additionally for many parameters a deviation from the initial mean value is observed with increasing noise. This is indicative that the complexity this non-linear model contains can lead to inaccuracies in obtaining exact fitting parameters, and there is a more significant impact on certain parameters with increasing noise. However from the magnitude data, noise in the real and imaginary signal components was estimated as $\approx 0.05\%$ and at these simulated levels of noise, there is little discrepancy between expected and obtained results. It should be noted that the average standard deviation values for initial parameters are higher than those obtained at 0.05% noise and falls at around the 0.1% level. The residual values in Figure 8.15 give an indication that there are additional sources of variation which are not accounted for in the model which could help explain this discrepancy.

Due to the large number of parameters, it is difficult to indicate from results in Figure 8.14 the direct cause of variation in the frequency difference curves. To test this, starting with obtained parameters for the middle body ($A_{a,m,e}$, $T^*_{2,a,m,e}$ and $\Delta f_{a,m}$) as defined in Figure 8.14, the frequency difference evolution was simulated with individual parameters adjusted to the values in other regions of the corpus callosum (genu, anterior body, posterior body and splenium), with results displayed in Figure 8.17. From Figure 8.17, it is apparent that variations between regions at low TE are due the properties of the myelin pool, with the largest contribution to variation due to the myelin frequency offset, $\Delta f_m$. Variations at higher TE are dominated by changes in the axonal and external pools, with the largest effects arising from the variation of $T^*_{2,a,e}$. Combining this information with the simulated results in Figure 8.14, Figures 8.16 and 8.17 imply the potential sensitivity of this technique to small variations of white matter properties.

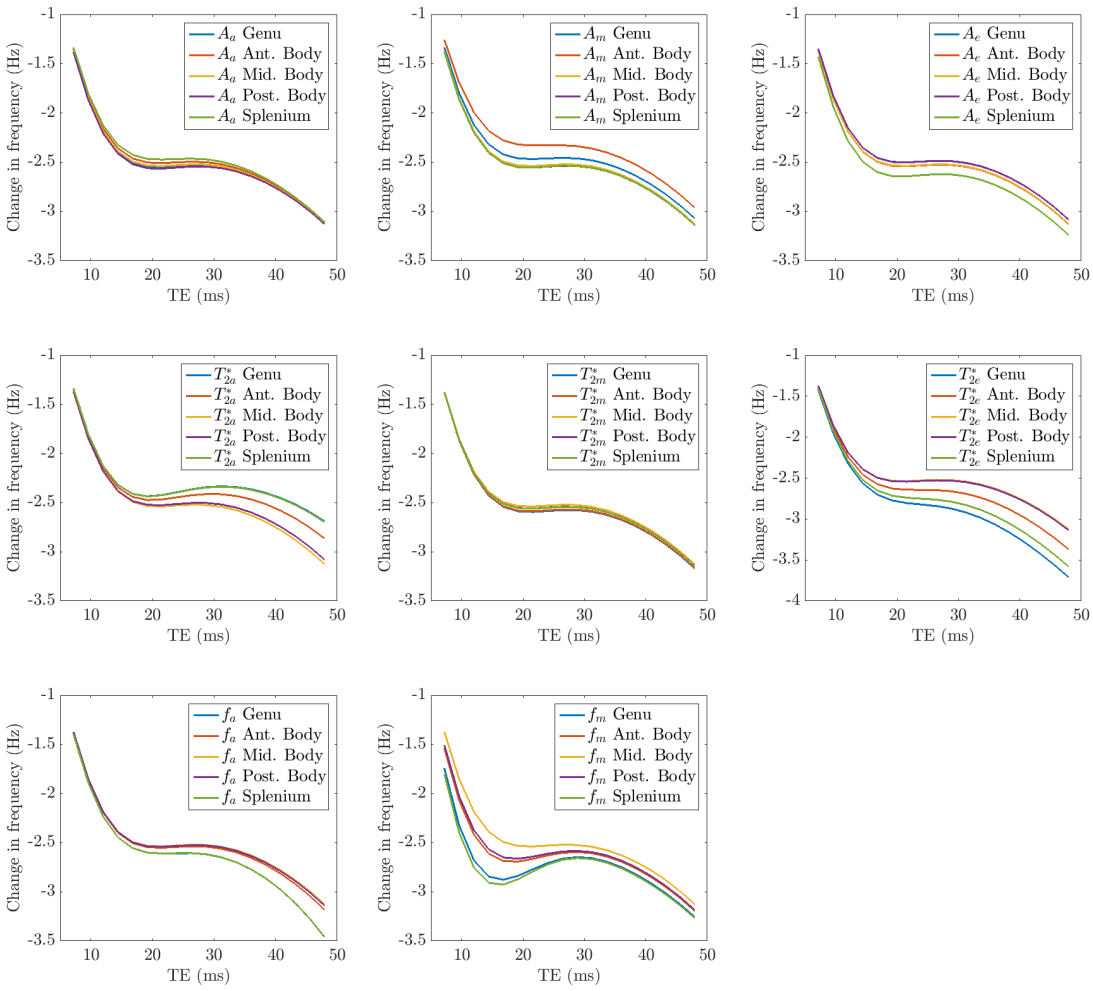



Figure 8.17: Simulations varying individual parameters to observe effect on signal evolution. Initial parameters defined as those calculated in the middle body of the corpus callosum (Table 8.2).

## 8.8 Conclusion

Frequency difference mapping yields contrast in areas with microstructure content and could be a useful technique for understanding the sources of contrast in phase imaging. Post-processing is fast, simple and requires little computer processing power. Issues associated with the formation of these frequency difference maps are experimental issues which could be removed with improved pulse sequences and further understanding of the underlying contrast. This concept could be expanded to other sources of microstructure, including iron content in tissue and deoxyhemoglobin in blood vessels, suggesting that any voxel with significant microstructure content will lead to an observable non-linear phase evolution.

Examination of the signal evolution over the corpus callosum reveals an apparent sensitivity to microstructure, with simulations indicating that signal variation at low TE corresponds to myelin properties and variation at high TE corresponds to

axonal/external properties. The description of signal evolution in terms of physical properties of the nerve fibres could be improved by using the geometric form of the three-pool model [6], rather than considering the average field perturbations in the different compartments (Section 8.3.3). The higher order components included in the fitting process could provide a more physically meaningful interpretation of the signal evolution. However, fitting would be significantly more troublesome and time consuming due to the computational demands of the geometric model. This could be extended further by incorporating multiple fibres in the model to provide sensitivity to the packing geometry, which has been identified as a significant influence on the form of signal evolution [30].

The robustness of obtained fitting parameters with simulated noise makes it suitable for parameter estimation over white matter regions. However the residual differences between the model fit and experimental data (Figure 8.15) show clear trends, with larger residuals at low and high TE, indicating that there are further sources of signal contrast in FDM to be understood beyond the three-pool model.

# Bibliography


[1] Alex Mackay, Kenneth Whittall, Julian Adler, David Li, Donald Paty, and Douglas Graeb. *In-vivo* visualization of myelin water in brain by magnetic resonance. *Magnetic Resonance in Medicine*, 31(6):673–677, 1994.

[2] Kenneth P Whittall, Alex L Mackay, Douglas A Graeb, Robert A Nugent, David KB Li, and Donald W Paty. *In-vivo* measurement of $T_2$ distributions and water contents in normal human brain. *Magnetic Resonance in Medicine*, 37(1):34–43, 1997.

[3] Mark D Does and Richard E Snyder. Multiexponential $T_2$ relaxation in degenerating peripheral nerve. *Magnetic resonance in medicine*, 35(2):207–213, 1996.

[4] Peter van Gelderen, Jacco A de Zwart, Jongho Lee, Pascal Sati, Daniel S Reich, and Jeff H Duyn. Nonexponential $T_2^*$ decay in white matter. *Magnetic resonance in medicine*, 67(1):110–117, 2012.

[5] Pascal Sati, Peter van Gelderen, Afonso C Silva, Daniel S Reich, Hellmut Merkle, Jacco A de Zwart, and Jeff H Duyn. Micro-compartment specific $T_2^*$ relaxation in the brain. *Neuroimage*, 77:268–278, 2013.

[6] Samuel Wharton and Richard Bowtell. Fiber orientation-dependent white matter contrast in gradient echo MRI. *Proceedings of the National Academy of Sciences*, 109(45):18559–18564, 2012.

[7] Mark D Does and John C Gore. Compartmental study of $T_1$ and $T_2$ in rat brain and trigeminal nerve *in-vivo*. *Magnetic resonance in medicine*, 47(2):274–283, 2002.

[8] Jack L Lancaster, Trevor Andrews, L Jean Hardies, Stephen Dodd, and Peter T Fox. Three-pool model of white matter. *Journal of Magnetic Resonance Imaging*, 17(1):1–10, 2003.

[9] Trevor Andrews, Jack L Lancaster, Stephen J Dodd, Carmen Contreras-Sesvold, and Peter T Fox. Testing the three-pool white matter model adapted

for use with $T_2$ relaxometry. *Magnetic resonance in medicine*, 54(2):449–454, 2005.

[10] Dosik Hwang, Dong-Hyun Kim, and Yiping P Du. *In-vivo* multi-slice mapping of myelin water content using $T_2^*$ decay. *Neuroimage*, 52(1):198–204, 2010.

[11] Se-Hong Oh, Michel Bilello, Matthew Schindler, Clyde E Markowitz, John A Detre, and Jongho Lee. Direct visualization of short transverse relaxation time component (ViSTa). *NeuroImage*, 83:485–492, 2013.

[12] Daeun Kim, Hyo Min Lee, Se-Hong Oh, and Jongho Lee. Probing signal phase in direct visualization of short transverse relaxation time component (ViSTa). *Magnetic resonance in medicine*, 74(2):499–505, 2015.

[13] Samuel Wharton and Richard Bowtell. Gradient echo based fiber orientation mapping using $R_2^*$ and frequency difference measurements. *Neuroimage*, 83:1011–1023, 2013.

[14] F Schweser, A Deistung, D Gullmar, M Atterbury, BW Lehr, K Sommer, and JR Reichenbach. Non-linear evolution of GRE phase as a means to investigate tissue microstructure. *Proceedings of 19$^{th}$ International Society of Magnetic Resonance in Medicine*, 4527, 2011.

[15] Matthew J Cronin, Nian Wang, Kyle S Decker, Hongjiang Wei, Wen-Zhen Zhu, and Chunlei Liu. Exploring the origins of echo-time-dependent quantitative susceptibility mapping (QSM) measurements in healthy tissue and cerebral microbleeds. *NeuroImage*, 149:98–113, 2017.

[16] Ferdinand Schweser, Simon Daniel Robinson, Ludovic Rochefort, Wei Li, and Kristian Bredies. An illustrated comparison of processing methods for phase MRI and QSM: removal of background field contributions from sources outside the region of interest. *NMR in Biomedicine*, 2016.

[17] Yoonho Nam, Jongho Lee, Dosik Hwang, and Dong-Hyun Kim. Improved estimation of myelin water fraction using complex model fitting. *NeuroImage*, 116:214–221, 2015.

[18] Xu Li and Peter Zijl. Mean magnetic susceptibility regularized susceptibility tensor imaging (MMSR-STI) for estimating orientations of white matter fibers in human brain. *Magnetic resonance in medicine*, 72(3):610–619, 2014.

[19] Wei Li, Bing Wu, Alexandru V Avram, and Chunlei Liu. Magnetic susceptibility anisotropy of human brain *in-vivo* and its molecular underpinnings. *Neuroimage*, 59(3):2088–2097, 2012.

[20] Karin Shmueli, Stephen J Dodd, Tie-Qiang Li, and Jeff H Duyn. The contribution of chemical exchange to MRI frequency shifts in brain tissue. *Magnetic resonance in medicine*, 65(1):35–43, 2011.

[21] Jianqi Li, Shixin Chang, Tian Liu, Hongwei Jiang, Fang Dong, Mengchao Pei, Qianfeng Wang, and Yi Wang. Phase-corrected bipolar gradients in multi-echo gradient-echo sequences for quantitative susceptibility mapping. *Magnetic Resonance Materials in Physics, Biology and Medicine*, 28(4):347–355, 2015.

[22] E Mark Haacke, Robert W Brown, Michael R Thompson, Ramesh Venkatesan, et al. *Magnetic resonance imaging: physical principles and sequence design*, volume 82. Wiley-Liss New York:, 1999.

[23] Mark Jenkinson and Stephen Smith. A global optimisation method for robust affine registration of brain images. *Medical image analysis*, 5(2):143–156, 2001.

[24] Mark Jenkinson, Peter Bannister, Michael Brady, and Stephen Smith. Improved optimization for the robust and accurate linear registration and motion correction of brain images. *Neuroimage*, 17(2):825–841, 2002.

[25] Douglas N Greve and Bruce Fischl. Accurate and robust brain image alignment using boundary-based registration. *Neuroimage*, 48(1):63–72, 2009.

[26] Ping Hou, Khader M Hasan, Clark W Sitton, Jerry S Wolinsky, and Ponnada A Narayana. Phase-sensitive $T_1$ inversion recovery imaging: a time-efficient interleaved technique for improved tissue contrast in neuroimaging. *American journal of neuroradiology*, 26(6):1432–1438, 2005.

[27] Chris Rorden, Hans-Otto Karnath, and Leonardo Bonilha. Improving lesion-symptom mapping. *Journal of cognitive neuroscience*, 19(7):1081–1088, 2007.

[28] Francisco Aboitiz, Arnold B Scheibel, Robin S Fisher, and Eran Zaidel. Fiber composition of the human corpus callosum. *Brain research*, 598(1):143–153, 1992.

[29] Winston X Yan, Karen J Mullinger, Matt J Brookes, and Richard Bowtell. Understanding gradient artefacts in simultaneous EEG/fMRI. *Neuroimage*, 46(2):459–471, 2009.

[30] Way Cherng Chen, Sean Foxley, and Karla L Miller. Detecting microstructural properties of white matter based on compartmentalization of magnetic susceptibility. *Neuroimage*, 70:1–9, 2013.

# Chapter 9

# Examination of the Magnetic Properties of Skeletal Muscle Tissue at 7T

## 9.1 Introduction

Previous chapters within this thesis have discussed the potential of field perturbation maps, $\Delta B(\vec{r})$, obtained from MRI phase data to reveal quantitative information about tissue, including susceptibility (Sections 5.4 and 7.1), chemical exchange (Section 7.2), structural (Section 7.3) and compartmentalisation (Section 7.4) properties. A significant amount of MRI phase research has been performed on the brain (examples discussed in Sections 6.2, 7.2, 7.3, 7.4 and Chapter 8) and this research is beginning to reveal a detailed understanding of the magnetic properties of brain tissue *in-vivo*, with a particular emphasis on white matter. However, outside the brain, little phase imaging research has been performed.

This chapter aims to provide an insight into the magnetic properties of tissue beyond the brain, describing an experiment examining skeletal muscle. There has been long-standing interest in the magnetic properties of skeletal muscle tissue [1], but to date there has been little examination of these properties using MRI-based measurements of field perturbations. Here, a preliminary study of the magnetic properties of skeletal muscle was performed with a phantom consisting of a piece of pork tenderloin embedded in agar. This was scanned at multiple orientations to $\vec{B}_0$ in a 7T scanner. By analysis of $\Delta B(\vec{r})$ maps, a least-squares minimisation protocol was developed to examine the full susceptibility tensor, $\underline{\underline{\chi}}(\vec{r})$, and chemical exchange, $E(\vec{r})$, properties of skeletal muscle. Additionally, novel algorithms for simultaneously examining the susceptibility and chemical exchange properties are introduced.

In this chapter, field perturbations are described using the notation $\Delta B$ in units of Hz, defined as evolving *positively* for a positive frequency as per the Philips convention ($\phi = +2\pi\Delta f t$). Conversions can be performed using the information in Table 3.3.

## 9.2 Motivation

Skeletal muscle is characterised by highly organised, long, cylindrical muscle fibres [2] and quantification of the magnetic properties of skeletal muscle tissue could have a significant impact on both our understanding of skeletal muscle structure and the mechanisms underlying muscular diseases [3]. From a practical perspective, it could be hypothesised that multi-orientation COSMOS-QSM (discussed in Section 5.4.4), STI (Discussed in Section 7.1.4) or any other multi-orientation protocol is more practical to implement in skeletal muscle *in-vivo* than in the brain, due to the flexibility of the extremities (arms, legs etc.) in the human body. The work presented in this chapter aims to provide a foundation for future examination of the magnetic properties of skeletal muscle *in-vivo*.

In 1958 (prior to the invention of MRI), Arnold et al. [1] attempted to determine the susceptibility anisotropy of rabbit psoas muscle (implications and theoretical considerations of anisotropy susceptibility discussed in detail in Section 7.1), by suspending the sample within a homogeneous magnetic field and measuring the induced torque. From analysis of the experimental data, Arnold et al. [1] described two major observations:

1. Skeletal muscle tissue is most paramagnetic along the direction of the muscle fibres.

2. The susceptibility anisotropy, $\chi_A$, of the psoas muscle, defined by Arnold et al. [1] as the difference between the susceptibility parallel and perpendicular to the muscle fibres:

$$\chi_A = \chi_{\parallel} - \chi_{\perp} \tag{9.1}$$

   is equal to 250 ppb.

Arnold et al. [1] concluded their research with the hypothesis that 'magnetic measurements can be made to give useful information about the structure of biological tissue'.

Despite the improvements in methods to quantify the susceptibility properties of tissue, the work by Arnold et al. [1] is the most current publication for direct measurement in skeletal muscle. A recent paper examining the susceptibility

properties of the myocardium [4] could be considered the first 'follow-up' study examining the susceptibility properties of muscle tissue. In this research, Dibb et al. scanned samples of *ex-vivo* mouse hearts at 12 orientations to $B_0$, observing higher paramagnetism in the direction along the myocardium muscle fibres in agreement with the observations in skeletal muscle tissue by Arnold et al. [1]. Examination of ROIs over the multi-orientation myocardium data indicated a small anisotropic susceptibility contribution on the order of 10 ppb, with significant variation over different regions of the heart. However, the substantial structural differences between skeletal and cardiac muscle tissues prevents direct generalisation of these results to the research presented by Arnold et al. [1].

## 9.3 Method

### 9.3.1 Experimental Prep and Data Collection

A sample of pork tenderloin purchased from a local supermarket was trimmed and stripped of external fat prior to placement in agar. The sample was placed in the centre of an 18 cm diameter spherical perspex phantom shell filled with agar (1.2% agar, 0.9% NaCl and 0.006% Milton sterilising fluid) using the recipe outlined in [5]. To achieve this, one hemisphere of the phantom shell was first filled with agar. The skeletal muscle sample was placed on-top of the flat surface of the set agar and the second hemisphere of the perspex phantom was then attached to the first hemisphere, encasing the sample within the phantom. The second half of the phantom was then filled with agar via a hole in the top of the phantom, surrounding the sample. A photograph of the experimental phantom is shown in Figure 9.1. To ensure the phantom could be rotated freely without the skeletal muscle sample reorienting with respect to the external casing, plastic struts were fitted around the edge of the phantom shell.

Initial work performing a single-slice frequency difference mapping protocol (details in Chapter 8) on skeletal muscle tissue revealed no evidence of multi-compartment phase evolution and a protocol was developed assuming that the magnetic properties of tissue are independent of the echo-time. Magnitude and phase images of the phantom were collected using a dual-echo, GE scan on a Philips Achieva 7T MR scanner. Each scan generated images at two different echo times ($TE_1$=8 ms, $TE_2$=20 ms). A 3D volume, encompassing the entire skeletal muscle sample and a large portion of the external agar was collected per orientation (resolution=$1\times1\times1\,mm^3$, FOV =$160\times160\times\,160\,mm^3$, with TR=21.6 ms and flip angle=15°. The sample was scanned at 29 angles to $\vec{B}_0$. The $\vec{B}_0$ orientation vectors in the sample frame of reference (discussed further in Section 7.1.4) are shown

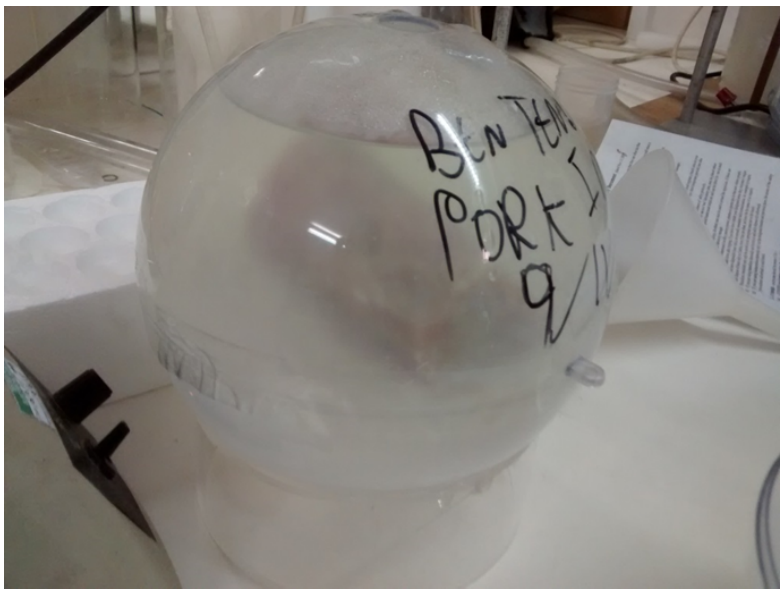


Figure 9.1: Photograph of the phantom used in experimental analysis. Here the skeletal muscle sample is seen in the centre of the phantom, resting on a flat surface of set agar. Surrounding the sample is setting agar inserted through a hole in the top of the phantom.

in Figure 9.2. A single dataset was discarded due to artefacts generated during experimental acquisition, reducing the number of datasets used in experimental analysis to 28. Each dataset was collected in 553 s. A diffusion tensor imaging (DTI) protocol was additionally attempted at 3T to quantify the diffusion properties of the skeletal muscle sample, however due to challenges in acquisition this data was discarded.

### 9.3.2 Post-Processing of Experimental Data

To remove effects of time-independent phase-offsets (discussed in Sections 5.2.2, 6.5.1 and 8.2.2), $\phi_0(\vec{r})$, in the phase data, complex division was performed between the two collected echoes:

$$\phi_{\mathrm{w}}(\vec{r}) = \arg \frac{e^{i\cdot\phi_{\mathrm{w}}(\mathrm{TE}_{20\mathrm{ms}},\vec{r})}}{e^{i\cdot\phi_{\mathrm{w}}(\mathrm{TE}_{8\mathrm{ms}},\vec{r})}} \tag{9.2}$$

where $\phi_{\mathrm{w}}(\vec{r})$ refers to the unprocessed wrapped phase map. An example of unprocessed magnitude and phase data after complex division is shown in Figure 9.3. $\phi_{\mathrm{w}}(\vec{r})$ was unwrapped using the Hussein path-based filtering algorithm [6], with background fields removed using a Laplacian-based vSHARP filtering algorithm (described in Section 5.3.3), with $|\vec{r}_{\mathrm{max}}| = 8\,\mathrm{mm}$ and regularisation performed as a high-pass filter [7] (cut off frequency $= 0.005\,\mathrm{mm}^{-1}$). Masks of signal-containing regions at each orientation to be utilised in the vSHARP filtering algorithm were obtained by thresholding the magnitude data collected at TE = 20 ms. $\Delta B(\vec{r})$ maps for three separate orientations are displayed in Figure 9.4.

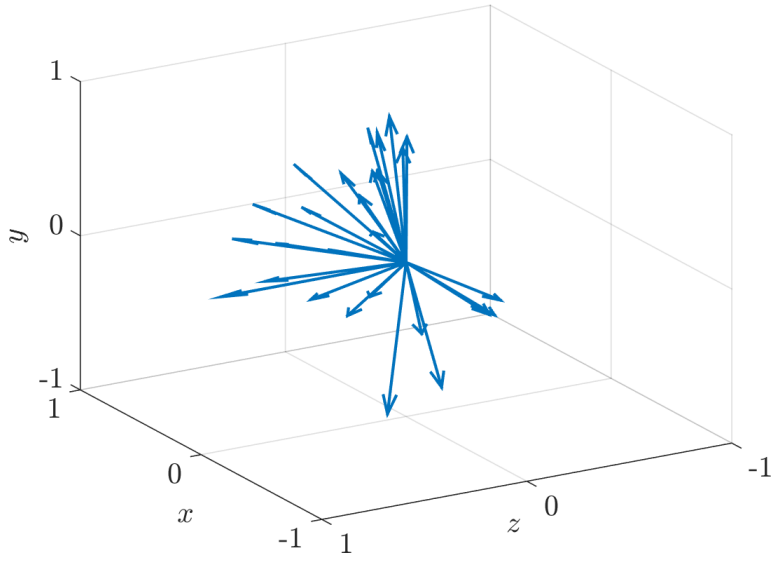


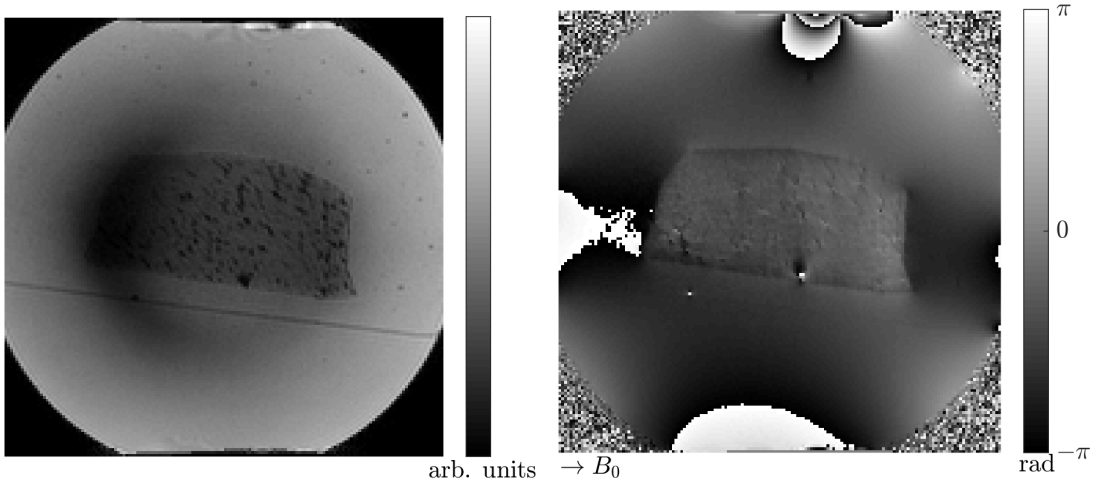

Figure 9.2: Defined orientations of the 28 sampled $\hat{B}_0$ vectors in the sample frame of reference. The majority of of $\hat{B}_0$ vectors fall on the quadrant of the spherical surface between $x = 0 \rightarrow 1$ and $y = 0 \rightarrow 1$.

Datasets were co-registered prior to the analysis of magnetic properties using the sample frame of reference (discussed in Section 7.1.4). Due to the geometry of the agar phantom and skeletal muscle sample (which can be approximated as a cylindrical object within a sphere), in addition to the large range of orientations scanned with respect to $\vec{B}_0$, it was not possible to co-register the data using automated co-registration packages. To ensure accurate co-registration, the datasets were co-registered using a combination of manual and computational methods [8] via the mrAlign function in the mrTools software package (Gardner Lab, Department of Psychology, Stanford University). Magnitude data was co-registered to the first collected magnitude dataset, ensuring excellent alignment of the skeletal muscle sample between datasets, with the subsequent rotation matrix applied to the $\Delta B(\vec{r})$ maps. This proved far simpler than direct co-registration of the $\Delta B(\vec{r})$ maps, due to the external field perturbations surrounding the skeletal muscle sample preventing an accurate assessment of the tissue boundary. Co-registration results are shown in Figure 9.5.

### 9.3.3 Least Squares Minimisation

The minimisation protocols for examining the magnetic properties of skeletal muscle were written in-house using MATLAB (Release 2013a, The MathWorks Inc., Natick, MA, United States), with minimisations performed using the 'LSQR' function. Fitting was assessed using two main criteria:

1. Do the determined solution matrices ($\chi_I(\vec{r})$, $\underline{\underline{\chi}}(\vec{r})$, $E(\vec{r})$) display a distri-




(a) $\mathrm{Mag}(\vec{r})$ (b) $\phi_{\mathrm{w}}(\vec{r})$

Figure 9.3: Example of unprocessed magnitude (Figure 9.3a) and phase (Figure 9.3b) data after complex division for a single orientation of the phantom. The skeletal muscle sample is clearly visible in the centre of the phantom, surrounded by a spherical shell of agar.

bution that is physically representative of the underlying geometry of the phantom?

2. Are the determined solution matrices able to explain the observed field perturbations in the experimental $\Delta B(\vec{r})$ maps?

The first criteria was assessed by visual observation of the results. As the skeletal muscle sample is surrounded by a large volume of agar, it can be assumed that the $\chi_I(\vec{r})/\underline{\underline{\chi}}(\vec{r})/E(\vec{r})$ distribution should be homogeneous over this region. Visual examination is also useful to assess the second criteria, comparing the experimental $\Delta B(\vec{r})$ maps and reconstructed $\Delta B_{\mathrm{rec}}(\vec{r})$ maps from the $\chi_I(\vec{r})/\underline{\underline{\chi}}(\vec{r})/E(\vec{r})$ distributions and examining remaining residuals. The second criteria can also be more quantitatively assessed by examining the relative residual value, relres:

$$\mathrm{relres} = \sqrt{\frac{\|\Delta B_{\mathrm{rec}}(\vec{r}) - \Delta B(\vec{r})\|_2^2}{\|\Delta B(\vec{r})\|_2^2}}. \tag{9.3}$$

relres returns a value greater than 0, where 0 indicates a perfect reconstruction of the experimental data from $\Delta B_{\mathrm{rec}}(\vec{r})$. A low relres is indicative of a solution that is able to explain the variation in experimental results (though as a stand-alone test of the fidelity of the reconstruction it is not sufficient as it does not quantify the heterogeneity of the differences).

As can be observed in Figure 9.5, datasets acquired at different orientations are defined by unique phantom masks. To take account of this, all minimisations were weighted by a phantom mask, $\mathrm{M_p}(\vec{r})$. Due to the large scale inhomogeneity in the

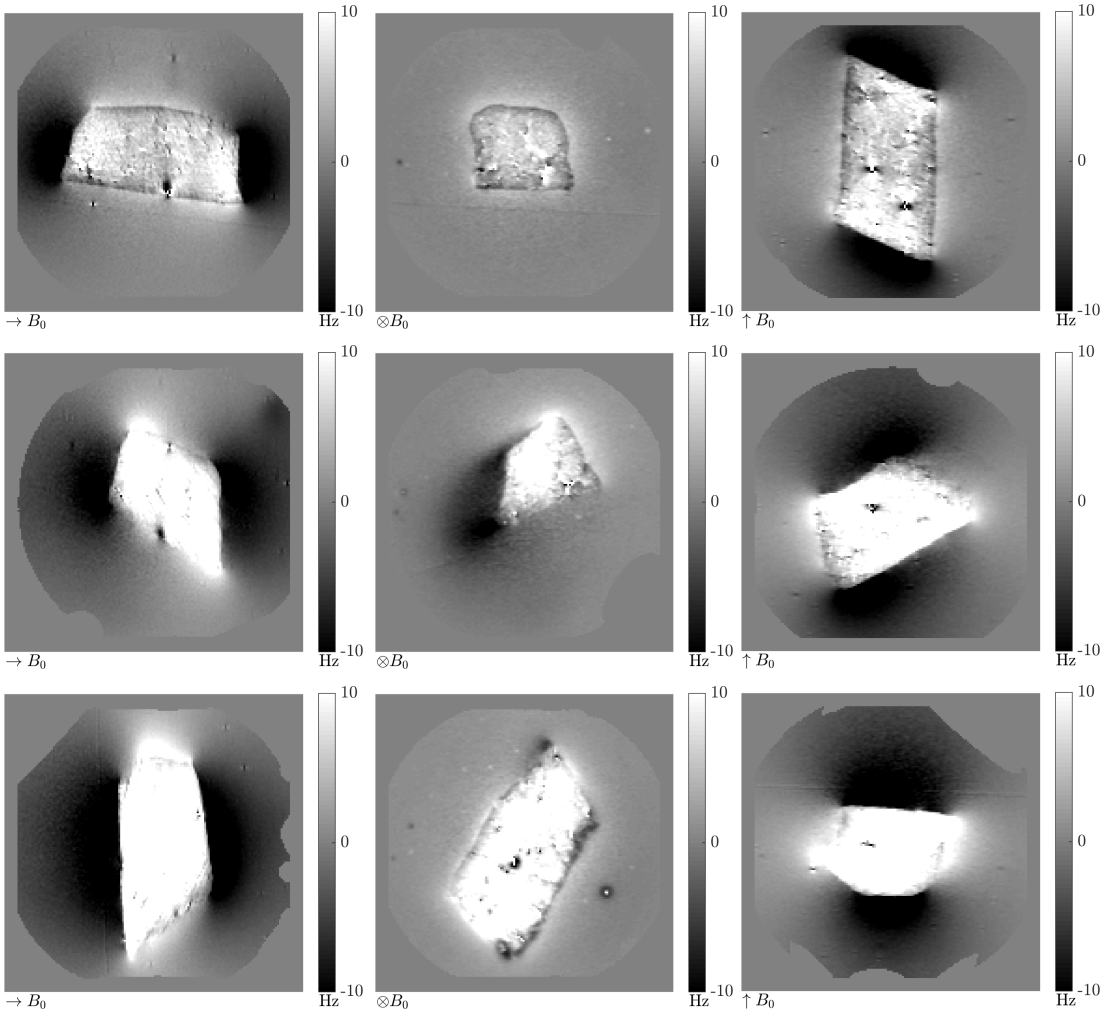



Figure 9.4: $\Delta B(\vec{r})$ maps for the 1$^{\text{st}}$ (top row), 13$^{\text{th}}$ (middle row) and 22$^{\text{nd}}$ (bottom row) for three perpendicular slices through the phantom. Here the variation of the orientation of the skeletal muscle sample can be observed between the datasets, in addition to the field perturbations induced both internally and externally to the sample.

magnitude data (indicated in Figure 9.3a), the fitting was not weighted by $\text{Mag}(\vec{r})$ as previously discussed in Section 5.4.5, to prevent an increased weighting near the boundary of the agar phantom where signal was highest (variation induced by $B_1(\vec{r})$ inhomogeneity throughout the phantom).

To assist in rapid convergence of the minimisation algorithm and prevent fitting beyond the agar boundary, all minimisations were additionally regularised by the inverse of the mask, $\text{M}_{\text{inv}}(\vec{r})$ (discussed in Section 5.4.5). $\text{M}_{\text{inv}}(\vec{r})$ was defined so as to set regions that do not contain $\Delta B(\vec{r})$ information in all orientations equal to one. This is shown in Figure 9.6. Full forms of the minimisation algorithms are detailed in the individual sections below.

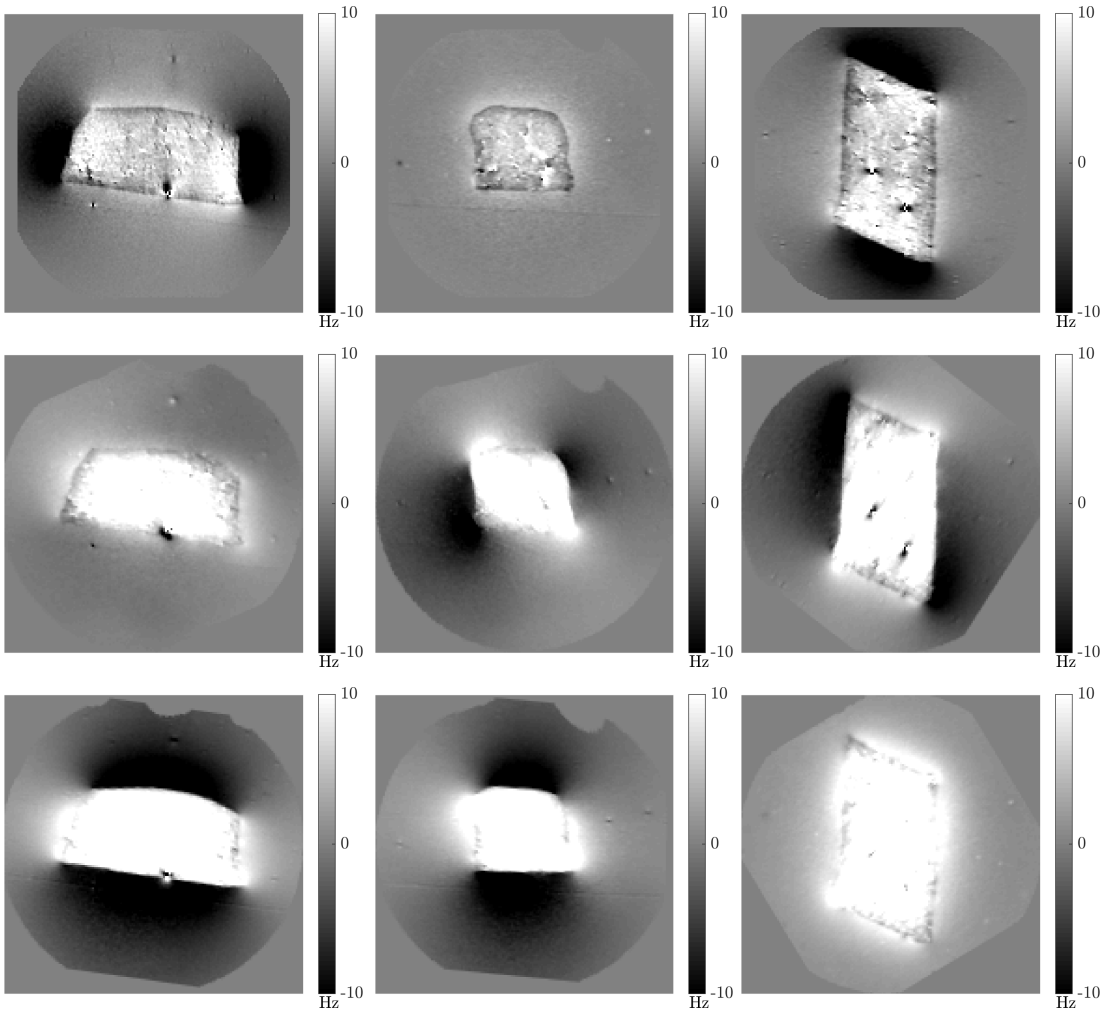
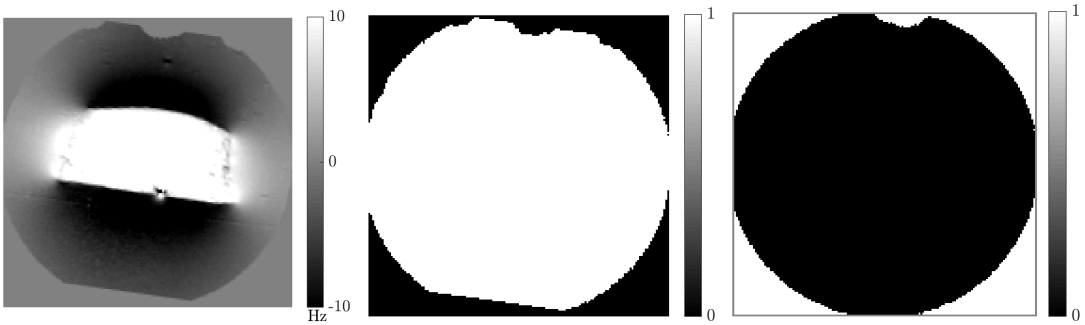



Figure 9.5: $\Delta B(\vec{r})$ maps for the 1$^{\text{st}}$ (top row), 13$^{\text{th}}$ (middle row) and 22$^{\text{nd}}$ (bottom row) dataset for three perpendicular orientations *after* co-registration to the 1$^{\text{st}}$ dataset (unco-registered datasets shown in Figure 9.4). Examination of the figures shows excellent co-registration between the different datasets, with a clear visualisation on the impact of the orientation of the object on the induced field perturbations. Here the variation of the field perturbations induced both internally and externally to the skeletal muscle sample can be clearly observed.




(a) $\Delta B(\vec{r})$ (b) $\mathrm{M_p}(\vec{r})$ (c) $\mathrm{M_{inv}}(\vec{r})$

Figure 9.6: Experimental field perturbations for the 22$^{\text{nd}}$ orientation (Figure 9.6a with minimisation weighting mask (Figure 9.6b) specific for the 22$^{\text{nd}}$ orientation and the regularisation inverse mask (9.6c) used for all orientations.

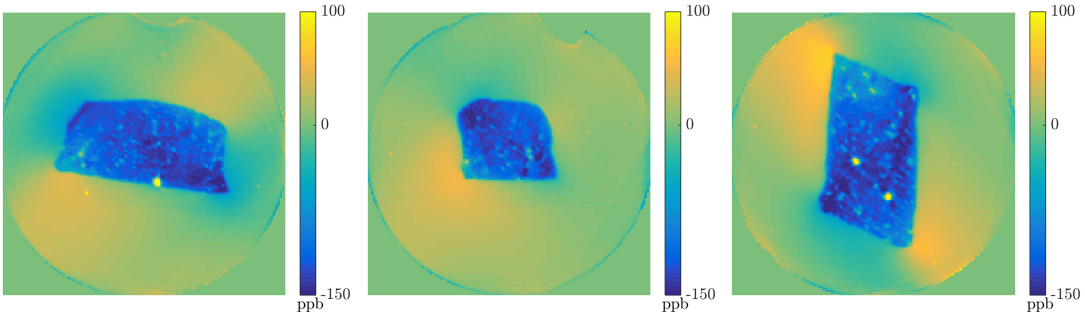



Figure 9.7: $\chi_I(\vec{r})$ distribution in three orthogonal planes determined using the protocol described in Section 9.4.

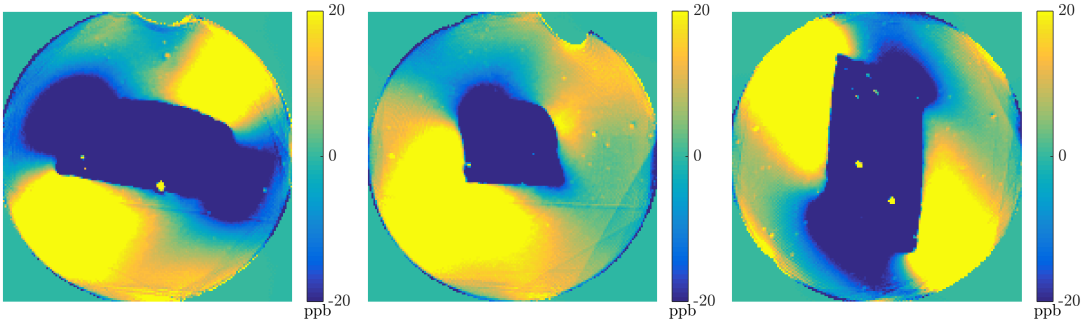



Figure 9.8: $\chi_I(\vec{r})$ distribution in three orthogonal planes determined using the protocol described in Section 9.4, now thresholded between $\pm 20$ ppb.

## 9.4 Isotropic Susceptibility Minimisation

When measurements are made at a sufficient number of orientations with respect to $\vec{B}_0$, solution of the inverse problem to generate quantitative isotropic susceptibility maps, $\chi_I(\vec{r})$, via COSMOS-QSM (discussed in Section 5.4.4) is a well-posed problem with a low condition number, $C$, providing a unique solution for $\chi_I(\vec{r})$. For the experimental data presented here, from Equation 5.35 (ignoring the undefined value $d(\vec{k} = 0)$), $C = 2.4$. To investigate the assumption that all phase contrast originates from $\chi_I(\vec{r})$, a COSMOS-QSM protocol was applied to the multi-orientation phantom data, with additional mask weighting and regularisation as discussed in Section 9.3.3, defining:

$$\min_{\chi_I(\vec{r})} \left\{ \|O_1\|_2^2 + \|O_2\|_2^2 + \cdots + \|O_S\|_2^2 + \beta^2 \left\| \mathrm{M}_{\mathrm{inv}}(\vec{r}) \cdot \chi_I(\vec{r}) \right\|_2^2 \right\} \tag{9.4}$$

and

$$\|O_i\|_2^2 = \left\| \mathrm{M}_{\mathrm{p}_i}(\vec{r}) \cdot \left( B_0 \cdot \mathcal{F}^{-1} \left[ d_i(\vec{k}) \cdot \mathcal{F} \left[ \chi_I(\vec{r}) \right] \right] - \Delta B_i(\vec{r}) \right) \right\|_2^2 \tag{9.5}$$

where $\beta^2 = 10^5$. The minimisation was set to terminate when the tolerance fell below $10^{-8}$ and the minimisation converged to this tolerance after 16 iterations. The obtained $\chi_I(\vec{r})$ map is shown in Figure 9.7.

Initial visual assessment of the $\chi_I(\vec{r})$ map indicates that the skeletal muscle sample is significantly more diamagnetic than the surrounding agar. However, further

analysis via thresholding the $\chi_I(\vec{r})$ map reveals large, dipole-like patterns occurring outside the muscle sample within the agar (Figure 9.8). It can be reasonably assumed that the large-scale susceptibility properties of the well-mixed, homogeneous agar solution used within the phantom should be independent of position. The large-scale $\chi_I$ inhomogeneity observed over the agar suggests that the generated $\chi_I(\vec{r})$ map describes a non-physical susceptibility distribution. Averaging over masks of the skeletal muscle sample and agar (defining the agar mask as a 10 mm shell surrounding the skeletal muscle sample), $\chi_{I_{\text{musc}}} = (-110 \pm 33)$ppb and $\chi_{I_{\text{agar}}} = (7 \pm 29)$ppb, where $\pm$ indicates the standard deviation.

A mismatch is additionally observed when comparing the $\Delta B_{\text{rec}}(\vec{r})$ maps, reconstructed from the calculated $\chi_I(\vec{r})$ distribution, with the original experimental data (Figure 9.9), with a significant residual, $\text{res}_{\text{iso}}(\vec{r}) = \Delta B(\vec{r}) - \Delta B_{\text{rec}}(\vec{r})$, observed within the skeletal muscle sample and a small residual external to the sample. The minimisation returned a value of relres = 0.62, implying that a substantial proportion of the experimental $\Delta B(\vec{r})$ maps are not being described with a model of $\chi_I(\vec{r})$ alone. The low condition number ($C = 2.4$) combined with the non-physical $\chi_I(\vec{r})$ distribution and large remaining experimental residual implies that that there are contributions to $\Delta B(\vec{r})$ from other effects than $\chi_I(\vec{r})$ alone.

To examine the residual within the phantom more thoroughly, a voxelwise minimisation protocol was performed on $\text{res}_{\text{iso}}(\vec{r})$ [9]:

$$\min_{A(\vec{r}),E(\vec{r}),\hat{v}(\vec{r})} \left\| \text{res}_{\text{iso}}(\vec{r}) - \left( A(\vec{r}) \cdot \sin^2 \left( \arccos |\hat{B}_0 \cdot \hat{v}(\vec{r})| \right) + E(\vec{r}) \right) \right\|_2^2 \tag{9.6}$$

where $\hat{B}_0$ is the unit vector describing each $\vec{B}_0$ orientation (visualised in Figure 9.2), $\hat{v}(\vec{r})$ is a single unit vector defining the principal direction of the muscle fibres, $A(\vec{r})$ defines the amplitude of the $\sin^2$ dependence and $E(\vec{r})$ defines the chemical exchange offset. The origins and properties of chemical exchange have been previously discussed in Section 7.2. However, the other component of the minimisation protocol:

$$A(\vec{r}) \cdot \sin^2 \left( \arccos |\hat{B}_0 \cdot \hat{v}(\vec{r})| \right) \tag{9.7}$$

may initially look unfamiliar, but is derived from the previous discussion of cylindrical symmetric tissue architecture in Section 7.3. This component of the minimisation aims to provide evidence of a local $\sin^2$ dependence within the skeletal muscle sample. As previously discussed within Section 9.2, skeletal muscle is composed of small, highly organised cylindrical muscle fibres, indicating an ordered sub-voxel cylindrical symmetry. Cylindrically symmetric microstructure is characterised by a local $\sin^2$ dependence in $\Delta B(\vec{r})$ maps (discussed in Section 7.3).

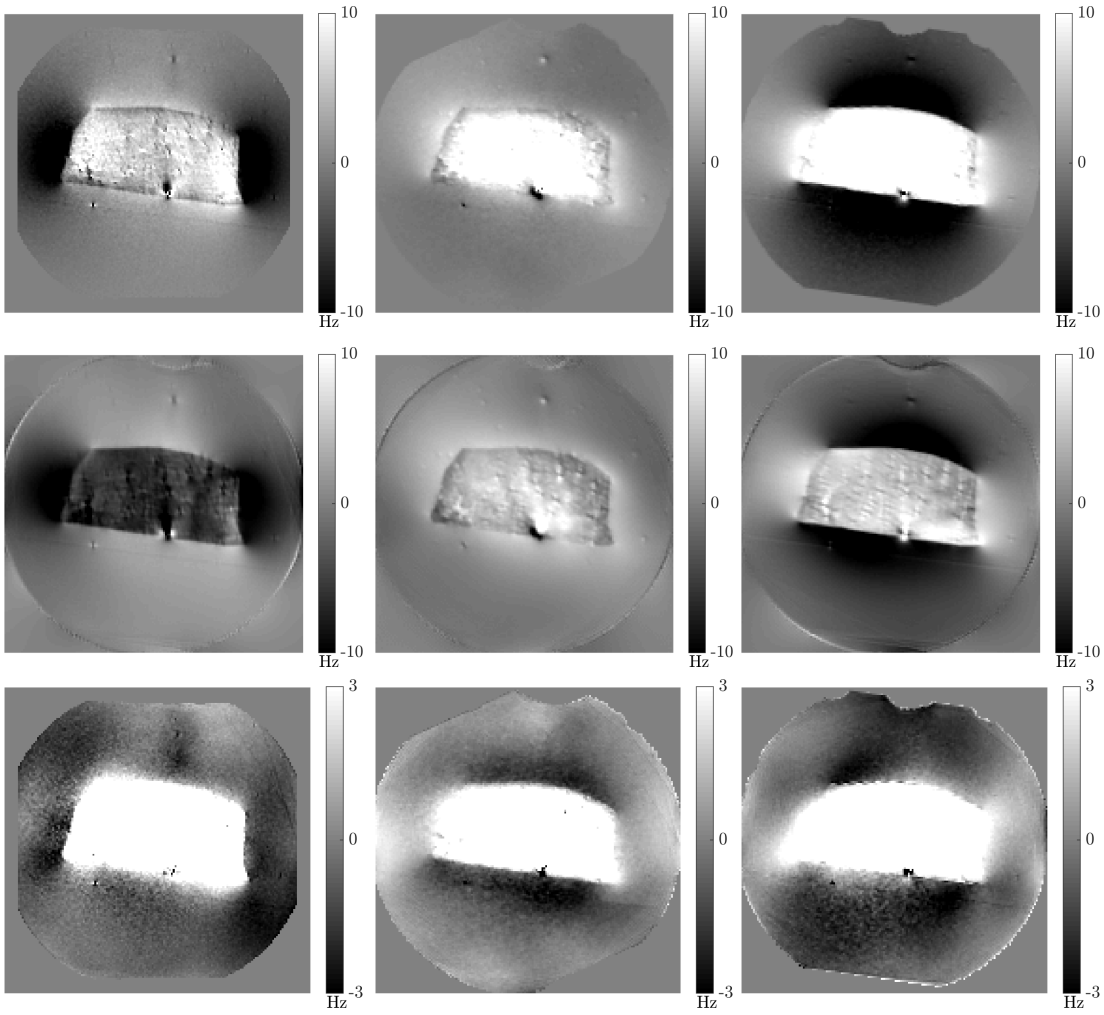
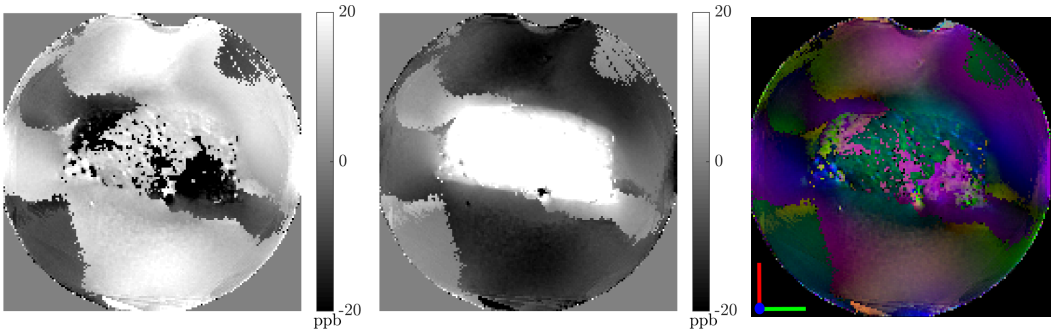



Figure 9.9: Single-plane of the experimental $\Delta B(\vec{r})$ maps (top row) for the 1$^{\text{st}}$ , 13$^{\text{th}}$ and 22$^{\text{nd}}$ dataset, with reconstructed $\Delta B(\vec{r})$ maps, $\Delta B_{\text{rec}}(\vec{r})$, (middle row) and residual (bottom row) thresholded between $\pm 3\,\text{Hz}$ from fitting to a model of $\chi_I(\vec{r})$ using the protocol described in Section 9.4.

Fitting Equation 9.7 to experimental data to calculate $A(\vec{r})$ and $\hat{v}$ provides evidence for the existence of cylindrical microstructure within the skeletal muscle sample, the magnitude of the cylindrical microstructure's contribution to $B(\vec{r})$ (characterised by $A(\vec{r})$) and the direction of the principal axis of the cylindrical muscle fibres (characterised by $\hat{v}(\vec{r})$).

The minimisation in Equation 9.6 returned relres = 0.33. A single slice of the obtained $A(\vec{r})$, $E(\vec{r})$ and $\hat{v}(\vec{r})$ maps are visualised in Figure 9.10. Examination of these maps reveals substantial, large-scale inhomogeneities within the images, suggestive of poor estimates of the parameters. The existence of artefacts within the $A(\vec{r})$, $E(\vec{r})$ and $\hat{v}(\vec{r})$ maps is expected considering the non-physical $\chi_I(\vec{r})$ distribution determined from the original minimisation (Figure 9.8) and high relres value, despite the well-conditioned nature of the minimisation protocol. As previ-

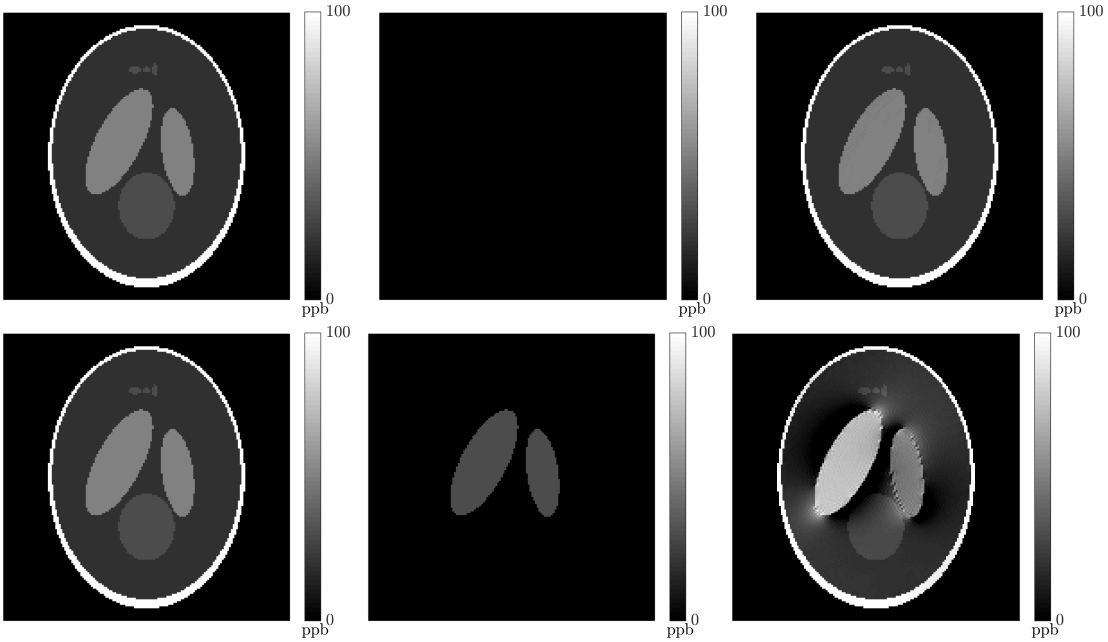



(a) $A(\vec{r})$ (b) $E(\vec{r})$ (c) $\vec{v}(\vec{r})$ scaled by $|A(\vec{r})|$

Figure 9.10: Microstructure amplitude (Figure 9.10a), chemical exchange contribution (Figure 9.10b) and principal axis of the cylindrical muscle fibres (Figure 9.10c) determined by fitting Equation 9.6 to $\text{res}_{\text{iso}}(\vec{r})$ (displayed in Figure 9.9 in a single slice though the muscle phantom). The $\vec{v}(\vec{r})$ map is weighted by $|A(\vec{r})|$ to determine the extent of the orientation dependence, with direction colour-key shown in corner.

ously discussed in Section 5.4.5, a least-squares minimisation algorithm is designed to return a minimum relres when fitting a model to experimental data, regardless of whether the returned solution is physically representative of the expected distribution. The $\chi_I(\vec{r})$ minimisation performed previously within this chapter attempted to describe the origin of all field perturbations with a model of $\chi_I(\vec{r})$ alone. Field perturbations originating from other magnetic properties (chemical exchange, cylindrical microstructure and susceptibility anisotropy) are not directly separable from $\chi_I(\vec{r})$, indicating that the minimisation algorithm will not return a $\chi_I(\vec{r})$ map identical to the experimental $\chi_I(\vec{r})$ distribution, despite the well-posedness of the problem. This is demonstrated in Figure 9.11.

Due to these limitations, results obtained by fitting to the residual field perturbations are not truly 'quantitative' and must be considered carefully. The obtained $A(\vec{r})$ map (Figure 9.10b) implies the existence of a a large, local $\sin^2$ orientation dependence within the agar. As there is no underlying cylindrically symmetric structure within agar, the calculated orientation dependence is a non-physical property of the agar, induced by the residual external field perturbations of the skeletal muscle sample. The remaining field perturbations external to the skeletal muscle tissue in the $\text{res}_{\text{iso}}(\vec{r})$ maps (Figure 9.9) suggest the existence of susceptibility anisotropy (discussed in Section 7.1) within skeletal muscle, particularly when observing how the orientation of the residual field perturbations are different to the experimental $\Delta B(\vec{r})$ maps. However, despite artefacts within the dataset, examination of the generated $E(\vec{r})$ map (Figure 9.10b) provides evidence of a large, local, orientation-independent, homogeneous field offset within the sample, suggestive of a chemical exchange contribution.




(a) $\chi_I(\vec{r})$ (b) $E(\vec{r})$ (c) Reconstructed $\chi_I(\vec{r})$

Figure 9.11: Example of reconstructed $\chi_I(\vec{r})$ maps (right column) obtained by applying a least-squares minimisation to multi-orientation $\Delta B(\vec{r})$ maps containing $\chi_I$-induced field perturbations (top row) and $\chi_I$ and $E$-induced field perturbations (bottom row). The left and central column show the $\chi_I(\vec{r})$ and $E(\vec{r})$ distributions used within the minimisations. Here it is observed that though both systems have identical $\chi_I(\vec{r})$ distributions, the solution for the minimisation is not identical to $\chi_I(\vec{r})$ when additional sources of field perturbations are present within the $\Delta B(\vec{r})$ maps. Reconstructed $\chi_I(\vec{r})$ maps generated from the minimisation in Equation 9.4. Field orientations used in simulated $\Delta B(\vec{r})$ maps identical to the experimentally used $\hat{B}_0$ vectors (Figure 9.2). Minimisation applied to data simulated using $\chi_I$ only (top row) returned relres = $6.9 \times 10^{-6}$. Minimisation applied to data simulating both $\chi_I(\vec{r})$ and $E(\vec{r})$ (bottom row) returned relres = 0.45.

## 9.5 Isotropic Susceptibility and Chemical Exchange Minimisation

Chemical exchange produces a local, orientation-independent field offset in $\Delta B(\vec{r})$ maps (discussed in Section 7.2) and examination of the $\Delta B(\vec{r})$ residuals in the $\chi_I(\vec{r})$ protocol (described in the previous section) revealed a large, local offset within the skeletal muscle sample. Further examination of $\text{res}_{\text{iso}}(\vec{r})$ via fitting to Equation 9.6 showed evidence of an orientation-dependent local field offset within the sample (Figure 9.10b), suggestive of a chemical exchange contribution. With a sufficient number of scanning orientations, it should be possible to design and implement a minimisation protocol to separate and determine the unique contributions of $\chi_I(\vec{r})$ and $E(\vec{r})$ to $\Delta B(\vec{r})$. To assess this, the COSMOS-QSM protocol was repeated as above with the additional assumption that chemical

exchange also contributes to the experimental $\Delta B(\vec{r})$ maps, defining:

$$\min_{\chi_I(\vec{r}),E(\vec{r})} \left\{ \|O_1\|_2^2 + \|O_2\|_2^2 + \cdots + \|O_S\|_2^2 + \beta^2 \left( \left\| \mathrm{M}_{\mathrm{inv}}(\vec{r}) \cdot \chi_I(\vec{r}) \right\|_2^2 + \left\| \mathrm{M}_{\mathrm{inv}}(\vec{r}) \cdot E(\vec{r}) \right\|_2^2 \right) \right\} \tag{9.8}$$

and

$$\|O_i\|_2^2 = \left\| \mathrm{M}_{\mathrm{p}_i}(\vec{r}) \cdot \left( B_0 \cdot \left( \mathcal{F}^{-1} \left[ d_i(\vec{k}) \cdot \mathcal{F} \left[ \chi_I(\vec{r}) \right] \right] + E(\vec{r}) \right) - \Delta B_i(\vec{r}) \right) \right\|_2^2 \tag{9.9}$$

where $\beta^2 = 10^5$. The minimisation was set to terminate when the tolerance fell below $10^{-8}$ and the minimisation converged to this tolerance after 65 iterations. The obtained $\chi_I(\vec{r})$ and $E(\vec{r})$ maps are shown in Figure 9.12.

Examination of the $\chi_I(\vec{r})$ map again indicates that the skeletal muscle sample is significantly more diamagnetic than the surrounding agar and the $E(\vec{r})$ map reveals a significant positive chemical exchange contribution originating within the tissue. Small inhomogeneities are observed over the agar in both the thresholded $\chi_I(\vec{r})$ and $E(\vec{r})$ maps (Figure 9.13). However, unlike the $\chi_I(\vec{r})$ map determined in the previous section, the large length-scale dipole patterns observed when thresholding the $\chi_I(\vec{r})$ map are substantially reduced when additionally fitting for $E(\vec{r})$, suggesting that the chemical exchange contribution prevented an accurate determination of $\chi_I(\vec{r})$ when fitting a model of $\chi_I(\vec{r})$ alone. Averaging over the skeletal muscle sample and agar phantom (using an agar mask consisting of a 10 mm shell surrounding the skeletal muscle sample) yields $\chi_{I_{\mathrm{musc}}} = -116 \pm 30$ppb and $\chi_{I_{\mathrm{agar}}} = 6.2 \pm 5.7$ppb, $E_{\mathrm{musc}} = 32 \pm 11$ppb and $E_{\mathrm{agar}} = -2.3 \pm 1.9$ppb.

The minimisation returned relres = 0.18, implying that the model of $\chi_I(\vec{r})$ and $E(\vec{r})$ provides a significantly improved fit to the experimental $\Delta B(\vec{r})$ maps compared to using $\chi_I(\vec{r})$ alone, in addition to $\chi_I(\vec{r})$ and $E(\vec{r})$ maps that are physically representative of the underlying phantom composition. It is also worth noting that the standard deviation of $\chi_{I_{\mathrm{agar}}}$ is much smaller than when fitting for $\chi_I$ alone (see Section 9.4). Comparisons of the reconstructed $\Delta B_{\mathrm{rec}}(\vec{r})$, from the $\chi_I(\vec{r})$ and $E(\vec{r})$ distributions with the original experimental data are shown in Figure 9.14. With the inclusion of $E(\vec{r})$ in the fitting process, excellent visual agreement is observed between $\Delta B(\vec{r})$ and $\Delta B_{\mathrm{rec}}(\vec{r})$, with a significantly reduced residual, $\mathrm{res}_{\mathrm{iso\&exc}}(\vec{r})$ both internally and externally to the skeletal muscle sample. High residual values appear to be confined to regions containing blood vessels within the sample and air bubbles in the surrounding agar.

Examining the $\mathrm{res}_{\mathrm{iso\&exc}}(\vec{r})$ maps further (Figure 9.14), residual field perturbations external to the skeletal muscle sample are substantially reduced compared to those provided when fitting to $\chi_I(\vec{r})$ alone (Figure 9.9), suggesting that susceptibility anisotropy, if existing within the sample, is very small. Using a similar protocol

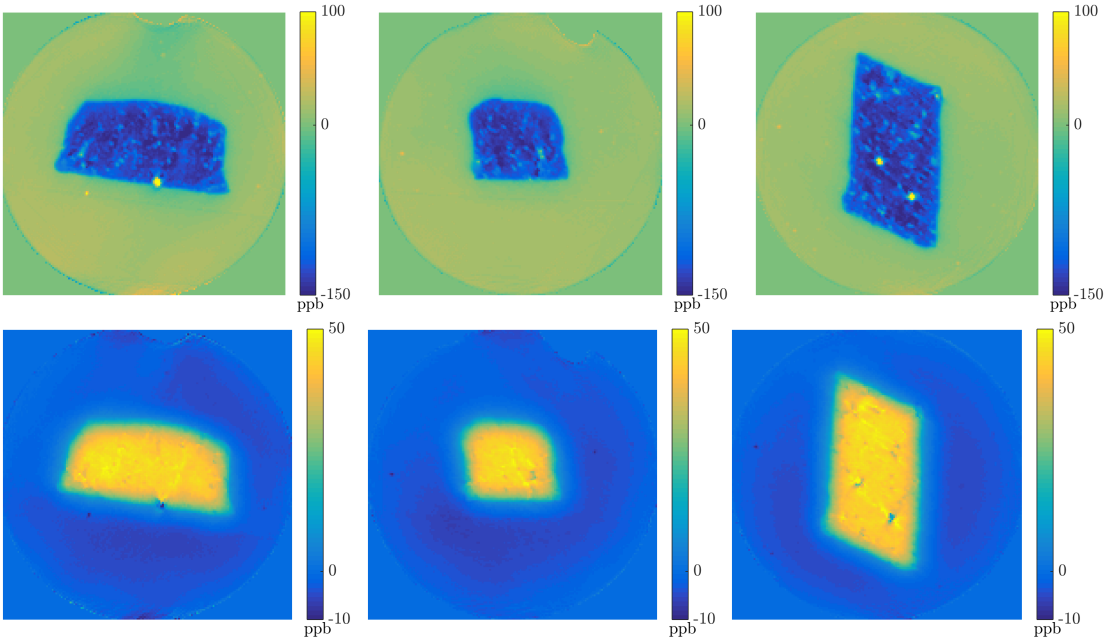



Figure 9.12: $\chi_I(\vec{r})$ (top row) and $E(\vec{r})$ (bottom row) distributions in three orthogonal planes determined from the protocol in Section 9.5.

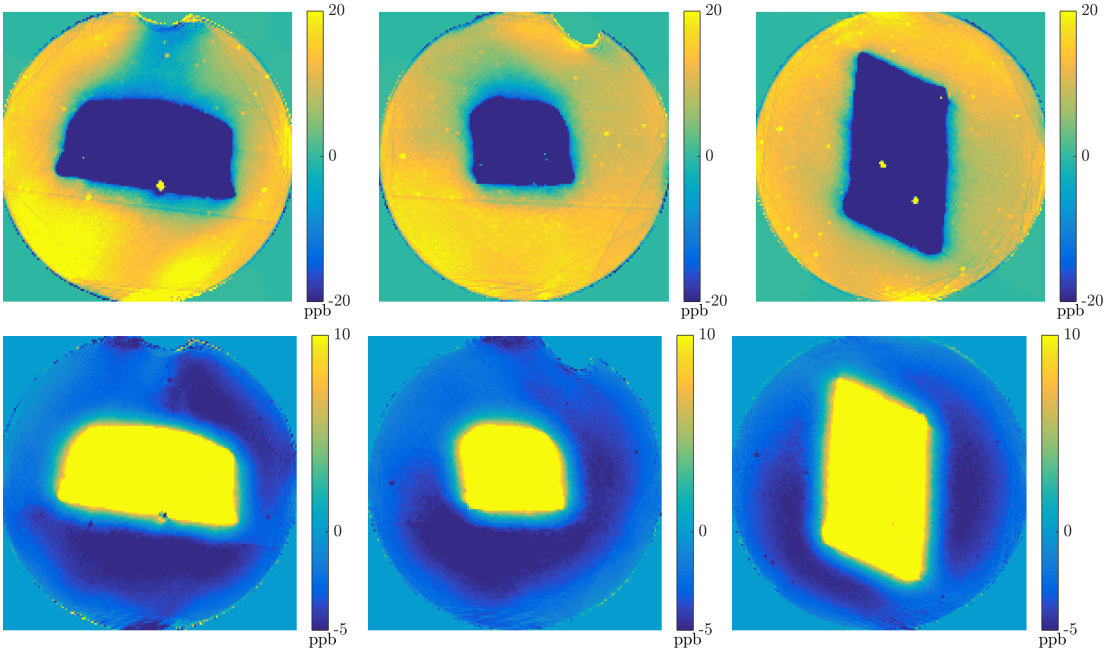



Figure 9.13: $\chi_I(\vec{r})$ (top row) and $E(\vec{r})$ (bottom row) distributions in three orthogonal planes determined from the protocol in Section 9.5, thresholded between $\pm 20$ ppb for the $\chi_I(\vec{r})$ maps and $-5$ to 10 ppb for the $E(\vec{r})$ maps.

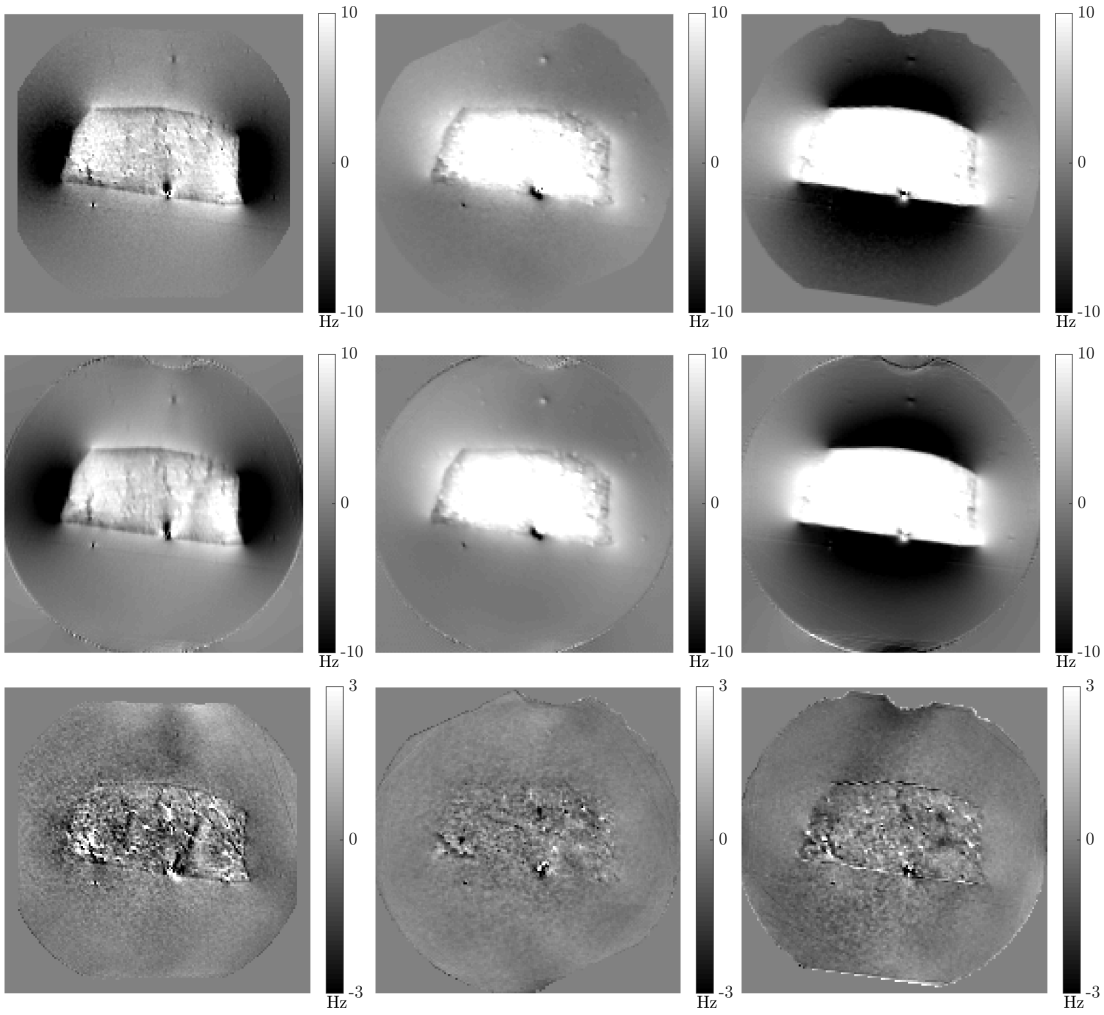
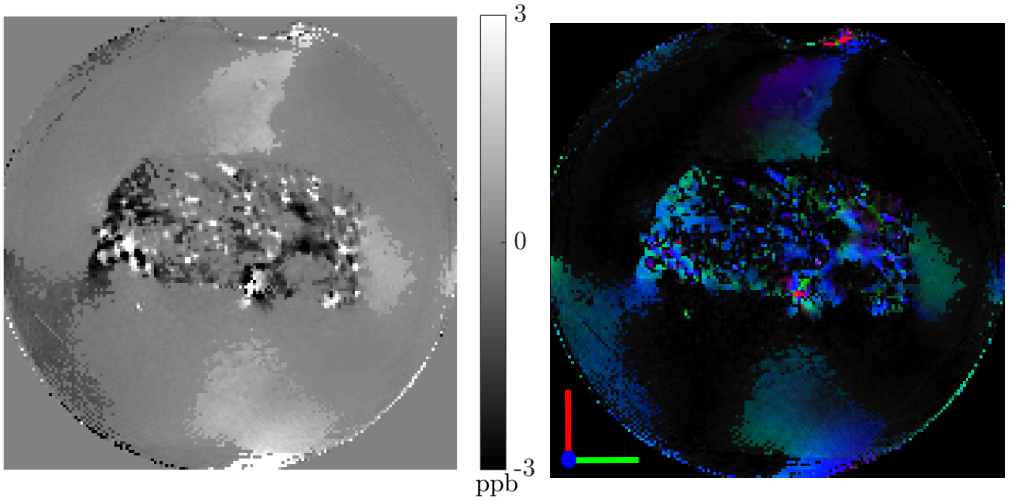



Figure 9.14: Single plane experimental $\Delta B(\vec{r})$ maps (top row) for the 1$^{\text{st}}$ , 13$^{\text{th}}$ and 22$^{\text{nd}}$ dataset, $\Delta B_{\text{rec}}(\vec{r})$, (middle row) and residual (bottom row) thresholded between $\pm 3$ Hz from fitting to a model of $\chi_I(\vec{r})$ and $E(\vec{r})$ using the protocol in Section 9.5.

to that described in the previous section, to examine the existence of cylindrical field perturbers within the sample, $\text{res}_{\text{iso\&exc}}(\vec{r})$ was fitted to the following model:

$$\min_{A(\vec{r}),\hat{v}(\vec{r})} \left\| \text{res}_{\text{iso\&exc}}(\vec{r}) - \left( A(\vec{r}) \cdot \sin^2 \left( \arccos |\hat{B}_0 \cdot \hat{v}(\vec{r})| \right) \right) \right\|_2^2 \tag{9.10}$$

with results shown in Figure 9.15. The minimisation returned relres $= 0.97$, indicating that the model fails to explain the sources of $\text{res}_{\text{iso\&exc}}(\vec{r})$, further suggesting that NMR invisible cylindrical field perturbers, if existing within the sample tissue, have a tiny contribution to $\Delta B(\vec{r})$.




(a) $A(\vec{r})$ (b) $\hat{v}(\vec{r})$

Figure 9.15: Obtained microstructure amplitude (Figure 9.15a) and principal axis of the cylindrical muscle fibres (Figure 9.15b) determined from fitting Equation 9.10 to $\text{res}_{\text{iso\&exc}}(\vec{r})$ (displayed in Figure 9.14). The $\vec{v}(\vec{r})$ map is weighted by $|A(\vec{r})|$ to determine the extent of the orientation dependence, with direction colour-key shown in corner.

## 9.6 Susceptibility Tensor and Chemical Exchange Minimisation

The $\chi_I(\vec{r})$ and $E(\vec{r})$ fitting protocol described in the previous section produced $\chi_I(\vec{r})$ and $E(\vec{r})$ maps that are representative of the underlying phantom distribution, revealing skeletal muscle as being diamagnetic and having a substantial positive chemical exchange offset compared to the surrounding agar. The low relres and excellent agreement between $\Delta B_{\text{rec}}(\vec{r})$ and $\Delta B(\vec{r})$ suggests that any further contributions to $\Delta B(\vec{r})$ in addition to isotropic susceptibility and chemical exchange must be small. However, previous research [1, 4] has provided evidence of an anisotropic susceptibility component within skeletal muscle tissue, as previously discussed in Section 9.2.

The full $\underline{\underline{\chi}}(\vec{r})$ tensor can be obtained via STI (Discussed in Section 7.1.4) to assess the anisotropic susceptibility properties of skeletal muscle. With a sufficient number of well-defined orientations, the inversion should be well-posed, producing a unique solution. From Equations 7.17 and 7.18 (ignoring the undefined value at $k = 0$), the condition number of the unregularised STI minimisation for the multi-orientation data, $C = 24.6$. To assess the contribution of $\chi_A$, the $\chi_I(\vec{r})$ and $E(\vec{r})$ protocol was repeated as above with the additional extension that susceptibility

is now defined as a full $3 \times 3$ $\underline{\underline{\chi}}(\vec{r})$ tensor:

$$\min_{\underline{\underline{\chi}}(\vec{r}),E(\vec{r})} \left\{ \|O_1\|_2^2 + \|O_2\|_2^2 + \cdots + \|O_S\|_2^2 + \beta^2 \left( \left\| \mathrm{M}_{\mathrm{inv}}(\vec{r}) \cdot \underline{\underline{\chi}}(\vec{r}) \right\|_2^2 + \left\| \mathrm{M}_{\mathrm{inv}}(\vec{r}) \cdot E(\vec{r}) \right\|_2^2 \right) \right\} \tag{9.11}$$

and

$$\|O_i\|_2^2 = \left\| \mathrm{M}_{\mathrm{p}_i}(\vec{r}) \cdot \left( B_0 \cdot \left( \mathcal{F}^{-1} \left[ \frac{1}{3} \hat{B}_{0_i} \cdot \underline{\underline{\chi}}(\vec{k}) \cdot \hat{B}_{0_i} - \frac{\left( \vec{k} \cdot \hat{B}_{0_i} \right) \vec{k} \cdot \underline{\underline{\chi}}(\vec{k}) \cdot \hat{B}_{0_i}}{k^2} \right] + E(\vec{r}) \right) - \Delta B_i(\vec{r}) \right) \right\|_2^2 . \tag{9.12}$$

Unfortunately, although an increased sensitivity to noise and artefacts compared to the previous models is expected due to an increased condition number, repeated application of this minimisation protocol yielded $\underline{\underline{\chi}}(\vec{r})$ maps dominated by both noise and artefacts induced by the boundary condition violation at the air-agar surface from the vSHARP protocol (discussed in Section 5.3.3). In addition, large susceptibility artefacts were observed within and surrounding blood vessels in the skeletal muscle sample.

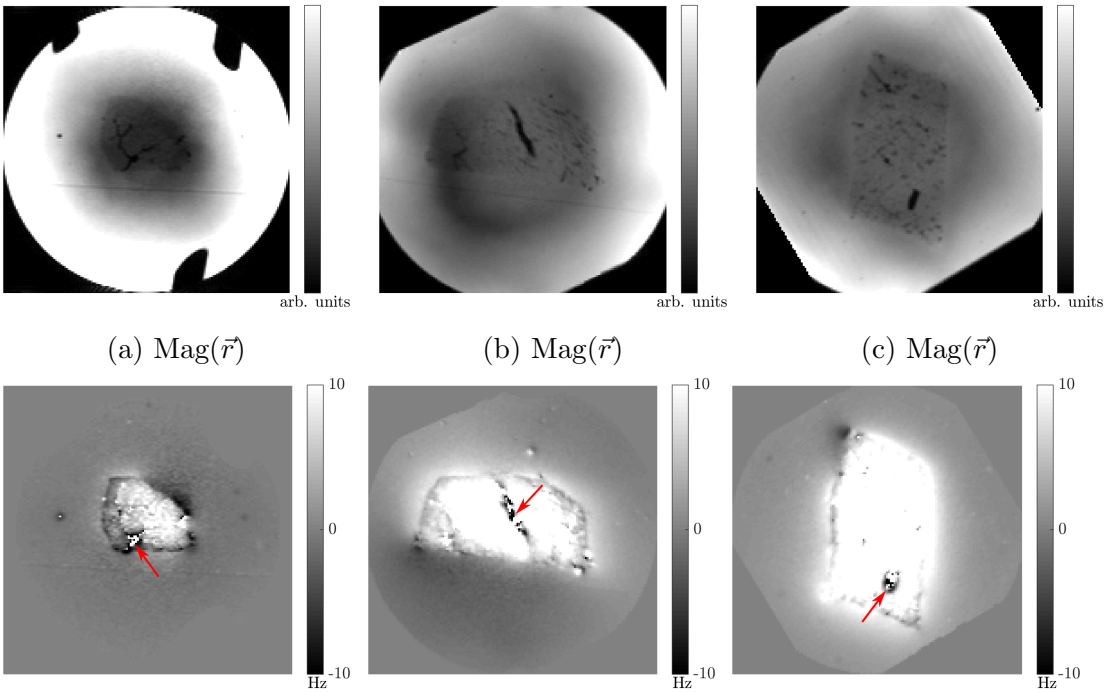
Closer inspection of the experimental $\Delta B(\vec{r})$ maps identified artefacts within and surrounding blood vessels (visualised in Figure 9.16), indicative of remaining phase wraps within the processed phase data, generated due to rapid phase evolution in these regions at a rate higher than the Nyquist limit (discussed in Section 5.2.3). The low $C$ of the $\chi_I(\vec{r})/E(\vec{r})$ protocol in the previous section explains why the minimisations presented there were less sensitive to these experimental and post-processing artefacts. To account for the problems associated with an increased sensitivity to noise, post-processing errors and blood vessel artefacts, the $\underline{\underline{\chi}}(\vec{r})/E(\vec{r})$ minimisation protocol was redesigned as follows:

1. Utilising a modified form of the MMSR-STI protocol [10] (discussed in Section 7.1.5), the volume surrounding the skeletal muscle sample was forced to have an isotropic susceptibility distribution.

2. Areas identified as containing unreliable phase values in the $\Delta B(\vec{r})$ maps (most notably within/surrounding blood vessels and air bubbles) were removed from the weighting masks, $\mathrm{M}_{\mathrm{p}_i}(\vec{r})$, to prevent them for being included in the residual calculation.

This generated the following minimisation protocol:

$$\begin{aligned} \min_{\underline{\underline{\chi}}} \Bigg\{ & \|O_1\|_2^2 + \|O_2\|_2^2 + \cdots + \|O_S\|_2^2 + \beta_1^2 \left\| \mathrm{M}_{\mathrm{inv}}(\vec{r}) \cdot E(\vec{r}) \right\|_2^2 + \\ & \sum_{m=1}^{3} \sum_{n=m+1}^{3} \beta_2^2 \left( \left\| \mathrm{M}_{\mathrm{iso}}(\vec{r}) \cdot \chi_{mn} \right\|_2^2 + \left\| \mathrm{M}_{\mathrm{iso}}(\vec{r}) \cdot (\chi_{mm} - \chi_{nn}) \right\|_2^2 \right) \Bigg\} \end{aligned} \tag{9.13}$$




(a) Mag($\vec{r}$) (b) Mag($\vec{r}$) (c) Mag($\vec{r}$)

(d) $\Delta B(\vec{r})$ (e) $\Delta B(\vec{r})$ (f) $\Delta B(\vec{r})$

Figure 9.16: Experimental magnitude (top row) $\Delta B(\vec{r})$ (bottom row) maps for the 1$^{\text{st}}$ (left column), 13$^{\text{th}}$ (centre column) and 22$^{\text{nd}}$ (right column) dataset, revealing significant artefacts in the vicinity of blood vessels as indicated by the red arrows.

and

$$\|O_i\|_2^2 = \left\| \left( \mathrm{M}_{\mathrm{p}_i}(\vec{r}) - \mathrm{Mun}(\vec{r}) \right) \cdot \left( B_0 \cdot \left( \mathcal{F}^{-1} \left[ \frac{1}{3} \hat{B}_{0_i} \cdot \underline{\underline{\chi}}(\vec{k}) \cdot \hat{B}_{0_i} - \frac{\left( \vec{k} \cdot \hat{B}_{0_i} \right) \vec{k} \cdot \underline{\underline{\chi}}(\vec{k}) \cdot \hat{B}_{0_i}}{k^2} \right] + E(\vec{r}) \right) - \Delta B_i(\vec{r}) \right) \right\|_2^2 \tag{9.14}$$

defining $\mathrm{M}_{\mathrm{iso}}(\vec{r})$ as a mask over the region surrounding the skeletal muscle sample, where susceptibility isotropy is enforced and $\mathrm{M}_{\mathrm{un}}(\vec{r})$ is a mask of unreliable phase voxels. Mask regularisation was again performed on the $E(\vec{r})$ map. Due to computational memory constraints, it was not possible to perform mask regularisation on $\underline{\underline{\chi}}(\vec{r})$.

$\beta_1^2$ and $\beta_2^2$ were both set equal to $10^5$. To assist in rapid convergence, the results for the fit to $\chi_I(\vec{r})$ and $E(\vec{r})$ (Figure 9.12) were input as the initial solution vector. The minimisation was set to terminate when the tolerance fell below $10^{-8}$ and the minimisation converged to this tolerance after 189 iterations, with relres = 0.10.

$\mathrm{M}_{\mathrm{iso}}(\vec{r})$ is visualised in Figure 9.17. $\mathrm{M}_{\mathrm{un}}(\vec{r})$ was generated using the protocol for identifying unreliable phase voxels described in the experimental chapter on *in-vivo* rodent QSM (Section 6.5.2), utilising a combination of empirically thresholded $R_2^*$ maps and phase offset gradients, $\nabla\phi_0(\vec{r})$. $\phi_0(\vec{r})$ was estimated from the phase evolution of the first collected dataset using the protocol outlined in Section

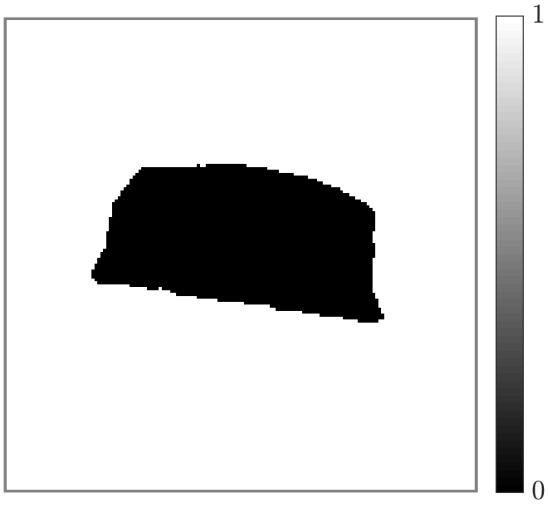



Figure 9.17: Single slice of $\mathrm{M}_{\mathrm{iso}}(\vec{r})$.

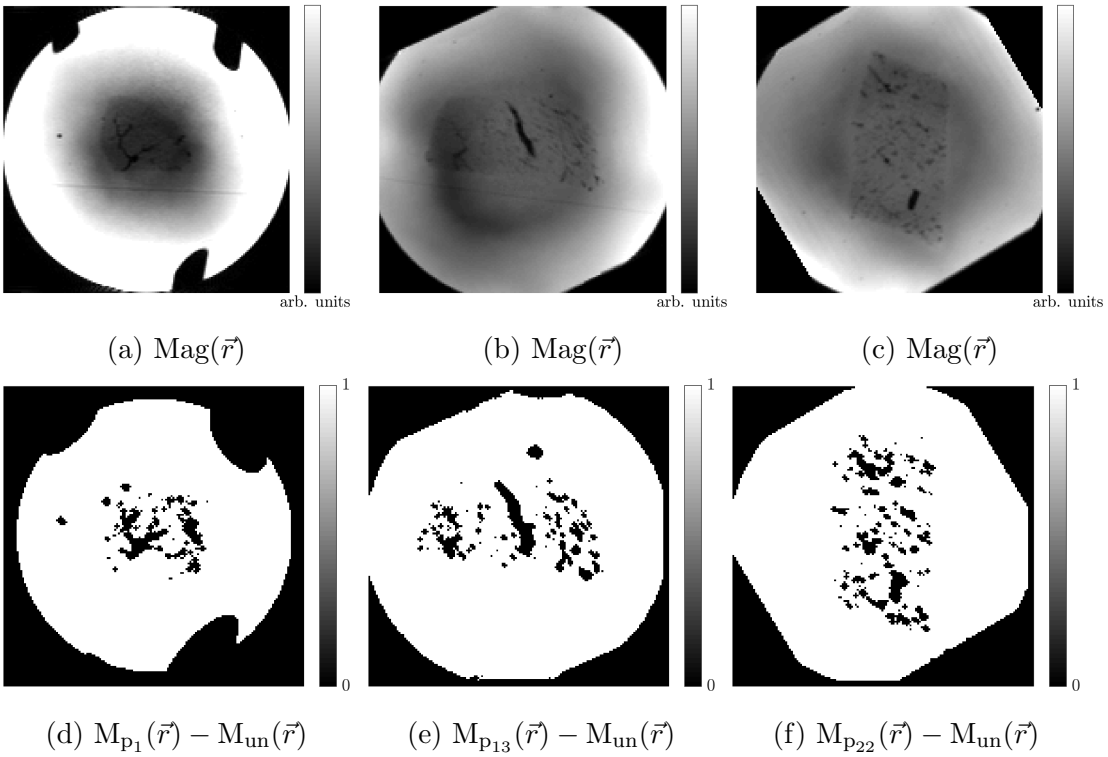
6.5.1. Voxels were considered unreliable if:

$$\left|\frac{\partial\phi_0}{\partial x}\right| + \left|\frac{\partial\phi_0}{\partial y}\right| + \left|\frac{\partial\phi_0}{\partial z}\right| \geq 1\,\mathrm{rad/pixel} \tag{9.15}$$

where the cut-off value was determined empirically. Further unreliable phase voxels were removed by examining the $R_2^*(\vec{r})$ map generated from the dataset acquired at the first orientation. Phase was empirically determined as unreliable if $R_2^* \geq 70\,\mathrm{s}^{-1}$. Due to the sensitivity of the minimisation algorithm to unreliable phase, the in $\mathrm{M}_{\mathrm{un}}(\vec{r})$ mask was dilated by a single voxel in all directions. A single slice of $\mathrm{M}_{\mathrm{p}_i}(\vec{r}) - \mathrm{M}_{\mathrm{un}}(\vec{r})$ for three separate datasets is visualised in Figure 9.18. The mean magnetic susceptibility (equivalent to $\chi_I(\vec{r})$ for anisotropic susceptibility distributions - discussed in Section 7.1.3), $\mathrm{MMS}(\vec{r})$, and eigenvalue/eigenvector distributions, $\lambda(\vec{r})/\vec{v}(\vec{r})$ were derived from the $\underline{\underline{\chi}}(\vec{r})$ data. The anisotropic component, $\chi_A(\vec{r})$, was defined as the difference between the maximum and minimum eigenvalues:

$$\chi_A(\vec{r}) = \lambda_{\max}(\vec{r}) - \lambda_{\min}(\vec{r}) \tag{9.16}$$

consistent with the definition of $\chi_A$ in Equation 9.1, retaining the hypothesis that skeletal muscle is most paramagnetic along the muscle fibres. $\mathrm{MMS}(\vec{r})$ and $E(\vec{r})$ distributions in three orthogonal planes using the modified MMSR-STI protocol and thresholded images are shown in Figures 9.19 and 9.20. Averaging over masks of the skeletal muscle sample and agar phantom (avoiding regions where $\mathrm{M}_{\mathrm{un}}(\vec{r}) = 1$ and defining the agar mask as a 10 mm shell surrounding the skeletal muscle sample), $\mathrm{MMS}_{\mathrm{musc}} = -120 \pm 22\mathrm{ppb}$ and $\mathrm{MMS}_{\mathrm{agar}} = 5.9 \pm 5.8\mathrm{ppb}$, $E_{\mathrm{musc}} = 31 \pm 11\mathrm{ppb}$ and $E_{\mathrm{agar}} = -2.2 \pm 1.8\mathrm{ppb}$, repeating the previous observations that the skeletal muscle sample is more diamagnetic than the surrounding agar and that there is a positive chemical exchange offset originating within skeletal muscle. Comparisons of the reconstructed $\Delta B_{\mathrm{rec}}(\vec{r})$, from the $\underline{\underline{\chi}}(\vec{r})$ and $E(\vec{r})$




(a) $\mathrm{Mag}(\vec{r})$ (b) $\mathrm{Mag}(\vec{r})$ (c) $\mathrm{Mag}(\vec{r})$

(d) $\mathrm{M}_{\mathrm{p}_1}(\vec{r}) - \mathrm{M}_{\mathrm{un}}(\vec{r})$ (e) $\mathrm{M}_{\mathrm{p}_{13}}(\vec{r}) - \mathrm{M}_{\mathrm{un}}(\vec{r})$ (f) $\mathrm{M}_{\mathrm{p}_{22}}(\vec{r}) - \mathrm{M}_{\mathrm{un}}(\vec{r})$

Figure 9.18: Experimental magnitude (top row) and subsequent $\mathrm{M}_{\mathrm{p}_i}(\vec{r}) - \mathrm{M}_{\mathrm{un}}(\vec{r})$ (bottom row) masks for the 1$^{\mathrm{st}}$ (left column), 13$^{\mathrm{th}}$ (centre column) and 22$^{\mathrm{nd}}$ (right column) dataset.

distributions with the original experimental data are shown in Figure 9.21. The minimisation returned relres = 0.10 (avoiding regions where $\mathrm{M}_{\mathrm{un}}(\vec{r}) = 1$). Excellent residual 'flatness' and visual agreement is observed between $\Delta B(\vec{r})$ and $\Delta B_{\mathrm{rec}}(\vec{r})$, though a significant local residual remains in regions containing blood vessels within the skeletal muscle sample. As these blood vessel regions contain artefacts, it is expected that a physically meaningful $\underline{\underline{\chi}}(\vec{r})$ distribution would not be able to explain the field perturbations with these regions. Masking out regions containing field perturbation artefacts ($\mathrm{M}_{\mathrm{un}}(\vec{r}) = 1$), a very small residual is observed between the experimental and simulated data.

A single plane of the obtained $\underline{\underline{\chi}}(\vec{r})$ map with the associated orthogonal eigenvalue/eigenvector matrices are shown in Figures 9.22 and 9.23. Figure 9.24a displays the $\chi_A(\vec{r})$ map, where it can be observed that no susceptibility anisotropy exists surrounding the skeletal muscle sample and the modified MMSR-STI protocol has been successful. However, averaging over a mask of the skeletal muscle sample (avoiding regions where $\mathrm{M}_{\mathrm{un}}(\vec{r}) = 1$), $\chi_{A_{\mathrm{musc}}} = 57 \pm 25\mathrm{ppb}$. This value is much larger than the suggested estimates from the examination of the residual in the previous section and further examination concluded that the high sensitivity to experimental noise, artefacts and post-processing prevented an accurate value of $\chi_A$ from being determined within the skeletal muscle sample.

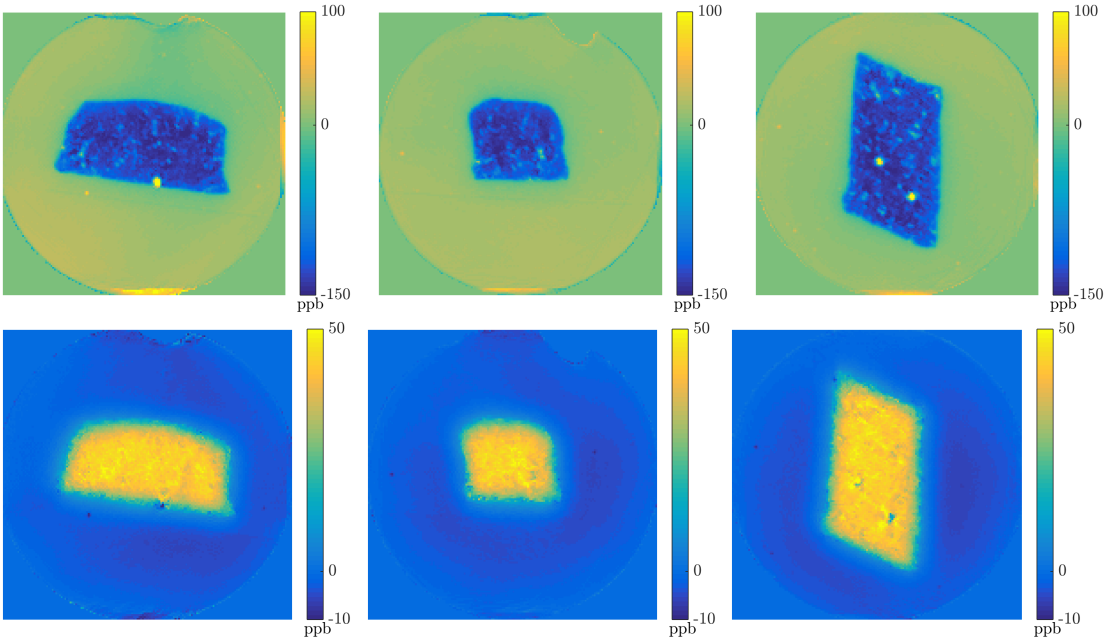



Figure 9.19: MMS($\vec{r}$) (top row) and $E(\vec{r})$ (bottom row) distributions in three orthogonal planes determined from the modified MMSR-STI minimisation in Equations 9.13 and 9.14.

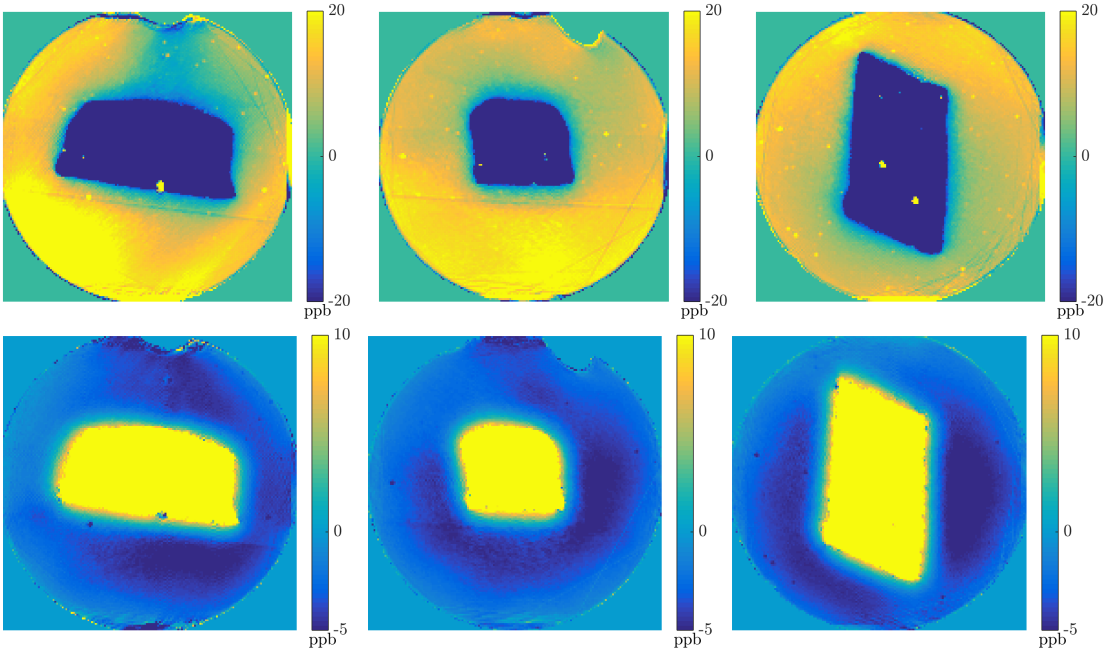



Figure 9.20: MMS($\vec{r}$) (top row) and $E(\vec{r})$ (bottom row) distributions in three orthogonal planes determined from the modified MMSR-STI minimisation in Equations 9.13 and 9.14, thresholded between $\pm 20$ ppb for the $\chi_I(\vec{r})$ maps and $-5$ to 10 ppb for the $E(\vec{r})$ maps.

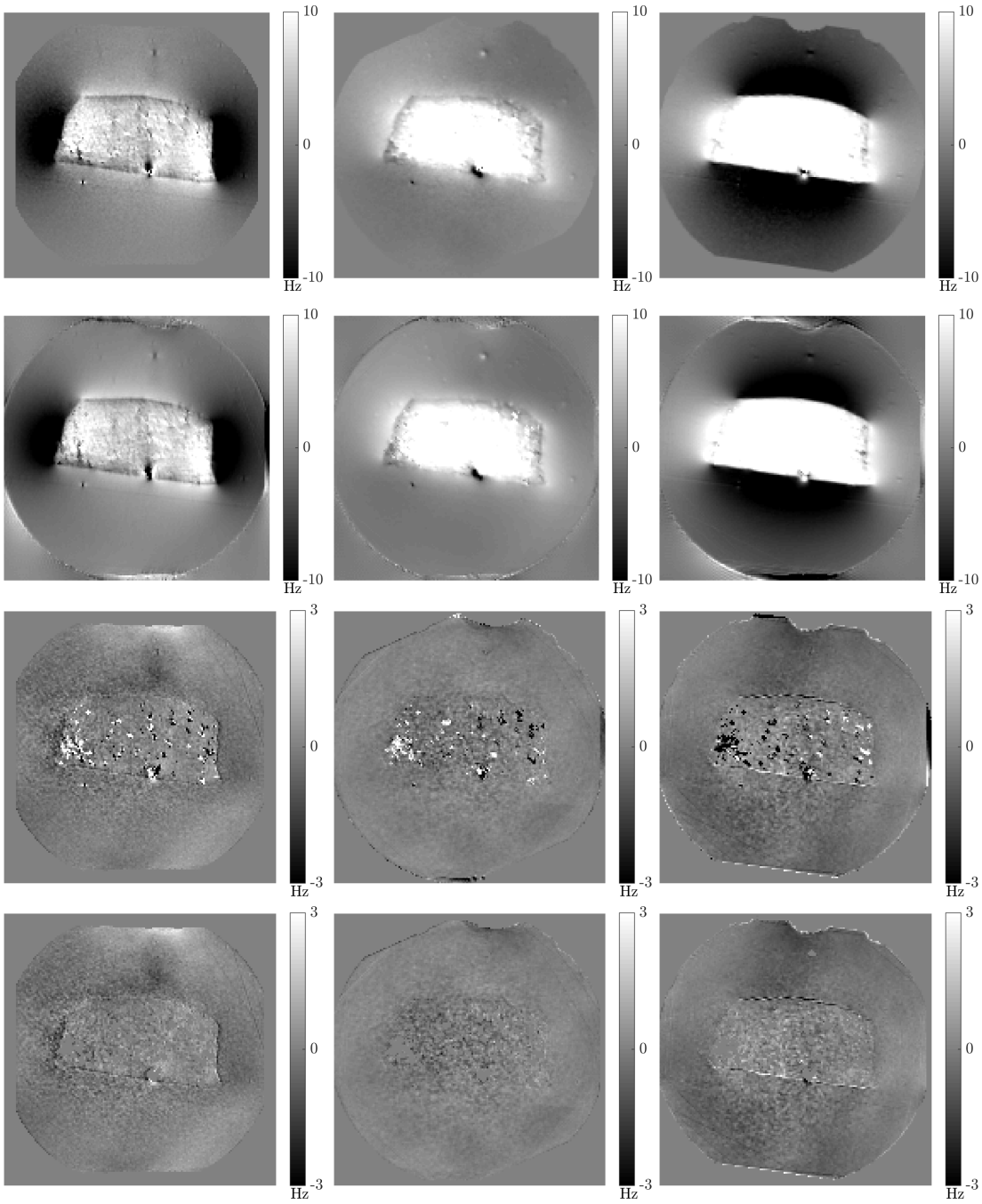



Figure 9.21: Experimental $\Delta B(\vec{r})$ maps (top row) for the 1$^{\text{st}}$ , 13$^{\text{th}}$ and 22$^{\text{nd}}$ dataset, $\Delta B_{\text{rec}}(\vec{r})$, (row second from top) and residual over entire phantom volume (row second from bottom) and over phantom volume avoiding regions where $\text{M}_{\text{un}}(\vec{r}) = 1$ (bottom row) from fitting to a model of $\underline{\underline{\chi}}(\vec{r})$ and $E(\vec{r})$ using the protocol defined in Section 9.6.

## 9.7 Discussion

A complete list of susceptibility and exchange values obtained from the different minimisation models is displayed in Table 9.1. Inclusion of $E(\vec{r})$ substantially reduced the standard deviation of $\chi_I$ over the agar surrounding the sample and

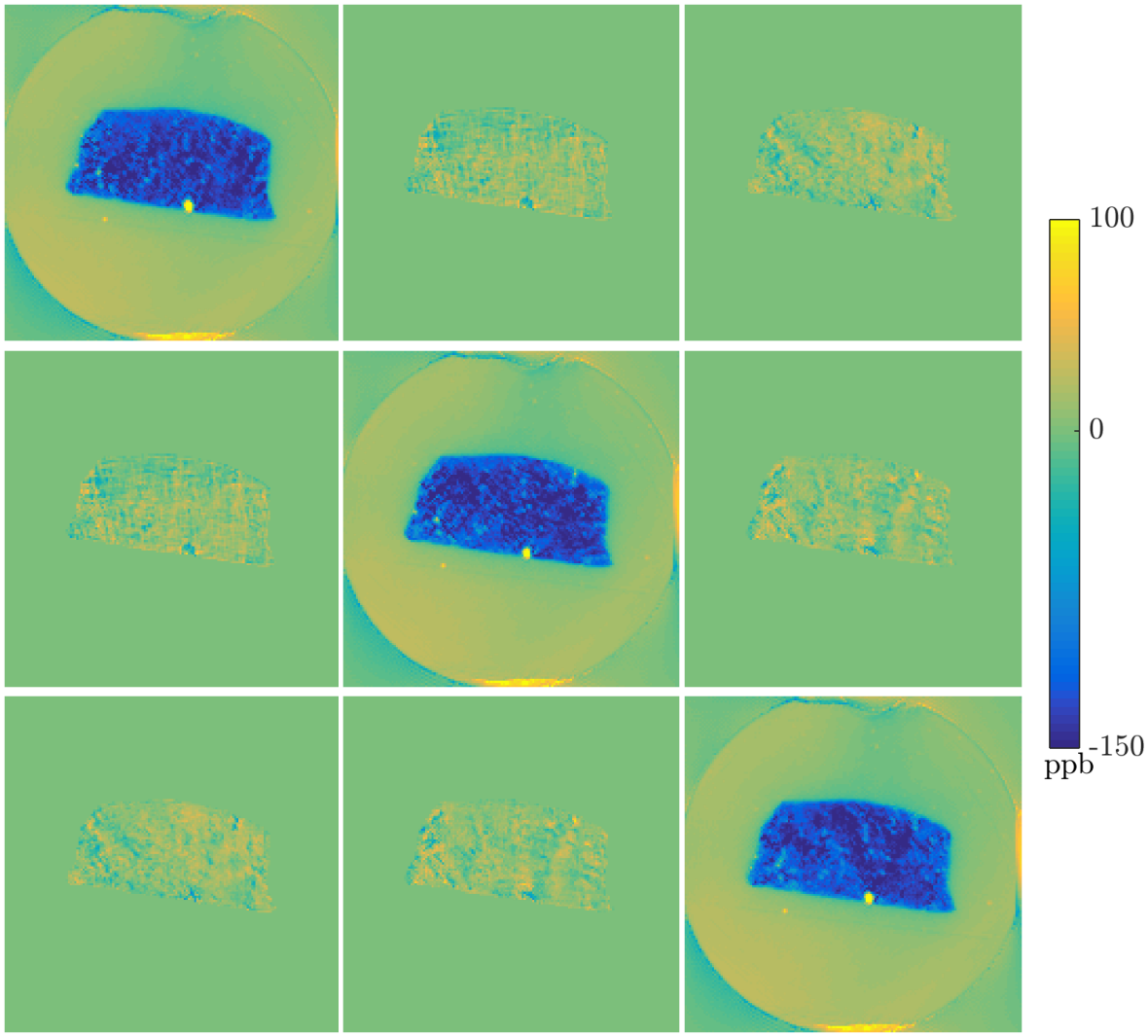
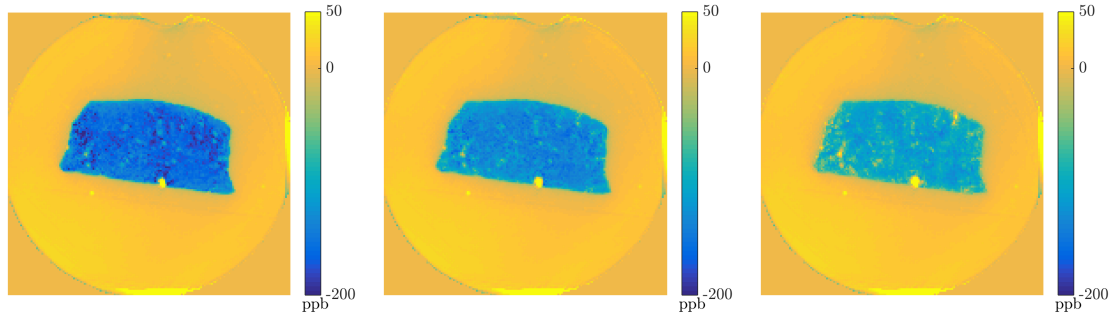


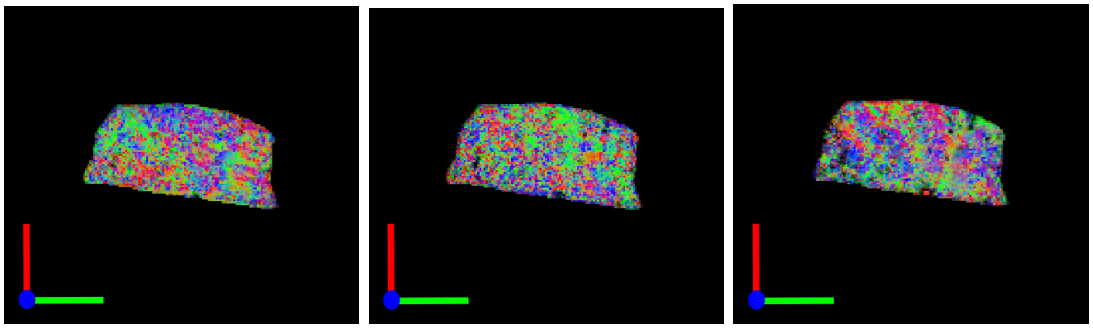

Figure 9.22: Full $3 \times 3$ $\underline{\underline{\chi}}(\vec{r})$ tensor for a single plane determined from the modified MMSR-STI minimisation in Equations 9.13 and 9.14.

| **Parameter** | $\boldsymbol{\chi_I}_{\text{musc}}/\textbf{MMS}_{\text{musc}}$ | $\boldsymbol{\chi_I}_{\text{agar}}/\textbf{MMS}_{\text{agar}}$ | $\boldsymbol{E}_{\text{musc}}$ | $\boldsymbol{E}_{\text{agar}}$ |
|---|---|---|---|---|
| $\boldsymbol{\chi_I}(\vec{\boldsymbol{r}})$ | $-110 \pm 33$ | $7 \pm 29$ | - | - |
| $\boldsymbol{\chi_I}(\vec{\boldsymbol{r}})/\boldsymbol{E}(\vec{\boldsymbol{r}})$ | $-116 \pm 30$ | $6.2 \pm 5.7$ | $32 \pm 11$ | $-2.3 \pm 1.9$ |
| **Modified MMSR-STI** | $-121 \pm 22$ | $5.9 \pm 5.8$ | $31 \pm 11$ | $-2.2 \pm 1.8$ |

Table 9.1: Parameter values obtained from fitting the different magnetic property models to the experimental $\Delta B(\vec{r})$ maps. All units in ppb.




(a) $\lambda_{\text{min}}(\vec{r})$ (b) $\lambda_{\text{mid}}(\vec{r})$ (c) $\lambda_{\text{max}}(\vec{r})$

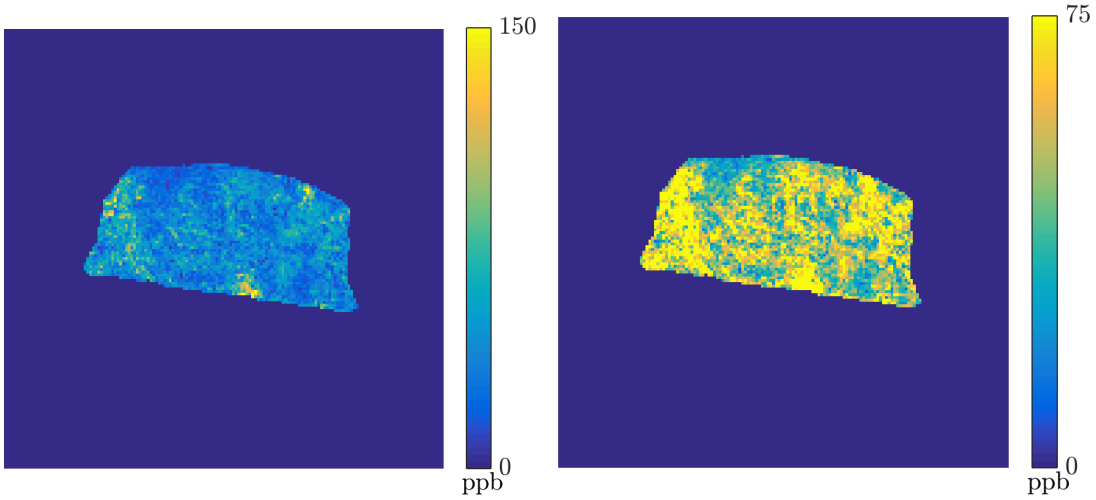


(d) $v_{\text{min}}(\vec{r})$ (e) $v_{\text{mid}}(\vec{r})$ (f) $v_{\text{max}}(\vec{r})$

Figure 9.23: The minimum, middle and maximum eigenvalues/eigenvectors, $\lambda_{\text{min,mid,max}}(\vec{r})/v_{\text{min,mid,max}}(\vec{r})$ of the $3 \times 3$ $\underline{\underline{\chi}}(\vec{r})$ tensor in Figure 9.22 obtained by eigenvalue/vector decomposition. $\vec{v}(\vec{r})$ maps are weighted by $|\lambda(\vec{r})|$ to determine the extent of the orientation dependence, with direction colour-key shown in corner.

analysis of the results indicates that chemical exchange is critical in correctly describing the magnetic properties of *ex-vivo* skeletal muscle embedded in agar. This research is currently inconclusive as to the origin of the chemical exchange and whether or not it is a property of skeletal muscle, the agar, or a combination of the two. Understanding the origin of this effect is important for research on the magnetic properties of skeletal muscle and also generally for *ex-vivo* studies of tissue embedded in agar - knowledge of chemical exchange within the muscle tissue will enhance our understanding of the magnetic properties of skeletal muscle. An observed chemical exchange within the agar highlights the importance of accounting for this effect when performing *ex-vivo* phantom studies with agar. The origin of the chemical exchange could be simply assessed by examining the magnetic properties of an agar phantom with different densities of agar. However, previous experiments have observed chemical exchange contributions originating from the contribution of lipid compartments within skeletal muscle [11], reinforcing the hypothesis that the observed chemical shift is a property of skeletal muscle.

The observation of diamagnetism within the skeletal muscle sample agrees with the research performed by Arnold et al. [1], in addition to preliminary research by Faraday in 1855 [12]. Despite numerous repeats and variations in experimental




(a) $\chi_A(\vec{r})$ (b) $\chi_A(\vec{r})$ thresholded

Figure 9.24: Obtained $\chi_A(\vec{r})$ map (Figure 9.24a) and thresholded $\chi_A(\vec{r})$ map (Figure 9.24b) between 0 to 75 ppb. Results obtained from fitting to a model of $\underline{\underline{\chi}}(\vec{r})$ and $E(\vec{r})$ using the protocol in Section 9.6. $\chi_A(\vec{r})$ defined in Equation 9.16.

analysis, it was not possible to obtain a physically meaningful value of susceptibility anisotropy within the skeletal muscle sample using STI. A thorough analysis of the experimental data led to the following conclusions:

1. Blood vessels within the skeletal muscle sample were not properly accounted for with the dual-echo experimental protocol, due to rapid phase evolution within these regions. The substantial number of blood vessels within the tissue (visualised in the $M_{un}(\vec{r})$ map) generated significant artefacts due to a failure to post-process the phase data within these regions (Figure 9.16). To improve on this, a multi-echo GE protocol is required with short echo spacing, to perform unwrapping over regions of rapid phase evolution using temporal-based unwrapping, similar to that utilised in the experimental chapter on *in-vivo* rodent QSM (Section 6.5.1) .

2. Each orientation was scanned for 553 seconds, providing an SNR that may not be sufficient for STI. In previous studies [13–15], including the recent investigation of the myocardium [4], the samples were scanned at each orientation for a substantially longer period of time, typically on the order of hours. If the anisotropy contribution is small and SNR is too low, experimental noise will dominate the fitting, despite the availability of scans obtained at a large number of different orientations.

3. The SNR within the phantom displayed a heterogeneous distribution beyond the underlying anatomical structure of the skeletal muscle sample, increasing the sensitivity to noise within certain regions of the phantom. The

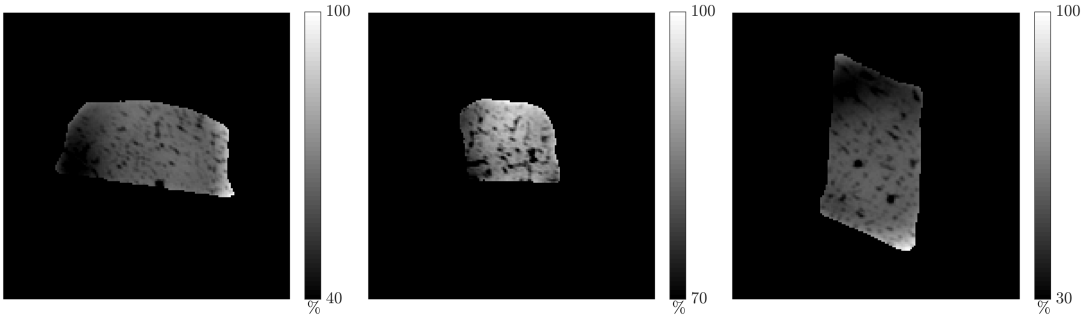



Figure 9.25: Average experimental SNR over the skeletal muscle in three orthogonal planes as a relative percentage.

heterogeneity of the SNR resulted mainly from $B_1(\vec{r})$ inhomogeneity, which is significant at 7T [16] and was clearly observed in the experimental magnitude images of the phantom (example in Figure 9.3a). However, problems induced by a heterogeneous SNR distribution could be reduced in a multi-orientation study with a spherical agar phantom. If the $B_1(\vec{r})$ distribution remains independent of the phantom orientation (due to the spherical symmetry and constant density of the agar), if numerous datasets are collected at different orientations, different regions of the phantom will be sampled with both low and high SNR. Orientation-independent $B_1(\vec{r})$ inhomogeneity was observed in the collected experimental magnitude data of the phantom. However, as the multi-orientation datasets were only sampled over a section of the spherical surface (Figure 9.2) rather than the entire sphere, certain regions of the agar phantom were repeatedly sampled with a significantly lower SNR (visualised in Figure 9.25).

From analysis of the residual in the $\chi_I(\vec{r})/E(\vec{r})$ protocol, an upper bound can be placed on the susceptibility anisotropy of the skeletal muscle sample of $\sim 10\,\text{ppb}$, in agreement with the myocardium paper [4], but substantially lower than 250 ppb quoted by Arnold et al. [1]. Previous studies investigating skeletal muscle via DTI protocols [2, 3, 17] have reported a low fractional anisotropy within *ex-vivo* and *in-vivo* skeletal muscle samples ($\sim$ 0.15-0.3) which reinforces the observation that the susceptibility anisotropy within muscle tissue is low.

As the sample was purchased from a local supermarket, little is known about the treatment of the sample prior to scanning: the time taken between slaughter and scanning, in addition to any treatment of the sample post-slaughter, is undocumented. This is important when considering the magnetic properties of skeletal muscle tissue, as tissue degeneration and treatment may have an impact on the magnetic properties of the sample. For example, Arnold et al. [1] noted that an increased dryness of the tissue sample reduced the diamagnetism of the tissue.

Furthermore, it can be hypothesised that an increased time between slaughter and scanning will increase the degradation of the well-ordered muscle fibres, reducing the susceptibility anisotropy.
Bonny et al. [2] reported that different skeletal muscle samples are characterised by significant variations in muscle fibre arrangement, with some samples displaying a more complex 'fan-like' structural composition and a lower degree of fractional anisotropy. Exact details of the expected composition of the skeletal muscle sample used in this experiment are not known, as the position of the loin cut is not known. Due to challenges in performing a successful DTI acquisition on the sample at 3T, it was not possible to include this as an addition contrast. However, DTI, combined with an improved GE experimental acquisition could assist in further quantifying and validating the observations made within this experiment. Furthermore, DTI on skeletal muscle tissue is a well-established field (details can be found in a recent review paper by Oudeman et al. [3]), which will assist in directly comparing results to quantify skeletal muscle properties further.

## 9.8 Conclusion

This project confirms skeletal muscle as diamagnetic relative to agar, the existence of a large chemical exchange contribution within an agar-muscle phantom and the importance in accounting for chemical exchange contributions to quantify the magnetic properties of *ex-vivo* skeletal muscle using least-squares minimisation algorithms. To extend this project, improvements will be required both in the experimental protocol and the quality of the acquired sample to allow the susceptibility anisotropy of the tissue to be assessed. A multi-echo GE protocol with improved SNR and increased orientation range should produce adequate experimental data for analysis. Furthermore, obtaining a sample of skeletal muscle tissue a short period of time post-slaughter will ensure the quality of the tissue structure in addition to reducing artefacts within blood vessels further amplified by a reduced water content. With continued research, the magnetic properties of skeletal muscle will be successfully quantified and progress can be made towards *in-vivo* study.

# Bibliography


[1] William Arnold, Richard Steele, and Helmut Mueller. On the magnetic asymmetry of muscle fibers. *Proceedings of the National Academy of Sciences*, 44(1):1–4, 1958.

[2] Jean-Marie Bonny and Jean-Pierre Renou. Water diffusion features as indicators of muscle structure *ex-vivo*. *Magnetic resonance imaging*, 20(5):395–400, 2002.

[3] Jos Oudeman, Aart J Nederveen, Gustav J Strijkers, Mario Maas, Peter R Luijten, and Martijn Froeling. Techniques and applications of skeletal muscle diffusion tensor imaging: a review. *Journal of Magnetic Resonance Imaging*, 2015.

[4] Russell Dibb, Yi Qi, and Chunlei Liu. Magnetic susceptibility anisotropy of myocardium imaged by cardiovascular magnetic resonance reflects the anisotropy of myocardial filament $\alpha$-helix polypeptide bonds. *Journal of Cardiovascular Magnetic Resonance*, 17(1):60, 2015.

[5] Winston X Yan, Karen J Mullinger, Matt J Brookes, and Richard Bowtell. Understanding gradient artefacts in simultaneous EEG/fMRI. *Neuroimage*, 46(2):459–471, 2009.

[6] Hussein S. Abdul-Rahman, Munther A. Gdeisat, David R. Burton, Michael J. Lalor, Francis Lilley, and Christopher J. Moore. Fast and robust three-dimensional best path phase unwrapping algorithm. *Appl. Opt.*, 46(26):6623–6635, Sep 2007.

[7] Pinar Senay Özbay, Andreas Deistung, Xiang Feng, Daniel Nanz, Jürgen Rainer Reichenbach, and Ferdinand Schweser. A comprehensive numerical analysis of background phase correction with V-SHARP. *NMR in Biomedicine*, 2016.

[8] Oscar Nestares and David J Heeger. Robust multiresolution alignment of MRI brain volumes. *Magnetic Resonance in Medicine*, 43(5):705–715, 2000.

[9] Samuel Wharton and Richard Bowtell. Gradient echo based fiber orientation mapping using $R_2^*$ and frequency difference measurements. *Neuroimage*, 83:1011–1023, 2013.

[10] Xu Li and Peter Zijl. Mean magnetic susceptibility regularized susceptibility tensor imaging (MMSR-STI) for estimating orientations of white matter fibers in human brain. *Magnetic resonance in medicine*, 72(3):610–619, 2014.

[11] Lidia S Szczepaniak, Robert L Dobbins, Daniel T Stein, and J Denis McGarry. Bulk magnetic susceptibility effects on the assessment of intra-and extramyocellular lipids *in-vivo*. *Magnetic resonance in medicine*, 47(3):607–610, 2002.

[12] Michael Faraday. *Experimental researches in electricity*, volume 3. 1855.

[13] Wei Li, Bing Wu, Alexandru V Avram, and Chunlei Liu. Magnetic susceptibility anisotropy of human brain *in-vivo* and its molecular underpinnings. *Neuroimage*, 59(3):2088–2097, 2012.

[14] Chunlei Liu, Wei Li, Bing Wu, Yi Jiang, and G Allan Johnson. 3D fiber tractography with susceptibility tensor imaging. *Neuroimage*, 59(2):1290–1298, 2012.

[15] Luke Xie, Russell Dibb, Gary P Cofer, Wei Li, Peter J Nicholls, G Allan Johnson, and Chunlei Liu. Susceptibility tensor imaging of the kidney and its microstructural underpinnings. *Magnetic resonance in medicine*, 73(3):1270–1281, 2015.

[16] John Thomas Vaughan, Michael Garwood, CM Collins, W Liu, L DelaBarre, G Adriany, P Andersen, H Merkle, R Goebel, MB Smith, et al. 7T vs. 4T: RF power, homogeneity, and signal-to-noise comparison in head images. *Magnetic resonance in medicine*, 46(1):24–30, 2001.

[17] Martijn Froeling, Aart J Nederveen, Dennis FR Heijtel, Arno Lataster, Clemens Bos, Klaas Nicolay, Mario Maas, Maarten R Drost, and Gustav J Strijkers. Diffusion-tensor MRI reveals the complex muscle architecture of the human forearm. *Journal of Magnetic Resonance Imaging*, 36(1):237–248, 2012.

# Chapter 10

# Conclusion

## 10.1 Overview

The work presented within this thesis underlines the importance of extending beyond a model of isotropic susceptibility to explain the sources of experimental field perturbations observed within tissue, highlighting the need to take great care in describing results as quantitative. In particular:

- Anisotropic susceptibility and NMR-invisible non-spherical susceptibility inclusions within tissue generate important orientation-dependent susceptibility effects.
- Chemical exchange introduces local, orientation-independent field perturbations within $\Delta B(\vec{r})$ maps which can prevent physically meaningful distributions of $\chi_I(\vec{r})$ being generated using QSM methodology. This is most clearly observed in the work examining the magnetic properties of skeletal muscle (Chapter 9), where failure to account for chemical exchange generated a non-physical distribution of $\chi_I(\vec{r})$ within and surrounding the skeletal muscle sample.
- Multi-compartmental signal evolution implies that in some tissue types, phase is TE-dependent.

Without a thorough consideration of these additional magnetic properties, a quantitative interpretation of results is challenging. Furthermore, if protocols do not consider the impact of these additional sources of field perturbations, inconsistencies will appear when comparing experimental results to previously obtained literature in some tissue types. However, these additional magnetic field perturbations provide researchers with the opportunity to quantify the magnetic properties of tissue beyond isotropic susceptibility, which has fantastic implications for our

understanding of tissue structure and disease mechanisms. The groundbreaking work on these additional sources (discussed in detail in Chapter 7) has already begun to quantify the properties of tissue and substantially expand the potential of MRI as a technique to examine microstructural content.

Finally, the research presented within this thesis highlights the importance of exercising care when applying post-processing protocols and thoroughly scrutinising results, to ensure that observations are not the product of experimental or post-processing artefacts. As detailed in Chapters 5 and 7, there are numerous methods to process phase datasets and an optimised post-processing timeline requires careful consideration. In this thesis, the three experimental chapters utilised three different post-processing protocols, designed to consider the experimental data properties, ensuring that the protocols could be successfully implemented and minimising artefacts. However it was not always possible to prevent artefacts in the post-processed data (e.g. artefacts within and surrounding blood vessels within the muscle tissue - Chapter 9) and as post-processing of phase is not necessarily a voxelwise technique, this must be considered when interpreting results over the entire ROI.

## 10.2 Future Work

Future directions for the three projects presented within this thesis are clear. In Chapter 6, further analysis and comparisons of the multi-modal experimental data collected in *in-vivo* rats is necessary to quantify the neuroplasticity changes before and after the water maze task and to examine correlations between the experimental data. This work is currently being undertaken by researchers within CUBRIC and the Department of Neurobiology in Tel-Aviv University, with SPMIC input when discussing the $\chi_I(\vec{r})/R_2^*(\vec{r})$ maps.

In Chapter 8, further work is required to optimise the novel FDM algorithm, quantifying and removing sources of artefacts within the frequency difference maps, in addition to the development of a rapid 3D FDM sequence via improved pulse sequences. Beyond this, FDM will become a valuable tool in further quantifying signal compartmentalisation within the brain and beyond. Work is currently ongoing at the SPMIC to develop a pulse sequence to implement these improvements, with a thorough analysis being undertaken to understand the sources of induced signal inhomogeneity within the frequency difference maps.

In Chapter 9, a repeated experimental protocol accounting for blood vessel artefacts and low SNR will allow the quantification of susceptibility anisotropy within the skeletal muscle sample. Furthermore, a fresh sample obtained directly after

slaughter with a known underlying tissue composition (from details of the cut), in addition to a separate DTI acquisition will further the quantification of the magnetic properties of skeletal muscle. Results from the *ex-vivo* analysis will provide a greater understanding of the requirements of an *in-vivo* examination of the magnetic properties of skeletal muscle, in addition to a hypothesis of the expected properties of *in-vivo* skeletal muscle.

## 10.3 Final Remarks

Quantitative phase imaging has a clear future status in progressing human understanding of microstructural tissue properties *in-vivo* and research performed thus-far highlights its potential as a clinical tool for disease diagnosis and treatment planning. The work presented within this thesis details both the necessity of careful consideration of experimental data acquisition and a well-designed post-processing protocol, in addition to the numerous mechanisms that quantitative phase imaging can provide a user about tissue microstructure. With careful analysis, the sources of contrast within phase maps will continue to be revealed and the technique's potential/limitations as both a research and clinical tool will be well understood. Only further investigation will reveal the future of quantitative phase imaging within modern medicine.